FEASIBILITY OF EXTERIOR AIR BARRIERS IN TIMBER FRAME CONSTRUCTION

Jelle LANGMANS

Supervisor:
Prof. dr. ir. arch. S. Roels

Members of the Examination Committee:
Prof. dr. ir. C. Vandecasteele, chair
dr. ir. R. Klein, co-supervisor
Prof. dr. ir. D. Berckmans, assessor
Prof. dr. ir. arch. A. Janssens, assessor
(Ghent University)
Prof. dr. ir. H. Janssen
Prof. dr. ir. S. Geving
(Norway University of Science and Technology)
Prof. dr. ir. J. Grunewald
(Technical University of Dresden)

Dissertation presented in partial fulfilment of the requirements for the degree of Doctor in Engineering Science

May 2013

© 2013 KU Leuven, Science, Engineering & Technology
v.u. Leen Cuypers, Arenberg Doctoraatsschool, W. de Croylaan 6, 3001 Heverlee

Alle rechten voorbehouden. Niets uit deze uitgave mag worden vermenigvuldigd en/of openbaar gemaakt worden door middel van druk, fotokopie, microfilm, elektronisch of op welke andere wijze ook zonder voorafgaandelijke schriftelijke toestemming van de uitgever.

All rights reserved. No part of the publication may be reproduced in any form by print, photoprint, microfilm, electronic or any other means without written permission from the publisher.

ISBN 978-94-6018-647-9
D/2013/7515/33

Voorwoord

I think we have all experienced passion that is not in any sense reasonable.
Stephen Fry

Hoe jammer het vanuit wetenschappelijk oogpunt ook mag klinken vormt het dankwoord - ook al wordt het haast in één adem op de vooravond van het drukproces geschreven - zonder twijfel de meest gelezen paragraaf van een doctoraatsthesis. Waarom dan vier jaar gepassioneerd zweten en zwoegen aan die andere tweehonderd bladzijden? Het antwoord ligt voor de hand; zonder de input en steun van de mensen die hierin aan bod komen, was dit werk nooit uit de printer gerold! Ik wens hen dan ook graag uitvoerig te danken hier.

In eerste instantie wil ik het belang van mijn wetenschappelijk promotor sterk in de verf zetten. Staf, het was een voorrecht te kunnen leren van jouw jarenlange ervaring in de hygrothermische analyse van bouwcomponenten. Je zorgeloos optimisme en haast onbegrensd geduld werkte ongelooflijk aanstekelijk. Bedankt voor het grote vertrouwen en de vrijheid die je mij liet om dit pad te bewandelen, maar het toch bij te sturen waar nodig. Niet alleen als wetenschapper maar ook als mens heb je me de afgelopen jaren enorm geïnspireerd.
Daarnaast wil ik het belang van mijn copromotor zeker niet vergeten. Ralf, al groeide onze onderzoeksinteresse steeds verder uit elkaar, je verdient een grote erkenning voor jouw aandeel in deze tekst. Als promotor van mijn masterproef triggerede je mijn interesse in wetenschappelijk onderzoek. Jouw steun en vertrouwen in mij gaven een boost aan de opstart van dit project. Hiervoor wil ik je erg bedanken!

Naast mijn promotoren wil ik ook de andere leden van mijn Begeleidingscommissie, Arnold Janssens en Daniël Berckmans, bedanken voor hun kritische opmerkingen en hulpvolle suggesties onderweg en de hulp bij het bijvijlen van de finale tekst. Ook de bijdrage van andere leden van de Examencommissie wil ik voor dit laatste erkennen. Hans in het bijzonder. Met jou toptransfer naar België heb ik nog een jaartje kunnen genieten van je expertise in dit veld. De energie, passie en efficiëntie gecombineerd met de nodige zin voor relativering, waren een voorbeeld voor mij.

Een behoorlijke fractie van dit werk kwam tot stand op de lijn Leuven-Gent. De motivatie om deze verbinding telkens te halen in de vroege uurtjes was soms ver zoek, ware het niet dat ik fantastische collega's mocht kennen aan het labo Bouwfysica. Hun tips and tricks rond software en meetmethoden, de interessante discussies, praktische hulp maar ook (en laat ons dat vooral niet vergeten) de onderbroeken humor tijdens de koffiepauze hebben de efficiëntie in het realiseren van dit werk getild. Toch een paar mensen in het bijzonder. Wout, E-man, vriend. Ik herinner nog steeds je enthousiasme toen ik voor de eerste keer het labo binnenstapte (en jij je verlost zag van je Rookie-status). Sindsdien bleef je een onmisbare pion in deze vier jaar. We deelden lief en leed en ik ben potverdikke fier dat we hier samen over de finish stappen. Roel, jou wil ik bedanken om mij af en toe van mijn bureau af te sleuren om te gaan zwemmen of lopen en je onmetelijke gastvrijheid in casa Hendrickx. Mijn culinaire hoogtepunten in het Leuvense waren ongetwijfeld in jouw aanwezigheid. Ook je grote interesse in mijn - soms mini - resultaatjes werkte zeer motiverend. Evy, ook jou wil ik speciaal vermelden omwille van de vele nuttige discussies en gezelschap tijdens de avondshiften (voor mij was het alleszins toch avond). De spaghetti in Alma 3 smaakte toch net iets beter met jou erbij. Ook bedankt voor de vele keren dat je van op afstand dat kleine muisklikje deed of één van mijn metingen kon checken. Het heeft me heel wat kopzorgen en treinritten bespaard. Wim, Patricia merci voor de belangrijke ondersteuning bij de vele metingen. Naast het feit dat ik zoveel van jullie jarenlange expertise heb kunnen genieten (ik denk dat ik de haperende sensoren op één hand kan tellen), was het ook gewoon steeds heel leuk met jullie samen te werken in het labo.

Daarnaast wil ik ook uitdrukkelijk de collega's van KaHo Sint-Lieven bedanken. In het bijzonder Luc, Alexis en Ralf die me in de zomer van 2008 de kans gaven een IWT-specialisatiebeurs voor te bereiden. Al kon ik mij destijds moeilijk inbeelden wat jullie beslissing van die middag zou inhouden, het heeft veel deuren geopend om internationaal onderzoek te verrichten in mijn grote interessegebied. Daarnaast wil ook de andere DuBo's expliciet vermelden. Hilde, Barbara bedankt voor jullie enthousiasme! Alexis, Veerle jullie praktische inzichten en contacten in de Vlaamse 'houtskeletbouw-scene' hebben met een heel eind op weg geholpen.

Maar het waren niet alleen déze twee onderzoeksgroepen die mijn onderzoek vooruit hielpen. Ook de groepen van Michel en Arnold aan de UGent wil ik bedanken voor de vele keren dat ik jullie BlowerDoor mocht lenen, voor de interessante discussies en tips en de gezellige momenten op congressen en PhD-days. In addition, also the help from the Delphin-guys from the Technical University of Dresden (TUD) should be highlighted here. It was an honour to collaborate with this strong research group under the expert guidance of Prof. Grunewald. Special thanks to Andreas, Ulli, Stefan for the great support and pleasant

moments in the 'biergarten' during my research visits.

Naast alle onderzoekers wil ik nog enkele zeer belangrijke personen in mijn leven bedanken, die uiteraard ook een groot aandeel in dit verhaal hebben. Eerst en vooral mijn ouders. Zonder jullie was er van mij niet veel in huis gekomen. Nee, serieus. Jullie wil ik niet alleen uitdrukkelijk bedanken voor het vele geduld, begrip en steun in de aflopen vier jaar, maar ook voor alles ervoor. Nu ik zelf half de twintig ben, besef ik meer en meer wat voor prachtige opvoeding en kansen ik van jullie kreeg. Daarnaast wil ook mijn schoonouders, Eric en Annick, vermelden. Door het toeval dat ik reeds op mijn 15de op de vrouw van mijn leven botste, loop ik bij jullie toch ook al een tiental jaar de deur plat. Jullie waren zeker een stimulans in de keuze om dit doctoraat aan te vatten én af te maken. Ook Dieter, "de groten broer", wil ik hier bedanken voor de ontspannende weekendjes tussendoor. Verder hebben ook mijn petekindjes, Aaron en Aiko, al beseffen ze het zelf nog niet, toch bijgedragen. Al was het maar door me af en toe te laten beseffen met hun glimlach, dat er belangrijkere dingen zijn dan convectiestromen in minerale wol.

En dan eindelijk, mijn lievelingsduif. Aurélie, jij verdient zonder twijfel de grootste dankjewel. Met je lieve woorden, uitdagende prikkels en je buitengewone boboti, gumbo of meatballs (om er maar enkele te noemen) kon je steeds mijn batterijen weer opladen. Ik besef nu (bij zien van je overstock aan confituur en kilometers gebreide sjaals) dat ik er weinig voor je was de laatste maanden. Ik hoop - al is het waarschijnlijk onevenaarbaar - dat ik nu een even grote steun mag zijn tijdens het schrijven van jouw doctoraat.

Jelle

Gent, mei 2013

Onderzoek gefinancierd door een specialisatiebeurs (nr. 81153) van het Instituut voor de Aanmoediging van Innovatie door Wetenschap en Technologie in Vlaanderen (IWT-Vlaanderen). Deze steun wordt in dank erkend

Abstract

The primary objective of the present work is assessing the feasibility of exterior air barrier systems in highly insulated timber frame construction. The first part of this thesis presents *in situ* and laboratory measurements that verify whether acceptable airtightness levels can be achieved through improving the continuity of the wind barrier. These investigations quantify typical air leakage paths in such systems and, further, shed light on the practical aspects of its execution. The second part of the study examines the hygrothermal behaviour of lightweight elements with an exterior air barrier. This aspect covers both experimental and numerical work and is restricted to wall elements only. A new vertical hotbox/coldbox test setup was applied to simulate the hygrothermal performance of full-scale walls under controlled climate conditions. In addition to these measurements, the study examined the onset of interstitial condensation on hygroscopic and/or capillary active air barrier materials on smaller test specimens. The thesis at hand will further outline a numerical modelling strategy to assess the heat, air and moisture (HAM) transport in lightweight walls. Herein, strong emphasis lies in the evaluation of the presented modelling approach with a combination of benchmarks from the literature and the experimental data obtained in this work. Finally, annual numerical simulations assessing the hygrothermal performance of exterior air barriers in cold and moderate climates will be presented. A parameter study will examine the (1) behaviour of various wall assemblies, (2) identify the impact of bad workmanship and (3) illustrate its behaviour in several European climates.

Keywords: exterior air barrier, natural convection, laboratory investigation, numerical HAM-modelling, timber frame construction.

Samenvatting

Het voornaamste doel van dit onderzoek is de beoordeling van sterk geïsoleerde lichtgewicht constructies met een extern luchtscherm. Het eerste deel van de thesis onderzoekt of aanvaardbare luchtdichtheidsniveau's kunnen behaald worden door het gebruik van verbeterde windschermen. Dit gebeurt aan de hand van *in situ* en laboratorium metingen. Dit experimenteel onderzoek quantificeert typische luchtlekken in deze systemen en brengt belang-rijke praktische aspecten in de realisatie van externe luchtschermen naar voor. Het tweede luik van dit doctoraatsonderzoek bestudeert het hygrothermisch gedrag van houtskelet ele-menten met een extern luchtscherm. Dit aspect werd onderzocht door een combinatie van experimenteel en numeriek werk en is beperkt tot buitenwanden. Een nieuwe meet-opstelling werd gerealiseerd om het hygrothermisch gedrag van lichtgewicht wanden op ware grootte te testen onder gecontroleerde klimaatcondities. Verder onderzoekt dit werk inwendige condensatie op hygroscopische en/of capillaire luchtschermen in een kleinere meetopstelling. Ook stelt deze thesis een numerieke modelleringsmethode voor om het warmte, lucht en vochttransport in lichtgewicht constructies te simuleren. Hierin ligt de focus sterk op de evaluatie van het numeriek model met een combinatie van validatie projecten uit de literatuur en de in dit werk gegenereerde experimentele dataset. Het laatste deel van deze verhandeling beoordeelt aan de hand van jaarlijkse simulaties het hygrothermisch gedrag van externe luchtschermen in koude en gematigde klimaatzones. Deze simulaties bestuderen (1) het gedrag van verschillende wandopbouwen, (2) de impact van uitvoeringsfouten en (3) de prestatie in verschillende Europese klimaten.

Keywords: externe luchtdichtheid, natuurlijke convectie, experimenteel, numerieke simulatie, houtskeletbouw.

Contents

Voorwoord i

Abstract v

Samenvatting vii

1 Introduction and Problem Statement 1

1.1 Aims . . . 3

1.2 Methodology and outline of the work . . . 3

2 State-of-the-art 5

2.1 Global building airtightness and requirements . . . 5

2.1.1 Characterisation of building airtightness . . . 7

2.1.2 Building airtightness requirements in Europe . . . 8

2.1.3 Common practice in timber frame Passivhaus construction in Belgium 10

2.2 Experimental work on hygrothermal performance of lightweight components . 12

2.2.1 Thermal effects of air movement in timber frame wall elements . . . 13

2.2.2 Hygric effects of air movement in timber frame wall elements . . . 17

2.2.3 Review of experimental methods . . . 23

2.3 Numerical models for Heat, Air and Moisture in building components . . . 29

2.3.1 Air transport implementations . . . 30

2.3.2 Consideration of cavity ventilation in HAM-modelling . . . 31

2.4 Moisture control in timber frame building envelopes . . . 33

2.4.1 Moisture performance limit states . . . 33

2.4.2 Moisture control strategies . . . 35

2.5 Conclusions . . . 37

2.5.1 Research questions . . . 39

3 *In situ* Air Leakage Measurements of Exterior Air Barriers Systems 41

3.1 Experiences from Norway: stepwise pressurisation testing . . . 42

3.1.1 Summary . . . 46

3.2 Investigation on the practical implications of exterior air barriers: case study I 48
3.2.1 Description of the test house and realisation of the exterior air barrier . 49
3.2.2 *In situ* pressurisation tests 52
3.2.3 Observed air leakages in the exterior air barrier 52
3.3 Quantifying typical air leakage paths: case study II 54
3.3.1 Description of the test house and realisation of the exterior air barrier . 55
3.3.2 *In situ* pressurisation tests 56
3.3.3 Laboratory measurements 61
3.3.4 Comparison laboratory and *in situ* measurements 66
3.3.5 Summary 67
3.4 Conclusions 68

4 Hygrothermal laboratory studies of components with an exterior air barrier 71
4.1 Hot and cold box measurements on highly insulated timber frame walls 71
4.1.1 Test equipment 72
4.1.2 Wall configuration studied 73
4.1.3 Boundary conditions and test sequence 75
4.1.4 Sensor positioning and accuracy 77
4.1.5 Material properties 79
4.1.6 Results 84
4.2 Onset of condensation on hygroscopic and/or capillary active materials 96
4.2.1 Test setup and methodology 97
4.2.2 Results 98
4.3 Conclusions 99

5 Description and evaluation of numerical Heat, Air and Moisture model 103
5.1 Introduction 103
5.1.1 Delphin framework 104
5.2 Principal Model Equations 105
5.2.1 Heat and mass transport in porous building materials 106
5.2.2 Heat and mass transport in air channels 109
5.2.3 Boundary conditions 112
5.3 Numerical implementation of the quasi-steady state air flow transport 113
5.3.1 Spatial discretisation 113
5.3.2 Integration in time 115
5.4 Evaluation of the model 117
5.4.1 Steady state natural convection in porous media 117
5.4.2 Transient free convection in a cavity filled with a porous medium 118
5.4.3 Impact of air convection on the hygrothermal behaviour of timber frame walls 123

5.5 Conclusion 134

6 Numerical Investigation of Exterior Air Barrier Systems Performance Under Real Climate Conditions 137

6.1 Wall configuration and material properties 138
6.2 Climate conditions 141
6.2.1 Radiation 142
6.2.2 Air pressure difference 144
6.2.3 Interior relative humidity 147
6.3 Selection of moisture limit state criterion 150
6.3.1 Mould growth 151
6.3.2 Interstitial condensation 154
6.3.3 Proposed moisture limit states 156
6.4 Precision/simplification of simulation grid 157
6.4.1 Simulation grid 158
6.4.2 Interior finishing materials 162
6.4.3 Top and bottom plate 162
6.4.4 Update interval of air pressure field 163
6.4.5 Summary 163
6.5 Reference simulation 164
6.5.1 Orientation 164
6.5.2 Inner climate - ventilation rate 165
6.5.3 Exterior climate 166
6.5.4 Summary 168
6.6 Parameter variation 168
6.6.1 Insulation material 169
6.6.2 Interior vapour retarder 172
6.6.3 Bad workmanship in exterior air barrier 174
6.6.4 Exterior air barrier material 178
6.6.5 Different European Climates 181
6.6.6 Summary 183
6.7 Conclusions 185

7 Conclusions and perspectives 189

7.1 Main results and general conclusions 190
7.2 Limitations and future perspectives 192
7.3 Recommendations for practice 193

Curriculum vitae 205

Nomenclature

Abbreviations

BIFB	bituminous impregnated wood fibreboard
CLx	cellulose insulation, with a density of x kg/m^3
DAE	differential algebraic equation
FCB	fibre cement board
GB	gypsum board
MWx	mineral (glass) wool insulation, with a density of x kg/m^3
np	neutral plane
ODE	ordinary differential equation
OP	overpressure
OSB	oriented strand board
UP	underpressure

Subscripts

$\parallel$	parallel
$\perp$	perpendicular
50	at a reference pressure of 50 Pa
a	air
atm	atmospheric
B	bottom
cond	conduction
conv	convection
d	dry air
diff	diffusion
int	interface
joint	joint
lw	long wave
M	middle
m	bulk material
mat	material

rad	radiation
rain	rain
sat	saturated
spec	specimen
sw	short wave
T	top
v	water vapour
w	liquid water

Dimensionless numbers

Nu	Nusselt number	-
Ra	Rayleigh number	-
Re	Reynolds number	-

Greek symbols

α	absorption coefficient	-
α_h	heat transfer coefficient	W/(m^2 K)
β	thermal expansion coefficient	1/K
β_v	vapour transfer coefficient	s/m
δ	vapour permeability	s
η	dynamic viscosity	Pa.s
λ	thermal conductivity	W/(m K)
μ	vapour resistance factor	-
ν	kinematic viscosity	m^2/s
ϕ	relative humidity	%
Π_y	climate factor	kg/m^3
ρ	density	kg/m^3
τ	non-dimensional time	-
θ	temperature	°C
φ	open porosity	m^3/m^3
ξ	ratio material heat capacity to fluids heat capacity	-
σ	Stefan-Boltzmann constant	

Roman symbols

$\dot{u}$	heat source	W/m^3
$\overline{u}$	averaged velocity	m/s

AC_{max}	maximum accumulated condensate	kg/m^2
C_p	wind pressure coefficient	-
D_H	hydraulic diameter	m
G_{vp}	vapour production	kg/s
H_e	evaporation enthalpy	J/kg
Q	airflow rate	m^3/h
s_d	water vapour diffusion-equivalent air layer thickness	m
A	absorption coefficient	$kg/(m^2\,s^{-0.5})$
A	area	m^2
a	anisotropy ratio	-
c	heat capacity	J/(kg K)
D	width	m
d	thickness	m
g	airflow rate density	$m^3/(m^{(2)}\,h)$
g	gravity acceleration	m/s^2
h	specific enthalpy	J/kg
HIR*	hygric inertia	$kg/(m^3\%RV)$
j	mass flux	$kg/(m^2\,s)$
K	conductivity	s
K	permeance	$m^3/(m^2\,h\,Pa)$
k	air permeability	m^2
L	length	m
M	mould index	-
MC	moisture content	%
n	air change rate	1/h
p	pressure	Pa
q	energy flux	W/m^2
R	gas constant	J/(kg K)
RH	relative humidity	%
T	absolute temperature	K
t	time	s
v	moisture concentration	kg/m^3
v	seepage velocity	m/s
w	water content	kg/m^3

1

Introduction and Problem Statement

A sound global building airtightness is one of the prerequisites to achieve energy efficient buildings (Jokisalo et al. 2009). In this context the European directive 2002/91/EG (EPBD) gave a clear signal to incorporate global building airtightness into the certification process of buildings energy demand. As a consequence, several European member states recently increased their airtightness requirements. Moreover, labels to certify standardised low energy buildings, requiring very high airtightness standards, are becoming more and more popular across Europe. For example the 'Passivhaus'-standard[1] and the 'Minergy-P'-standard[2] explicitly require a building airtightness of 0.6 air changes per hour (ACH) at 50 Pa. Apart from improving energy efficiency, the second major motivation for creating airtight building envelopes is moisture control. Interstitial condensation in building enclosures is primarily the result of forced air exfiltration in winter conditions (Tenwolde & Rose 1996). According to Janssens & Hens (2003), condensation quantities related to exfiltration are typically two to three orders of magnitude higher than those transported by vapour diffusion.

For timber frame construction an airtight building envelope is traditionally realised by an interior 'air barrier system', by sealing all the joints and intersections in the interior sheathing. In cold and moderate climates, such as North-West European areas, this air barrier function is often combined with that of the 'vapour retarder' (Janssens & Hens 2007). To protect the insulation layer from unwanted infiltration of outside cold air by natural or forced convection a 'wind barrier' is provided at the outside of the insulation (Uvsløkk 1996). In addition, this

[1] www.passiv.de
[2] www.minergie.ch

exterior layer often serves as drainage plane to prevent water infiltration into the structure. The performance criteria for wind barrier systems regarding air permeance are less severe than for air barriers (Janssens & Hens 2007). Therefore, the joints in the wind barrier are usually left unsealed.

Achieving the above-mentioned high standards regarding global building airtightness with an interior barrier is very labour-intensive. When installing an interior barrier a high number of difficult intersections, such as the connection between the intermediate floor and the outer walls, and perforations for electrical and plumbing services have to be sealed (Aho et al. 2008, Kalamees 2007). Additionally, the execution of a highly airtight inner layer requires an adjusted coordination. For example, Figure 1.1a shows how a pre-installed airtight strip needs to be provided between the installation of the purlin and the roof trusses. A similar procedure is required at the level of structural floors (Figure 1.1b) and at junctions between inner and outer walls. As a consequence, interior air barrier systems require special attention during several steps of the building process.

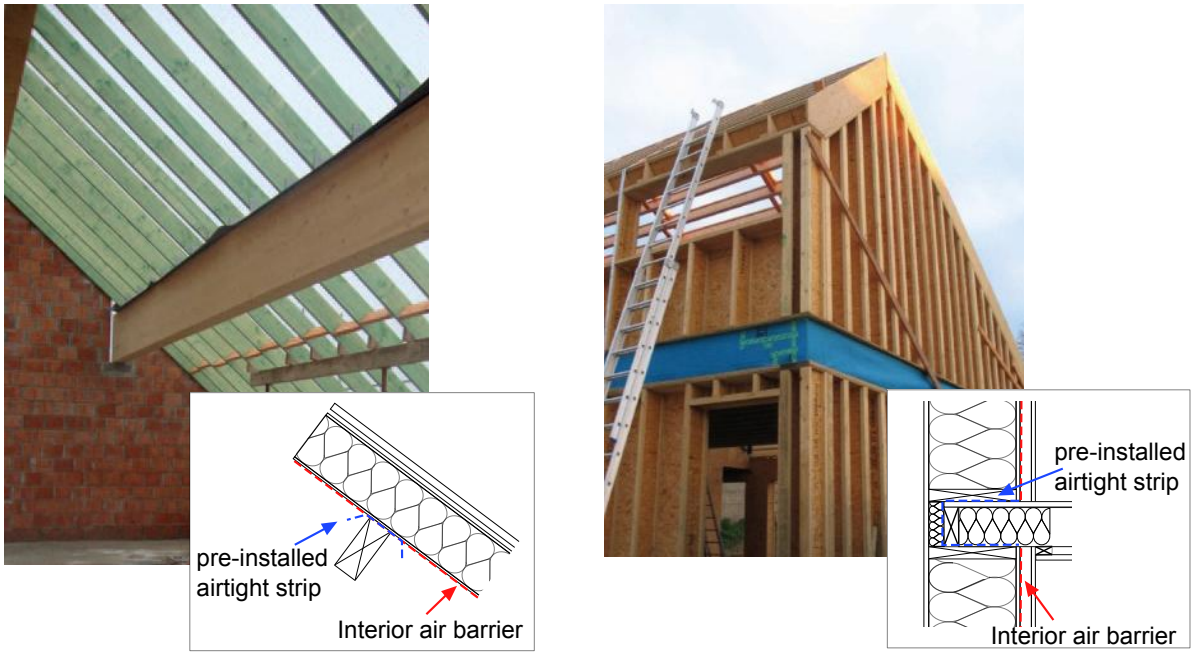

Figure 1.1: (a) Labour intensive sealing of interior air barrier at the level of roof trusses (Photo: WTCB) and (b) Pre-installed airtight strip to connect the interior air barrier across different building levels (Photo: Passiefhuisplatform).

As a result, building industry is looking for cost-effective alternative techniques to meet the severe airtightness requirements. One of the possibilities would be realising the airtight layer on the exterior of the building envelope where fewer joints and perforations are present.

Applying exterior air barriers in lightweight construction, however, may significantly influence the hygrothermal behaviour of these elements in cold and moderate climates. Given the fact that only limited knowledge on its practical feasibility and hygrothermal performance

exists, this approach is currently not recommended for timber frame construction.

1.1 Aims

The general aim of the present work is assessing the feasibility of exterior air barrier systems in highly insulated timber frame construction. In this context the term 'feasibility' captures two important subdomains: (a) **practical feasibility** and (b) **hygrothermal feasibility**. The first major aspect includes collecting detailed air leakage data on component and global building level. Challenge here is to investigate **real case studies**. In combination with laboratory work this would result in realistic air leakage data. Additionally, this allows assessing practical aspects, such as identifying advantages and disadvantages in the realisation of exterior air barriers.
The second major target is identifying the hygrothermal performance of these systems. Aim here is to verify the risks for moisture problems in timber frame construction with an exterior air barrier. One particular goal in this context is to acquire detailed **experimental results** on full-scale test walls. In addition this hygrothermal aspect includes the ambition to develop a reliable **numerical approach** to study the heat, air and moisture transport in these components. Final intention is to combine the acquired knowledge on these various fronts to develop **recommendations** for building industry.

1.2 Methodology and outline of the work

To reach the above-mentioned goals, the present work is subdivided in six main parts. **Chapter 2** outlines the current state-of-the-art on global building airtightness and the effects of air transfer on the hygrothermal behaviour of lightweight walls. Furthermore, attention will be drawn on existing hygrothermal building component models, taking air transport into account. Finally, this chapter will briefly summarise the current practice in controlling moisture in timber frame building envelopes.
Next, **chapter 3** will describe field and laboratory measurements, verifying whether acceptable airtightness levels can be achieved in practice by improving the wind barrier layer. This chapter will discuss in addition practical aspects of exterior air barriers in lightweight construction.
Thereafter, **chapter 4** will provide experimental work on the hygric performance of timber frame building elements with an exterior air barrier. This investigation will be restricted to highly insulated full-scale wall elements in laboratory conditions. This chapter will discuss the results of in total eight different wall assemblies, tested under various boundary conditions and including typical installation defects. Furthermore, this chapter will study the onset of interstitial condensation on hygroscopic and/or capillary active air barrier materials

on smaller test specimens. Both the small-scale and full-scale experiments will seek to generate valuable validation data for numerical simulation models.

Based on the experimental results, **chapter 5** will propose a numerical modelling strategy to assess the hygrothermal transport in lightweight walls with an exterior air barrier. Herein, the implementation of a quasi-steady state airflow model in the state-of-art simulation tool DELPHIN, developed at the Technical University of Dresden (Grunewald 1997, Nicolai 2007*a*) will be outlined. Main focus of this chapter will be on evaluating the presented modelling approach with benchmarks from the literature and the experimental data of chapter 4.

After defining its applicability and limitations, the numerical model will be applied in **chapter 6** to investigate the hygrothermal performance of lightweight walls with exterior air barriers under real climate conditions. This chapter will conduct a parameter study to examine the response of different lightweight wall assemblies, identify the impact of bad workmanship and illustrate its behaviour in several European climates.

Finally, **chapter 7** will draw general conclusions and will outline perspectives for further research and recommendations for building practice.

2

State-of-the-art

This introductory chapter provides an overview of related international literature and is divided in four main parts. The first section gives general background on global building airtightness and its corresponding requirements. This section further briefly discusses the current building practices regarding interior air barrier systems in timber frame Passivhaus construction in Belgium.
The second part deals with previous experimental work on the hygrothermal behaviour of lightweight building elements. Focus here, lies on the influence of air convection on the overall heat and moisture transfer in these components. In addition to these experimental findings, the applied measuring methods are discussed as well.
Thirdly, this chapter reviews existing numerical models to simulate heat, air and moisture transport in building components. Yet the discussion of these models is restricted to the different air flow implementations.
The last part of this chapter outlines moisture performance limit states, commonly applied to asses timber frame building envelopes. This section will also discuss today's moisture control strategies to fulfil these requirements.

2.1 Global building airtightness and requirements

For centuries people have sought to protect themselves from air infiltration and unpleasant cold drafts that comes with it, by closing cracks and holes in the building envelope with all kinds of materials. The first attempts towards a more structural approach in identifying

and reducing buildings air leakages date from the late 1970's. In 1973, the first oil crisis forced governments and organisations to rethink their use of fossil fuels and the reduction of building energy use became one of the key attention points. In search of improving building energy efficiency, a Swedish research group (Kronvall 1978) developed a system to characterise global building airtightness (the so-called pressurisation test).
A few years later, in 1981, an American company, 'The Energy Conservatory' in Minneapolis, commercialised this test equipment. This introduction of the BlowerDoor™ enabled building professionals to measure and improve the global building airtightness for the first time. The International Energy Agency likewise recognised the significant impact of ventilation on energy use and on indoor air quality. In reaction it launched the Air Infiltration and Ventilation Centre with an accompanying newsletter 'Air Information Review'. Herein, an article entitled 'Build tight - Ventilate right' (Elmroch 1980), published in August 1980 described the challenges at hand very well. Though from the 1980's onwards building airtightness has become a popular theme on international conferences, its impact on the building practice has remained limited so far. In his literature survey Janssens (1998) showed how in practice large differences in global building airtightness occurred. He further revealed that the average air permeance of building envelopes was only about $1\,10^{-4}\,m^3/(m^2\,s\,Pa)$ at that time. Such air leakage levels may induce severe condensation problems within timber frame construction, as Janssens (1998) and other scholars have found. Yet their recommendations have never led to a legislative framework to minimise building airtightness in European member states. A Canadian directive, however, did establish based on one-dimensional computer simulations (Di Lenardo et al. 1995), suggesting a maximum air permeance of timber frame construction of $2.7\,10^{-6}\,m^3/(m^2\,s\,Pa)$. This threshold value, however, was unrealistically low for that time. Consequently, it can be questioned whether this Canadian directive reached the local building practice.

At the turn of the century global building airtightness caught even more attention through interest in very low energy buildings. The European directive 2002/91/EG (EPBD) gave a clear signal to incorporate building airtightness into the certification process of buildings' energy demand. Labels certifying standardised low energy buildings, requiring very high airtightness levels, became more popular. The launch of the Air Barrier Association of America (ABAA)[1] in 2001 and a similar European platform in 2011, TightVent[2], that sought to improve the exchange of experiences on practical issues regarding building airtightness, illustrate that building airtightness has become a subject of increasing interest. The yearly international BUILDAIR conference, inaugurated in 2006, further shows that building airtightness is an important research topic today.

[1] www.airbarrier.org
[2] www.tightvent.eu

The current section seeks to introduce how global building airtightness is measured and expressed. The next section briefly outlines the requirements in European member states and discusses the threshold values applied within the main volunteering labels. The final section emphasises the current views in realising sound building airtightness in high performance timber frame construction in Belgium.

2.1.1 Characterisation of building airtightness

Several techniques to quantify building airtightness have been developed over the years. Overviews of existing methods are, for example, provided by Liddament (1996) and Limb (2001). The majority of airtightness measurements on residential buildings, however, are determined through constant external fan pressurisation.

The basic methodology of constant pressurisation testing is straightforward. A fan, installed into a door or window frame, is applied to pressurise or depressurise the building to levels, sufficiently high to eliminate the influence of stack and wind pressures. This procedure is performed for both overpressures and underpressures from which the averaged result is determined. The European standard EN13829:1996 defines the measuring protocol for pressurisation testing. This standard requires that a pressure difference from 25 Pa up to 70 Pa needs to be realised across the building envelope in steps of 5 Pa. During this stepwise increase, air flow rates and associated pressure difference across the building envelope are measured. The data sets gained in this way are curve fitted to a power law (Sherman & Palmiter 1994):

$$Q_a = a\Delta P_a^b \tag{2.1}$$

where Q_a (m^3/h) refers to the airflow rate, ΔP_a (Pa) stands for the pressure difference across the building envelope, a ($m^3/(h\,Pa^b)$) is the air permeance coefficient and b (-) the air permeance exponent. If the leakage paths are dominated by large, short leaks (e.g. orifices) the exponent is expected to be closer to 0.5, which corresponds to turbulent flow; if the leakage is dominated by long-path leaks the expectations are that the exponent is closer to 1, which equals laminar flow conditions (Sherman & Chan 2004). The calculation of the airflow rates in Eqn. 2.1 needs to consider compensations for density differences between indoor and outdoor air and pressure offsets. The EN13829:1996 describes two methods (A or B) to perform a pressurisation test. The key difference between both methods lies on the openings that are sealed during testing. Method A requires that only openings with closing devices are closed, whereas all additional openings have to be sealed for method B.

The principle metric used to quantify building airtightness is the air flow through the envelope at a specific reference pressure. Most recognised reference pressures are 50 Pa and 4 Pa, but 1 Pa, 10 Pa, 25 Pa, and 75 Pa are used as well. The obtained airflow rates at a reference pressure are most commonly normalised, so, buildings with different sizes can be

compared. Again several methods to express this normalised global building airtightness exist; (1) heated volume (n), (2) floor area (w), (3) building envelope area (q). Global building airtightness levels are commonly expressed by their normalisation method (n, w or q) combined with the applied reference pressure in subscript. The most recognised method in Europe is the n_{50}-value (1/h), also adopted in EN13829:1996. The following section outlines the current state regarding global building airtightness requirements in Europe.

2.1.2 Building airtightness requirements in Europe

With the implementation of the European Performance of Building Directive[3] (EPBD), global building airtightness became a growing attention point in many European countries (Wouters et al. 2008). A survey within the ASIEPI project[4] revealed that the majority of European member states reward sound global building airtightness in their energy performance calculation (Guyot et al. 2010). In addition, few European countries have minimum requirements regarding envelope airtightness. Table 2.1 summarises the existing airtightness requirements in Europe. This table illustrates large differences between the threshold values in these countries. Moreover, Aurlien & Rosenthal (2008) state that apart from U.K. where pressurisation tests are compulsory for large buildings, airtightness levels are not systematically tested. The question thus remains to what extent the local building practice follows these various national requirements.

Country	**Airtightness requirements at 50 Pa**[a]	
	Natural ventilation	Mechanical ventilation
Czech Republic	4.5 1/h	no heat recovery: 1.5 1/h with heat recovery: 1.0 1/h
Denmark	5.4 $m^3/(m^2\,h)$ (floor area)	
France	0.6 $m^3/(m^2\,h)$ at 4 Pa (envelope area)	
Norway	2.5 1/h	
The Netherlands	dwellings: 720 m^3/h (at 10 Pa) non-residential: 1.4 1/h (at 10 Pa)	
U.K.	buildings > 500 m^2: 10 $m^3/(m^2\,h)$ (floor area)	
Germany	3.0 1/h or 7.8 $m^3/(m^2\,h)$ (floor area)	1.5 1/h or 3.9 $m^3/(m^2\,h)$ (floor area)
	3.0 $m^3/(m^2\,h)$ (envelope area)	
Estonia	3.0 $m^3/(m^2\,h)$ (envelope area)	

[a] International workshop: Achieving relevant and durable airtightness levels: status, options and progress needed, 2012, Brussels

Table 2.1: Existing airtightness requirements in European member states.

[3] 2002/91/EG

[4] Assessment and Improvement of the EPBD Impact

Table 2.1 demonstrates the differences in the applied reference pressures in these countries, which makes a direct comparison difficult. For example, the same requirement of 3 $m^3/(m^2\,h)$ at 50 Pa is used in Estonia, Germany and France, if the latter is converted to 50 Pa[5]. The use of different normalisation methods, on the other hand, even impedes a direct comparison between different countries. In this respect it should be noted that requirements on the n_{50}-values are less severe (on component level) for large buildings, as these buildings are more compact. The German requirement seeks to answer this issue by imposing an additional threshold q_{50}-value. A further restriction towards a direct comparison between these international requirements of Table 2.1 is the use of different measuring methods (A/B) in these countries (Caillou & Van Orshoven 2010). Finally, also the application of different determination methods for the buildings dimensions impedes a direct comparison. It is often not well-documented whether interior or exterior dimensions are applied in the requirements listed in Table 2.1.

In addition to the requirements mentioned, several countries provide recommendations regarding global building airtightness. For instance the Belgian standard (NBN D50-001) prescribes an n_{50}-value of 3 1/h for buildings with mechanical ventilation and 1 1/h if heat recovery is likewise applied. Yet the legal impact of such national recommendations has remained limited. A recent Belgian example of a low energy building with an n_{50}-value, exceeding more than an order of magnitude the recommended value of 1 1/h (Roels & Langmans 2009) illustrated that, not even in such extreme circumstances the contractor can be held responsible. To avoid such extreme situations in the future, the establishment of at least moderate requirements is desirable. Notwithstanding such requirements would have only a limited impact on the overall building practice, they would provide a legal framework to penalise if extreme shortcomings are found. Key potential to increase the awareness of global building airtightness (without obliging a pressurisation test for new buildings) still remains its incorporation in the energy performance calculation in the EPBD-framework. Most of the European countries already reward good building airtightness in the energy performance calculation, so, at present an increasing number of pressurisation tests are performed. For example, Carrié & Rosenthal (2008) noted that around 2008 the airtightness of new buildings in Denmark and Germany was measured for 5 % and 15-20 % respectively. In Belgium (Flemish region) this was 22 % in 2010 (Wouters et al. 2012). Future reductions of the threshold values for the energy performance level will increase the need of performing pressurisation tests, and thus, improve the building practice regarding airtightness.

Apart from these national regulations, the increasing popularity of voluntary labels to certify low energy buildings stimulates a growing awareness of building airtightness. Er-

[5] assuming a flow exponent of 0.64 (Sherman & Chan 2004)

horn et al. (2011) provide an overview of existing labels for high performance buildings in Europe. The most recognised label is the 'Passivhaus'-standard developed in Germany (Feist et al. 2005). This label explicitly requires an n_{50}-value of 0.6 1/h. Its Swiss variant, the 'Minergy-A/P'-standard[6], requires the same severe airtightness level. In addition, for BREEAM certified buildings a strict building airtightness level can be specified as well.
Within the existing volunteering programs in Europe the maximum n_{50}-value of 0.6 1/h, postulated by the 'Passivhaus'-standard, is most ambitious. Reiss & Erhorn (2003) concluded that such threshold values are feasible in building practice. Yet they emphasised that n_{50}-values below 1 1/h are difficult to achieve. Though many experiences from successful projects are currently available, achieving such severe airtightness levels remains a challenge. The next section outlines how timber frame Passivhaus construction in Belgium currently realise these airtightness levels.

2.1.3 Common practice in timber frame Passivhaus construction in Belgium

Belgium has a long tradition in masonry buildings. Yet the vast majority of dwellings following to the Passivhaus-standard are timber frame. This specific building method, mainly based on German experiences, emerged around a decade ago in Belgium. This section aims to introduce the current building practice regarding airtightness in timber frame Passivhaus construction.

Wall and roof elements

The airtightness for both roof and wall elements is realised by an interior 'air barrier system', by sealing all the joints and intersections in the interior sheathing. Often the interior structural boards - mostly Oriented Strand Board (OSB) or other chipboards - are applied for this purpose (see Figure 2.1a). This interior airtight layer is also frequently realised with (additional) foils (see Figure 2.1b). The air barrier function is mostly combined with that of the 'vapour retarder'. Though common building practice took for granted that OSB is sufficiently airtight to realise n_{50}-values below 0.6 1/h, some recently built Passivhaus dwellings have proved the opposite. In these cases an extra airtight foil or an airtight paint on top of the OSB was the only remedy to achieve the required n_{50}-value. Langmans et al. (2010) showed by laboratory measurements that large variations in the air permeance between different OSB brands exist (<0.001 - 0.01 $m^3/(m^2\,h\,Pa)$). This study confirmed that the airflow through the most air permeable OSB brands may increase the n_{50}-value up to 0.3-0.6 1/h. As a consequence, the establishment of minimum requirements for the air permeability of air barrier materials seems to be necessary to avoid these problems in the future.

[6] www.minergie.ch



(a) (b)

Figure 2.1: 'Air barrier' and 'vapour retarder' function by (a) Interior structural board (OSB) and (b) combination of structural board and foils.

To protect the inner air barrier layer from penetrations, a service cavity is often provided for the installation of electrical and plumbing services. This cavity is frequently filled with thermal insulation.
Realising the airtightness of these opaque elements is rather straightforward. The connections between different building components, however, are often a challenging and labour intensive process.

Connections between building components

A synthetic foil usually realises a continuous connection between the concrete slab on the ground foundations and the wall elements. Figure 2.2a shows how these foils are glued on the concrete foundation and sealed to the walls. This figure further illustrates how a pre-installed airtight strip is required at the connection between interior and exterior wall elements. Similar strips are necessary at the level of intermediate floors and roof purlins (see Figure 1.1). The application of such pre-installed strips, necessary to obtain high airtightness levels, has an important impact on the coordination of the building process. All different subcontractors, such as electricians and plumbers, should be informed on the purpose of these foils and their importance for the overall air barrier (Acke et al. 2012).

Two common solutions occur for the connection around doors and windows. The most recognised method glues the window into a plywood frame, which can be easily sealed to the interior structural board (see Figure 2.2b). The alternative method equips the window with a prefabricated foil. Figure 2.2c shows how the window is installed with anchors, whereafter the foil can be folded and sealed to the structural board to provide an airtight connection.



(a) (b) (c)

Figure 2.2: (a) Connection between slab on the ground foundation and exterior wall, pre-installed airtight strip at wall connection (b) Window mounted in plywood frame for connection to wall and (c) Window equipped with foils, so, it can be installed with traditional anchors, whereafter the foils are sealed to the interior air barrier.

2.2 Experimental work on hygrothermal performance of lightweight components

Several experimental studies have examined the hygrothermal performance of lightweight components. The problems at hand cover a wide range of physical phenomena, such as pure vapour diffusion transport (e.g. Kalamees & Vinha 2003, Vinha 2007), summer condensation (e.g. Derome & Carmeliet 2010), interstitial condensation (e.g. Ojanen & Kohonen 1995, Janssens 1998) and mould growths (e.g. Rao et al. 2009).

The current section outlines previous experimental work that assesses the impact of air transfer on the overall heat and moisture behaviour of lightweight components. Air convection within building enclosures can be subdivided in natural and forced convection problems. Although in reality these mechanisms commonly occur as mixed processes, for the scope of the present work it is important to distinguish between them. Temperature gradients across the component may result in internal natural convection (air rotations). Forced convection, however, is driven by a total air pressure difference across the component induced by (a) wind, (b) stack effect and/or (c) mechanical ventilation. Figure 2.3 illustrates the distinction between natural and forced convection. Depending on the position of air leakages and cracks in the components and considering different boundary conditions, a high number of derived air flow patterns can occur, such as (internal) air rotations, wind-washing, diffuse or concentrated air flows (Ojanen & Kohonen 1989).

The first part of this literature survey focusses on thermal effects of air movements within vertical building components with permeable insulation systems. Previous research has extensively studied this topic, ranging from pure natural convection problems, forced convection scenarios, prospects of dynamic insulation and wind-washing of the insulation layer.

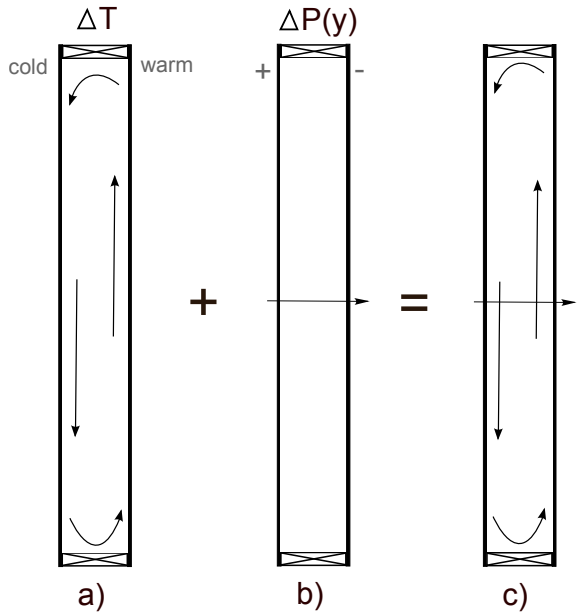

Figure 2.3: Natural and forced convection phenomena in timber frame wall elements: (a) natural convection, (b) forced convection and (c) combined air flow pattern.

However, in the scope of this work the main interest lies on the impact of free heat convection and wind-washing of the insulation layer in particular. Consequently, the discussion is restricted to a selective review of experimental work on these two phenomena. The main focus of the present section lies on the second part, studying the hygrothermal consequences of air movement in building components. Again, a distinction is made between experimental work studying the effects of natural convection and investigations on combined natural and forced convection processes. In addition, the final section discusses different measuring techniques described in the literature to study the effects of air convection on the hygrothermal performance of lightweight components.

2.2.1 Thermal effects of air movement in timber frame wall elements

The impact of air movements on the thermal performance of lightweight building components has been extensively studied in the literature. For the research project at hand, two air transfer processes are of special interest: (1) free heat convection and (2) wind-washing. The first corresponds to a reduced thermal performance of the building envelope as a result of natural air convection in and around the insulation layer. For elements with an exterior air barrier this convection loop may introduce an increased moisture load into the structure. Therefore, this review seeks to quantify and clarify this air transfer mechanism. The second process, wind-washing, refers to a reduced thermal performance caused by of wind-induced air flows in the insulation layer. The application of exterior air barriers systems, however, can impede such air flows.

Thermal effects of internal air rotation

The first studies investigating the effects of air movement on the thermal performance of permeable insulation systems occurred in the early sixties in Norway (Lorentzen & Brendeng 1959). These experimental studies demonstrated that low density insulations may lead to convection loops in and around the insulation layer, significantly reducing its thermal performance. Hereafter many authors have examined the same effect for various configurations and temperature differences across the components (e.g. Bankvall 1972, Silberstein et al. 1990, Klarsfeld & Combarnous 1980, Lecompte 1989, Dyrbøl et al. 2002). A comprehensive literature review on this topic has been written by Powell et al. (1989). Their review mainly distinguishes between two configurations, studied at that time: (1) a cavity filled with an open porous insulation material and (2) an air cavity partly filled with a thermal insulation layer. Figure 2.4 summarises the three types of convection scenarios that can occur within these configurations. The left hand side pattern in this figure corresponds to free convection inside the insulation layer, the middle pattern to convection that bypasses the insulation layer through small gaps around this layer and, finally, the right hand side pattern shows a convection loop in partially filled cavities. Surely, combinations of these three air flows likewise occur. In summary, the studies under review, generally conclude that the

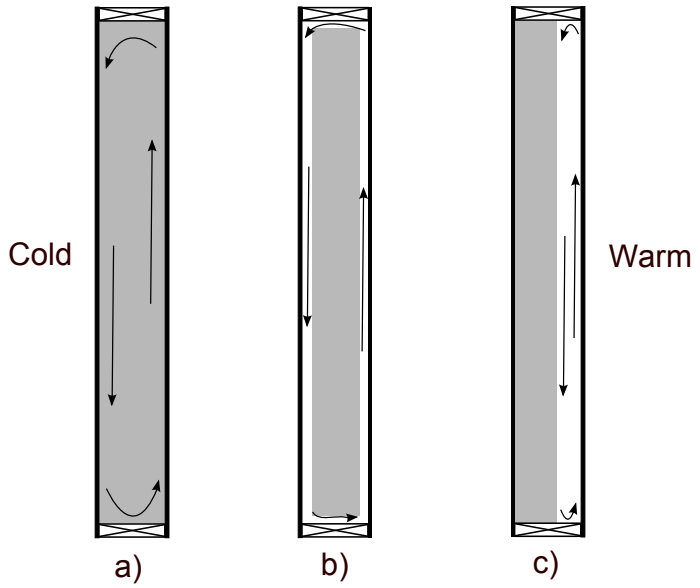

Figure 2.4: Free convection air flow patterns in stud cavities: (1) internal loop, (2) loop bypassing insulation (air gaps), (3) partially filled cavity (insulation in grey).

impact of natural convection on the thermal performance is limited when at least one of the adjacent layers is airtight, air gaps along the interface between the sheathing and insulation are avoided and sufficiently dense insulation materials (>20-30 kg/m^3) are applied. The effect of internal convection amplifies most significantly with increasing: (1) temperature difference (ΔT), (2) air permeability of insulation layer (k) (3), thickness to height ratio d/h. The modified Rayleih number (Ra_m) commonly expresses the risk for decreased thermal

performance of vertical insulation layers (Klarsfeld & Combarnous 1980):

$$Ra_m = g\beta D\Delta T\left(\frac{\rho c}{\nu}\right)\frac{k}{\lambda} \tag{2.2}$$

in which D is the width of the layer, β represents the thermal expansion coefficient of air, ν the kinematic viscosity of air, g the gravity acceleration and λ the thermal conductivity of the layer. According to ISO:10456(2007) the effect of natural convection on the overall thermal performance of walls can be neglected when Ra_m is lower than 2.5.
Though many of the above-mentioned experimental studies discussed the susceptibility of these systems for bad workmanship, none of them analysed the impact of typical installation defects in detail. Therefore, the next paragraph zooms in on literature results, quantifying the effect of typical installation errors.

Three typical installation defects are documented in the literature: (1) air leakages around the corners of insulation blankets (2) a vertical air path between the interface of insulation blankets and sheathing material (3) a horizontal air cavity at the top of loose fill insulation.
The first defect typically occurs in installing insulation blankets, which are cut slightly oversized, so they can be squeezed in the stud cavity. As a result, typical imperfections are located at the corners of the insulation layer. An extensive study on the influence of these minor installation defects on the thermal performance has been performed in Canada by Brown et al. (1993) on full-scale test walls in laboratory conditions. They investigated three insulation densities ranging from 9 to 35 kg/m^3 and three levels of defects. Though the air leakages were only concentrated in the corners of the cavity, their study indicated an increased presence of natural convection over the entire width of the component. Brown et al. (1993) concluded that even for the highest insulation densities tested, the thermal performance was decreased with 2 % as a result of these minor defects (ΔT = 25°C). For lower insulation densities and higher temperature differences the reduction reached up to 40 %.
A second type of imperfection occurs when the insulation blanket is not in tight contact with the adjacent surfaces. The effect of such (very) small vertical cavities on the thermal behaviour has been studied in Norway by Bjerkevoll (1994), Johannessen (1995) and Janssen (1997). They conducted a comprehensive laboratory investigation combined with numerical simulations to study the effect of natural convection in highly insulated timber frame walls. A first series of simulations, presuming tight contact between the insulation and adjacent surfaces, systematically underestimated the measured heat transport. Yet additional numerical simulations including small vertical leakages at these interfaces showed better agreement with the measurements. The simulations of Janssen (1997) indicated that gaps of 3 mm on both sides of the insulation layer decreased the overall thermal resistance with 3 % (at ΔT = 20°C). This reduction becomes far more pronounced when the vertical channels are

accompanied with (small) horizontal paths at the top and bottom of the wall, resulting in a convection loop bypassing the insulation layer (Figure 2.4b). To overcome this reduced thermal performance of highly insulated walls in Norwegian Passivhaus construction, Uvsløkk et al. (2010) recommends[7] to divide the insulation in two layers by providing a vertical convection barrier. In addition, Uvsløkk et al. (2010) state that the threshold Ra_m-value of 2.5, proposed by ISO:10456(2007), is insufficient in that typical installation effects are not considered.

A third kind of imperfection corresponds to settling of loose fill insulation leaving a horizontal gap at the top of the stud cavity. The impact of such defects on free heat convection has been studied by Riesner (2003) on full-scale test walls for cellulose and expanded polystyrene loose fill insulation. The test walls studied had a total height of 2 m of which the upper 6 cm was left un-insulated providing an air gap over the entire depth of the wall. This study showed the development of a second convection loop inside the upper air gap. Consequently, this convection loop in the upper air gap counterattacked the main convection loop within the insulation layer. Based on the measured temperature profiles in the middle of the insulation layer, Riesner (2003) demonstrated that the heat transport in the insulation was only influenced in the upper 25 cm of the insulation layer. The overall heat transfer of this configuration increased with 13 % as a result of the settled insulation. It should be emphasised, however, that this reduced thermal performance was the result of local effects at the top of the wall. This is in contrast to the first two installation defects in which the main convection loop in the insulation was amplified.

Wind-washing

The previous section restricted the discussion to internal air rotations effects, presuming an ideal situation in that the insulation layer is closed between two airtight layers. Nevertheless, in reality the exterior protective layer (wind barrier) is most often not sufficiently airtight. As a consequence exterior air may flow through permeable insulation materials driven by pressure gradients on the building envelope. First laboratory investigations on the thermal impact of wind-washing emerged in Scandinavia by Timusk et al. (1991) and Uvsløkk (1996). Timusk et al. (1991) performed experiments on full-scale corners of wood frame walls exposed to wind conditions (Figure 2.5a). They found that defects in the wall sheathing resulted in a significant decrease of its thermal performance. Later, Uvsløkk (1996) conducted full-scale laboratory measurements on wind-washing effects in timber frame walls (Figure 2.5b). The applied exterior pressure difference, based on *in situ* measurements, was realised by imposing a pressure difference at the walls cladding in and outlet. Based on these measurements, Uvsløkk (1996) proposed a maximum overall air permeability of the wind barrier system of 14.10^{-6} m^3/(m^2 s Pa). Ojanen & Kohonen (1995), at there turn, found sim-

[7] based on these Norwegian laboratory measurements performed in the period 1994-1997 (Bjerkevoll (1994), Johannessen (1995) and Janssen (1997))

ilar threshold values by numerical simulation. These additional simulation results illustrated that compartmentation of the insulation layer reduced wind-washing. As a consequence, Ojanen & Kohonen (1995) suggested a maximum air permeance of 10.10^{-6} m^3/(m^2 s Pa) when strong corner convection is possible and 25.10^{-6} m^3/(m^2 s Pa) when the building envelope is divided in separate structures.

In addition to these laboratory measurements, Janssens & Hens (2007) studied wind-washing effects on *in situ* duo-pitched roofs in Belgium (Figure 2.5c). They examined the overall air flow patterns with tracer gas tests and temperature and heat flux sensors installed at three heights. Results revealed a clear correlation between the exterior wind speeds and the reduction of the thermal performance. Most significant impact on the thermal performance was located at the level of the ridge. The measured reduction of the overall thermal resistance of roofs for a southwest wind of 4 m/s was 10 % for entirely insulated elements (compact roof) and 40 % for partly insulated roof elements (vented roof). Based on these *in situ* measurements Janssens & Hens (2007) recommended to seal underlay materials in Belgian duo-pitched roofs to improve their air permeance levels to the proposed values of Uvsløkk (1996) and Ojanen & Kohonen (1995). These postulated recommendations notwithstanding, the vast majority of the current building practice in Belgium still not seals the wind barrier to prevent wind-washing.

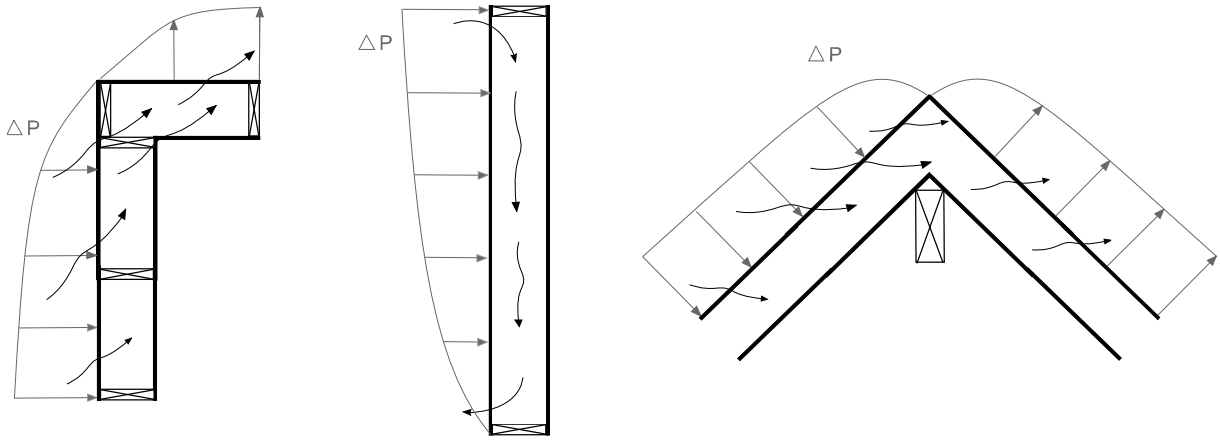

a) Corner (Timusk 1991) b) Wall (Uvsløkk 1996) c) Roof (Janssens 2007)

Figure 2.5: Wind-washing of air permeable insulation layers (a) at the level of building corners, (b) in wall elements and (c) roofs.

2.2.2 Hygric effects of air movement in timber frame wall elements

Most experimental research on the hygrothermal performance of lightweight construction, considering air transport, focusses on the effects of forced exfiltration (Figure 2.3c). Moisture redistribution by buoyant driven air rotation (2.3a), however, remains only scarcely documented in the literature. The present section seeks to distinguish between these two

convection scenarios. The first part provides a detailed discussion of the limited number of studies on buoyant dominated problems. The second part briefly outlines the current literature on forced exfiltration within lightweight construction, emphasising the applied measuring techniques.

Hygric effects of internal air rotation

A continuous air barrier system, either at the inside or outside of the insulation layer, prevents forced vapour convection through a lightweight building component. However, such configurations may still suffer from increased moisture loads induced by natural convection. Homb et al. (1993) and Thue et al. (1996), for example, briefly mention the observation of moisture redistribution by natural convection within lightweight walls. Both studies discussed extensive full-scale laboratory investigations to verify the potential of vapour open wall designs and concluded on guidelines for $s_{d,i}/s_{d,e}$ ratio in Norwegian climates. Though these studies intended to focus on vapour diffusion only, the effects of internal air rotation can be noticed. Wall sections with a limited vapour resistance at the inside corresponded to increased moisture contents in the upper cold parts of the walls. In addition, Homb et al. (1993) stated that this effect was more pronounced in the mineral wool insulated elements compared to the walls filled with less permeable loose fill cellulose insulation.
In Germany, Riesner (2009) examined this effect of moisture redistribution in greater detail. Riesner (2009) performed full-scale laboratory experiments on wood frame walls using a wide range of different insulation materials, such as mineral wool, wood fibres, cork pellets and other organic granular materials. All walls tested were executed with an interior and exterior airtight layer, so, pure internal natural convection was the only air transfer mechanism possible. The outer layers were executed with vapour open materials such as wood fibreboards, while vapour retarding OSB was used at the warm side of the insulation. The measurements gave clear evidence of moisture redistribution as a result of buoyant driven air flow in the insulation. Vapour entered the building enclosure by vapour diffusion and accumulated subsequently on the upper cold side of the wall driven by buoyant air rotation (Figure 2.6). Both condensation and mould growth were observed at the upper 40 cm of the exterior layer. The order of magnitude of this process highly depended on the level of natural convection, which can be expressed in term of Ra_m-numbers (Eqn. 2.2). In addition to these parameters involved, Riesner (2009) stated that this phenomena is enhanced by (1) higher vapour resistances of the exterior layer $s_{d,e}$, (2) lower ratios of the vapour resistance of the inner to the outer layers $s_{d,i}/s_{d,e}$, and (3) a lower vapour resistance of the insulation material. In contrast to free heat convection, the impact on the moisture behaviour reduced with a decreasing height of the component. The study revealed non-negligible effects of moisture redistribution for air permeability levels around $5.10^{-9}\,m^2$, corresponding to stan-

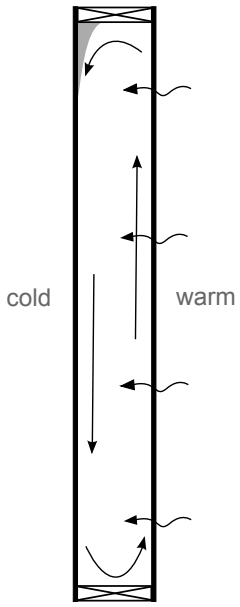

Figure 2.6: Moisture redistribution in vapour open wall designs (moisture accumulation in grey).

dard mineral wool[8]. In addition, Riesner (2009) noticed a different response for hygroscopic and non-hygroscopic insulation materials in this context. For non-hygroscopic insulation materials interstitial condensation occurred relatively fast while this could be postponed or completely avoided with hygroscopic insulation materials. On the other hand, the walls with hygroscopic insulation materials had longer drying times, resulting in longer periods of high moisture contents. As stated in section 2.2.1, the presence of air cavities along the insulation layer highly increased the level of internal convection. Riesner (2009) showed that vertical air gaps along both sides of the insulation significantly increased the rate of interstitial condensation. Yet the presence of such channels likewise improved the drying rate of the component, when it was exposed to drying conditions. Furthermore, Riesner (2009) concluded that for a horizontal air gap at the upper region of the insulation layer, the critical zone moves from the upper cold side to the warm side of the insulation layer. As a result of a second convection loop and radiation in this air cavity, the exterior side of the interior sheathing became colder. Consequently, moisture collected at this interface, increasing its risk for mould growth. In an attempt to decrease the rate of free convection through adding an exterior EPS insulation layer, the component became even more vulnerable to interstitial condensation. The exterior insulation layer increased the vapour resistance of the exterior layer, and thus, reduced its drying potential.

In summary, this study of Riesner (2009) has established the risk for moisture problems as a result of internal natural convection in vapour open wall designs. The results should be placed in perspective, however, as most insulation materials studied were highly air permeable (k = 4-40.10^{-9} m^2). In addition, the ratio of the inner to the outer vapour resistance

[8] with a ratio of the vapour resistance of the interior and exterior layer $s_{d,i}/s_{d,e}$ is around 4

of the applied materials was also relatively low (2-4) in comparison with ratios commonly applied in practice. Furthermore Riesner's conclusion that hygroscopic insulation materials increase the risk for damage as a result of natural convection has to be reconsidered since these materials corresponded to the most air permeable materials applied in her study.
Based on additional numerical simulations Riesner (2009) defines the following thresholds values for the insulation permeability:

- $k \leq 1.10^{-9}$ m^2
- $k \leq 5.10^{-9}$ m^2 for $s_{d,i}/s_{d,e}$>10 m and $s_{d,i}$>1 m
- $k \leq 5.10^{-8}$ m^2 for $s_{d,i}/s_{d,e}$>30 m

Yet these recommendations, based on numerical simulation, did not consider effects of increased air permeability levels of the insulation layer triggered by (small) installation errors. From this it follows that, similar to the comment of Uvsløkk et al. (2010) (section 2.2.1), the recommendations of Riesner (2009) may prove insufficient in practice.

Økland (1998) performed a similar study on the effect of internal air rotation on the hygric performance of highly insulated wall components in Norway. In total six full-scale test walls were verified in laboratory conditions. The walls were insulated with standard mineral wool[9] of 30 cm. Both sides of the insulation were finished with wood fibreboard linings. In contrast to Riesner (2009), Økland (1998) applied a vapour barrier (PE-foil) at the interior side, which reduced the vapour supply by diffusion to a very minimum, avoiding the mechanism depicted in Figure 2.6. This studied considered on the other hand built-in moisture by supplying 4 liters water to the insulation layer as initial conditions. The walls, exposed to extreme Norwegian winter conditions (ΔT = 40°C), showed a clear redistribution of the moisture induced by buoyant driven air rotation. After an initial period in which the supplied water drained to the bottom plate, Økland (1998) measured a continuously increasing moisture content of the upper plate. At the end of the measurement a high ice formation on the upper cold side of the insulation layer was visible. In addition, the results showed that the test walls in which I-profile studs were applied, were more vulnerable to natural convection compared to those walls equipped with traditional studs. It is highly likely that this relates to the increased difficulty of realising close contact between the mineral wool and the studs. Finally, Økland (1998) demonstrated how this moisture redistribution was significantly higher for the test wall in which vertical air channels (23 mm) were left at both sides of the insulation layer. These important effects of the (large) deficiencies in the installation of mineral wool insulation were further confirmed by numerical simulation of this experimental data set ((Økland 1998) and (Geving 1997)).

[9] $k_\perp = 2.10^{-9}$ m^2 $k_\parallel = 4.10^{-9}$ m^2

Hygric effects combined natural and forced convection

The experimental studies in the previous section were executed with an continuous airtight layer on at least one side of the insulation layer. Deficiencies in this air barrier layer, however, may result in forced convection conditions induced by pressure differentials across the building envelope. For forced air exfiltration scenarios, the corresponding moisture ingress can be significantly higher than the above-mentioned effects of moisture redistributions caused by internal air rotations in cold and moderate climates.
Hens (1987) performed a laboratory investigation on full-scale test walls, studying the impact of deficiencies in the interior air and vapour barrier (PE-foil) for Belgian climate conditions. The test walls were exposed to averaged winter conditions and the measurement was conducted in two steps: (1) without a pressure difference across the wall and (2) with an overpressure of 10 Pa in the warm chamber. Though that the interior air and vapour barrier had been punctured for some walls, the first stage reported no significant moisture problems. In the second step, however, high levels of interstitial condensation were observed. Similar to the process illustrated in Figure 2.6, an increased moisture load in the first measuring step can be expected as a result of concentrated diffusion through the deficiencies in the interior air and vapour barrier combined with internal air rotations. But, the results of Hens (1987) indicated that this impact was much smaller than the amount of moisture transported by forced exfiltration, when a pressure difference of 10 Pa was realised in the following step. Janssens (1998), who applied the same laboratory procedure to verify the influence of air movements within different roof assemblies has reported similar results. The results of Desta et al. (2011), describing the hygrothermal performance of lightweight walls under real climatic conditions, further, confirmed that the hygric effects of forced convection outrange the moisture redistribution by vapour diffusion and internal air rotations. In summary, these studies illustrate that the effects of forced exfiltration can be far more important than the moisture loads that correspond to diffusion and/or internal air rotations. Yet these studies were performed on moderately insulated elements (12-20 cm) which are less vulnerable to natural convection. Moreover, these studies applied a constant overpressure of 10 Pa, which amplified the impact of forced convection to unrealistic levels. Finally, it should be stressed that the forced convection conditions in these studies resulted in severe moisture problems, far beyond acceptable levels. Though the increased moisture loads by diffusion and internal air rotations were significantly lower, it can not be stated that these phenomena do not hold hygrothermal risks.

The impact of forced exfiltration conditions depends to a great extent on the distribution of the air leakage paths. Lightweight components with an equal overall air permeance levels may have a completely different hygric response (Desmarais et al. 2000). Air leakage paths can be divided in (a) long paths, (b) short paths, (c) concentrated leakage paths and

(d) diffuse air exfiltration (Figure 2.7).

The highest moisture loads are located at the opposite side of the deficiencies in the vapour barrier (Desmarais et al. 2000, Janssens 1998, Kurnitski & Kalamees 2000). Long air leakage paths can effectively cool down the indoor air, corresponding to the highest local moisture deposit. Short exfiltration paths, on the other hand, result in lower condensation levels as the exfiltrating air is cooled down less (Desmarais et al. 2000, Derome 2005). These experimental observations confirm the numerical results of Ojanen & Kumaran (1996), who demonstrated that long exfiltration paths correspond to the highest moisture problems. The third group of air leakage paths, concentrated air leakages, are composed of short and long air flow paths. From this follows that the resulting moisture loads depend on the ratio between both. Finally, diffuse air convection remains a rather academic air flow path in that building envelopes have in reality at least one material with a low air permeance, that impedes such air flow patterns. Simplified analytical and numerical models, such as the ones by Tenwolde (1985), Burch & Tenwolde (1993), Hagentoft & Blomberg (2000), often apply this one-dimensional air convection concept. In this context Desta et al. (2011) reported *in situ* experimental work on diffuse air convection to provide validation data for such models. The results of Desta et al. (2011) demonstrated that this airflow pattern results in high surface-averaged moisture loads. Moreover, Janssens (1998) demonstrated with numerical simulations how diffuse exfiltration can be applied as a worst-case scenario for two-dimensional structures with low and moderate exfiltration rates (<0.002 $m^3/(m^2\,s)$). For elements exposed to higher exfiltration rates, however, this one-dimensional approach will underestimate the actual moisture load.

In addition to the air leakage paths, the hygrothermal properties of the exterior sheathing influence the effects of forced exfiltration to a large extent. Desmarais et al. (2000) and Riesner (2009) reported the highest moisture loads when an exterior EPS insulation layer is provided to the wind barrier. The low vapour permeability of this insulation layer, impeding a fast drying of the wind barrier to the outside, explains this observation. Derome

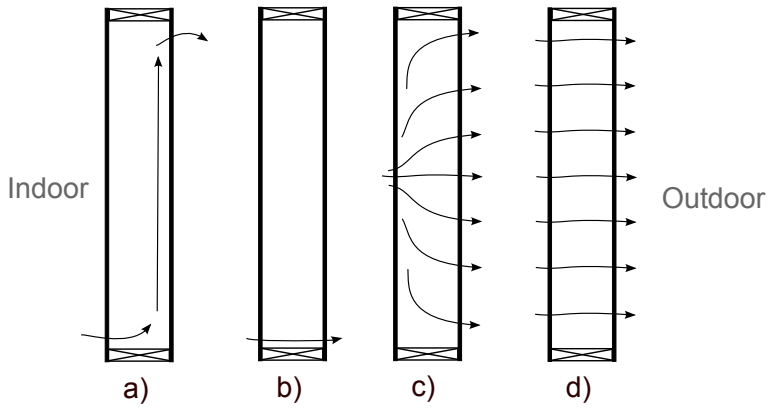

Figure 2.7: Different forced exfiltration air leakage paths: (a) long paths, (b) short path, (c) concentrated paths and (d) diffuse leakage paths.

(2005), who studied air leakages in compact flat roofs which have a vapour tight exterior layer, found similar effects. The application of very vapour open wind barriers combined with a minimum of thermal insulation is the most effective way to limit moisture problems induced by forced convection (Janssens 1998, Kalamees & Kurnitski 2009). These studies showed that the properties of the interior vapour barrier become subordinated to these of the exterior sheathing, when forced convection dominates. In addition, Derome (2005) and Vinha & Kakela (2000) showed that condensation can be postponed by using hygroscopic insulation materials. This buffer, however, is also limited and can not compensate for the deficiencies in the air barrier layer.

2.2.3 Review of experimental methods

This section reviews existing measuring strategies to quantify the hygric behaviour of lightweight components influenced by air movements. Some experimental test setups have been reported in multiple studies. For brevity, the overview seeks to avoid multiple citations to the same set-up. The outline, however, is not limitative because it is most likely that other experimental studies have been published in (older) national and international conference proceedings, which are not easy accessible.
Table 2.2 lists the considered studies and indicates whether the study concerns field tests or laboratory work. Additionally, this table shows which components were tested and in which country the tests were performed. The discussion of these experimental methods is restricted to (1) the applied boundary conditions, (2) the used sensors and corresponding locations, (3) the considered cladding systems, (4) additional moisture loads and (5) to which extend the generated data is applicable for the evaluation of numerical HAM-models.

Boundary conditions Major differences between the various investigations are related to the applied boundary conditions. Table 2.2 indicates whether the study was performed in laboratory or *in situ* conditions. The main advantage of a field test is that the components are exposed to realistic climatic conditions. Yet at the same time it is difficult to isolate specific effects and field measurements require long time spans. As a remedy, several research projects combined both (e.g. Vinha 2007, Økland 1998, Geving & Uvsløkk 2000). The advantage of (additional) laboratory test is that the boundary conditions can be controlled. In this respect, several authors have applied multi-step boundary conditions, inducing different air flow scenarios (indicated in Table 2.2 as MS). Most often, the first step did not impose an air pressure difference. The following steps, however, realised different air pressure levels. In this way, the corresponding results provide detailed information on the impact of air exfiltration conditions. Nevertheless, it should be noted that several authors, such as Hens (1987), mentioned that also during the first step forced exfiltration may occur because the coldbox is in underpressure due to the ventilators in this chamber. Studies which apply the

Study	in-situ	laboratory			component	country
		<0°C	SS	MS		
Hens (1987)				x	wall	BE
Hens (1990)	x				roof	BE
Homb et al. (1993)		x	x		wall	NO
Ojanen & Kohonen (1995)		x	x		wall	FI
Tenwolde et al. (1995)	x				wall	USA
Thue et al. (1996)		x	x		wall	NO
Janssens (1998)				x	roof	BE
Økland (1998)	x	x		x	wall	NO
Desmarais et al. (2000)		x	x		wall	CA
Kurnitski & Kalamees (2000)				x	wall	EST
Vinha & Kakela (2000)		x		x	wall	FI
Geving & Uvsløkk (2000)	x				wall	NO
Salonvaara & Nieminen (2002)	x				roof	FI
Ge & Fazio (2004)		x		x	wall	CA
Derome (2005)		x		x	roof	CA
Vinha (2007)	x	x	x		wall	FI
Alturkistani et al. (2008)			x		wall	CA
Riesner (2009)		x	x		wall	GE
Kalamees & Kurnitski (2009)		x		x	roof	FI
Mao et al. (2009)			x		wall	CA
Maref et al. (2010)	x				wall	CA
Geving & Holme (2010)	x				roof	NO
Desta et al. (2011)	x				wall	BE

Table 2.2: Overview of experimental work on the hygrothermal performance of lightweight components considering air movement (MS: multiple air pressure steps and SS: single air pressure step).

same pressure difference - 'single step' - across the test component are indicated with SS in Table 2.2. Finally Table 2.2 lists whether the laboratory test considered negative temperatures. Especially for Northern countries it is vital to incorporate the effects of freezing. Yet for these conditions, some authors have reported related difficulties, e.g. the experiment had to be interrupted frequently to defrost the convector elements (Thue et al. 1996, Økland 1998).

Measuring sensors and locations All studies listed in Table 2.2 applied thermocouples and electric resistance or gravimetric measurements to register the temperature and moisture content at specific points. Given the difficulties mentioned in measuring moisture content levels, these methods will be outlined separately in the following paragraph.
Most of the studies registered the temperatures and moisture contents of the exterior sheathing at two or three heights (e.g. Hens 1987, Riesner 2009, Desta et al. 2011). Desmarais et al. (2000) and Alturkistani et al. (2008), however, measured the moisture content of the

exterior sheathing up to 8 different heights to obtain more detailed information on the effects of various air leakage paths. In addition to the exterior sheathing, some investigations measured the temperature and moisture content in the wooden studs and/or top and bottom plates (e.g. Hens 1987, Tenwolde et al. 1993). The extra information of these sensors in the studs and plates, however, was limited as the highest moisture loads were often located at the level of the exterior sheathing. A large-scale overview of moisture-related damage in timber frame construction in USA by Merill & Tenwolde (1989) confirmed these findings. These authors found that interstitial condensation is more likely to damage the wall sheathing than the wall framing. Site visits and inspection revealed that decay of the wooden wall framing occurred only if there was severe damage to the wall sheathing. The overall focus of the experimental studies listed in Table 2.2 on the exterior sheathing reflects these findings of Merill & Tenwolde (1989). Nevertheless, Homb et al. (1993), Thue et al. (1996) and Geving & Holme (2010) only measured the temperature and moisture profiles in the vertical studs and top and bottom plates. Consequently these authors only registered condensation on the sheathing from the moment moisture started to drain and reached the moisture sensors at the bottom plate. Finally, most authors installed thermocouples at materials interfaces. Only few researchers, such as Økland (1998), had installed sensors within the insulation layer as well. In this way forced exfiltration paths could be better visualised and understood. Yet Økland (1998) mentioned difficulties in installing these additional sensors without introducing air gaps around the insulation layer.

In contrast to temperatures and moisture contents, only few authors measured heat fluxes. Hens (1987), for example, installed heat flux sensors at the top and bottom of both the exterior and interior sheathing, providing valuable information on the level of internal air rotations. Furthermore, more recent studies, such as Vinha (2007), Maref et al. (2010) and Desta et al. (2011), utilised relative humidity sensors within the component tested. But from the older studies only Tenwolde et al. (1993) applied relative humidity sensors (with a measuring accuracy of 10 %). Drawbacks of relative humidity sensors are their sensitivity for condensation conditions. Desta et al. (2011) have reported problems with relative humidity sensors exposed to condensation conditions.
Nearly all studies listed used pressure gauges to measure the pressure difference across the wall. Only Derome (2005) and Maref et al. (2010) installed additional pressure gauges within the test component to register pressure drops across the air barrier layer. In addition to pressure gauge sensors, Hens (1990) and Janssens (1998) installed gas concentration sensors, which could be applied to identify airflow paths and permeability levels when exposed to tracer gas (Liddament 1996). More advanced methods from the field of fluid-dynamics, such PIV[10] or smoke visualisation, have not been reported in the current academic debate which studies the influence of air transport on the hygrothermal performance

[10] Particle Image Velocimetry.

of lightweight walls. Thermo-anemometers that measure local air velocities are likewise scarcely applied to identify flow patterns in building components (Gudum 2003).

Finally, only limited information is reported on the influence of installing sensors on the actual hygrothermal behaviour of the wall. For example, Maref et al. (2010) applied moisture pins, protruding at least 1 cm from the OSB sheathing into mineral wool insulation layer. It thus becomes impossible to realise close contact between the sheathing and mineral wool layer, disturbing the hygrothermal behaviour of the wall (Brown et al. 1993). Other problems might be related to the introduction of air leakages in the test component at locations where sensors cables penetrate airtight layers or air leakages created by weight samples (Alturkistani et al. 2008). Also larger sensors, such as heat flux transducers or condensation detection strips, may influence the components hygrothermal performance when applied on (very) vapour permeable layers.

Measured moisture content The above-listed studies have applied several different methods to measure the local moisture contents. In general, the approaches can be divided in two groups: (1) electrical resistance measurements and (2) gravimetric measurements. The first group, the so-called moisture pin sensors, have the main advantage that they can provide continuous data. Two metal pins are installed in the material, measuring the moisture content of the intermediate zone in terms of its dielectric property (Said 2007) (see Figure 2.8). This method can only be applied, however, in sufficiently dense materials, such as wood (Derome 2005). Often these sensors are installed in top and bottom plates and/or vertical studs of the lightweight walls (Homb et al. 1993, Thue et al. 1996). The limited accuracy levels are the drawbacks of these sensors, however. For example, Nore (2009) mentioned important measuring errors of these sensors, that depend on the length of the electrodes, thickness of the test sample, distance of sensor to the surface and surface treatments. In addition, Geving & Holme (2010) showed the large difference between the calibration curves of plywood and spruce, indicating the sensitivity of the applied curve on the overall accuracy of this method. Moreover, Geving (1997) and Økland (1998) demonstrated the impact of measuring errors as a result of a small discontinuities between the sensor and wood, inducing capillary moisture uptake along the sensor.
The second group of methods, gravimetric measurements, is based on the periodical (manual) weighing of elements of the building component. Most often small weight samples (e.g. Figure 2.8) are installed at specific accessible locations (e.g. Desmarais et al. 2000, Derome et al. 2007, Desta et al. 2011). The main difference between the applied methods lies in the number, size and location of the weight samples. Desta et al. (2011) installed 20 by 20 cm samples at the top, mid an bottom height of the wind barrier layer. In contrast, Alturkistani et al. (2008) used 25 cylindrical samples with diameter 38 mm within each test wall. An important disadvantage of this measuring protocol is its time-consuming charac-

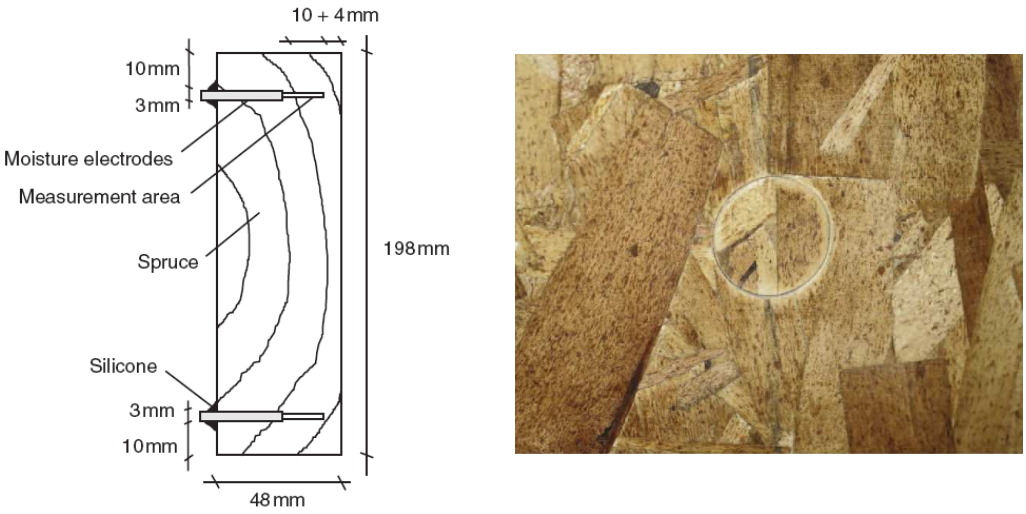

Figure 2.8: Left: moisture pin in spruce (Geving & Holme 2010) and right: weight specimen installed in exterior OSB sheathing (Alturkistani et al. 2008).

ter and its temporary disturbance of the experiment (Janssens 1998). In addition, several authors have emphasised the importance of avoiding additional air leakages around the test samples (Hens 1987, Mao et al. 2009). Another measuring error reported is spalling of small pieces from gravimetric samples (Alturkistani et al. 2008). Finally, the removal and reassembly of insulation materials, such as performed by Derome (2005) and Janssens (1998), may introduce different air leakage paths around these layers. In the group of gravimetric measurements, Maref et al. (2002) reports one exceptional test protocol. In contrast to other studies, the applied test facility allows to monitor the overall weight of the complete component tested. Yet the main drawback of this system is that it only allows to quantify the global moisture performance but not to provide local information.
Besides these direct measurements of the moisture content, researchers often apply two related methods: (1) moisture detection strips (Hens 1990, Maref et al. 2010) and (2) collection of drained condensation (Ojanen & Kohonen 1995, Janssens 1998). The first method alarms when condensation occurs on such strips, but provides no information on the actual moisture amounts. The second method, however, collects drained condensation at the bottom of the component tested.

Initial conditions/ moisture load The majority of the studied listed in Table 2.2 apply dry initial conditions. Some authors, however, have reported increased initial conditions to simulate water penetration or to reduce the overall time of the experiment. The *in situ* measurements of Geving & Holme (2010) and the laboratory tests of Ojanen & Kohonen (1995), for example, were provided with small irrigation systems, that enabled the introduction of moisture in the structure at specific times. Li et al. (2009) and Mao et al. (2009) applied a similar approach by installing a water tray below the mineral wool insulation layer of the test wall. The weight of this tray was continuously monitored, providing information on the

drying potential of the walls system. However, it can be question to which degree the presence of the air cavity with the water tray below the mineral wool layer increased the level natural convection within these walls (Teasdale-St-Hilaire & Derome 2007). Furthermore, Økland (1998) simulated built-in moisture through supplying 4 liters of water to the mineral wool insulation layer at the start of the experiment. Maref et al. (2002) and Derome et al. (2007) applied the most extreme initial conditions. They used OSB sheathings and bottom plates respectively, which were first soaked in water.

Cladding Opinions vary on the necessity of including the exterior cladding system in the test components. For example, Vinha (2007), who studied walls with different cladding systems in a Finish climate, concluded that the overall humidity conditions in the ventilated cavity were lower than the exterior climate. Based on these field measurements, he stated that it is justified to exclude the cladding layer in laboratory tests. Gudum (2003), on the other hand, found that the walls hygrothermal performance was highly influenced by the presence of a (non)-ventilated cladding. In addition, Nore (2009) emphasised the importance of considering cladding systems in the hygrothermal assessment of wall elements. The majority of the laboratory tests (listed in Table 2.2) exclude the cladding, while this layer is mostly provided in the field investigations. The majority of the *in situ* investigations applied common cladding materials, such as vinyl sidings (Maref et al. 2010), wooden cladding (Geving & Uvsløkk 2000) or brick cladding (Vinha 2007). Desta et al. (2011), however, used a non-conventional water and vapour tight board, provided with ventilation holes as cladding material. In contrast to the field measurements, most of the laboratory investigations did not provide a cladding layer in the test walls. But, the reasons for excluding these cladding layer from the test component have not been not addressed in these studies.

Validation data Nearly all experimental studies set as an initial goal to generate validation data for numerical simulation models. Yet in most cases these model evaluations were limited to a qualitative approach only as result of (a) limited measuring accuracy (b) unknown deviations in the geometry of the component tested and (c) limitations of the model. The first problem, insufficient measuring accuracy, corresponds to various aspects. The most common deficiencies documented in the literature were related to measuring moisture contents, such as calibration difficulties of moisture pin sensors (Økland 1998) and the impact of air leakages through built-in weights specimens (Li et al. 2009). Kalamees & Vinha (2003) also mentioned the lack of detailed hygrothermal material properties (as a function of temperature and moisture content). The second deficiency, unknown geometry, is mostly related to air transfer. Small installation defects may result in increased air transport (Brown et al. 1993) and, consequently, have a large impact on the moisture accumulation, as mentioned in section 2.2.2. Thirdly, the omission of dominant transport mechanisms in the simulation model may cause large discrepancies between simulation and measuring

results. In this respect Teasdale-St-Hilaire & Derome (2007) mentioned the lack of considering air convection in their simulations of the drying rate of exterior sheathings with a commercial simulation package.

2.3 Numerical models for Heat, Air and Moisture in building components

Experimental investigations are rather time consuming and expensive. Therefore a great number of numerical simulation tools have been developed over the years to asses and predict the hygrothermal behaviour of building components, mostly focusing on the heat and moisture transport (e.g. Kohonen 1984, Burch & Tenwolde 1993, Rode Pedersen 1990, Künzel 1995, Janssen et al. 2007). These numerical models basically evolved from the Glaser-method, a one-dimensional hand calculation approach for combined heat conduction and vapour diffusion through insulated components (Glaser 1958). The developed HAM-models differ from each other by various assumptions in both the physical description and numerical implementation. A first step in centralising and improving the knowledge on HAM-models was made by the International Energy Agency ECBCS Annex 24 project. An enquiry by Hens & Janssens (1996) at the start of this project showed that only 20 % of the existing numerical models at that time considered air transfer in combination with heat and moisture transport through building components. During and after this international research project several new HAM-models were developed (e.g. Grunewald 1997, Janssens 1998, Økland 1998, Hagentoft & Blomberg 2000), partly summarised by Trechsel (2001). An important next step in standardising the various HAM-modelling procedures was made by the EU-initiated HAMSTAD[11]-project (Hagentoft et al. 2004). Apart from suggesting useful benchmark cases, this project concluded on the physical equations describing the combined heat, air and moisture transport in multilayered porous building components. Yet the HAMSTAD-project mainly focussed on a detailed description of heat and moisture transport, while air transport was only briefly included and treated as a one-dimensional phenomenon. Though the major part of today's hygrothermal building component modelling focusses exclusively on heat and moisture transfer, several developed HAM-models have included air transport to some extent. The aim of the present section is to outline the different approaches applied to model air transport in combination with heat and moisture transport in building components.

Table 2.3 gives an overview of developed HAM-models, that consider air transport. In total the literature reports around twenty HAM-models that include air transport. The calculation domain and dimensions, airflow model and considered moisture transport functions of these models are listed in Table 2.3. The next section discusses the different implementa-

[11] Heat, Air and Moisture Standards Development

tions of air transfer. The following section then outlines the incorporation of cavity ventilation in HAM-models.

NAME	REFERENCE	DIM.[a]	AIR[b]	MOIST.[c]	DOMAIN[d]
1-HAM	Hagentoft et al. (2000)	1D	F	V	P
2DHAV	Janssens (1998)	2D	F/B	V	P/HN
DIM/DELPHIN	Grunewald (1997)	2D	F	V/L	P
HamBe	Li et al. (2009)	2D	F/B	V/L	P
HAMFitPlus	Tariku et al. (2010)	2D	F	V/L	P
HAMlab	Van Schijndel (2007)	2D	F	V/L	P
HAMwall	Kurnitski (2000)	1D	F	V	P
HygIRC-2D	Maref et al. (2002)	2D	F/B	V/L	P
LATENITE	Karagiozis (1999)	2D	F/B	V/L	P
MOIST.-EXPERT	Karagiozis (2001)	2D	NS	V/L	P/A
SIMPLE-FULUV	Økland (1998)	2D	NS	V/L	P/A
SMAHT	Cunningham (1990)	3D	F	V	P
TCCC2D	Ojanen & Kumaran (1996)	2D	F/B	V/L	P
TRATMO	Kohonen (1984)	2D	F/B	V/L	P
WALLDRY/FEM	Gusdorf (1992)	1D	F	V	P
WINHAM2D	Wang & Hagentoft (2001)	2D	F	V	P
WUFI2D	Zirkelbach et al. (2009)	2D	S	V/L	P
/	Dos Santos (2009)	2D	F	V/L	P
/	Mukai et al. (2008)	3D	F	V	P

[a] Dimensions

[b] Implementation of airflow: F: forced convection (Darcy), F/B: forced and natural convection (Darcy), NS: Navier-Stokes, S:source and sink terms

[c] Moisture transport: V: vapour transport, V/L: vapour and liquid transport

[d] Modelling domain: P: porous media, P/HN: porous media + hydraulic network to model air leakages, P/A: porous and air domain

Table 2.3: Overview of existing HAM-models, considering air transport.

2.3.1 Air transport implementations

Most challenging attempts have been reported by Karagiozis (2001) and Økland (1998) in that they modelled the complete Navier-Stokes equation for conservation of momentum in combination with heat and mass transfer. This would allow a detailed simulation of porous building materials in combination with air spaces, such as air leakages and ventilation cavities (two-domain approach). Yet the simulation results of these models are only poorly documented and major drawback mentioned are their extreme slow simulation performance (Trechsel 2001).

The next group of models restricts air transport to porous building materials (one-domain approach). This omits possible air spaces in between (e.g. Hagentoft & Blomberg 2000, Li et al. 2009, Tariku et al. 2010, Van Schijndel 2007, Mukai et al. 2008). The air transport considered in these models corresponds to the Darcy formulation in porous media. This group

of one-domain Darcy approaches can be divided, first, in models that only consider forced convection, such as Tariku et al. (2010), Gusdorf (1992) and Dos Santos & Mendes (2009) and, second, models that describe both forced and buoyant driven air transport, such as Kohonen (1984), Maref et al. (2002), Li et al. (2009). The first, essentially decouples the air transport from the combined heat and moisture transport. The latter, however, couples the heat and moisture balance equation with the air mass balance equation through the air densities that are considered in the buoyancy term of the air transport calculation. Given the large differences between the response time between air transport and heat and moisture transfer (Hens 2003, p.103), the majority of models neglects the transient term in the Darcy formulation. An important simplification of this group of models is that building components are assumed consisting of porous materials only. Experimental studies, however, have identified the importance of possible small air channels between the porous building materials (see section 2.2.1). Janssens (1998) tackled this problem through introducing a hydraulic network in combination with the porous medium (two-domain approach). This method, applied by several authors to model the impact of air channels on the thermal performance of building components (e.g. Kohonen et al. 1985, Lecompte 1989, Hagentoft 1991), assumes fully-developed laminar airflow in the channels (Hagen-Poiseuille flow conditions) around the porous media.
Finally, Zirkelbach & Künzel (2009) proposed the most simplified airflow implementation. This approach introduces moisture source terms on predefined locations, based on its local temperature and the dew point temperature of the interior climate, to include effects of air convection.

In the field of computational fluid dynamics (CFD) several recent attempts have been made to couple fluid domains with heat and moisture transport in adjacent porous media (Gnoth 2007, Steeman et al. 2009, Defraeye et al. 2012). Yet the computational speed of these CFD-HAM simulations is, in general, not acceptable for long-term simulations of building enclosures. Furthermore, these CFD-HAM models still assume airtight porous media. Therefore, these models were not included in the overview of Table 2.3.

2.3.2 Consideration of cavity ventilation in HAM-modelling

Cavity ventilation may have a large impact on the hygrothermal performance of building enclosures. Consequently, various researchers have investigated this topic. However, the results of these studies are not always conclusive and are sometimes even contradictive. For example, while North American studies (e.g. Straube & Finch 2009) emphasised the necessity of cavity ventilation, European studies questioned its effectiveness to remove moisture (e.g. Gudum 2003, Vinha 2007). Künzel et al. (2008) attributed this contradiction to differences in the applied materials. Traditional masonry cavity walls in Europe are less

vulnerable to high moisture contents compared to timber frame buildings in North America. As a consequence, Künzel et al. (2008) stated that cavity ventilation is less important in masonry building envelopes compared to timber frame construction. The contradictive findings are in addition likewise caused by the physical complexity of cavity ventilation, and thus, the difficulty in determining the corresponding ventilation rates. Large deviations in the assumed air change rates can be noticed between different numerical studies. For example, while the numerical study of Burch & Tenwolde (1993) applied only a constant air change rate of 6 1/h, Künzel et al. (2008) used a ventilation rate of 50 1/h and Salonvaara et al. (1998) varied the ventilation rate between 1.5-150 1/h. On the other hand, field tests by Gudum (2003) reported mean air change rates between 144 - 576 1/h in the cavity ventilation of a North facing test wall for wind speed of 0.69-2.12 m/s. Also, the CFD investigation of Nore et al. (2010) documented higher values up to 500-1500 1/h for wind speeds of 0 to 8 m/s.

The international literature has proposed several model assumptions to account for cavity ventilation. These methods ranged from: (1) the omission of ventilation effects, (2) effective cladding diffusion permeance, (3) the removal of the cladding system, (4) the application of constant air change rate, and (5) simplified coupled implementations.
The first approach ignores air movement within the cavity, and thus, applies the specifics of still air. As a result, in cold winter conditions the moisture in the cavity can be evacuated only by liquid and vapour transport through the cladding system. Hence, this approach typically overestimates the humidity conditions in the cavity (Karagiozis & Künzel 2009).
A second method, applied by Tenwolde & Carll (1992) and Straube & Burnett (2005), modifying the vapour permeance of the cladding to compensate for the cavity ventilation produces more realistic results. Yet because there exists no physical background for this method, ascribing an equivalent vapour permeance to the cladding material introduces large uncertainties in the simulation results.
The third approach removes the cladding and corresponding cavity from the calculation domain. To compensate for the thermal properties of these layers, an additional thermal resistance is included via the heat transfer coefficient. Janssens & Hens (2003) demonstrated that this approach is justified for the prediction of interstitial condensation in roofs systems without moisture buffer capacity. Nevertheless, this method basically assumes high ventilation rates, so that, the vapour pressure in the cavity equals the vapour pressure of the outer air. Hence, for lower ventilation rate scenarios the moisture influx towards the cavity may exceed its vapour evacuation. This would underestimate the imposed outer vapour pressure. Certainly when the moisture content of a hygroscopic wind barrier is the decisive moisture control limit state, this method might be too optimistic.
This problem can be tackled, however, by applying the fourth approach. Here, the cavity ventilation is introduced in the model by means of source and sinks terms. These methods,

applied by e.g. Künzel et al. (2008) and Salonvaara et al. (2007), assume a constant air change rate in the cavity throughout transient simulations. The conditions in the cavity are then determined by solving the moisture and heat balance inside the cavity. This approach has the potential to verify the hygrothermal impact of cavity ventilation through variation in the air change rates. The key question, however, still remains the magnitude of the air change rate, which largely affects the simulation results. To improve the simulation accuracy of this approach, empirical relations have been developed to derive ventilation rates as a function of the wind speed (e.g. Gudum 2003, Nore 2009) or solar radiation (Labat et al. 2012).

The final method, applied by Janssens (1998), models the cavity ventilation as laminar, fully-developed flow in air channels in interaction with adjacent material layers. Because this method calculates the air change rate in a transient way, more realistic air change rates can be expected. Though this approach corresponds to the most detailed formulation mentioned in the literature, it should be noted that its behaviour still largely simplifies the reality. Many factors such as shading, ground temperature and the pressure distribution across the building envelope largely affect the air flow pattern in these cavities.

2.4 Moisture control in timber frame building envelopes

The previous sections have provided a literature review on experimental investigation and numerical simulation tools to predict the hygrothermal behaviour of lightweight building components. The present section seeks to outline the moisture performance limit states, applied in building engineering, to assess the performance of such components. In addition, this section briefly lists standard moisture control strategies to fulfil these requirements in timber frame construction.

2.4.1 Moisture performance limit states

Moisture performance limit states in timber frame building envelopes often relate to the onset of biological processes inside the component. These processes can imply biodeterioration, which results in structural damage, and thus, shortens the buildings service life. In addition, surface mould formation may occur. This can be harmful to the inhabitants health and comfort, without inducing structural damage, however. The majority of the existing moisture performance limit states are designed to prevent surface mould growth. The key parameters influencing this biological process are humidity, temperature, exposure time and the exposed materials.

The literature puts forward two different methods to prevent biological activities in wood frame building enclosures: direct and indirect methods. The first approach consists of assessment methods that directly evaluate the main parameters inducing biological growth on

organic materials (e.g. Sedlbauer 2001, Hukka & Viitanen 1999). The second method, on the other hand, assesses the level of interstitial condensation on (non)-organic materials, such as spunbonded polyethylene foil (Janssens 1998). Here, the limit state corresponds to the onset of drainage which can result in accumulation of moisture, and thus, degradation of lower positioned wood based materials such as bottom plates.
As the study at hand seeks to evaluate the performance of organic and non-organic exterior air barrier materials, the introduction requires a discussion on both moisture limit state approaches.

Biological growth The first group of moisture performance limit states directly evaluates the mould growth conditions on the critical surfaces. The literature discusses various prediction methods to assess the mould risk.
The most simple methods evaluate only the moisture content of wood based materials (Viittanen & Salonvaara (2001)). Most often a moisture content of 0.2 kg/kg is put forward as a critical value for the onset of fungi growth in wood.
A second simplified approach often applied in the literature assesses the duration of suitable exposure conditions required for microbial growth. According to Viittanen & Salonvaara (2001) the lowest relative humidity level for mould growth is around 75-80 % and for biodeterioration above 95-98 %. Critical relative humidity levels as a function of temperatures and response time can be found in Peuhkuri et al. (2008).
A third assessment method for suitable conditions for biological growth are the so-called isopleth diagrams (e.g. Clarke et al. 1998, Hens 1999, Sedlbauer 2001). These curves, determined under steady state laboratory conditions, separate favourable from unfavourable temperature and relative humidity conditions for mould growth. Although these isopleth diagrams give a good indication for the risks for mould growth, their simplifications neglect transients effect in the mould growth prediction.
More advanced models for the prediction of mould growth are the biohygrothermal model of Sedlbauer (2001) and the VTT-model of Hukka & Viitanen (1999).
The first method - the biohygrothermal model- enables a dynamic calculation of the relative humidity, temperature and exposure time needed for the spore germination of mould fungi based on the osmotic potential of spores. The interior of the spores are characterised by a moisture retention curve and the spores' wall by a humidity-dependent vapour permeability. The spores are supposed to have germinated when a certain critical moisture content is reached from which the mould growth can start. The results of this transient calculations are expressed in mould growth intensity (mm). The main criticism on this method is that mould is treated as a material in the HAM calculations. This implies the need for defining its material properties, such as moisture retention curves which are highly uncertain for these substances. In addition, examples or guidelines to create these properties are only poorly documented by Sedlbauer (2001).

The second advanced mould prediction method - the VTT model - applies mathematical relations to predict mould growth in different conditions, considering the exposure time, temperature, relative humidity and periods of unfavourable conditions. The model is purely mathematical in nature and is based on linear regression analyses of laboratory data on mould growth in constant and transient conditions.
Both advanced mould prediction approaches include, however, various simplifications and assumptions to model the complex phenomenon of biological growth. Consequently it can be questioned how accurate these prediction models are. In this respect Vereecken & Roels (2012) conduced an interesting independent comparison between these two models for several steady state and transient conditions. The outcome of the study revealed that large differences between both models occurred. Therefore, great care should be taken in analysing the produced results of these models.

Interstitial condensation This second type of moisture limit state, on the other hand, is an indirect method to prevent biological growth. This approach restricts the amount of interstitial condensation inside building envelopes, most often on the inner side of wind barrier layer. This limit state corresponds to the starting point of drainage of the condensate. Here, run-off should be avoided as this might result in moisture accumulation, and thus, biological decay at lower positioned biological materials. Typical examples are interstitial condensation on spunbonded polyethylene underlay materials which results in high moisture contents of the bottom plate (e.g. Økland 1998, Thue et al. 1996).
The starting point of drainage of condensate on solid materials is complex, depending mainly on the materials contact angle, surface roughness, moisture retention curve and moisture transport properties. Most limit states discussed in the literature refer to the onset of drainage on non-capillary materials, so, only the contact angle and material roughness are of importance. For example, Janssens (1998) conduced experimental work to investigate the maximum condensation on a typical spunbonded polyethylene foils for various surface slopes. Based on this experiment Janssens (1998) has put forward a maximum value of 0.1 kg/m^2 to avoid run-off on vertical non-capillary surfaces. In addition, several maximum condensation levels are reported in international standards, such as 0.03-0.2 kg/m^2 in Belgium (TV215) and 0.5 kg/m^2 in Germany (DIN4108). However, the origin of these values, applied as threshold condensation levels for simplified hand calculations, are not reported.

2.4.2 Moisture control strategies

The previous section discussed existing moisture performance limits states for timber frame construction. In the literature several measures and system approaches to fulfil these requirements are documented. Tenwolde & Rose (1994) distinguished between two major

control strategies: (1) limiting the moisture load conditions and (2) design building component with sufficient tolerance for high moisture contents. This is subdivided in three categories by Lstiburek et al. (2002): (1) control of moisture ingress, (2) control of moisture accumulation and (3) removal of moisture. Based in on this classification system, Figure 2.9 lists an overview of moisture control strategies for timber frame building envelopes in cold winter climates.

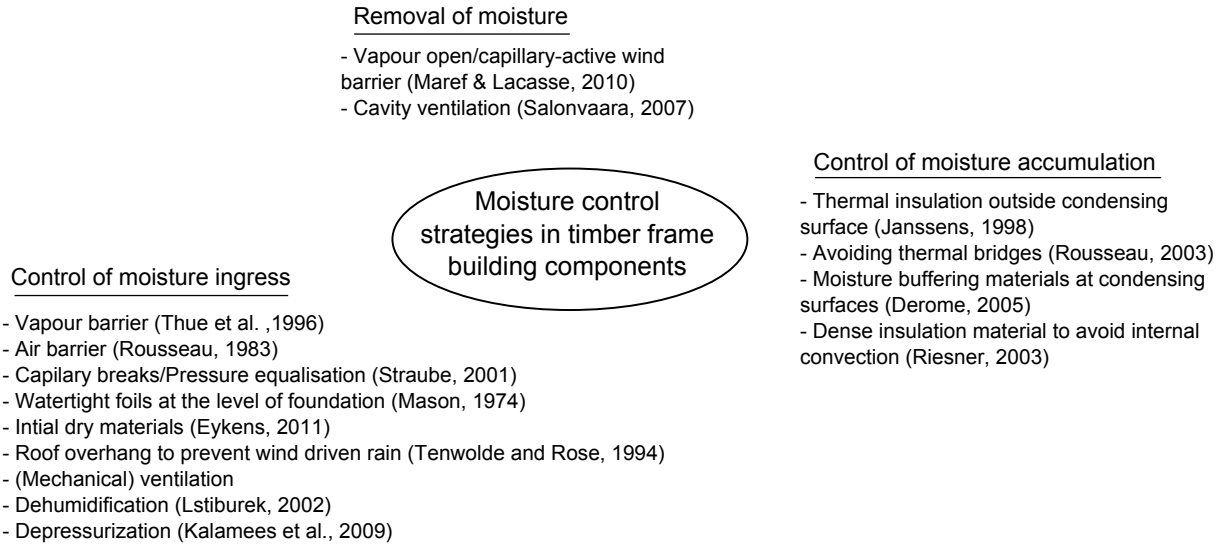

Figure 2.9: Classification of moisture control strategies based on Lstiburek et al. (2002).

The measures depicted in Figure 2.9 are generic moisture control strategies. Most are straightforward and generally accepted in building practice today. Their effectiveness, of course, depend on the specific configuration of the component and the exposed climate. For example, promoting moisture removal by applying extremely vapour open wind barrier materials is only effective if a limited amount of thermal insulation is positioned outside the condensing surface (Janssens 1998). Also, the use of initially dry materials is far more important for building components with vapour retarding exterior layers, such as compact roofs, in comparison with elements with vapour open wind barrier layers (Borsch-laaks 2011). However, some of the control measures mentioned are criticised in the literature. In this respect Steskens et al. (2012) stated, based on numerical simulations, that the use of capillary-active underlay materials may be ineffective to reduce interstitial condensation. In addition, Tenwolde & Rose (1994) criticised the depressurisation of buildings to avoid moisture problems related to moisture convection. Tenwolde & Rose (1994) stated that negative pressures have potential for increased radon release from the soil and might result in back drafting of combustion products, such carbon monoxide.

Among the moisture control strategies listed in Figure 2.9, cavity ventilation, is by far the most dubious measure. For example, Karagiozis & Künzel (2009) and Straube & Finch (2009) emphasised the importance of ventilated cavities to increase the drying potential of timber frame walls. In contrast, however, Tenwolde et al. (1993) noted that the conditions

inside the cavity are not always dry enough to provide sufficient drying. As a consequence, the cavity can actually have a negative effect by contributing to an additional source of hygroscopic moisture load (e.g. undercooling condensation). In this context Gudum (2003) demonstrated that ventilating walls with a perfect interior air and vapour barrier results in a higher moisture load. However, for walls with unintended air leakages or accidental water infiltration, cavity ventilation improves drying according to Gudum (2003). An extensive literature review on this topic can be found in Salonvaara et al. (2007).

2.5 Conclusions

This chapter outlined the current state-of-the-art on global building airtightness, air transport effects on the hygrothermal behaviour of lightweight walls and the corresponding moisture control strategies. The first section illustrated the increased awareness of global building airtightness during the last decade. The main origin of this trend lies in its implementation in the mandatory building energy certification in Europe and the increasing popularity of volunteering building energy labels, such as the Passivhaus-standard. Figure 2.10 compares the Belgian airtightness recommendations, the requirements of the Passivhaus-standard and the averaged air permeance in construction practice in the period between 1976 and 1998 (Janssens & Hens 2003). The figure is given as a function of the building compactness to overcome the different normalisation methods.

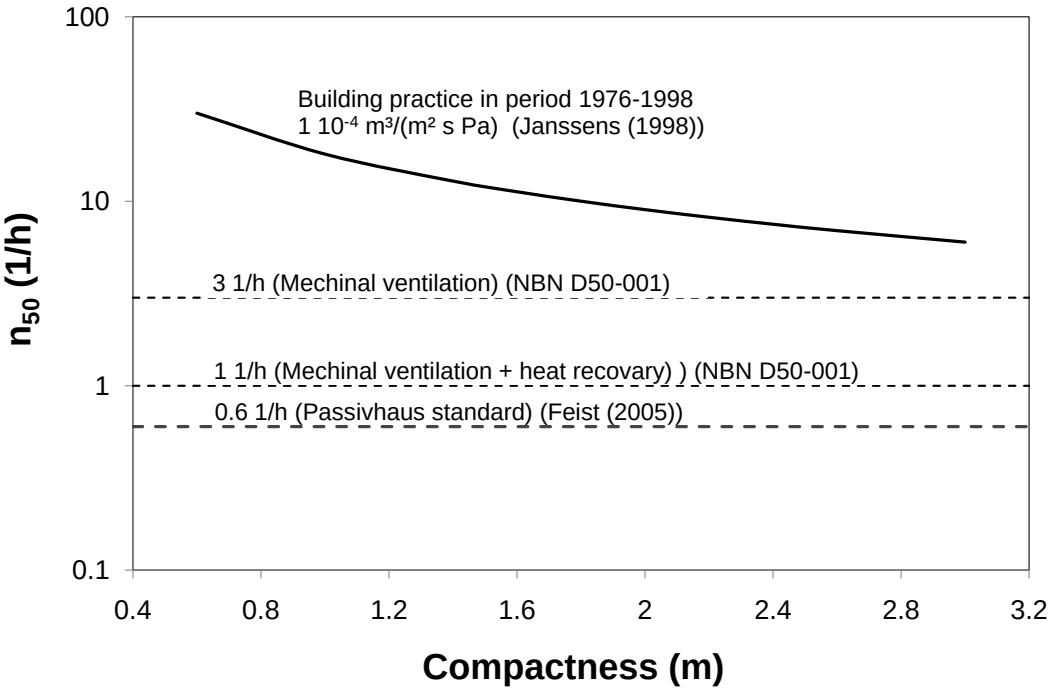

Figure 2.10: Airtightness requirement of the Passivhaus-standard, Belgian airtightness recommendations and averaged airtightness levels in period 1976-1998 as a function of building compactness in a semi-log plot.

This figure demonstrates that today's airtightness targets, such as 0.6 1/h (Passivhaus) and 1 1/h (low energy buildings), are more than an order of magnitude lower than the building practice of ten years ago. Although many experiences from successful projects are currently available, it remains a challenge to achieve these severe airtightness levels with traditional interior air barrier systems (Reiss & Erhorn 2003). The main reasons for this are the high number of difficult intersections in this interior air barrier, such as the connection between the intermediate floor and the outer walls, and perforations for electrical and plumbing services (Aho et al. 2008, Kalamees 2007). As a result, the timber frame building industry is looking for cost-effective alternatives to meet the strict airtightness requirements for low energy buildings and Passivhaus dwellings. One of the possibilities would be realising the airtight layer on the exterior of the building envelope where fewer joints and perforations are present. However, the practical feasibility of such systems is not yet verified in detail.

Apart from the practical issues, exterior air barriers systems may significantly influence the hygrothermal behaviour of highly insulated timber frame elements in cold and moderate climates. Though the hygrothermal performance of lightweight construction with an exterior air barrier has not been examined to date, several studies indicate that such elements may suffer from increased moisture loads. Many authors have addressed the importance of natural convection within highly insulated timber frame walls. In contrast to interior air barriers, such internal air rotations may induce an increased moisture ingress through discontinuities in the inner vapour barrier in assemblies with an exterior air barrier. The importance of these phenomena on the overall wall performance, however, is not yet addressed in the literature.

The third part of the literature review showed that today's hygrothermal component modelling mainly focuses on heat and moisture transport, neglecting the effects of air transport. As a consequence, no commercial HAM-model that considers air as an active mass component is currently available. In the past, however, several HAM-models including air transfer have been developed for specific research purposes. This chapter summarised the corresponding implementation methods for air transport. Yet the current applicability of these models is limited because only their authors know how to operate the majority of the related programming codes. As a consequence, many older models have not been updated with current operating systems. In addition other aspects, such as limitations in the moisture transport, omission of natural convection or long computational times, make that none of these existing HAM-models are suitable to achieve the goals of the research project at hand.

The final section briefly discussed the commonly applied moisture limit states in timber frame building engineering. Mould growth and drainage of interstitial condensation are the most recognised moisture limit states. Various authors have studied the prediction of mould

growth. As a consequence, detailed mould prediction models are currently available. Yet an independent comparison of these models by Vereecken & Roels (2012), revealed significant uncertainties on their results.
Drainage of interstitial condensation, on the other hand, is scarcely addressed in the literature. For this limit state only conservative guidelines have been documented.
In summary, this section stated that further research improving the reliability of the existing moisture limit states is desirable. These aspects fall beyond the scope of the current research project, however.

2.5.1 Research questions

The present study will investigate the practical and hygrothermal feasibility of timber frame construction with an exterior air barrier. Based on the above-mentioned literature survey five research questions are postulated:

- Can exterior air barriers reach sufficient airtightness levels, required for low energy houses (1 1/h) and Passivhaus constructions (0.6 1/h)?
- What are the practical advantages and disadvantages of this technique?
- What are the hygrothermal risks involved?
- Which are the decisive parameters, influencing the hygrothermal behaviour?
- Which wall assemblies will result in a sound hygrothermal performance in Belgian climate conditions?

3

In situ Air Leakage Measurements of Exterior Air Barriers Systems

The aim of the present chapter is to verify whether acceptable airtightness levels can be achieved in practice by improving the continuity of the wind barrier. After an introductory section based on experiences from Norway, this chapter discusses the airtightness evolution during the consecutive construction stages of two Belgian timber frame houses with an exterior air barrier. For the first case study, attention is drawn on the practical feasibility of this approach. The second test case focusses on quantifying typical air leakages through these systems. Therefore, additional laboratory measurements on specimens of the exterior air barrier, including typical joints, will be presented in order to verify the influence of different types of local air leakage paths. The obtained data from both the in situ and laboratory study enables that realistic air leakage rates will be applied in the hygrothermal analysis of chapters 4 and 6.

3.1 Experiences from Norway: stepwise pressurisation testing

In many European countries the standards regarding global building airtightness have been revised recently. As a result of these stricter requirements, the awareness of building airtight starts to reach the architects, building contractors and craftsmen. Especially in Norway, where the threshold n_{50}-value has been reduced from 4 1/h to 2.5 1/h for residential buildings in 2009, the impact of the stricter requirements on how airtightness is realised in practice can be noticed. For an increasing number of Norwegian dwellings, the airtightness is measured twice; first, when the building is windtight ($n_{50,w}$) and, second, when the building is finished with an interior air barrier ($n_{50,f}$). Legally, only the latter is of importance. Yet as will be shown in this chapter, Norwegian contractors experienced that this stepwise measuring approach decreases the labour for realising the required airtightness levels. As a result of this procedure, an increasing number of pressurisation tests during windtight stage are conducted in Norway, which in fact corresponds to the configuration of an exterior air barrier system. Therefore, this first section seeks to outline the current literature on this stepwise pressurisation approach, providing a first indication of the airtightness levels that can be realised with exterior air barriers.

Myhre & Aurlien (2005)

The first publication on this stepwise pressurisation method dates from before the stricter Norwegian airtightness requirements. Myhre & Aurlien (2005) first measured the airtightness of three residential dwellings during the windtight stage, and next, after finishing the buildings. The buildings concern one detached house (in Rælingen) and two double-family houses (in Sola and Lillestrøm). These pilot projects were sponsored by the Norwegian State House Bank to promote low energy houses at that time. Therefore, several measures had been taken to increase the airtightness of the interior barrier such as the installation of service cavities. Additionally, attention was drawn on improving the airtightness of the exterior wind barrier by, for instance, allowing a continuous connection from the wall to the roof by means of ending the roof trusses with the wall. Furthermore, in one of the projects (Rælingen) the wind barrier consisted of a double layer: 9 mm gypsum board covered with a vapour open spunbonded foil. However, the authors describe the improved airtightness of the wind barrier only as a back-up and stress the importance of the continuity of the interior barrier to avoid moisture problems.

Table 3.1 presents the n_{50}-values measured by Myhre & Aurlien (2005). The results show that for the projects in Rælingen and Sola the airtightness improved after the interior air barrier had been finished. The authors assign the smaller decrease of the n_{50}-value of the house in Rælingen to the installation of a chimney in between the two measurements. In

contrast to the other two projects, the house in Lillistrøm had a higher n_{50}-value in the second measuring stage. Myhre & Aurlien (2005) attribute this to the volume of the basement which was not included in the first measurement.

Project	$n_{50,w}$ (1/h)	$n_{50,f}$ (1/h)
Sola I	1.2	0.3
Sola II	1.3	0.4
Lillestrøm I	1.5	1.7
Lillestrøm II	1.5	2.8
Rælingen	0.8	0.6

Table 3.1: Building airtightness during windtight ($n_{50,w}$) and finished ($n_{50,f}$) state (Myhre & Aurlien 2005).

In summary, these measurements showed that new wind barrier products and new design solutions can improve the airtightness of the external wind barrier in timber frame construction. The use of roll products at the exterior of the building envelope reduced the amount of joints, resulting in low n_{50}-values during the windtight stage.

Aurlien & Rosenthal (2008)

A similar study by Aurlien & Rosenthal (2008) presents the airtightness results of five different residential buildings, tested in windtight and finished state. The results are summarised in Table 3.2. The first three projects were executed by the same contractor who had little experience in realising very low airtightness levels. Nevertheless, the target was to achieve an n_{50}-value lower than 1.5 1/h. The first two projects failed to reach this goal. The results, given chronologically in Table 3.2, indicate however that the postulated threshold value already had been reached in the third project. Aurlien & Rosenthal (2008) mention that the increase of the n_{50}-value in the second step of the first two buildings was caused by the ventilation technicians who installed the ventilation ducts with little regard for airtightness.
The final two projects in Table 3.2, on the other hand, correspond to the results of a contractor who was experienced in achieving high airtightness levels. The obtained results are very low.

Project	$n_{50,w}$ (1/h)	$n_{50,f}$ (1/h)
I	1.9	2.0
II	1.4	2.0
III	0.5	0.4
IV	0.3	<0.2
V	<0.1	-

Table 3.2: Building airtightness during windtight ($n_{50,w}$) and finished ($n_{50,f}$) state (Aurlien & Rosenthal 2008).

To summarise, the $n_{50,w}$-values in Table 3.2 show that even extreme low airtightness

levels can be achieved with an exterior wind barrier only. Based on this study, it can be concluded that the key success factor is the experience of the contractor. Yet the trend in the first three projects suggests that the learning period is relatively short. Already after two dwellings the contractor was able to reach the required n_{50}-value. Furthermore, the results indicate that the stepwise measuring procedure might result in moving the most airtight layer, traditionally at the interior, to the exterior of the building envelope. As a consequence, it becomes impossible to control the airtightness of the interior air barrier when the exterior layer is already to a high degree tight. In addition, it is very likely that the contractor will be less motivated to carefully install the interior air barrier when the $n_{50,w}$-value is already meeting the required level, such as for the last three dwellings in Table 3.2. In this respect another interesting observation is that in contrast to Myhre & Aurlien (2005), Aurlien & Rosenthal (2008) do not mention the importance of the interior air barrier to reduce potential convective moisture transport.

Holøs & Relander (2010)

A third study on stepwise pressurisation testing was published by Holøs & Relander (2010). In contrast to the above-mentioned two studies, Holøs & Relander (2010) observed the airtightness of a whole residential district. In total 62 low energy apartments have been measured during the windtight and final stage. It is important to notice that none of the craftsmen involved had previous experience in realising specific airtightness requirements and the target n_{50}-value was 1 1/h. In all projects the exterior wind barrier consisted of a gypsum board combined with a spunbonded polyethylene foil. Figure 3.1 presents an overview of the obtained measuring results for the individual apartments. The figure shows a scatter plot in the middle, comparing $n_{50,f}$ with $n_{50,w}$. At the top and right of the figure, Holøs & Relander (2010) provided histograms of the data. The figure shows that only 60% of the buildings achieved the target n_{50}-value (blue and grey dots). Holøs & Relander (2010) explain this by the initial overestimation of the volumes. In most buildings the airtightness was improved while performing a pressurisation test until an n_{50}-value of 1 1/h was reached. After the projects were finished, however, it was noticed that the building volumes were overestimated. As a result, with corrected volumes, increased n_{50}-values were obtained. The authors mentioned that with the initial volumes, all but one apartment fulfilled the requirement.

Furthermore, Figure 3.1 indicates that improving the airtightness of the wind barrier increases the chances for better final $n_{50,f}$-values. For the $n_{50,w}$-values lower than 1 1/h (blue and black dots), 81 % of the final $n_{50,f}$-values fulfilled the requirement (blue dots). In contrast, when the $n_{50,w}$ exceeded 1 1/h (grey and red dots) this was only 49 % (grey dots).

In addition, Holøs & Relander (2010) conducted a survey to collect feedback from the carpenters on how the airtightness was realised on site. Most important measures reported

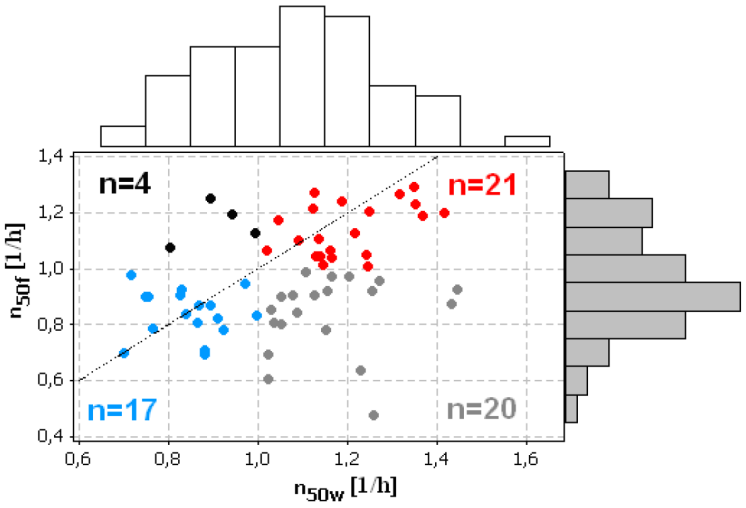

Figure 3.1: Measured n_{50}-values during windtight (w) and finished (f) state (Holøs & Relander 2010).

were window-to-wall joints which were filled with PU-foam. Also PU-foam was applied to reduce the air leakage between the bottom plate and the foundation. Finally, the time consuming caulking of ducts to the gypsum board was mentioned too.

Relander (2011)

Relander (2011) performed a statistical analysis on recent Norwegian building airtightness data to investigate the possibility to predict the $n_{50,f}$-value from the measured $n_{50,w}$-value. Relanders data set consisted of measuring results of 23 single family houses which had been measured during windtight and final stage. For his study, Relander tested 10 additional buildings. The other results were obtained from Norwegian reports (Jacobsen et al. 2008, Syversen & Ulimoen 2009) and the international publications, summarised above (Aurlien & Rosenthal 2008, Myhre & Aurlien 2005). Relander (2011) presented the $n_{50,w}$-values against the $n_{50,f}$-values using a log transformation. This resulted in rather scattered points for the applied data set, and thus, wide confidence and prediction intervals. Consequently, the proposed upper limits for $n_{50,w}$-values are rather conservative. For example, Relander (2011) claims that in order to achieve a final building airtightness of 2.5 1/h with a confidence of 95 %, one should realise an n_{50}-value lower than 0.95 1/h at the windtight stage.

Unpublished pressurisation data[1]

This paragraph discusses the results of 6 normal Norwegian dwellings (no Passivhaus standard, neither low energy houses) for which the airtightness was measured during the

[1] Data provided by Hans Ananiassen from the Norwegian company *Trykktesteren* (personal contact)

windtight stage. The houses were built by three different contractors and the pressurisation tests have been conducted by a local independent commissioning company.

	I	II	III	IV	V	VI
$n_{50,w}$ **(1/h)**	**0.52**	**0.30**	**0.56**	**0.29**	**0.61**	**0.28**
Volume (m^3)	683	723	434	870	778	518
Year	2009	2009	2009	2009	2010	2010
Wind barrier	BIFB+Foil	BIFB+Foil	BIFB+Foil	GB+Foil	BIFB+Foil	BIFB+Foil
Contractor	A	B	C	C	A	A

Table 3.3: Pressurisation results during windtight stage and additional building information (BIFB: bituminous impregnated fibreboard, GB: gypsum board).

House I was the contractor's first project to be tested on airtightness. This lack of experience resulted in several difficult construction details, such as the rafters penetrating the wind barrier at the roof overhang (Figure 3.2I). This resulted in a high number of difficult joints which were carefully caulked by the craftsmen. For this first dwelling, an example for the contractors' future projects, finally, a low n_{50}-value was achieved. However, to reach this value a tremendous amount of work was needed.

The second house was constructed by a contractor experienced in building airtight houses. As a result a very good building airtightness was achieved without many problems.

House III and IV were built according the 'standard delivery quality' of an experienced contractor. No additional measures to improve the airtightness of the wind barrier were mentioned explicitly by the contractor. This indicates that several measures were already seen as standard solutions. For example Figure 3.2III shows how the wind barrier was continuously mounted from the wall to the roof. The roof overhang was constructed on top of the wind barrier, so, no additional joints at the eaves were created. Furthermore, this contractor sealed all the joints of the exterior barrier with tape.

The last two houses in Table 3.3 were constructed by the contractor of House I. As a result of his experience of the first project, low airtightness levels could be reached with far less work. Again no tape had been applied for the wind barrier, expect to make the connections to the windows.

Again, the results of these additional six test cases show that values lower than 1 1/h can be achieved with a little amount of work if the contractor has a basic experience in building airtight.

3.1.1 Summary

This section presented the results of pressurisation tests on recent Norwegian residential buildings, measured in both the windtight and airtight construction stage. Driven by the

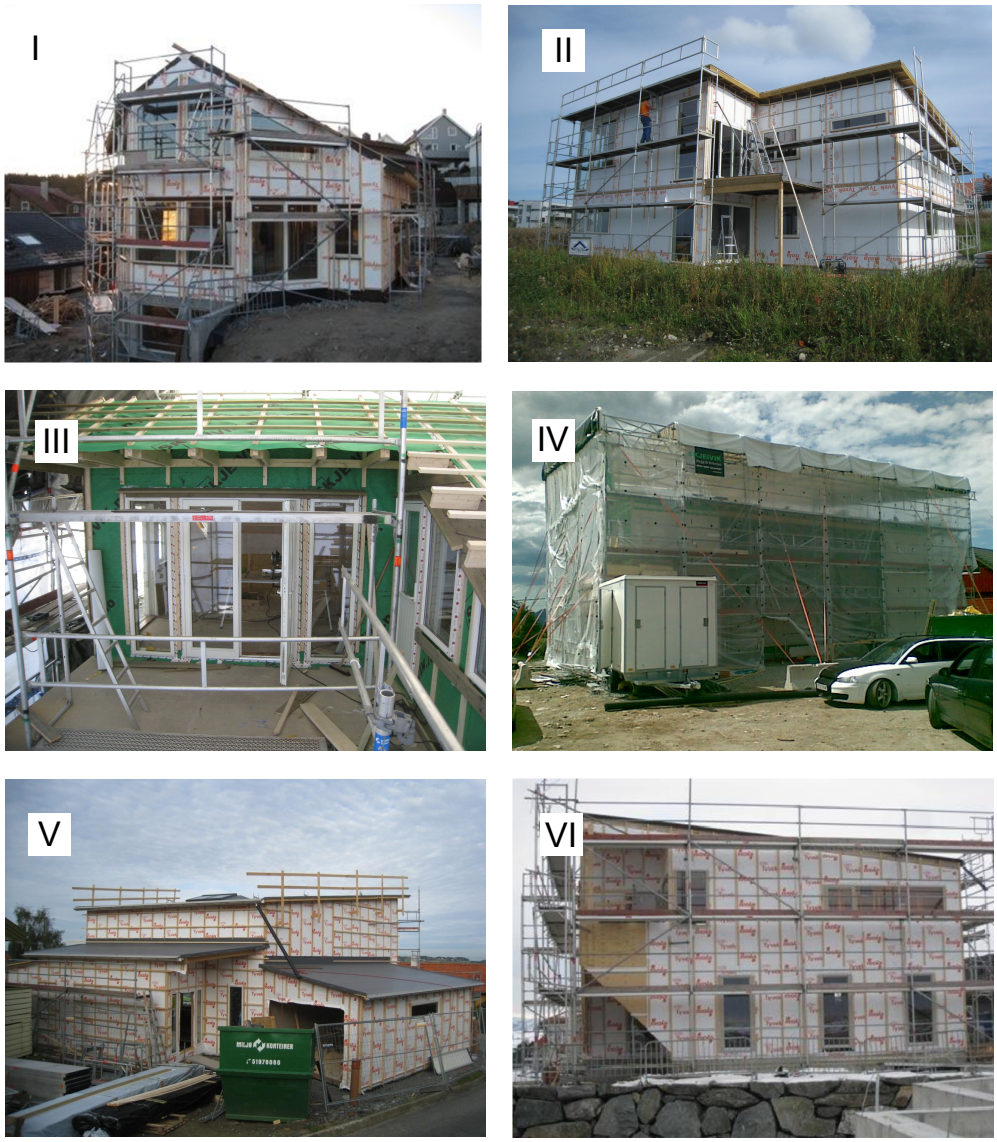

Figure 3.2: Pictures of the dwellings tested.

stricter requirements regarding building airtightness, emphasis on improving the airtightness of the wind barrier can be noticed in Norway. Overall, the results indicate that once the contractor has a basic experience in building airtight, sufficiently low levels can be reached with a wind barrier only. Several projects report n_{50}-values meeting the requirement put forward by the Passivhaus-standard[2] (Feist et al. (2005)).

None of these studies explicitly mentioned that exterior air barrier systems are easier to construct in comparison with inner systems. However, as great attention is drawn on increasing the airtightness of the wind barrier in a first step, it can be assumed that this approach must correspond to practical advantages to some extent. In this context, Holøs & Relander (2010) mentioned for example that craftsmen could easily increase the airtightness of the wind barrier during the pressurisation of the dwellings. Indeed, during the windtight stage most of

[2] n_{50}-value <0.6 1/h

the joints in the wind barrier can be reached either from inside or outside, as illustrated for a typical Norwegian dwelling in Figure 3.3.



Figure 3.3: Repaired defect in wind barrier in a residential building during windtight stage (Aurlien 2008).

Notwithstanding whether the required n_{50}-value is already reached after the first test, still a traditional interior air barrier is created by sealing the vapour barrier in Norway. Yet it can be questioned with which accuracy this interior barrier will be installed in case the $n_{50,w}$-value already meets the proposed value. Moreover, as a consequence of this stepwise pressurisation approach, it becomes impossible the verify the final airtightness of the inner air barrier. The final pressurisation test can only report the combined effect of both the interior and exterior barrier. As a result, it is very likely that this stepwise pressurisation method leads to buildings for which the most airtight layer, traditionally at the interior of building envelope, is positioned at the exterior of the insulation layer. Such configurations can have higher moisture damage risks in some circumstance. However, the majority of the studies summarised in this section do not even mention the hygrothermal implications and solely concentrate on improving the whole-building airtightness.

3.2 Investigation on the practical implications of exterior air barriers: case study I

The previous section, based on measurements on recent Norwegian dwellings, presented a first indication of the airtightness levels that can be obtained by exterior air barriers. However, the previous studies did not sufficiently document in detail how the airtightness was realised. Therefore, the aim of the current section is to gain more insight in the practical implications and possible time reduction by installing exterior air barriers. This section discusses the construction of a single family Passivhaus dwelling with an exterior air barrier in great detail. In this house a traditional interior air barrier was installed in addition to the

exterior air barrier. The realisation of both barriers was documented and, in between their installation, three pressurisation tests were conducted: (a) with only the exterior air barrier installed, (b) after inflation of cellulose insulation in the wood frame structure and (c) after finishing the interior air barrier. This section presents the results of pressurisation tests, outlines the encountered advantages and discusses the attention points and drawbacks of this approach from a practical point of view.

3.2.1 Description of the test house and realisation of the exterior air barrier

The test case (Figure 3.4) concerned a semi-detached Passivhaus dwelling located in Leuven, Belgium. The house, which has a heated volume of 545 m^3 and a compactness[3] of 2.7 m, was a light-weight construction with I-profile wooden studs between the internal structural board (OSB) and the outer wind barrier layer. Figure 3.5 shows a schematic



(a) (b)

Figure 3.4: Overall view of the house studied: (a) during construction of the wind barrier and (b) final stage.

overview of the building envelope. The studs are spaced at 400 mm and the cavity in between is filled with blown-in cellulose fibre insulation. The internal 15 mm OSB layer with overall dimensions of 575 by 2400 mm acts as a vapour retarder, in addition to its structural purpose. All the joints in this layer have been sealed, so, the OSB also performed as a continuous interior air barrier. To protect this layer from penetrations, a service cavity of 40 mm has been provided for the installation of electrical and plumbing services. Before the inner air barrier system was realised, however, the airtightness of the wind barrier was improved by sealing all the joints.

The wind barrier in the walls consists of 18 mm thick bituminous impregnated fibreboards (hereafter referred to as BIFB I), with overall dimensions of 1150 by 2400 mm. The

[3] ratio of building volume to building envelope area

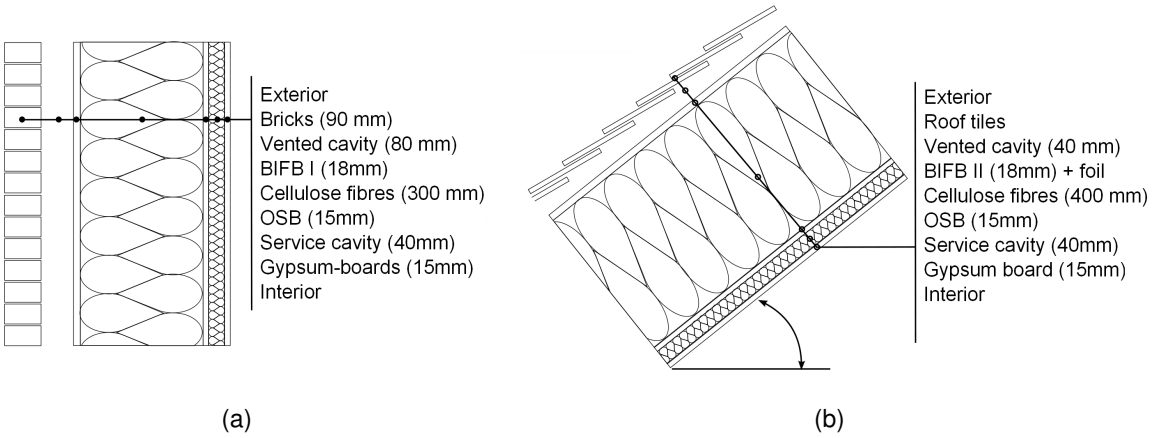

Figure 3.5: (a) Configuration of the wall and (b) roof (BIFB: Bituminous Impregnated Fibre Board and OSB: Oriented Strand Board).

boards have an additional layer on the exterior face, which significantly contributes to the airtightness of this material. Notwithstanding the high air resistance, the boards have a high vapour permeability which makes them applicable as breather membranes on the outside of thermal insulation. On the other hand, the wind barrier applied in the roof consists of a similar fibreboard, but without coating (BIFB II). To improve its airtightness, this layer was covered with an airtight and vapour permeable foil. The same foil was applied to guarantee the exterior airtightness of the common wall. Figure 3.4a shows how the number of joints in the wind barrier could be reduced to a minimum by using large panels in the wall and applying a spunbonded foil for the roof. The interior barrier, in contrast, had more complex details, such as the continuity around the intermediate floors, as illustrated in Figure 3.6a. In total 172 man hours were invested in sealing the interior barrier. For the exterior air barrier, on the other hand, only 72 man hours were needed.

Although the study showed that exterior air barriers may result in a significant labour reduction, several drawbacks have been noticed as well. One of the major disadvantages was the dependency of the weather, as the joints can only be sealed in dry conditions. Furthermore, to guarantee its durability, it was essential to provide a primer before sealing the joints in the fibreboards which increased the work with 3 to 4 man hours. For one joint, where the primer was not carefully enough applied and/or the tape not sufficiently pressed, the tape started to open up after a few weeks (Figure 3.6b). This example stresses the importance of an accurate execution in order to avoid degradation of the sealed joints. In this context, however, it should be noted that if correctly applied, these connections are resistant to extreme weather conditions. Field tests on the durability of such kind of joints were reported by Proclima (2009), showing that the connection between the fibreboard and the tape is even stronger than the material itself. In addition, two complex details have been encountered during the realisation of the exterior air barrier. First, the continuity of the air barrier is in conflict with its need for drainage to the gutter (Figure 3.7). This problem



(a) (b)

Figure 3.6: (a) Complex joint in the interior air barrier at the corners of the intermediate floors, (b) loosening of the tape by unprecise installation.

around the eaves was solved by sealing the foil with a double adhesive tape to the gutter board. Next, this airtight board was connected to the wind barrier of the wall. This last joint was difficult to realise, as this inner corner is very narrow. Typically induced by a lack of practical experience, such details are unnecessary complex and can be avoided by a thoughtful design, such as a separate roof overhang, installed after the wind barrier was finished as discussed in section 3.1 and illustrated in Figure 3.2III. The second problem encountered, concerned the connection of the wind barrier to the foundation. As depicted in Figure 3.8a, the wind barrier was sealed to the water barrier. However, both the water barrier and the lower part of the wind barrier are exposed to splashing rain and dirt, as this figure clearly illustrates. Consequently, this region is typically sandy, making it almost impossible the provide durable sealed joints.

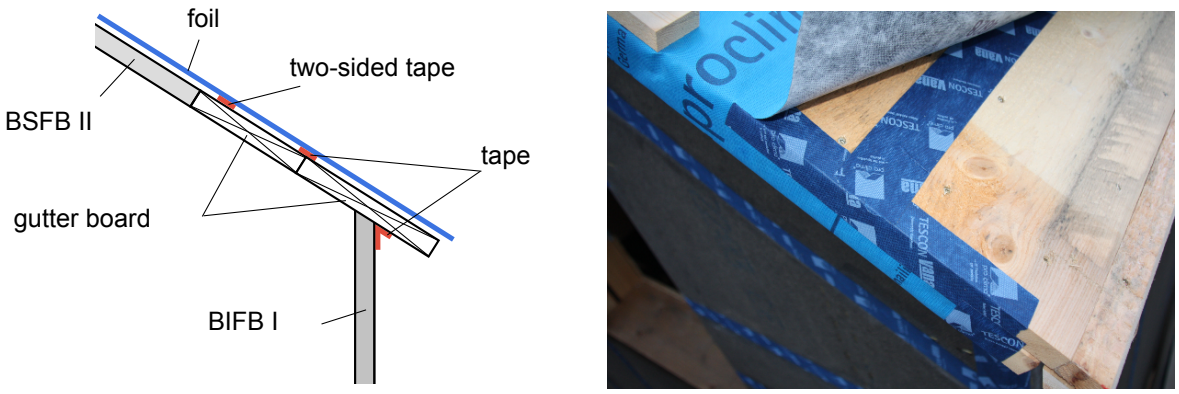

(a) (b)

Figure 3.7: Complex solution at the level of the eaves.

3.2.2 *In situ* pressurisation tests

During the construction of the building, three consecutive pressurisation tests have been conducted in accordance with EN13829:1996: (a) with the exterior air barrier finished, (b) after inflating the cellulose fibre insulation and (c) with the interior air barrier installed. The corresponding results in Table 3.4 show that the n_{50}-value of the first test equals the Passivhaus threshold value of 0.6 1/h. The second pressurisation test, conducted after the

	$\mathbf{n_{50}}$ **(1/h)**
Exterior air barrier	0.60
Cellulose insulation blown in	0.25
Interior air barrier	0.13

Table 3.4: Measured building airtightness levels.

cellulose insulation was blown in, shows a relatively large reduction of the n_{50}-value. The air permeability of the cellulose insulation layer of 30 cm is two orders of magnitude higher than the permeability of the exterior air barrier material of this instance (Table 3.9). Consequently, the cellulose insulation can only improve the airtightness of the building envelope at the level of (small) deficiencies in the exterior air barrier. Here, the cellulose will locally increase the resistance for air transport. Yet it should be noted that in terms of absolute values the contribution of the cellulose insulation to the global building airtightness was limited.

Finally, the last pressurisation test indicated that the airtightness of the inner barrier performed better than the exterior one. Yet the absolute difference between both was very limited.

3.2.3 Observed air leakages in the exterior air barrier

Given the effort put in realising the exterior air barrier, the obtained result of 0.6 1/h (Table 3.4) was higher than expected. Therefore, in order to detect the most important leakages, a smoke generator was placed inside the building during pressurisation. This smoke test revealed two explicit leakages: (1) at the level of the foundation and (2) below the windows.

The first leakage, at the level of the foundation, was clearly caused by a combination of two effects: (a) the joints were partly sealed on soiled surfaces and (b) the joint between the foundation and the water barrier was insufficiently sealed. This first problem, already mentioned in the previous section, is illustrated in Figure 3.8a. In addition to the difficulties of making the surface sand free before sealing the joint, the figure illustrates the complexity of making the exterior barrier continuous in the corners. The most explicit air leakages noticed with the smoke test, however, were located between the water barrier and the foundation, where no sealing was provided (Figure 3.8a). The water barrier, consisting of a PE-foil with

a honeycomb pattern, had a thickness of only 0.5-1 mm. A significant amount of leakages occurred at this interface as a result of the roughness of the concrete foundation.

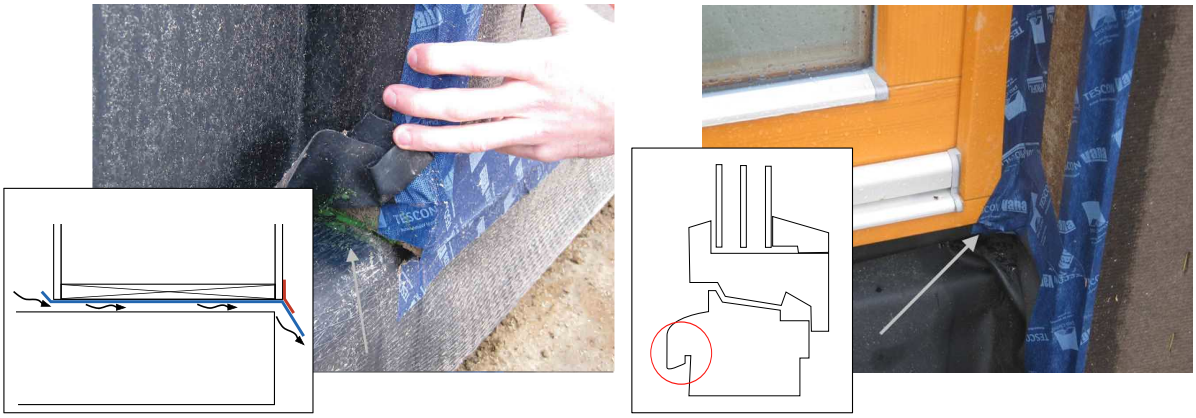

(a) (b)

Figure 3.8: (a) Air leakage at the level of the foundation (b) Air leakage caused by the drip edge.

In the literature several studies analysed air leakage rates through the joint between the bottom plate and the foundation wall (e.g. Axén & Pettersson 1977, Carlsson et al. 1980, Siitonen 1982, Lawton & Limited 1992, Relander, Heiskel & Tyssedal 2011). In summary, these studies have shown that, in addition to the sealing method, the magnitude of the leakage is highly depending on the roughness of the basement wall and the load on the bottom plate. As a result of these parameters, the spread on the results is rather large. Table 3.5 summarises literature results where thin materials have been applied between the bottom plate and the foundation wall, closely corresponding to the situation of the case study at hand. In addition, the results are also presented as the potential impact on the n_{50}-value[4]. Because the PE-foil and tar paper applied by these considered authors are not completely the same as the foil used in the test case, a detailed comparison between these leakage rates remains difficult. Nevertheless, the results give a first indication of the order of magnitude of possible air leakage rates through this joint. In order to obtain more specific data, laboratory measurements on the same configuration (Figure 3.8a) have been conducted with the test setup which will be described in section 3.3.3. The corresponding results of various foundation assemblies can be found in Cornelis & Appelmans (2011). Only the overall results for the configuration corresponding to the test case are included in Table 3.5 (abbreviated as KUL (2011)). This table shows that our measurements with the foil, applied in the test case result in lower values than reported for similar configurations in the literature. However, based on our laboratory results, it can be concluded that the air leakage of this joint can cover 20% up to 50% of the global n_{50}-value measured in the second pressurisation test (0.25 1/h).

The studies mentioned in Table 3.5 conclude that thicker and more malleable sealing ma-

[4]length of foundation joint in this case study is 39 m

	$\mathbf{g_{50}}$ ($m^3/(m\,h)$)	$\mathbf{n_{50}}$ (1/h)
PE-foil, Eek (2009)	0.2-6.4	0.01-0.46
tar paper (2 mm), Relander, Heiskel & Tyssedal (2011)	1.4-8.6	0.10-0.62
PE-foil, Mattsson (2004)	2.8-11.8	0.20-0.84
tar paper, Mattsson (2004)	16.6-28.2	1.19-2.02
PE-foil (0.5-1mm), KUL (2011)	**0.7-1.7**	**0.05-0.12**

Table 3.5: Air leakage data for joint between bottom plate and foundation wall.

terials, such as EPDM, rubber and PUR membrane, can reduce the air leakages through the joint between the bottom plate and the basement wall to negligible levels. Yet the joint between the exterior air barrier and the foundation remains problematic as these surfaces are typically dusty, and thus, difficult to seal from the outside.

The second leakage detected, at the level of the windows, was caused by the drip edge below the window (Figure 3.8b). The fixed frames of the applied windows were provided with a drip edge which impeded to continuously seal the window to the exterior air barrier. As suggested by Van den Brande & Wouter (2011) this problem can be avoided by applying foils to connect the windows to the exterior air barrier. In this context the laboratory work of Penne & Vandeweerd (2012) concluded that such foils around the windows perform even better in combination with an exterior air barrier, instead of an interior barrier.

3.3 Quantifying typical air leakage paths: case study II[5]

The previous two sections showed that sufficiently airtight buildings can be achieved with improved wind barrier systems. The studies performed pressurisation tests during the windtight and final stage. As a consequence, the generated data could only conclude on the overall airtightness of these buildings. For the hygrothermal analysis of chapter 4, however, it is important to estimate rates of typical air leakages which can occur in these barriers. Therefore, in addition to the previous section, a second test case provided with an exterior air barrier has been studied in great detail. To quantify the different leakage paths, the study applied the reductive sealing technique. In total 12 pressurisation tests have been conducted during the construction process of a detached Passivhaus construction. In addition to these field tests on the entire building, this section will present the results of laboratory measurements on specimens of the exterior air barrier including typical joints, in order to verify the influence of different possible types of local air leakage paths.

[5]partially published in Langmans, Klein, De Paepe & Roels (2010)

3.3.1 Description of the test house and realisation of the exterior air barrier

The house is located in Ghent, Belgium. It is a detached, three story single family house with two bed and breakfast guest rooms on the ground floor. Figure 3.9 shows an overall view of the house which has a heated volume of 1083 m^3. The house has the same light-weight timber frame construction as the test case of the previous section 3.2. Also, the configuration of the building envelope is identical. Only for the roof (Figure 3.5b), the same bituminous impregnated fibreboard as for the walls (BIFB I) has been applied instead of a combination of a more permeable fibreboard and a foil.



(a) (b)

Figure 3.9: (a) Wind barrier during construction stage (b) overall view of the finished house (West and South facades).

The exterior surface of the house is 630 m^2 and contains 90 m^2 windows and does not contain a chimney, nor skylights. Table 3.6 presents the length of the external joints. In the current building practice these joints between the exterior soft fibreboards are not sealed. However, for this study the airtightness of the wind barrier was improved, so, it would act as an exterior air barrier by sealing all the joints in this layer. In between, several pressurisation tests were performed to asses the air leakage through the different joints.

Figure 3.10a shows how the wind barrier was sealed at the windows and at the foundation. For the latter, an airtight foil[6] was glued to the foundation and sealed with tape to the wind barrier. In this way the air leakage between the bottom plate and the basement wall, mentioned in section 3.2 could be avoided. Figure 3.10b illustrates the sealed tongue and groove joints and the connections between adjacent walls. Similar to the previous study, a frost-free primer was applied before sealing the joints in order to ensure the adhesion of the tape on the fibreboards.

As shown in Figure 3.10b and 3.10c, the connection between adjacent walls and between walls and roof is continuous what makes the sealing of this joint relatively easy. These

[6] $K_{mat} < 0.001$ $m^3/(m^2\,h\,Pa)$

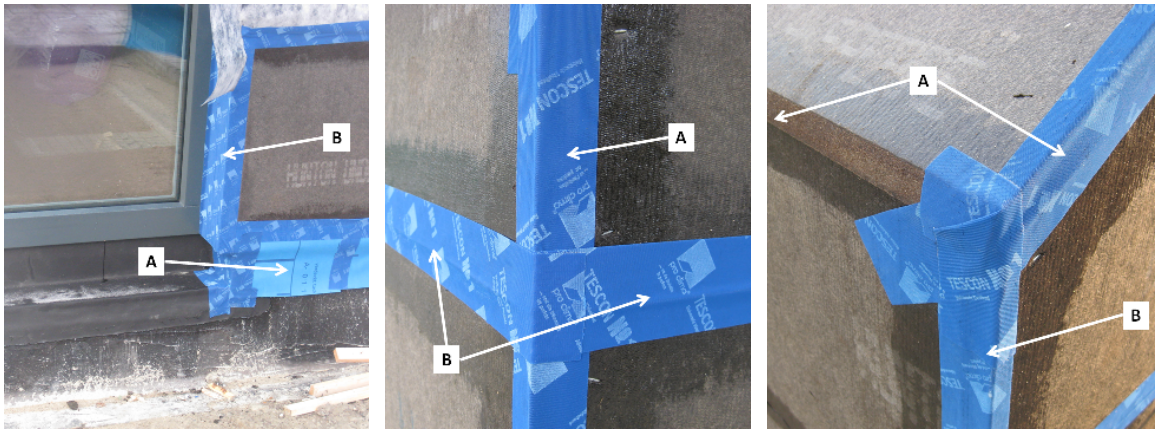

(a) (b) (c)

Figure 3.10: (a) Wind barrier sealed to foundation (A) and window (B), (b) sealed connection between adjacent walls (A) and sealed tongue and groove joint (B) and (c) continuous connection between wall and roof during sealing phase (A) and sealed connection between adjacent walls (B) (width of the tape is 6 cm)

.

corner joints should be differentiated between the ones describing an angle of 30°(21 m) and those describing an angle of 90°(78 m). Less air will escape through the corners of 90°, as these joints have more contact and are supported over the entire length by the studs (Figure 3.11).

Finally, as discussed above, a traditional interior air barrier was created by sealing the holes used to blown in the cellulose insulation and the tongue and groove connections along the interior vapour retarder (Figure 2.1a).

	North	South	West	East	Roof	Total
Wind barrier to window	32	68	17	15	-	132
Wind barrier to foundation	17	18	10	11	-	56
Wall-to-roof [a]	23	24	10	11	-	68
Wall-to-wall [b]	-	15	-	-	-	31
Tongue and groove joint	243	206	48	48	448	993

[a] West and East corresponds to an angle of 30°, North and South to 90°.

[b] Most of the joints are located at the corners of the house.Consequently, they can not be assigned to an orientation in this table. Only the South facade contains wall-to-wall joints, as depicted in Figure 3.10.

Table 3.6: Length of the joints in the wind barrier (m).

3.3.2 *In situ* pressurisation tests

Method and accuracy

Pressurisation tests have been conducted during the consecutive construction stages of the wind barrier, described above, to investigate the importance of the different leakage paths.

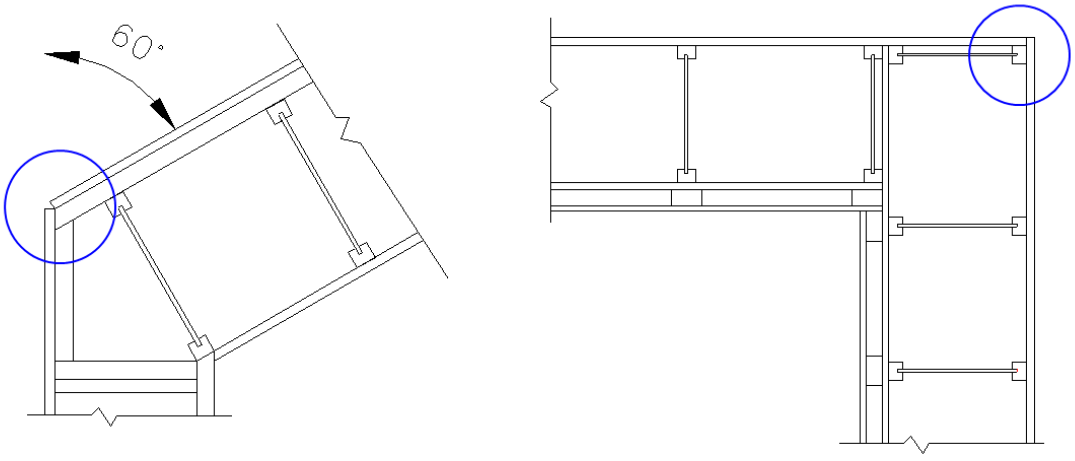

(a) (b)

Figure 3.11: (a) Wall-to-roof connection (30°) of the wind barrier in the West and East facade (21 m) (b) connections between the walls (90°).

With the straightforward technique of reductive sealing (Liddament 1996), the contributions of the different leakage paths through the building envelope can be examined. In total 12 tests have been performed in accordance with EN13829:1996. The airtightness was measured both in over-pressure (OP) and under-pressure (UP), except for four measurements where the progress in the building process only allowed to conduct a test in under-pressure. Because the generated data is applied to derive the air leakage rates through specific components, it is important to estimate first the overall error on these measurements. Measurement errors regarding fan pressurisation measurements can be divided in two: (1) bias errors and (2) precision errors (Sherman & Palmiter (1994)). The former refers to systematic errors, such as recurring human errors and accuracy of the equipment. The latter indicates the reproducibility of measurements which can be estimated by the standard deviation of repeated measurements. All tests have been performed by the same person with the same Minneapolis BlowerDoor^{TM}, Model 4 DG-700. The accuracy of the used pressure gauge is ±1%. The volumetric air flow is derived from the measured pressure drop across a calibrated orifice. As a result, the airflow rate is also determined with an accuracy of 1%. Because of the used orifice principle, the airflow rate needed to be corrected according to the inside and outside air density (EN13829:1996). The same person conducted with great care and under the same circumstances the measurements in order to reduce the precision errors. Measuring only at calm weather conditions, never exceeding 3 Beaufort, the influence of wind was minimised. In order to reduce the precision errors further, the software tool Tectite Express was used. This program, which allows an automatic run of the measurements, calculates the average out of 100 air flow measurements in each pressure step. When the pressure varies with more than 2 Pa during this process, the measurements restarts in order to reduce disturbances by wind gusts. Based on results

from Kim et al. (1986), where during one week several pressurisation tests were conducted on the same house at varying wind speeds from 0 to 4 Beaufort, the precision error can be estimated to be less than 5 %. However, workmanship is the most decisive source of errors in these experimental field situations. It can not be excluded that because of this, apart from planned improvements, other leakages have been created or sealed between the successive measuring steps. For the case study at hand, all craftsmen were aware of the measurements and reported all changes regarding airtightness to minimise this error.

Test Results

This section outlines the results of the different pressurisation tests (Table 3.7). When the first measurement took place, after installation of the wind barrier, the joints between windows and walls were already injected with PU-foam for seven windows. This implies that there is no measured value available with only the wind barrier installed and none of the joints sealed. Yet this value can be derived from the measurement with only seven windows injected and the measured value with all windows injected, taking into account the length of these joints (Table 3.6). Comparing steps 1, 2 and 3 leads to the conclusion that the injection of the joints between windows and walls with PU-foam has a large impact on the overall airtightness. The very labour-intensive external sealing of the windows to the wind barrier on the other hand did not strongly contribute to the airtightness of the house. The reason for this result is that at the time of the measurement, the PU-foam was only recently been injected and acted as an airtight barrier. It can be argued that when PU-foam dries, it becomes more brittle and may crack in time due to small displacements of the house. Small cracks in the PU-foam would lead to a decreasing airtightness, justifying the extra sealing around the windows. In step 4, after connecting the wind barrier to the foundation, the averaged n_{50}-value increased by 17%. This unexpected increase can most probably be attributed to the different weather conditions. Rain and higher outdoor humidity can influence the air permeability of the wind barrier board and might cause swelling of the joints. To visualise this, Figure 3.12 plots the evolution of the airtightness against the daily horizontal precipitation (mm) and outdoor relative humidity (%). The daily values are based on data, collected every 5 minutes from a 'Davis Vantage pro 2 station' located 3 km from the tested house. Interestingly, the n_{50}-value has increased between steps 3 and 4 and between steps 5 and 6 (Figure 3.12). Furthermore, measurements 7 and 8 confirm the importance of the moisture content of the wind barrier on the airtightness. Both measurements were conducted in the same construction stage with the weather being the only variable. Measurement 7 was performed on a sunny Friday afternoon, while measurement 8 was executed after that weekend on a rainy Monday morning. At this (high) level of airtightness the increased moisture content of the wind barrier reduces the overall airtightness by 227 m^3/h at 50 Pa, decreasing the n_{50}-value by 0.21 1/h. To quantify the importance of the weather

	Construction stage	OP	UP	Average
Step	Exterior			
1	Wind barrier installed[a]	3.38	3.37	**3.38**
2	PU-foam injected around doors and windows	0.98	0.94	**0.96**
3	Windows sealed to wind barrier	1.04	0.94	**0.99**
4	Wind barrier connected to foundation	-	1.16	**1.16**
5	Corner joints sealed[b]	-	0.79	**0.79**
6	North, West and South facade sealed[c]	-	0.83	**0.83**
7	Last corner joints from step 5 sealed	-	0.67	**0.67**
8	No improvements undertaken	0.46	0.46	**0.46**
9	East facade and roof sealed	0.30	0.33	**0.32**
	Interior			
10	Cellulose fibre insulation blown in	0.20	0.20	**0.20**
11	Inflation holes sealed[d]	0.17	0.17	**0.17**
12	Finished state	0.14	0.14	**0.14**

[a] At the moment of the first measurement, seven window joints were injected with PU-foam. The value of step 1 is calculated from this measurement taking into account the length of PU-foam injected joints.

[b] All the corner joints of the wind barrier were sealed, except for 11m wall-to-roof joints.

[c] 496 m of 990 m joints.

[d] At this stage already, some of the internal surface joints between the OSB-plates were sealed.

Table 3.7: Airtightness of the building envelope (n_{50} (1/h)) during different construction stages.

influences, additional air permeability tests of the wind barrier as function of the moisture content have been performed in laboratory conditions. The results will be discussed in the next section 3.3.3.

After connecting the wind barrier to the foundation, the next step consisted of sealing all the wall-to-wall and roof-to-wall joints. Since there were only three scaffolds on-site, this step was split up into step 5 and step 7. In between, the tongue and groove connections in the wind barrier on the North, West and South facades were sealed in step 6. In step 5, already 88 m of the corner joints were sealed and in step 7 the last 11 m were taped. The step to investigate the influence of sealing the tongue and groove connections of the wind barrier is split up in steps 6 and 9. Table 3.7 seems to indicate that sealing the joints in step 6 increased the n_{50}-value. Yet this can be explained by the window and door flashings, being temporary nailed on the wind barrier during this part of the construction. To seal the joints under these flashings, the nails had to be removed, each time resulting in a small holes. It is very probable that the leakage through these holes is comparable to the effect of sealing the tongue and groove connection, resulting in a zero operation. Prior to the measurement of step 9 all these small gaps were filled with silicone. As a result, both the

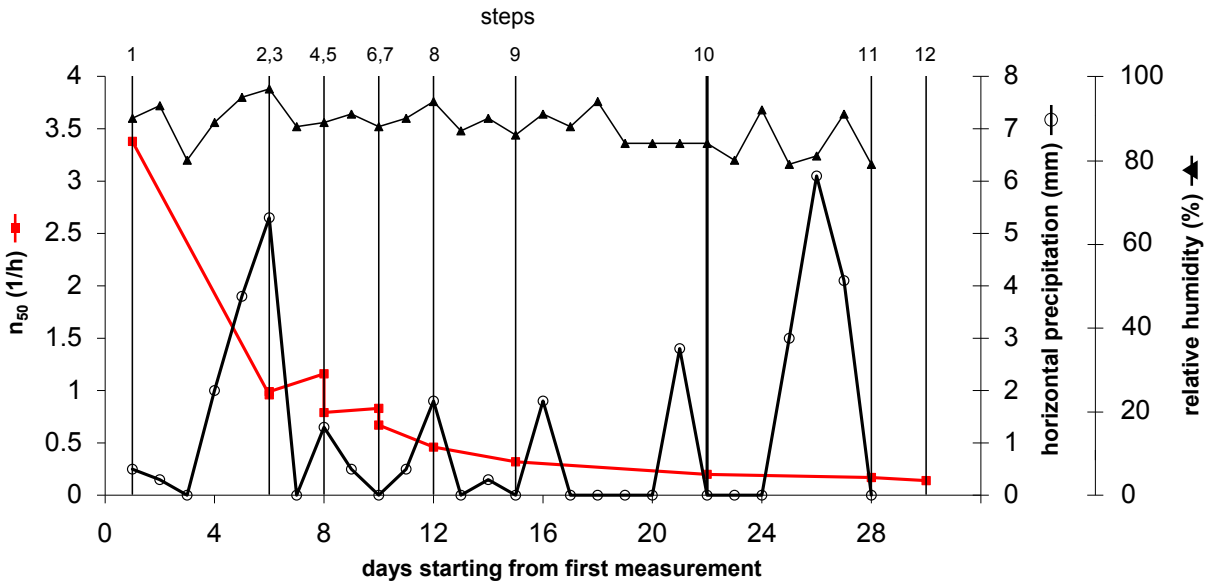

Figure 3.12: Evolution of the airtightness in the consecutive construction stages (corresponding to Table 3.7) against the daily horizontal precipitation (mm) and relative humidity (%).

enhancements of sealing the tongue and groove joints in steps 6 and 9 between the wind barrier boards are ascribed to step 9.

When all the exterior joints were sealed in step 9, an n_{50}-value of 0.32 1/h was measured. Hypothetically, if all exterior joints in the wind barrier were perfectly sealed, the only remaining air leakage path is directly through the wind barrier itself. Based on the wind barrier's air permeability and the exterior surface of the case study this would correspond to an n_{50}-value of 0.12 1/h. Of course it is unfeasible to achieve such a perfectly continuous air barrier in practice. From the difference between this theoretical value and the actually measured value it can be concluded that the unforeseen leakages are 212 ($\pm$13) m^3/h at 50 Pa, which is small given the size of the case study.

With the wind barrier completely sealed, the cellulose fibre insulation was blown in through the interior holes in the OSB. Similar to the previous case study, a considerable influence was measured. The n_{50}-value decreased from 0.32 1/h to 0.20 1/h. In theory, the overall airtightness of a building component is determined by the most airtight layer in a series. However in reality, building envelopes always contain three dimensional air leakages and the presence of insulation increases the length and tortuosity of these leakage paths resulting in an extra pressure drop in the wall. Similar results were found in by Relander (2011) where the influence of mineral wool insulation between an intermediate floor in laboratory conditions was studied.

Step 11 corresponds to the measurement for which the interior inflation holes were sealed. It should be noted that, at the time of this measurement, due to practical reasons in some of the rooms the tongue and groove joints between the OSB were already sealed.

Finally, an additional air barrier was realised at the interior by sealing all tongue and groove joints along the OSB and connecting the foils, provided around the interior wall and intermediate floor junctions. This final test was performed a few months later than the previous test, after all the interior joints were sealed. The final n_{50}-value of the house was 0.14 1/h.

The most significant leakages in the wind barrier are estimated in Table 3.8. Here, the leakage through the corner joints and the tongue and groove joints are deduced from the corresponding *in situ* tests, taking into account the length of the joints. For the leakage through the corners joints, both measurements were performed under dry weather conditions. Therefore, the deduced leakage is not influenced by the moisture content of the wind barrier. For the leakage through the tongue and groove connection on the other hand, the leakage is calculated from measurement 5 and 9. A small difference between weather conditions exists which might lead to an underestimation of the corresponding leakage. In addition to the estimated leakages, Table 3.8 includes also the man hours spent for each enhancement. While the overall leakage (m^3/h) through the different types of joints are in the same order of magnitude, the man hours related to seal the joints obviously are not. Sealing all the tongue and groove joints is obviously far more time consuming than sealing the other leakages paths.

	Q_{50} (m^3/h)	**g_{50} (m^3/(h m))**	**Manhours**
Corner joints (90°)	243	3.1	3
Corner joints (30°)	330	15.7	1
Tongue and groove joints	342	0.4	56

Table 3.8: Air leakage through the different joints (configuration in Fig. 3.14).

3.3.3 Laboratory measurements

Method and accuracy

In addition to the *in situ* pressurisation tests on the entire building, laboratory measurements on specimens of the wind barrier, including the most significant joints have been carried out. Two test setups were designed to investigate the air permeability on material and assembly level. The first test setup consisted of a metal frame box open at one side to measure specimens with a size of 0.27 by 0.27 m (Figure 3.13). This box was used to characterise the air permeance of the materials and the typical tongue and groove connections of the board products. The second apparatus has the same principle but was designed for specimens of 0.85 by 0.95 m and allows to mount larger specimens and 3D-construction details in a test rim on an airtight box. This box was used to test the corner joints between the fibreboard describing an angle of 90°(as in the wall junctions) and 30°(as in the wall to roof junctions). To avoid unwanted air leakages through the perimeter joints between specimen and the

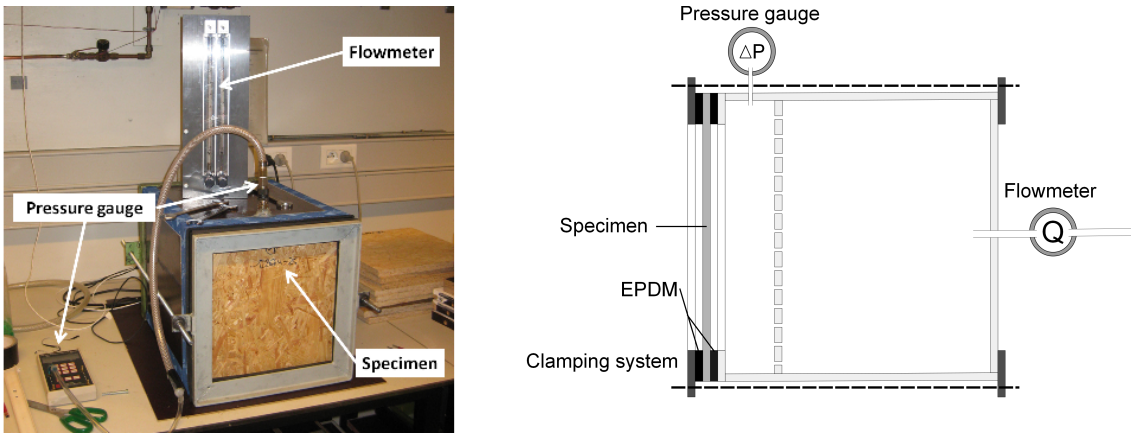

(a) (b)

Figure 3.13: Laboratory test equipment to determine air permeability.

airtight boxes, closed cell EPDM with a thickness of 2 cm on both sides of the specimen have been used to seal the specimen airtight with a metal frame to the airtight box. After installing the specimen on the airtight box, under-pressure was created in the box. This resulted in an air flow passing through the specimen. By stepwise increasing the pressure difference across the specimen and measuring the air flow rate and associated pressure difference across the specimen a data set was gained, which could be curved fitted with Eq.3.1:

$$g_a = a\Delta P_a^b \tag{3.1}$$

where g_a ($m^3/(m^2\,h)$) refers to the airflow rate density, ΔP_a (Pa) stands for the pressure difference across the building envelope, a ($m^3/(m^2\,h\,Pa^b)$) is the air permeance coefficient and b (-) the air permeance exponent of the specimen. The airflow rate density g_a ($m^3/(m^2\,h)$) can also be written as an air permeance K_a multiplied by the pressure drop across the specimen ΔP_a. After recombination with Eq.3.2, the air permeance K_a ($m^3/(m^2\,h\,Pa)$) is expressed as a function of the pressure drop across the specimen:

$$g_a = K_a\Delta P_a \qquad K_a = a\Delta P_a^{b-1} \tag{3.2}$$

The construction junctions are assumed to be a parallel circuit of air resistances. Hereby, the air permeance of a joint K_{joint} ($m^3/(m\,h\,Pa)$) can be deduced from the measured air permeance of the specimen K_{spec} with an area A_{spec} and a joint with a length l_{joint}, given that the air permeance of the material K_{mat} ($m^3/(m\,h\,Pa)$) is known from the small test setup (Hens 2006):

$$K_{joint} = \frac{(K_{spec} - K_{mat})A_{spec}}{l_{joint}} \tag{3.3}$$

In the remainder of this section all permeability levels will be fitted with Eqn. 3.2 to determine the permeability at 50 Pa. This allows a direct comparison with the field measurements of the case study and is denoted by '50' in subscript.

For the small test setup a pressure gauge 4 DG-700, with an accuracy of 1 % was applied. The flow rate was determined with a Vögtlin variable area flow meter. The flow rate could be measured with an accuracy of 2 % in a range from 0.02 m^3/h to 0.900 m^3/h. The overall leakage of the test setup itself, including the ductwork connections, was determined by performing a test on an airtight plexiglass specimen. The air leakage of the test setup, which could only be measured at higher pressures[7], is extrapolated to 50 Pa using Eqn. 3.1. The leakage of the small test setup was estimated to be 0.0035 m^3/h at 50 Pa[8]. The same pressure gauge was applied on the bigger test setup, but here the flow rate was measured with a turbine flowmeter (Trigas FI) measuring in a range from 3.4 m^3/h to 36 m^3/h with an accuracy of 0.6 %. The leakage of the bigger apparatus was 9.94 m^3/h at 50 Pa[9]. Because of this significant leakage, each test was repeated covering the sample with an airtight plastic foil[10]. The permeability of the samples was calculated from the difference between both measurements. Consequently, the fitting parameters *a* and *b* lose their meaning and are therefore excluded from Table 3.9.

Test Results

Table 3.9 lists the results for the air permeability of the used fibreboards in the case study and the corresponding joints which are depicted in Figure 3.14. In addition to the used bituminous impregnated fibreboards (BIFBI), the same material was also measured, however without an exterior layer (BIFBII). Table 3.9 reveals that BIFB becomes twenty times more permeable without this layer. Furthermore, this table shows that the BIFBI is five times more

[7] 300-1000 Pa

[8] Deduced from Eqn. 3.1 with the corresponding parameters; a = 0.000113 m^3/(h Pa) and b = 0.88

[9] Deduced from Eqn. 3.1 with the corresponding parameters; a = 0.55 m^3/(h Pa) and b = 0.74

[10] k_{mat}<0.001 m^3(m^2 h Pa)

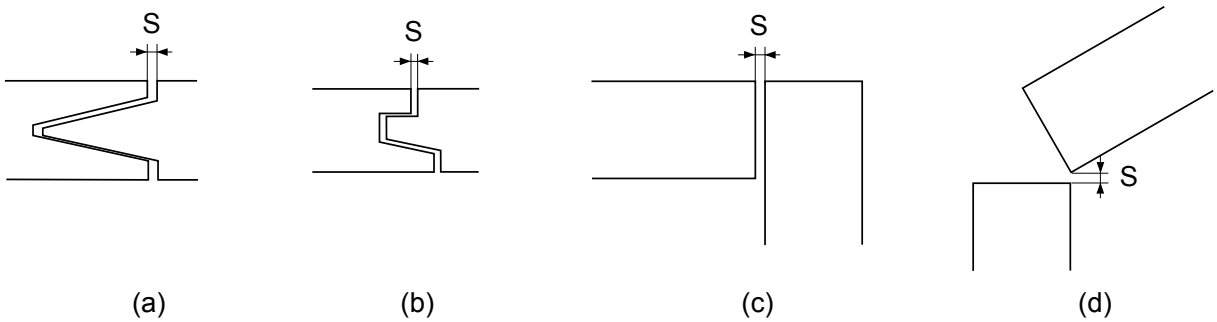

Figure 3.14: Geometry of the tested joints (S denotes distance of the joint): (a) BIFB (Bituminous Impregnated Fibreboard) tongue and groove joint, (b) OSB tongue and groove joint, (c) BIFB corner joint (90°), (d) BIFB corner joint (30°) (corresponding to Table 3.9).

air permeable than the used OSB. In addition, it was found that the air permeance of the tongue and groove connection between the plates of the BIFB and the OSB are in the same order of magnitude, as long as they are perfectly installed. When the spacing between the boards increases due to bad workmanship, this influences most significantly the OSB. Furthermore, the corner joints of the wind barrier depend even more on the execution quality. Table 3.9 shows that the air permeance can vary with a factor up to 20, depending on the spacing between the boards.

material	K_{mat}**(**$m^3/(m^2\,h\,Pa)$**)**	a **(**$m^3/(m^2\,h\,Pa^b)$**)**	b **(-)**
BIFB I	0.005	0.005	0.99
BIFB II	0.109	0.123	0.97
Cellulose (30 cm)	0.59	0.56	1.01
OSB	<0.001	0.001	0.97
S (mm)	$K_{joint,50}$**(**$m^3/(m\,h\,Pa)$**)**	a **(**$m^3/(m\,Pa^b)$**)**	b **(-)**
Tongue and groove joint: BIFB			
0	0.0094	0.010	0.99
2	0.0184	0.022	0.96
4	0.0260	0.036	0.92
Tongue and groove joint: OSB			
0	0.008	0.009	0.96
2	0.027	0.044	0.88
4	0.096	0.172	0.85
Corner joint BIFB: 90°			
0.5	0.013	-	-
2.5	0.116	-	-
4	0.222	-	-
Corner joint BIFB: 30°			
0.5	0.270	-	-
2.5	0.755	-	-

Table 3.9: Air permeance on material and assembly level (T = 23°C, RH = 50%) (BIFBI an BIFBII stands for Bituminous Impregnated Fibreboard with exterior layer and respectively without exterior layer).

From Figure 3.12 it followed that the influence of the weather on the permeance of the wind barrier should be considered. To investigate the importance of the moisture content of the wind barrier, two additional laboratory test series with the small apparatus have been conducted, examining the air permeability of the material and tongue and groove joints as function of the moisture content. Prior to the air permeability test, the specimens were conditioned to a constant moisture content. This was achieved by applying a known water volume to each specimen and storing the specimens, wrapped in plastic foil, for 4 weeks before measuring their airtightness. The analysis used three identical samples of 0.35 by 0.35 m for the investigation on material level. Figure 3.15 plots the results of the three samples tested. This figure shows that in equilibrium conditions, the air permeability of the BIFB is not affected by its moisture content in this range.

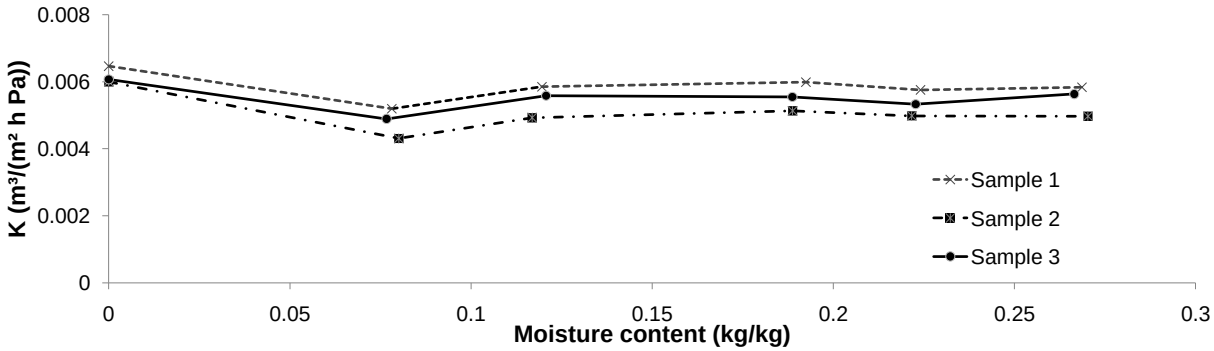

Figure 3.15: Wind barrier board as function of the moisture content (in equilibrium).

When the *in situ* measurements were performed, the moisture content of the wind barrier could not be in equilibrium with the fluctuating outdoor relative humidity. During or short after a period of rain, water will be drained from the wind barrier. To simulate this effect in laboratory conditions, the specimens were sprayed on the top layer until water starts to drain. Both, immediately after this wetting process and 30 minutes later, the permeability levels have been measured. For all three samples the permeability, straight after wetting was reduced within a range from 51-58 % compared to the dry situation. However, after 30 minutes, the permeance reached again 91-96 % of the level in dry conditions. From this it can be concluded that the air permeability at material level is rather independent of the moisture content as long it stays below acceptable limits. The same was found by Descamps (1996), who experimentally determined the air permeability of calcium silicate brick as function of the equilibrium moisture content. This study found a step-function, starting from the dry air permeability until the capillary moisture content is reached. At the capillary moisture content the air permeability drastically decreased to almost zero. Furthermore, this step-function can explain that only short after wetting the wind barrier board, the air permeability is significantly influenced. Immediately after spraying the boards, the first few millimetres from the wetting front will be capillary saturated, creating a significant air resistance. After the wetting process, the moisture starts to distribute within the boards. As a result, the air permeability of the boards increased again to the level at dry conditions.
In addition, the behaviour of the tongue and groove joint have been studied as well. Specimens of the wind barrier, including a tongue groove joint were mounted on a plastic frame. The specimens were only fixed parallel to the joints, to assure the joints' possibility to swell (Figure 3.16). In total four samples were constructed for this study. The joint of sample 1 was installed with a joint of 2 mm and the joints of samples 1,2 and 3 were installed perfectly. The above-mentioned wetting procedure was applied to condition the specimens in equilibrium. Figure 3.17 depicts test results as a function of its equilibrium moisture content. It appears that only the joint of 2 mm was significantly influenced by the moisture content of the boards. In a second step, the specimens were sprayed with water and measured again. This showed that the permeability of the joints was affected with less than 5 %, both

immediately after and 30 minutes after the specimens were sprayed. Hence, we conclude that the air permeance of the joints is only significantly affected by its moisture content, if the joints do not perfectly fit due to 'bad' workmanship.

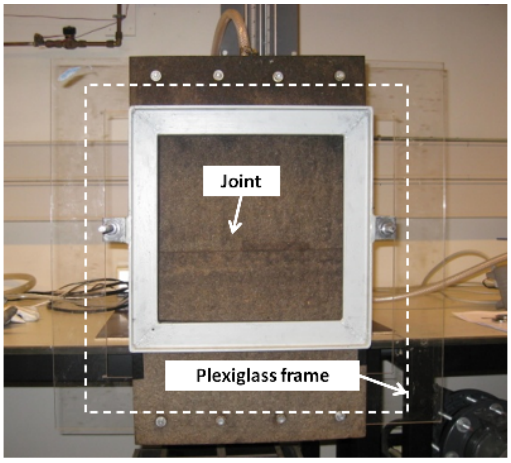

Figure 3.16: Specimen of the wind barrier with a tongue and groove joint attached to a plastic reference frame, mounted on the small test setup.

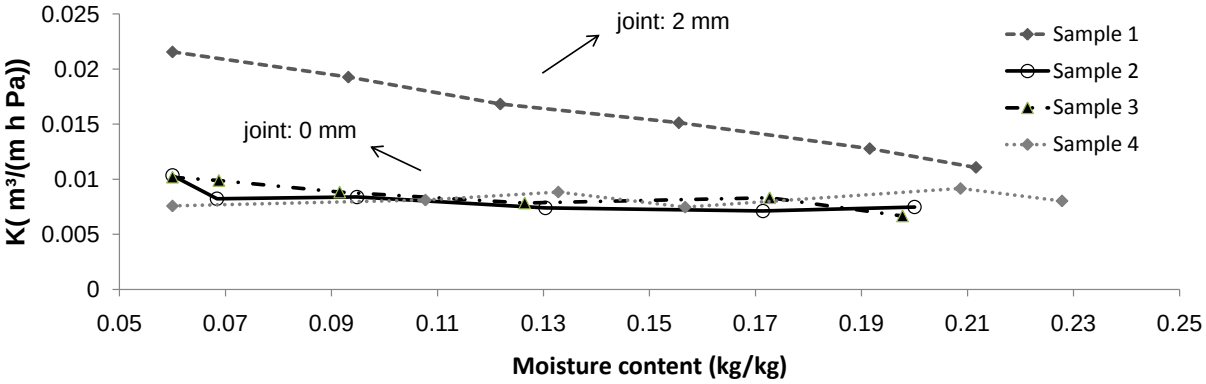

Figure 3.17: Tongue and groove joints through the wind barrier as function of the moisture content (in equilibrium).

3.3.4 Comparison laboratory and *in situ* measurements

This section compares the results of the laboratory measurements of Table 3.9 to the field data in order to verify how accurate the n_{50}-value can be predicted from laboratory tests. Table 3.10 deduces the air permeability of the bituminous impregnated fibreboard from the measuring step where all the joints of the wind barrier were sealed ($g_{50,house} = 0.6\,m^3/(m^2\,h)$). From the comparison with laboratory tests, it follows that this value is too high which can be ascribed to unforeseen leakage paths corresponding to 212 ($\pm$13) m^3/h at 50 Pa, as described above in section 3.3.2. These unsealed leakage paths do not further influence

	$g_{50,house}$ ($m^3/(m^{(2)}\,h)$)	$Q_{50,house}$ (m^3/h)	$g_{50,lab}$ ($m^3/(m^{(2)}\,h)$)	$Q_{50,lab}$ (m^3/h)
BIFBII	0.6	341	0.19-0.26	102-156
Tongue and groove joint (BIFBII)	0.4	342	0.47-1.30	465-1287
Corner joints (90°)	3.1	243	0.63-11.09	49-865
Corner joints (30°)	15.7	330	13.51-37.75	284-793

Table 3.10: Comparison between the leakage in laboratory and on site conditions.

the quantification of the joints studied since these leakages are eliminated by means of using the reductive sealing technique.

The *in situ* air leakage through the tongue and groove connection between the wind barrier board is closer to the lower limit than the upper limit of the laboratory tests. This was expected since the distance between the tongue and groove joints was small (0-2 mm) on site. The *in situ* measured leakage through the corners joints lies between the upper and lower limit determined in the laboratory. However, it seems very difficult to predict the real leakages from laboratory tests since the range between the upper and lower limits is large.

3.3.5 Summary

The results from this second case study showed that without any major effort, an overall airtightness lower than 1 1/h at 50 Pa can be reached with an improved wind barrier only. The joints between adjacent walls and between the walls and the roof appear to be the most significant (3.1-15.7 $m^3/(m^2\,h)$ at 50 Pa). It was found that by sealing only these joints, the n_{50}-value decreased by 0.5 1/h for the case study at hand. Sealing all the exterior joints, an n_{50}-value of 0.32 1/h at 50 Pa was measured, which meets the 'Passivhaus' and 'Minenergy' standard of 0.6 1/h at 50 Pa. Furthermore, the effect of the cellulose insulation on the airtightness should be considered. Even at a relatively high level of airtightness, the presence of the blown-in insulation decreases the n_{50}-value for the current case by 0.13 1/h at 50 Pa. The final n_{50}-value , with the interior lining also sealed, was 0.14 1/h.

Laboratory measurements on specimens of the wind barrier classify the different leakages in the same order of importance. However, a direct comparison of the *in situ* and laboratory measurements led to the conclusion that laboratory tests are only suitable to predict the lower limit of the overall airtightness of buildings.

Furthermore, it was observed that the air permeability of the wind barrier is influenced by its moisture content. At the time the pressurisation tests were conducted, the wind barrier was not protected by any exterior cladding, resulting in rain directly wetting the boards. The laboratory measurements revealed that this influence was induced by a decreasing air permeance of the wind barrier boards during, or short after, a rain shower. A higher overall moisture content in equilibrium conditions did not affect the permeability of the board material, nor of the correct installed tongue and groove joints. In this study the impact of the

weather conditions influenced the measured n_{50}-value of the building by more than 30 %. At airtightness levels around the Passivhaus-standard this can determine whether the building achieves the threshold of 0.6 1/h at 50 Pa put forward by this standard.

3.4 Conclusions

This chapter investigated the practical feasibility of exterior air barriers in timber frame construction based on field and laboratory measurements.

The first section discussed recent experiences from Norway. For an increasing number of Norwegian dwellings, the airtightness is currently measured twice; first, when the building is windtight ($n_{50,w}$) and, second, when the building is finished with an interior air barrier ($n_{50,f}$). In summary, the results indicate that once the contractor has a basic experience in building airtight, n_{50}-levels around 1 1/h or lower can be reached with an improved wind barrier only. Notwithstanding the required n_{50}-value is sometimes already reached after the first test, still a traditional interior air barrier is created by sealing the vapour barrier in Norway. It can be questioned, however, with which accuracy this interior barrier will be installed in case the $n_{50,w}$-value already meets the proposed value.

The second section sought to gain more insights in the practical aspects of exterior air barriers. This section provided a detailed discussion of the realisation of an exterior air barrier in a timber frame building in Belgium. In addition, a traditional interior air barrier has been installed as well. In between the realisation of these airtight layers, three pressurisation tests were conducted: (a) with only the exterior air barrier installed, (b) after inflation of cellulose insulation in the wood frame structure and (c) after finishing the interior air barrier. The case study at hand revealed that the labour for realising the exterior air barrier was around 60 % less than the construction of the interior barrier. Yet this investigation indicated several points of attention in creating the exterior barrier, such as air leakages at the level of the foundation and around windows.

The final section discussed measurements quantifying typical leakage paths. In total 12 pressurisation tests have been conducted during the consecutive construction stages of a timber frame dwelling in Belgium. This second case study demonstrated that with good workmanship and appropriate materials, an airtightness level lower than 1 ACH at 50 Pa can be reached with the wind barrier only. For the current case, the wind barrier joints between adjacent walls and between the roof and walls were the most critical. By sealing only these connections, an airtightness level fulfilling the requirements of the Passivhaus-standard (< 0.6 ACH at 50 Pa) was achieved.
Additional laboratory measurements on specimens of the wind barrier quantified the differ-

ent leakages noticed in the case study. Yet a direct comparison of the *in situ* and laboratory measurements led to the conclusion that laboratory tests are only suitable to predict the lower limit of the overall airtightness of buildings. Air leakages depend to a very high degree on the craftsmanship. Consequently, the uncertainty on a single leakage becomes too large to derive a reliable n_{50}-value of buildings from their summation.
Furthermore, the laboratory tests confirmed the observation of the field tests that the permeance of the wind barrier can be significantly affected by rain. Mainly the influence on not completely closed joints and the influence on the board material during and short after a rain shower were significant. Therefore, when pressurisation tests are performed at the windtight stage, it is recommended to measure at dry weather conditions.

Based on the above-mentioned case studies and the related laboratory measurements various practical advantages of exterior air barriers have been experienced:

- Reduced number of joints in the air barrier facilitates the realisation of the air barrier.
- Building airtightness can be realised simultaneously or even after services are installed, increasing the freedom to integrate airtightness in the building process.
- The pressurisation test should be performed between the installation of the windows and doors and the realisation of the cladding system. In this phase all joints in the exterior air barrier are accessible, so, possible leakages can be detected and repaired.
- Reduced risk for penetrations of the air barrier through user behaviour.
- Pre-installed strips can be avoided.
- The larger continuous surfaces of exterior air barriers offer opportunities for prefabricated elements.

On the other hand, several practical disadvantages have been encountered in the realisation of exterior air barriers as well:

- Sealing exterior air barriers is depending on the weather conditions.
- Increased environmental stresses on exterior barriers.
- Splashing of dirt at the level of the foundation impedes sound sealing conditions.
- Scaffolds should remain longer available.
- An additional primer to increase the durability of the exterior tapes increases the labour.
- Sealing exterior joints (e.g. roofs) can be more difficult than interior joints.
- Window and door flashings are temporarily nailed in the exterior barrier, destructing the exterior barrier.
- Scaffolds are usually fastened at the building, penetrating the exterior air barrier.

Apart from these practical aspects, the main reason why exterior air barriers are currently not applied in cold and moderate climates are the unknown hygrothermal risks involved. These risks will be examined in the laboratory investigation in the following chapter.

4

Hygrothermal laboratory studies of components with an exterior air barrier

The previous chapter has shown how exterior air barrier systems can potentially reduce the labour cost in realising sufficient building airtightness. In cold and moderate climates, however, the hygrothermal behaviour of highly insulated lightweight building components with an exterior air barrier has remained unstudied. Therefore, the objective of the present chapter is to investigate experimentally the hygric response when the air barrier system is moved from the interior to the exterior of the building envelope. Moreover, this chapter aims to provide detailed data for the validation of the numerical HAM model in chapter 5. The first section discusses hot and cold box measurements on full-scale test walls. In total eight different components have been tested under various boundary conditions and including typical installation defects. The second section studies the onset of interstitial condensation on hygroscopic and/or capillary active air barrier materials on smaller test specimens.

4.1 Hot and cold box measurements on highly insulated timber frame walls[1]

This section presents the results of a detailed laboratory experiment studying the hygrothermal behaviour of lightweight walls with an exterior air barrier system. In total eight potential

[1] partially published in Langmans, Klein & Roels (2012)

wall configurations have been tested in a hot and cold box test setup, operating at well-controlled temperatures, humidities and air pressures. Compared to *in situ* measurements (e.g. Desta et al. 2011, Geving & Uvsløkk 2000), the advantage of laboratory experiments is that specific phenomena can be studied isolated from each other by controlling the boundary conditions. Additionally, compared to field measurements where typically one or two winters are measured, laboratory experiments can be executed in shorter periods of time (3-4 months). Consequently, this approach is applied by several authors to study the performance of lightweight highly insulated building components (e.g. Derome 2005, Janssens 1998, Kalamees & Kurnitski 2009, Thue et al. 1996, Riesner et al. 2004). However, as hot box and cold box measurements are typically limited to steady state conditions, transient effects of real climate data on the components are not captured. Also the influence of radiation is most often not included in these analyses. In order to address these limitations, numerical simulations imposing real climate conditions on a annual basis will be investigated in chapter 6.

The objectives of the hot and cold box experiments are threefold: (1) study the overall effects of air transport on the hygrothermal performance of lightweight walls with an exterior air barrier system, (2) investigate the behaviour of various exterior air barrier and insulation materials and verify their impact on typical bad workmanship and (3) generate sufficiently detailed validation data for numerical HAM-models.

4.1.1 Test equipment

A new vertical calibrated hot and cold box was constructed to investigate the hygrothermal performances of highly insulated building components. The test setup consists of three major parts; a test frame to install the studied building component enclosed between two climate chambers to simulate indoor and outdoor conditions (Figure 4.1). To reduce the heat losses through the calibrated hot box to a very minimum, this chamber was insulated with 60 cm polyurethane ($R = 30\ (Km^2)/W$). The hot box has a cubic inner volume with sides of 2.4 m and is completely separated from the laboratory conditions without any thermal bridge (Figure 4.2). The test frame, constructed in the same way, has a measuring area of 2.4 m by 2.4 m and a depth of 0.6 m. The cold box, on the other hand, was insulated with only 0.1 m polyurethane boards. The clamping system, connecting the three parts, consisted of a screw system with 7 bars distributed over the total height of each side of the test setup (Figure 4.2). In combination with compressible closed cell polyurethane foam with a thickness of 2 cm, this clamping system provides an airtight and insulated connection between the different parts.

A controlled IR-bulb in the middle of the warm chamber creates the desired temperature conditions. Figure 4.2 (vertical section) shows how the IR-bulb is covered with a reflective foil to avoid direct long wave radiation towards the test component. The cold chamber



Figure 4.1: Vertical hot box - cold box test setup.

was provided with a liquid-to-air heat exchanger accompanied with a fan system to control and distribute the temperature. The fan system, which can simulate wind effects, allows a steady state air flow along the test wall with velocities between 0.5 - 10 m/s. The humidity in both the warm and cold chamber was conditioned with free evaporation of salt solutions. To create a total air pressure difference across the test section, a small ventilator is installed at the back of the warm chamber.

4.1.2 Wall configuration studied

Two hot and cold box experiments with each four test walls have been conducted. The design of the walls was based on the current practice for highly insulated timber frame houses in Belgium[2]. All test walls (each 2.3 m by 0.5 m) were insulated with 30 cm insulation to which OSB was applied as interior vapour retarder. In the first test series (I), the walls were insulated with standard mineral (glass) wool (20 kg/m^3 (MW20)) and differed from each other by the physical properties of the applied exterior air barrier: airtightness, moisture buffer capacity, vapour permeability and thermal resistance. Both the exterior sheathing of the first test wall (Ia) and the second test wall (Ib) consisted of a bituminous impregnated soft fibre board (herein referred to as BIFB I) with an exterior top layer which increases its airtightness. For the third test wall (Ic) a similar bituminous impregnated soft fibreboard was applied, but without the exterior top layer (BIFB II). Whereas the first three test walls were provided with a hygroscopic exterior sheathing, the fourth wall (Id) was executed with a spunbonded foil at the outside. The applied foil was extremely airtight but had no mois-

[2]www.passiefhuisplatform.be

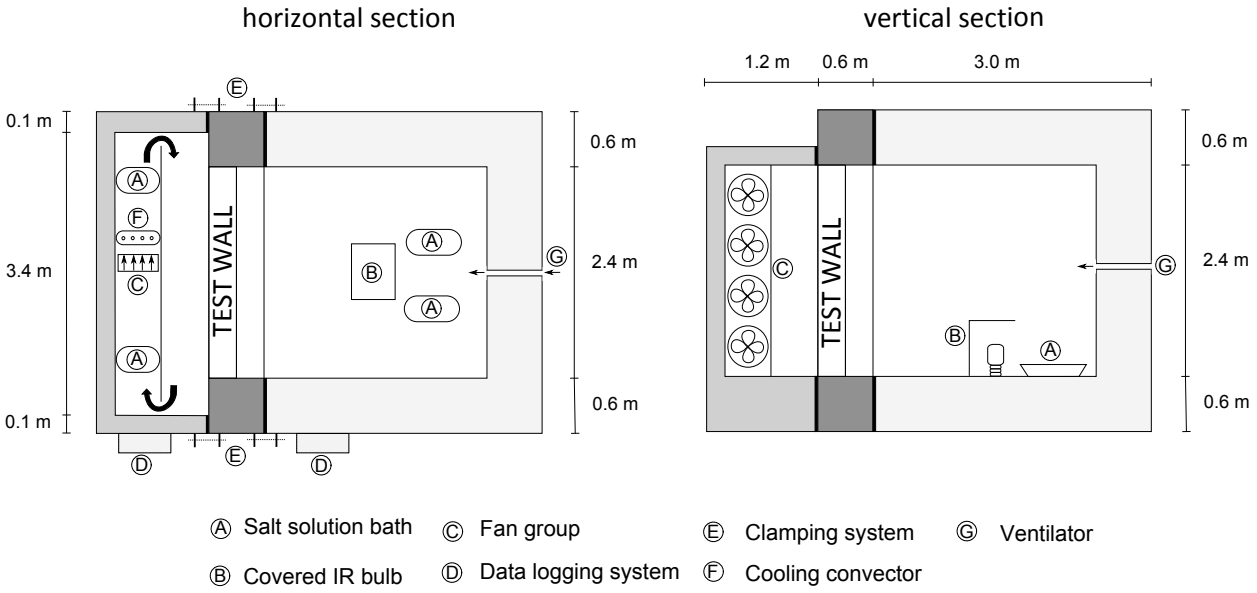

Figure 4.2: Vertical hot box - cold box experiment: horizontal and vertical cross section.

ture buffer capacity. In the second test series (II), BIFB I was applied as exterior air barrier material for all walls. Here, the test walls differed by the insulation material and by the introduction of bad workmanship in the insulation layer. The first two test walls were insulated with denser glass wool (30 kg/m^3 (MW30)) and the last two test walls with blown-in cellulose insulation (60 kg/m^3 (CL60)). In contrast to the perfect installed insulation layer of the second test wall (IIb), the first test wall (IIa) covered bad workmanship by introducing an air cavity of 1 cm along the entire height of the interface between the glass wool and the exterior air barrier. Also in the third test wall (IIc) an air cavity of 2 cm was left at the top of the insulation, representing potential settling of the cellulose. The fourth wall (IId) on the other hand was completely filled. Table 4.1 gives an overview of the different configurations of the test walls. In front of the exterior air barrier an air cavity of 5 cm was left, closed with a fly screen. This screen aimed to provide an air and vapour open layer which prevents vortices introduced by the air movement of the ventilator in the cold box. This was important in achieving equal air pressure differences across the different wall sections. The

	Air barrier	**Insulation (30 cm)**	**Air gap**
Ia	BIFB I	Mineral wool 20 kg/m^3	-
Ib	BIFB I	Mineral wool 20 kg/m^3	-
Ic	BIFB II	Mineral wool 20 kg/m^3	-
Id	FOIL	Mineral wool 20 kg/m^3	-
IIa	BIFB I	Mineral wool 30 kg/m^3	1 cm along cold side of mineral wool
IIb	BIFB I	Mineral wool 30 kg/m^3	-
IIc	BIFB I	Cellulose 60 kg/m^3	2 cm at top of insulation
IId	BIFB I	Cellulose 60 kg/m^3	-

Table 4.1: Configuration of test walls in test series I and II.

configuration of the test walls studied in series I is shown in Figure 4.3.

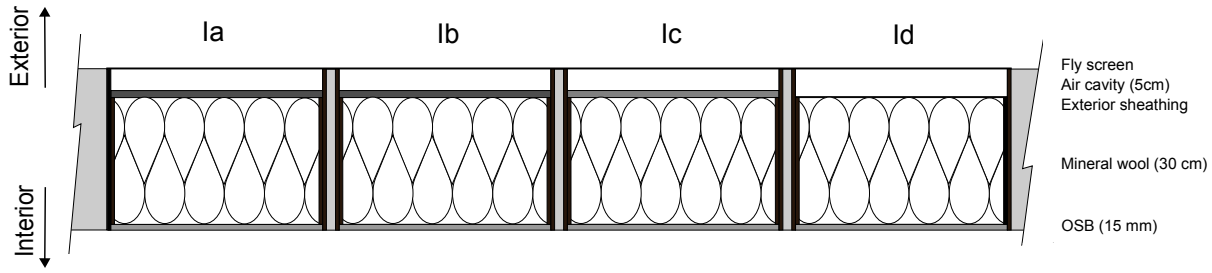

Figure 4.3: Wall configuration of test series I.

Besides studying the hygrothermal behaviour of wall constructions with an exterior air barrier, this hot and cold box investigation targets to generate detailed validation data for 2D HAM simulation models. Therefore, special care was given to eliminate unintended air leakages and to create two-dimensional measuring conditions. For instance, during their installation, the test walls were pressurised and with a combination of smoke and infrared inspection the remaining air leakages were detected and carefully caulked. Furthermore, the walls were separated with a polyurethane board (5 cm) in between two wood fibreboards (1.8 cm) which were covered with an airtight and watertight paint to prevent any significant heat or mass exchange between the test walls. Given the difficulties encountered in measuring the moisture transport in wood (see section 2.2.3), the test series were executed without studs or top and bottom plate. Consequently, the test walls were a simplified configuration of walls executed in practice. Nevertheless, for the generation of applicable validation data, minimising of the number of potential uncertainties proved to be necessary.

4.1.3 Boundary conditions and test sequence

The first test series (I), which lasted about four months, was subdivided in five main consecutive measuring steps. During the first step, both the interior and exterior sheathing were airtight. The second step introduced well-defined gaps in the interior barrier of all walls except for section Ia, which was used as a reference component. The gaps corresponded to slots of 1 cm at 20 cm from the top and bottom of the OSB and extended the full width of each test wall to maintain the two-dimensional situation (Figure 4.4a). In subsequent steps (3 and 4) the hot box was pressurised. Lastly, the conditions in the cold box were adapted to create drying conditions inside the walls. Table 4.2 summarises the boundary conditions for both the warm and cold chamber. Here, the first four climate conditions represent an averaged typical winter month in a temperate climate, such as Belgium. The fifth step, however, corresponds to arbitrary drying conditions. In this table the boundary conditions correspond to the median, based on 10-minute data for each measuring step. In addition, the 5 and 95 percentiles are given in grey. The percentiles which deviate more than 10 % from the corresponding median are underlined. The origins of these deviations are all tem-

porary disturbances in transition to a next step. For example, at the beginning of step 3, the inflated air from the laboratory was not yet pre-conditioned resulting in dryer conditions in the hot box. Or at the beginning of step 5, the ventilator in the hot box was still working, influencing the pressure difference across the wall, and thus, the temperature and humidity in the hot box. Overall it can be concluded that the boundary conditions were very stable during the measurements.

a) 

b) 

Figure 4.4: (a) Gaps in the interior vapour retarder from step 2 onwards (test series I) and (b) rigid mineral wool board to create a well-defined air gap above cellulose insulation in step 2 (test series II).

I	Days	T_{HB}(°C)	$P_{V,HB}$(Pa)	T_{CB}(°C)	$P_{V,CB}$(Pa)	P_a(Pa)	STEP
1	35	20.1	1181	3.0	653	1.9	initial
		20.0-20.1	*1169-1191*	*2.9-3.0*	*634-656*	*1.7-2.0*	
2	28	20.0	1178	3.2	680	0.8	gaps in OSB
		20.0-20.1	*1698-1205*	*3.1-3.7*	*676-698*	*0.6-1.4*	
3	24	20.1	1243	3.2	685	5.8	overpressure I
		20.0-20.1	*968-1333*	*3.1-3.2*	*678-689*	*5.7-6.0*	
4	11	20.1	1249	3.2	691	10.7	overpressure II
		20.1-20.2	*1232-1334*	*3.1-3.3*	*689-696*	*10.4-10.9*	
5	32	25.0	1688	22.6	1997	1.7	drying
		21.3-25.4	*1384-1723*	*22.4-22.6*	*1964-2149*	*1.1-5.3*	

Table 4.2: Boundary condition in hot box (HB) and cold box (CB) during the consecutive measuring steps of test series I (5 and 95 percentiles in grey).

The second test series (II) lasted about a month longer than the first one because the hygroscopic insulation material decelerated reaching equilibrium conditions. The measuring steps of the second series are similar to the first one. Yet additional steps were introduced in the test series II to study the impact of bad workmanship. After the first step, which is identical to the first test series, a gap of 2 cm was created at the top of the cellulose layer in wall section IIc. This was done by removing the rigid mineral wool board of 2 cm, built in this

wall before filling the cavity with cellulose insulation (Figure 4.4b). This second measuring step simulated in this way settling of blown-in cellulose insulation. Again, identical to test series I, step 3 and 4 created gaps in the vapour retarder, followed by the introduction of an overpressure in the warm box. Next, the fifth step created holes in the exterior air barrier to simulate bad workmanship in this layer. Small holes (Ø = 4 mm) were drilled every centimeter at a distance of 2 cm from the bottom of the wall. Table 4.3 summarises the boundary conditions of the second test series. In addition, their 5 and 95 percentiles are included as well, illustrating the stable conditions in the second test series.

II	Days	T_{HB}(°C)	$P_{V,HB}$(Pa)	T_{CB}(°C)	$P_{V,CB}$(Pa)	P_a(Pa)	STEP
1	39	20.0	1200	2.5	642	1.4	initial
		19.9-20.0	*1189-1213*	*2.4-2.6*	*622-649*	*1.3-1.4*	
2	13	20.0	1183	2.5	650	1.3	gap cellulose (IIc)
		20.0-20.0	*1178-1188*	*2.5-2.6*	*647-653*	*1.3-1.4*	
3	43	20.0	1200	2.5	654	1.5	gaps in OSB
		19.9-20.0	*1173-1228*	*2.4-2.5*	*649-660*	*1.3-1.6*	
4	14	20.0	1285	2.5	659	5.5	overpressure I
		20.0-20.0	*1143-1344*	*2.4-2.5*	*657-663*	*5.5-5.6*	
5	24	20.0	1274	2.4	663	5.5	gaps in BIFB
		20.0-20.0	*1107-1361*	*2.4-2.6*	*661-677*	*5.2-5.6*	

Table 4.3: Boundary condition in hot box (HB) and cold box (CB) during the consecutive measuring steps of test series II.(5 and 95 percentiles in grey)

4.1.4 Sensor positioning and accuracy

A comprehensive data logging system was designed to register the physical phenomena and generate validation data at the same time. The majority of the measurements in the vertical hot and cold box test set-up were done by a continuous logging system. For the data acquisition and logging, both chambers were equipped with a FLUKE:2680A/2686A. The cards to connect the sensors were installed inside the test chambers. The connection between these plug-in cards and the loggers was fixed, so, only the connection sensor to plug-in-card is changed when the test walls are changed. For the cold box the plug-in-cards are placed in a protected environment to shield the cards from the high relative humidity levels inside the chamber. Both loggers can process 120 signals, resulting in a maximum capacity of 240 sensors.

Each test wall in this study was provided with 18 thermocouples, 15 relative humidity sensors, 3 heat flux sensors and 1 pressure gauge sensor, covering the most important positions of the wall. The sensors were placed at 15 cm from the left side and were distributed in three rows: at 20 cm from the bottom, mid-height, and 20 cm from the top. Figure 4.5 depicts an overview of the sensor positions as placed within each wall. The insulation blankets were installed in two layers (15 cm-15 cm) in order to attach temperature and rel-

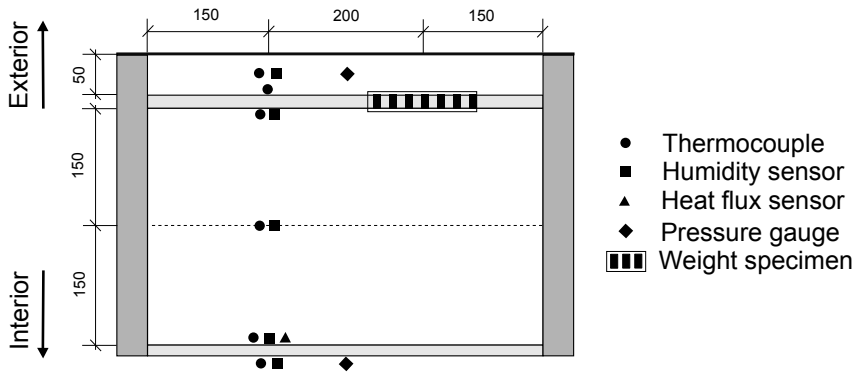

Figure 4.5: Sensor positioning within each wall section (distances in mm).

ative humidity sensors in between. The blankets were carefully installed by pushing them with a rigid board into the cavity. In doings so, the correct position of the blankets, and thus the sensors, could be guaranteed. A second advantage of this technique is the reduction of unforseen (small) leakages around the insulation blankets which is of great importance to provide applicable validation data. Sensors in the middle of the cellulose insulation layer were attached to a fine steel cable positioned in the cavity before insulating.

The reliability of the measurements was increased by calibrating the complete set of thermocouples and humidity sensors, connected to the plug-in cards. In comparison with the global sensor accuracy given by the manufacturer, the accuracy of reading could be increased through this sensors specific calibration. Hence, it became possible to compensate for errors such as the cold junction temperature and the position of the connection on the plug-in card. The thermocouples and relative humidity sensors were calibrated with an optical dew point transmitter[3] (accuracy of ±0.1°C on the global temperature and ±0.2°C on the dew point temperature). The thermocouples were calibrated at four temperatures (1, 10, 20 and 25°C) and the humidity sensors at three humidity levels (30, 80 and 99 %). Additionally, the heat flux sensors were calibrated in a heat flow apparatus, as described in the standard guidelines ISO 8302:1991. Table 4.4 summarises the applied sensors with the corresponding accuracy levels and measuring range.

Sensor	Manufacturer	Type/Model	Accuracy	Range
Thermocouple	Thermo Electric	Type T (class 1)	± 0.2°C	-20/60°C
Relative Humidity	Honeywell	HIH-4000/21	± 2 %	0/100 %
Heat flux	Phymeas	Model 7	± 6 % of reading	±100 W/m^2
Pressure gauge	Halstrup Walcher	P26	± 0.6 Pa	± 50 Pa

Table 4.4: Accuracy and measuring range of applied sensors.

[3]Optidew of Michell

In addition to the continuous logging system, the exterior layer consisting of fibreboards was constructed in such a way that each wall contained three removable specimens (18 cm by 18 cm), placed at 15 cm from the right side. These specimens were used to quantify the moisture evolution of the fibreboard by weighing the specimens at regular time intervals. Since the weight specimens were created in the exterior air barrier, preserving the airtightness of this layer was very important. Therefore, the perimeter of the specimens was step-like cut out of the fibreboard (Figure 4.6). Additionally, a very thin plexiglas layer was attached around the perimeter of the specimens and the board on which the joint was taped in between the measuring steps without destructing the soft fibreboard (Figure 4.6). To check the quality of the sealing, the airtightness of a board with a specimen was measured in the laboratory. The air permeability of the fibreboard with sealed specimen showed to deviate less than 5% from the air permeability of the intact fibreboard.

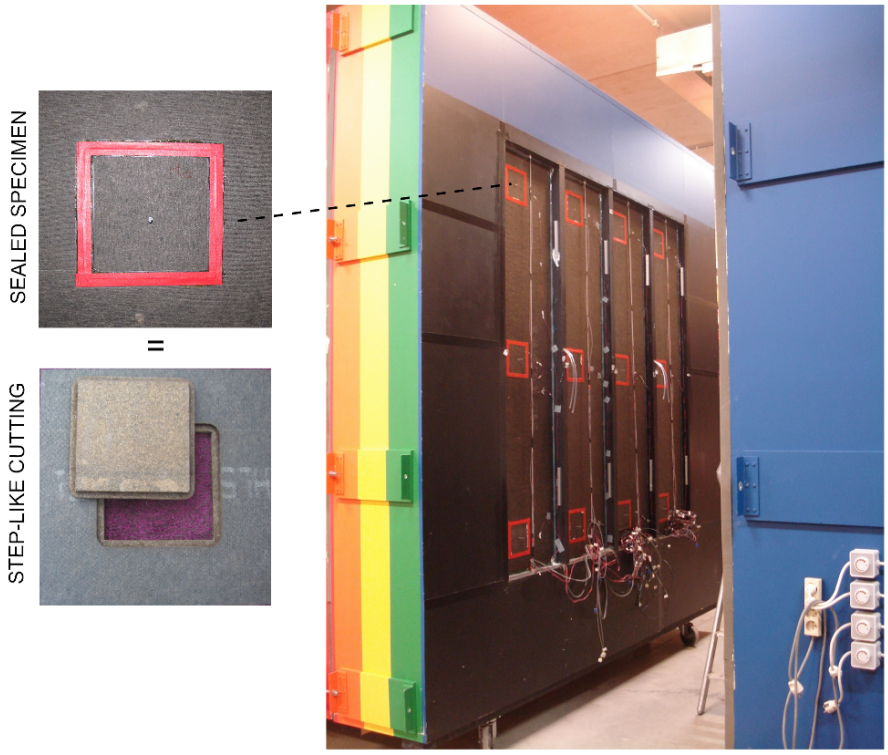

Figure 4.6: Weight specimens in hygroscopic exterior sheathing.

4.1.5 Material properties

This section outlines the hygrothermal properties of the applied materials in the experiment. In test series I the same interior vapour retarder (OSB) and mineral (glass) wool insulation (herein referred to as MW20) were used for all walls, while the exterior air barrier of the four test walls differed. Three different air barrier materials were selected carefully to compare a maximum number of different phenomena with the parameters investigated: (1) the thermal resistance (BIFB I = BIFB II > FOIL), (2) hygroscopic buffer capacity (BIFB I = BIFB II >

Vapour resistance (m) of outermost uninsulated (non-vented layer of the wall assembly)	**Maximum permissible air leakge rate (l/(s m^2)) at 75 Pa**
12.5 < s_d-value < 3.1	0.05
3.1 < s_d-value < 1.1	0.1
1.1 < s_d-value <0.23	0.15
s_d-value <0.23	0.2

Table 4.5: Maximum permissible air leakage rate - air barrier system (Di Lenardo 2009, p. 4).

FOIL), (3) air permeance (BIFB II > BIFB I > FOIL) and (4) vapour permeance (FOIL> BIFB II > BIFB I) of the different exterior sheathing materials.
Di Lenardo (2009) discussed the upper limits for the air permeance of air barrier systems, including joints and penetrations. These air leakage rates, given as function of the vapour permeance of the outermost layer, were established through a computer modelling program (TCCCD, Ojanen et al. (1994)) carried out by IRC researchers in conjunction with the Technical Research Center (VTT) in Finland (Table 4.5). Since all three exterior air barrier materials tested had a lower s_d-value than 0.23 m, Di Lenardo (2009) maintains that the air leakage rate should not exceed 0.2 l/(s m^2) at 75 Pa. In the light of these results, one exterior sheathing material was chosen to exceed this threshold value; the air leakage through BIFB II corresponded to 2.3 l/(s m^2) at 75 Pa. However, the other two materials, BIFB I (0.1 l/(s m^2)) and Foil (<0.02 l/(s m^2)) satisfied Di Leonardo's recommendations.
In the second test series all four walls were executed with BIFB II as exterior air barrier material. This second experiment draw attention on the impact of the applied insulation material and potential bad workmanship. Therefore, only two additional materials were applied: (1) mineral wool of 30 kg/m^3 and (2) blow-in cellulose insulation (60 kg/m^3) (hereafter referred to as MW30 and CL60 respectively).

Heat transfer properties

Table 4.7 gives an overview of the heat transfer properties of the used materials. The heat conductivity of the materials was measured at the laboratory according to ISO 8302:1991. The thermal conductivity λ was characterised as a function of the temperature and was fitted with the following linear relation:

$$\lambda = \lambda_0 + \lambda_\theta \theta \tag{4.1}$$

where λ_0 (W/m/K) corresponds to the thermal conductivity at 0°C, θ expresses the temperature (°C) and λ_θ describes the temperature dependency.
In addition, the thermal heat conductivity of hygroscopic materials depends on the moisture content as well. In this study the bituminous impregnated fibreboard sheathings can be

exposed to high moisture content levels. Consequently, their thermal conductivity as a function of the moisture content has been determined in laboratory conditions. This moisture dependency can be expressed by extending Eqn. 4.1 with an additional term λ_w:

$$\lambda = \lambda_0 + \lambda_\theta \theta + \lambda_w w \tag{4.2}$$

As the core material of BIFB I and II are identical (see section 4.1.5), a similar moisture dependency can be expected. Consequently, only for BIFB II this relation was studied. At a temperature of 1.5°C, this resulted in a λ_w of 0.021 and at a temperature 11.5°C this parameter was 0.027. The heat capacity c_p was collected either from product sheets or the literature (Kumaran 1996).

Air transfer properties

All the air permeability measurements were performed with the test setup described in section 3.3.3. Special care was given to the air permeability of the insulation materials. The permeability of the mineral wool was measured both perpendicular $K_\perp$ and parallel $K_\parallel$ to the fibres on specimens of 0.2 x 0.2 x 0.2 m^3. The results for MW20 are compared with values from the literature in Table 4.6. This table indicates that the permeability perpendicular to the fibres is lower than values from the literature. In addition, Table 4.6 presents the minimum and maximum measured values in this study between brackets which shows that there is a large variation on the permeability parallel to the fibre. It was noticed that, depending on the precision with which the specimen was installed in the test rig, large differences were measured. Consequently this impedes to determine the exact air permeability of the mineral wool as installed in the test walls.

	ρ (kg/m^3)	$K_\parallel$ (10^{-9} m^2)	$K_\perp$ (10^{-9} m^2)
Present study	21.3	5.3 (2.4 - 10)	1.7 (1.1-3.6)
Økland (1998)	18.3	3.7	1.9
Kumaran (1996) (I)	20	/	1.4-1.5
Kumaran (1996) (II)	17.9	/	1.9-2.4
Kronvall (1980)	20	4.1	2.2

Table 4.6: Air permeability of mineral wool (minimum/maximum between brackets).

The air permeability values of the sheathing materials were also measured in the laboratory (summarised in Table 4.7). So far, this section has only discussed the air permeability values of porous materials, which can be described by Darcy law, corresponding to a constant permeability. However, when it comes to air transport through air leakages, such as the horizontal slots in the OSB layer, the air resistance depends on the pressure difference, most often described as a power law function. Figure 4.7 presents the measured air flow through a 1 cm slot in an OSB specimen and the gaps in the exterior sheathing.

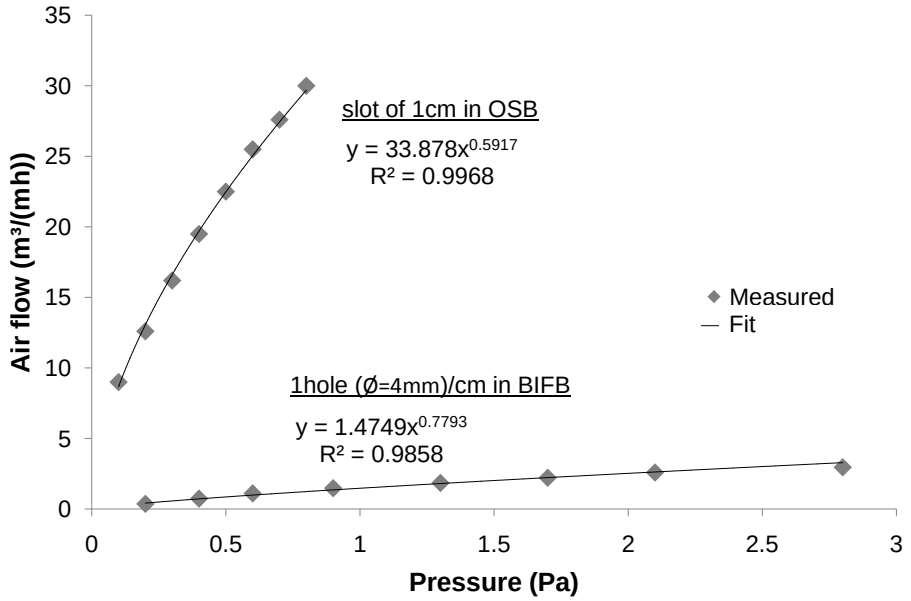

Figure 4.7: Air leakage through gap of 1 cm in OSB and gaps of Ø = 4 mm in BIFB.

Hygric properties

The moisture capacity of the building components was measured by determining the hygroscopic sorption curves. These sorption isotherms were determined based on the moisture equilibrium of specimens exposed to relative humidity conditions created by saturated salt solutions in closed desiccators. Figure 4.8a shows the results, fitted with equation 4.3:

$$u = v(1 + (m.ln(\phi))^n)^{\frac{1-n}{n}} \tag{4.3}$$

where u is referring to the moisture content (kg/kg), ϕ is the relative humidity (%) and v, m and n are fitting parameters. Water vapour transmission properties of the applied materials were measured at 23°C according to ISO 12572:2001. Figure 4.8b shows the results, fitted with equation 4.4:

$$s_d = \frac{1}{a + b.e^{c.\phi}} \tag{4.4}$$

in which s_d represents the water vapour diffusion-equivalent air layer thickness, ϕ is the relative humidity (%) and a, b and c are fitting parameters. Liquid water transport in the interior sheathing and mineral wool insulation is unlikely to occur. Therefore, only the water absorption coefficients of the exterior fibreboard sheathings were measured according to Roels (2004b). The results reveal that these materials were non-capillary. The moisture increase during the absorption experiment was in the same order of magnitude as the hygroscopic loading of the material. Additional contact angle measurements confirmed the hydrophobic behaviour of these materials. In summary, even as BIFB I and II are non-capillary, they are strongly hygroscopic, moisture buffering and vapour permeable.

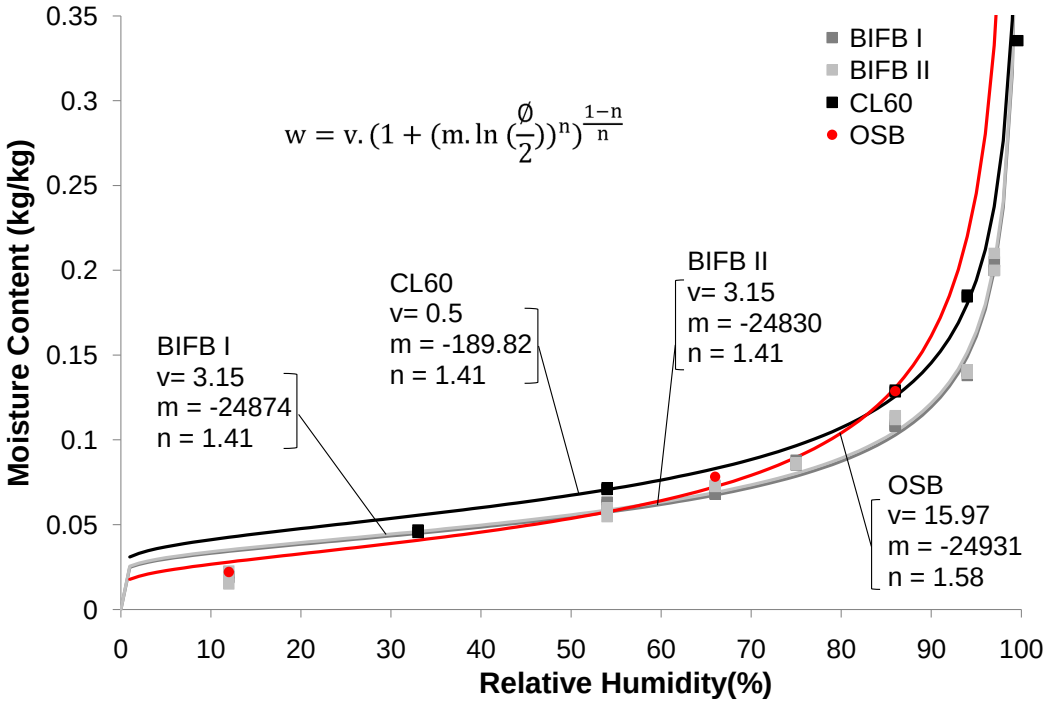

(a) sorption isotherm

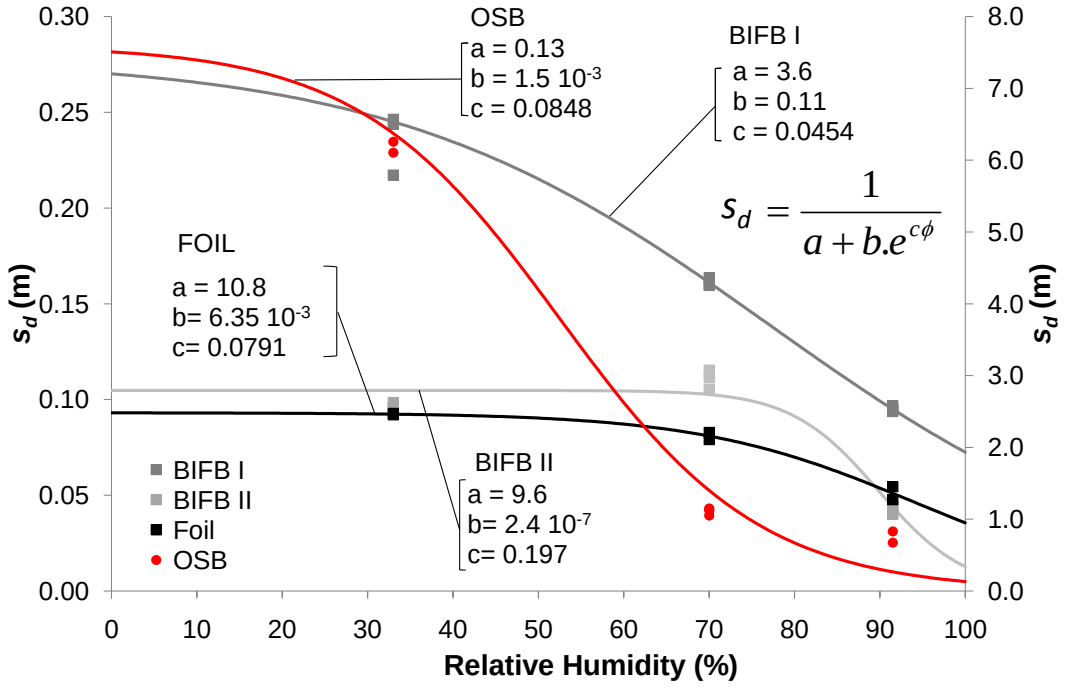

(b) vapour diffusion resistance (left axis: Foil and BIFBI/II, right axis: OSB)

Figure 4.8: Sorption isotherm and vapour diffusion resistance.

	BIFB I	**BIFB II**	**Foil**	**OSB**	**MW20**	**MW30**	**CL60**
d	18	18	0.2	15	300	300	300
ρ	285	274	-	630	21.3	31.3	60
c_p	2068	2068	-	1880	840	840	2544
λ_0	0.045	0.047	-	0.1	0.031	0.029	0.034
λ_θ	0.0001	0.0001	-	0.0002	0.0001	0.0001	0.00015
$K_\perp$	$4.65\ 10^{-13}$	$1.37\ 10^{-11}$	airtight	$<8.20\ 10^{-14}$	$1.7\ 10^{-9}$	$8.1\ 10^{-10}$	$8.8\ 10^{-10}$
$K_\parallel$	-	-	-	-	$5.3\ 10^{-9}$	$3.2\ 10^{-9}$	$8.8\ 10^{-10}$

Table 4.7: Overview of the material properties.

4.1.6 Results

This section presents the obtained laboratory results. First, the observed global air flow patterns are discussed. Next, the impact of the individual parameters on the hygrothermal response is given for: (a) properties of air barrier material, (b) the air permeability of the insulation layer, (c) bad workmanship and (d) hygroscopic insulation materials.

Observed air flow patterns

The aim of this section is to present the observed air flow patterns in lightweight components with an exterior air barrier and their impact on the heat flow, temperature and vapour pressure profiles across the test walls. Only the data of the first test series is applied for the identification of these profiles. This analysis first looks into the thermal distribution in the test walls. Figure 4.9a shows the dimensionless temperature profiles of the four walls at the top and bottom row for measuring stage 1, 2 and 4. This corresponds to the situations where (1) the interior OSB sheathing was intact, (2) top and bottom gaps in the interior sheathing were introduced and (3) a pressure differential of 10 Pa across the test wall was realised. This figure shows how, during the first step (blue triangles), the temperature distribution for all four walls bends upwards at the top (filled markers) and downwards at the bottom (open markers) indicating the existence of natural convection within the walls. During the second measuring step (red squares) this effect increased as a result of the introduction of the gaps in the interior sheathing. In addition, the temperature profile for the least airtight wall (Ic) bends also upwards at the bottom row as well. This means that the exterior sheathing is so air permeable that, as a result of the 1.9 Pa pressure differential across this wall (introduced by the ventilators in the cold chamber), forced exfiltration already dominates the air flow in this wall section. When, finally, step four realised a pressure difference of 10 Pa (green dots), this effect became even more pronounced. At this stage, also for wall Ib this effect was observed, however to a minor degree. For the most airtight wall (Id) the effect of forced convection on the temperature remained negligible.

Figure 4.9b presents, with the same notation as the temperature profiles, the dimensionless vapour pressure profiles across the test walls. Vapour pressures are derived from the

measured temperatures and relative humidity levels according to:

$$P_v = \phi \cdot exp(65.8 - \frac{7066.7}{T} - 5.976 \cdot ln(T)) \tag{4.5}$$

where P_v (Pa) corresponds to the vapour pressure, ϕ to the relative humidity (%) and T (K) to the temperature. During the first step, all four walls showed a similar vapour pressure profile; a steep drop behind the vapour retarder (OSB) followed by a slight decrease towards the outer side. Only in wall section Ib the vapour pressure at the top row was to some extent deviating from the expected values since the vapour pressure is slightly higher than in the other walls. This can not be explained by air exfiltration as this was not noticed in the temperature distribution. A more plausible explanation might be found in a local deviation of the vapour resistance in the interior or exterior sheathing material or the sealed gap.
In the subsequent step, when the gaps in the interior sheathing were opened, the influence of natural convection on the moisture load became very pronounced. For all walls with interior gaps the vapour pressure at the top row increased while the vapour pressure at the bottom row remained almost the same. Only in wall Ic the vapour pressure at the bottom row increased as well, induced by forced exfiltration as a result of the high air permeance of the exterior sheathing. When a pressure difference of 10 Pa is realised, the vapour pressure profiles confirmed the observation of the temperature profiles. In wall Ib a slight increase in vapour pressure was noticed as a result of forced exfiltration, while this effect is much stronger in section Ic. For the wall with the exterior foil (Id) this influence could hardly be noticed.

In addition to the temperature and vapour pressure profiles across the walls, Figures 4.10 summarises the impact of air convection on the local heat flows in the walls of test series I. This figure presents the evolution of the measured heat fluxes for the first four measuring stages. The heat flows at the top, mid and bottom position are given from left to right and the corresponding air pressure differences across each test wall are mentioned at the top of this figure. The heat flux transducers are the most sensitive sensors used in this experiment. The measured heat flux depends on the local thermal gradient across the sensors. Consequently, even small differences in the installation of the sensors endanger the comparison of their absolute values. Therefore, Figure 4.10 presents the heat fluxes relatively to their value during the first measuring stage, which enabled to filter errors induced by the installation of the sensors. Yet this method impedes the visualisation of the influence of internal natural convection on the heat fluxes across the height during the first measuring step, when no air gaps are present in the inner OSB layer.
The differences between the blue (step 1) and red markers (step 2) in Figure 4.10 indicate the increase of air convection inside the insulation as a result of creating openings in the interior layer. For wall section Ib and Id this corresponded to a decrease of the heat flux at the top and an increase at the bottom. In the middle of the wall the heat flux remained the

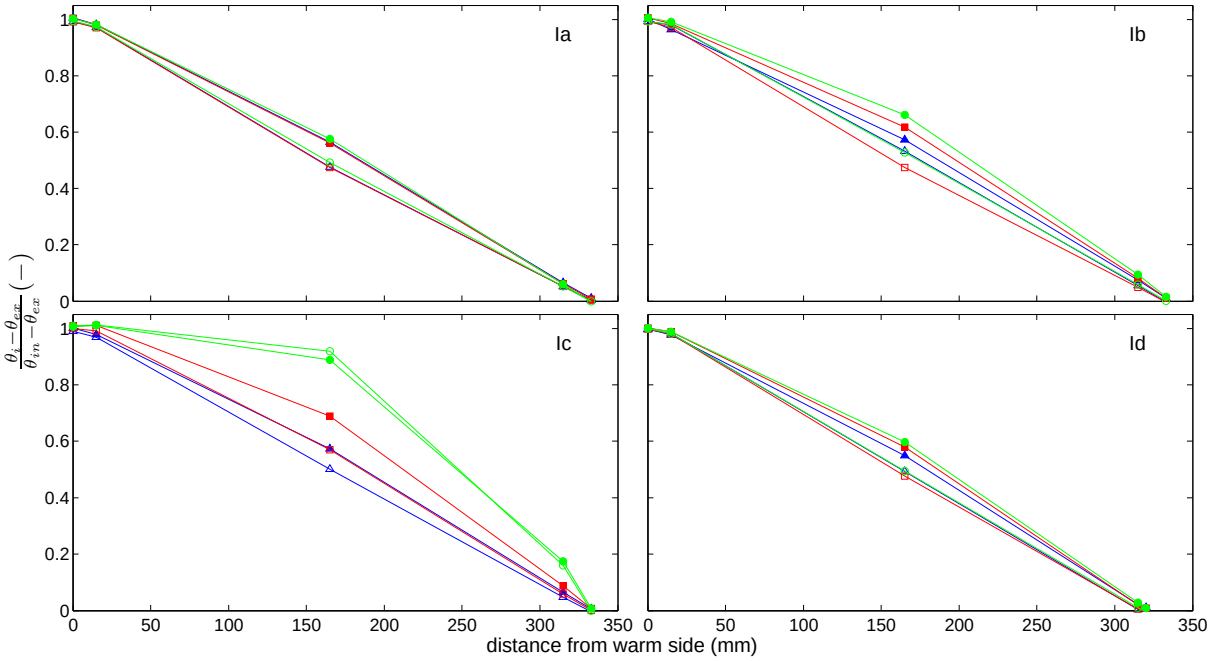

(a) Dimensionless temperature profile

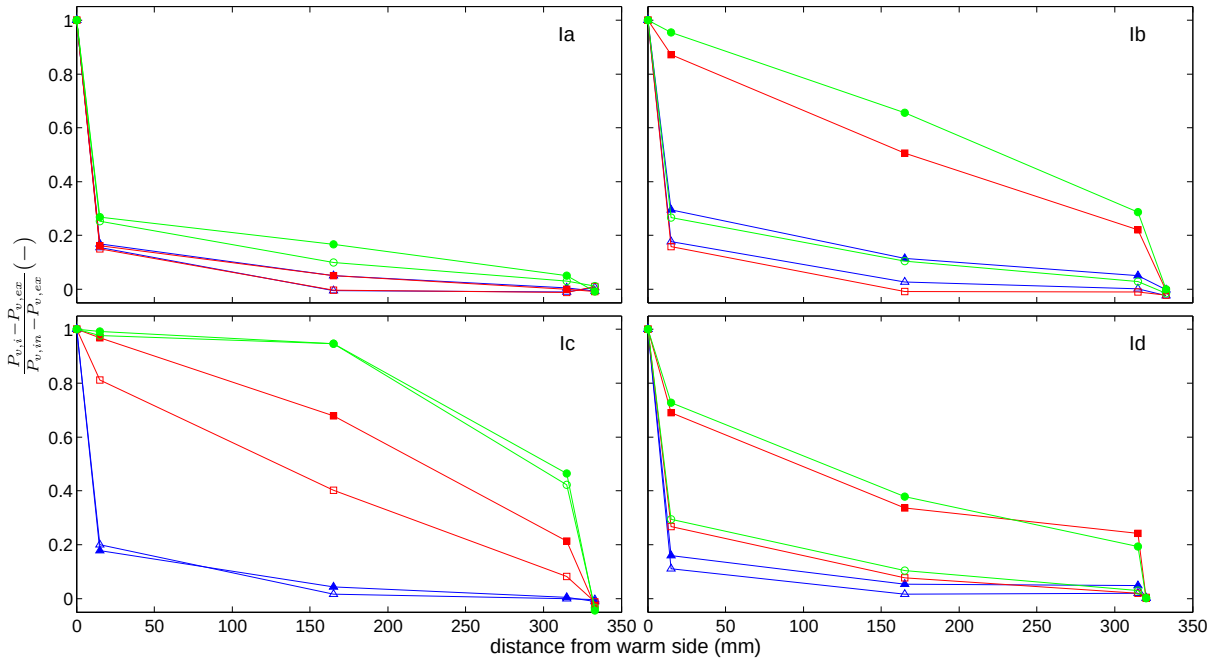

(b) dimensionless vapour pressure profile

Figure 4.9: dimensionless temperature profile and vapour pressure of the four test walls of series I at top row (filled markers) and bottom row (open markers) during measuring step 1 (blue triangle), step 2 (red square) and step 4 (green dot).

same. In section Ic both the heat flux at the top and the bottom row decreased after creating the gaps which suggests that forced convection dominated natural convection from step 2 onwards. From the moment a pressure was created in the third measuring step, forced convection was noticed in all walls. Although both the interior and the exterior sheathing of wall Ia remained intact, a small decrease of the heat flux at the top was noticed, most likely due to a small air leakage at the top of test wall. The largest decrease in the third step was noticed in the most air permeable wall (Ic), followed by wall section Ib and a negligible impact on the section Id. Doubling the air pressure differential in the next step, resulted -proportionally- in a smaller effect on the measured heat flows. The measured heat flow at the bottom row of wall Ic was almost reduced to zero. In this context it is important to note that the heat flux transducers only measured the conductive heat flux. The total heat flow across the walls is of course composed of a conductive and convective term.

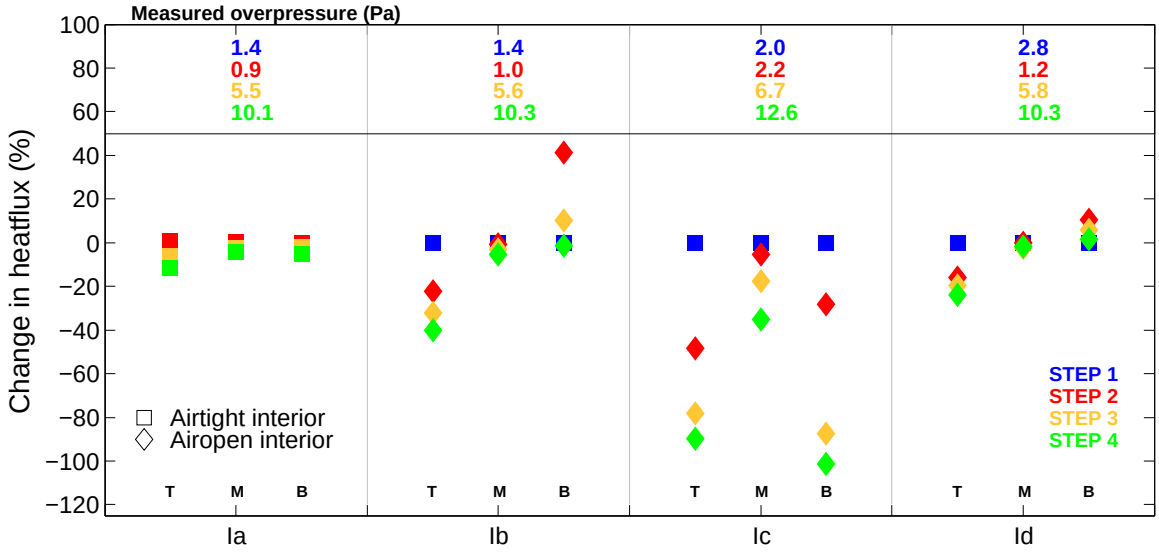

Figure 4.10: Impact of air convection on the heat flows for the four measuring steps of test series I (T=Top, M=Middle, B=Bottom position of the heat flux sensor).

In summary, three types of air flow patterns were observed, which are depicted in Figure 4.11. The temperature profiles during the first measuring stage indicated the existence of internal natural convection, illustrated in Figure 4.11a. However, the impact of this convection loop on the vapour transport, and thus moisture load in the wall was limited. In the second stage, which introduced air gaps in the interior barrier, the impact of natural convection increased (Figure 4.11b). This was noticed based on the measured temperature profiles and the heat fluxes. A second effect induced by the gaps was that the interior air came in direct contact with the insulation layer at the level of the gaps, bypassing the vapour retarder. This warm humid air entered at the upper gap driven by natural convection and increased the vapour pressure at this level of the insulation. As a third effect of penetrating the vapour retarder one would expect concentrated vapour diffusion at the level of the gaps. However, the measurements indicated that this phenomenon was outweighed by natural convection

as no moisture increase was noted at the level of the bottom gap. Lastly, when applying a pressure difference across the wall, forced convection (Figure 4.11c) became dominant for the least airtight air barrier material (BIFB I). In the case of the FOIL and BIFB I this effect was limited.

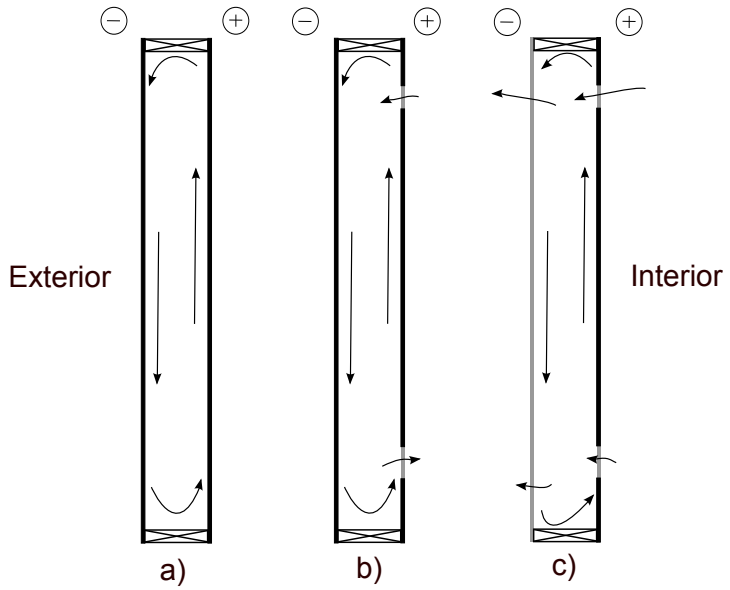

Figure 4.11: Observed air flow patterns.

Impact of air barrier material

The previous section described the observed global air flow patterns and their influence on the temperature and vapour pressure field. However, the risk for moisture problems within the walls is highly depending on the hygrothermal properties of the exterior air barrier material. Therefore, three potential exterior air barrier materials with different properties have been tested in test series I with varying as parameters: (1) the thermal resistance, (2) the hygroscopic buffer capacity and (3) the air and vapour permeance of the different exterior sheathing materials (see section 4.1.5).

To visualise the hygric response of these three materials, Figure 4.12 shows the evolution of the relative humidity at the interface of the exterior air barrier and the insulation for the three heights in test series I. In addition, this figure plots the relative humidity in the cold (blue surface) and warm chamber (red surface) as well. During the first step, when the interior gaps were still sealed, the relative humidity of the walls with an exterior fibreboard sheathing remained in the same range. As a result of the moisture buffer capacity, it took time before the relative humidity reached a quasi-equilibrium state. Real equilibrium was not obtained as the relative humidity in the cold chamber slightly increased during the measurement (blue surface). In contrast to the walls with the buffering sheathing, the wall with an exterior foil reached the quasi equilibrium almost immediately. Moreover, it was noticed

that the relative humidity of the wall was 6 % to 9 % higher compared to the reference wall. Even though the foil had a higher vapour permeance, the lack of thermal resistance caused lower temperatures at this position in comparison to the other walls. Consequently, this resulted in a lower saturation pressure, and thus, higher relative humidity levels. After opening

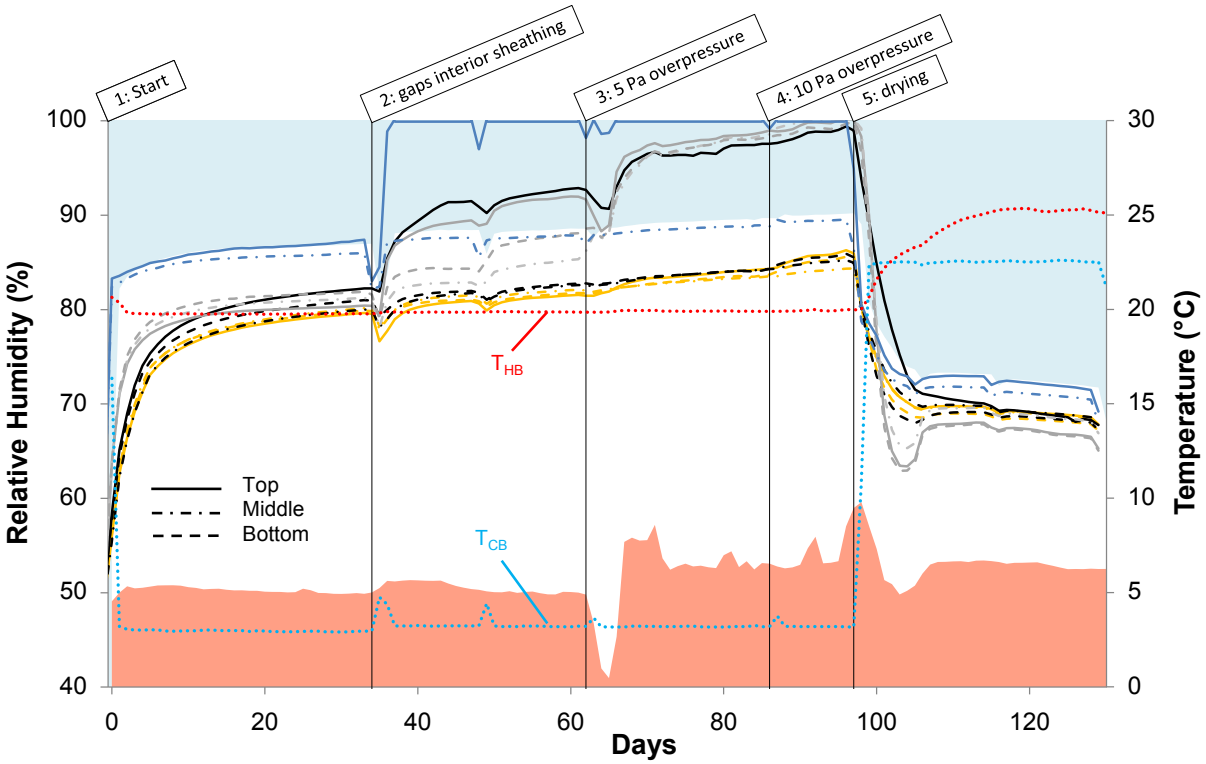

Figure 4.12: Relative humidity (%) at the interface insulation-exterior air barrier for Ia (orange), Ib (black), Ic (grey), Id (blue) (test series I), in hotbox (red surface), in coldbox (blue surface) and temperatures in hotbox and coldbox

the gaps in the interior OSB-layer in the next step, the upper relative humidity against the foil (Id) immediately peaked towards condensation conditions. A similar increase was noticed for the Ib and Ic, though with a slower progress as a result of the moisture buffer of the fibreboards. In contrast to Ib and Id, also the relative humidity at the mid and bottom position of Ic increased during the second step. As explained in the previous section, this was induced by the small pressure differential created by the ventilator in the cold box in combination with the high air permeance of this fibreboard. The next two steps (3 and 4), continued the same evolution for wall Ic. Driven by forced convection, the relative humidity at the mid and bottom position of Ic converged towards the upper one. At the end of step 4, the relative humidity levels at the upper position of Ib and Id and at all three heights of Ic corresponded to nearly the same high values. These high relative humidity levels (>95 %) corresponds to high equilibrium moisture contents of the fibreboard sheathing (see Figure 4.8a). Note, that the hygroscopic curve becomes very uncertain for such high relative humidity levels. Consequently, given the accuracy of 2 % on the relative humidity sensors, it becomes impossible to differentiate between the different walls at this step.

This problem was answered by installing weight samples in the exterior sheathing, as described in section 4.1.4. Notwithstanding that the relative humidity levels at the end of step 4 were in the same range in Figure 4.12, great differences between the moisture contents are shown in Figure 4.13. The dots in Figure 4.13 represent the measured moisture con-

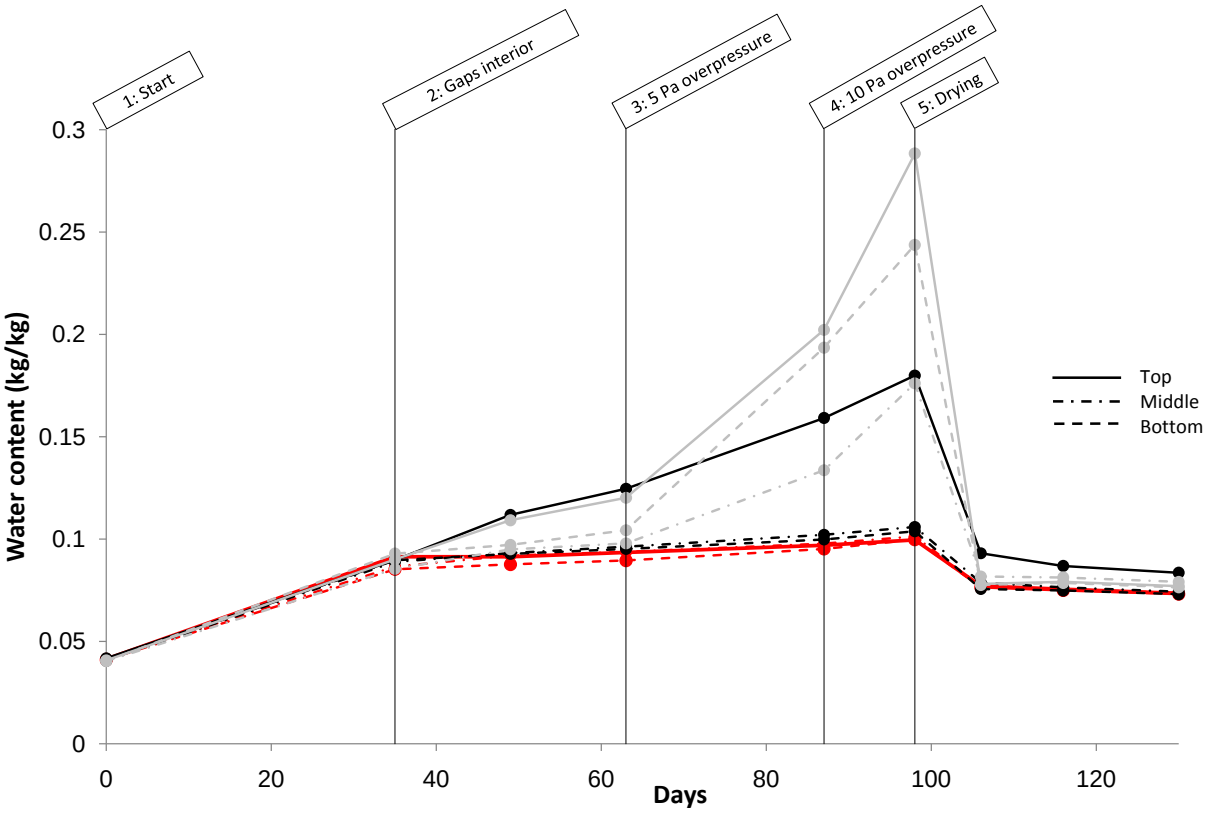

Figure 4.13: Moisture content evolution of the weight sample in the exterior sheathing: Ia (red), Ib (black), Ic (grey).

tent of the specimens at the top, mid and bottom height. During the first stage all weight specimens showed the same moisture content evolution. From the moment gaps were introduced, however, a significant moisture increase could be noticed at the top position. Furthermore, for section Ic the moisture content at the bottom and middle position slightly increased, indicating the existence of forced convection. The pressure difference across the walls in step 3 and 4 seemed to have no influence on the moisture content of Ib. The moisture content at the upper position continuously increased while the moisture content of the middle and bottom row remained the same as in test wall Ia. On the other hand for Ic, where the exterior sheathing was twenty times more air permeable, a correlation between the magnitude of the pressure differential and the moisture content of the weight samples at the three heights was observed. As a result of these high moisture contents, traces of water droplets were found on Ic at the end of step 3. At the top and bottom specimens this resulted in mould growth after the next step (Figure 4.14). But, a result of the high vapour permeance of all three tested exterior sheathing materials, the walls could dry out fast in the last measuring step (Figure 4.13).

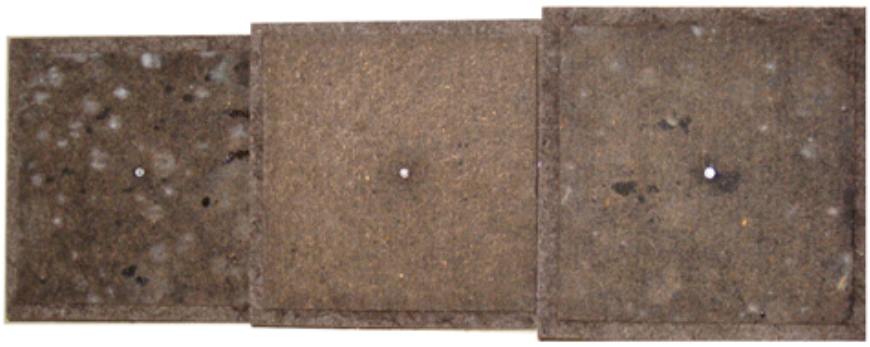

Figure 4.14: Mold growth on weight specimens of Ic at the end of step 4 (left to right: top, middle and bottom specimen).

To summarise, the results confirmed the observation that a sufficiently airtight air barrier material is a prerequisite for a safe building envelope. In this respect BIFB II (0.1 $m^3/(m^2\,h\,Pa)$) obviously failed, resulting in a forced exfiltration flow through the wall, and thus, very high moisture contents of the exterior sheathing, as numerically predicted by Di Lenardo (2009) (see Table 4.5). For BIFB I (0.005 $m^3/(m^2\,h\,Pa)$) and FOIL (<0.001 $m^3/(m^2\,h\,Pa)$) this effect was limited to a very minimum. Therefore, it can be concluded that such levels of air permeance are sufficiently low to prevent harmful amounts of forced exfiltration. Although this section revealed that even if forced convection is excluded (Ib and Id), an increased moisture load was introduced by realising an exterior air barrier system. For both test sections the results indicated that water vapour driven by natural convection entered through the upper gap and deposited at the cold side of the insulation layer. The danger of this process lies in its continuity. Driven by the temperature difference across the wall, this convection loop provides a constant moisture supply towards the upper cold side of the structure in winter conditions. Furthermore, this section demonstrated the positive impact of using exterior sheathing materials with a thermal resistance and a moisture buffer capacity. The thermal resistance increased the temperature, and thus, reduced the relative humidity at the cold side of the insulation. In addition, the moisture buffer capacity had a retarding effect on condensation. Fluctuations of the relative humidity could be attenuated in this way. But, although interstitial condensation could be postponed with these materials, the findings revealed how this could lead to more conducive conditions for mould growth at the inside of the exterior air barrier.

Effect of insulation density

The previous section illustrated how natural convection can lead to an increased moisture load entering the building envelope. Yet the order of magnitude of this buoyant driven air loop and the increased risk for moisture damage depends on various parameters. The cur-

rent section compares the response of wall sections Ib, IIb and IId, to investigate the impact of various typical insulation materials on the moisture load. These three walls only differed by the applied insulation materials (see Table 4.1). As shown in the previous section, the thermal performance gives a good indication of the level of natural convection. Therefore, Figure 4.15 compares the temperature profiles and the evolution in heat flow before and after opening the interior vapour retarder. This figure indicates that the use of more dense mineral wool results in a decrease of natural convection. Furthermore, the figure reveals how natural convection became almost negligible when applying cellulose insulation. An identical temperature before and after creating gaps in the interior vapour barrier in section IId was found. Consequently, the differences between the temperature at the top and bottom row could only be induced by differences in the insulation density across the width of the wall, and not by natural convection.

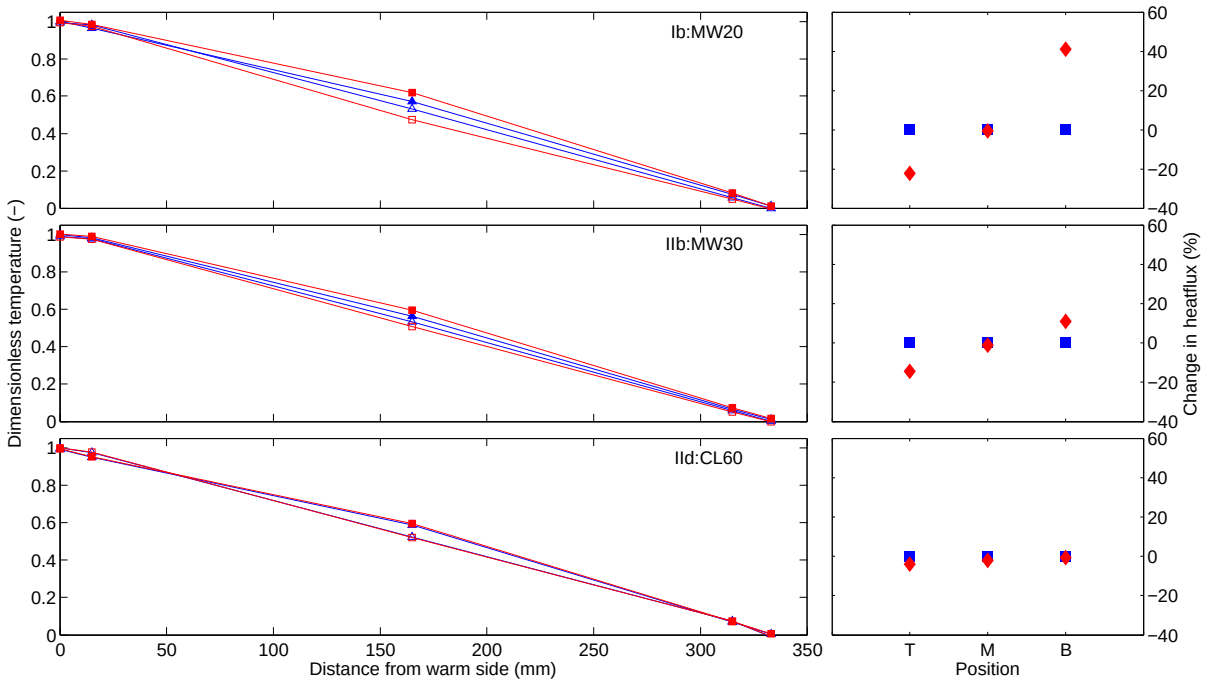

Figure 4.15: Influence of insulation material on dimensionless temperature profile and heat flux (before (blue) and after (red) creating gaps in the interior vapour barrier).

This important observation that natural convection becomes negligible for cellulose filled cavities, should mean that the moisture content of the exterior air barrier is not affected by small openings in the vapour barrier. To investigate this, Table 4.8 gives the moisture content at the top, mid and bottom row after measuring step 2 for Ib and measuring stage 3 for IIb and IId. The accuracy interval of the moisture content in this table (±2 kg/kg) was estimated by taking extra weight samples[4] after the fifth measuring step in wall IIa and IIc. This table confirms that the moisture content of the exterior sheathing in IId was not

[4]Extra weight specimens were taken by cutting cylinders with a diameter of 6 cm at the opposite side of the regular weight specimen.

significantly increased by natural convection. On the other hand, in the case of mineral wool insulation, the table clearly demonstrates the highest impact for the least dense material.

	material	$K_{\perp}$ (m^2)	$K_{\parallel}$ (m^2)	MC_T (%)	MC_M (%)	MC_B (%)	days
Ib	MW20	$1.7\ 10^{-9}$	$3.8\ 10^{-9}$	18 (±2)	11 (±2)	10 (±2)	98
IIb	MW30	$8.1\ 10^{-10}$	$3.2\ 10^{-9}$	14 (±2)	11 (±2)	11 (±2)	109
IId	CL60	8.810^{-10}	$8.8\ 10^{-10}$	12 (±2)	10 (±2)	11 (±2)	109

Table 4.8: Moisture content (MC) at the Top (T), Middle (M) and Bottom (B) row at the end of step 2 for Ib and step 3 for IIb and IId.

Impact of bad workmanship

So far, only the behaviour of walls with perfectly installed insulation layers have been discussed. As stated in section 4.1.4, the mineral wool blankets were carefully installed by pushing them with a rigid board into the cavity, realising close contact between the insulation and the adjacent fibreboards over the total height of the walls. In practice, however, such accurate installation can not be guaranteed, as installation defects are often the result of friction between the mineral wool and the studs resulting in gaps in the corners of the cavity (see section 2.2.1). Consequently, the insulation layer might not be in contact with the sheathing over the complete width between the studs. In order to asses this effect, a cavity of 1 cm between the insulation and the exterior air barrier was left in wall section IIa. Bad workmanship in cellulose filled cavities is mostly related to settling of blown-in insulation. This was simulated in wall section IIc by introducing a 2 cm air cavity on top of the insulation as described in section 4.1.3.

Figure 4.16 presents the measured temperature profiles and heat flow before and after creating gaps in the interior barrier. This figure indicates that the level of internal natural convection is significantly higher when a gap of 1 cm was left between the insulation and the air barrier in the first step. When opening the interior vapour barrier, however, the increase of buoyancy is relatively similar to the wall without this installation deficiency. Furthermore, the figure shows that settling of cellulose insulation had no effect on the temperature profiles. Only the temperature at the top slightly decreased. This can not be ascribed to global buoyancy in the wall, as the temperatures at the middle and bottom were not affected.

Figure 4.17 visualises the impact of the installation defects on the moisture content of the exterior air barrier sheathing. First, this figure shows an increase of the moisture content at the top of the walls with mineral wool from step 3 onwards (red/black). Notwithstanding the vertical air gap of 1 cm in section IIa, the moisture content evolution in both walls show a similar profile in step 3. In contrast to the mineral wool insulated walls, the components filled with blown-in cellulose were not largely affected by natural convection in the third

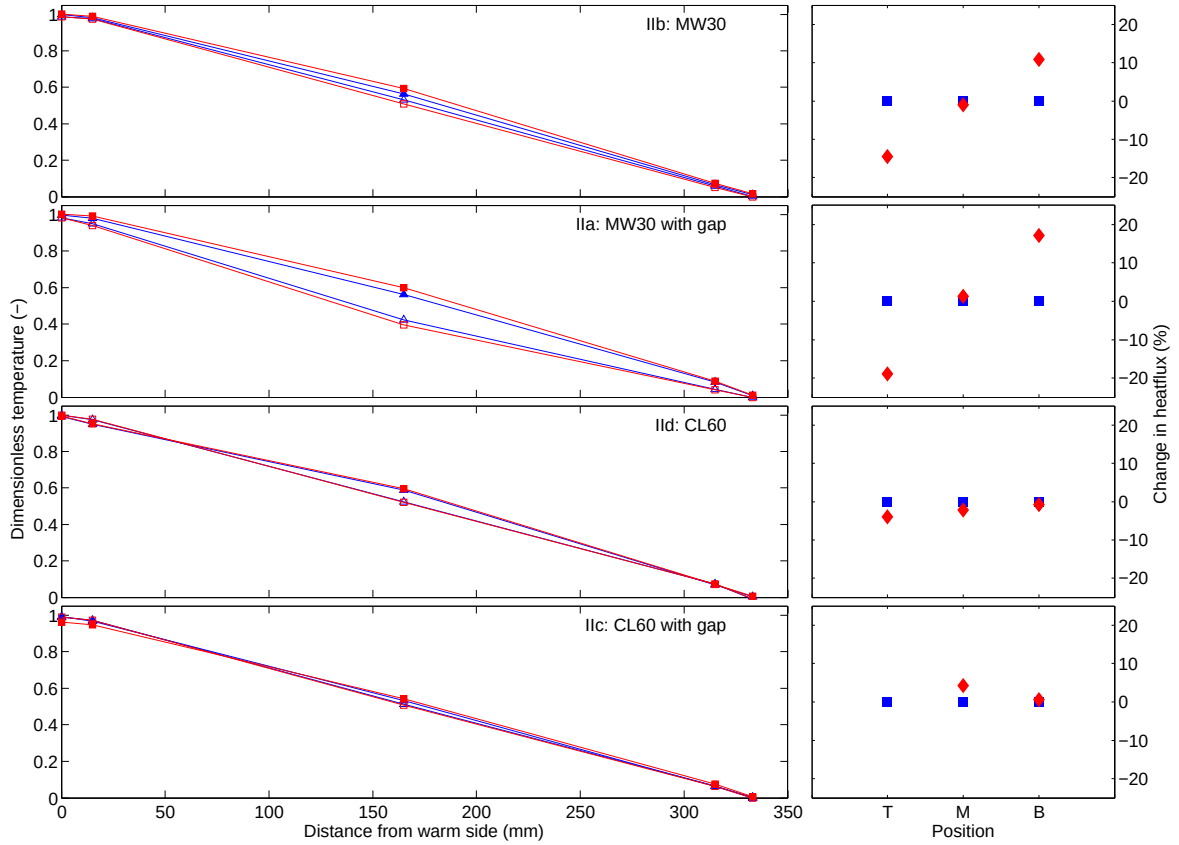

Figure 4.16: Impact of bad workmanship in the insulation on the temperature profile and heat flux (before (blue) and after (red) creating gaps in the interior vapour barrier).

stage. Also creating an air gap on top of the insulation in test section IIb in step 2 did not affect the moisture content levels.

In addition to installation defects in the insulation layer, the impact of air leakages in the exterior air barrier was investigated. As discussed in section 4.1.3, holes (Ø = 4 mm/cm) were drilled at the bottom of each test section in the fifth measuring step to simulate bad workmanship in this layer. As a result of these air leakages and the pressure differential of 5 Pa across the walls, forced exfiltration conditions were obtained. An important observation in these conditions was the different response of wall section IIa and IIb. As depicted in Figure 4.17 air leaks in the exterior barrier had a larger impact on the wall in which the mineral wool was improperly installed (IIa). This suggests that the vertical air gap between the insulation and the exterior air barrier largely affects the air flow pattern. The figure indicates that three air flow paths occurred in section IIa: (1) natural convection loop, (2) short air flow path at the bottom of the wall and (3) a long air flow path entering the upper gap in the OSB, passing the gap along the cold side of the insulation and leaving the wall at the bottom gaps in the exterior sheathing. The latter affected the largest surface since humid air, entering the upper gap, flowed over the total height of the wall near the cold exterior surface. As a result section IIa was the only test wall in which the moisture content

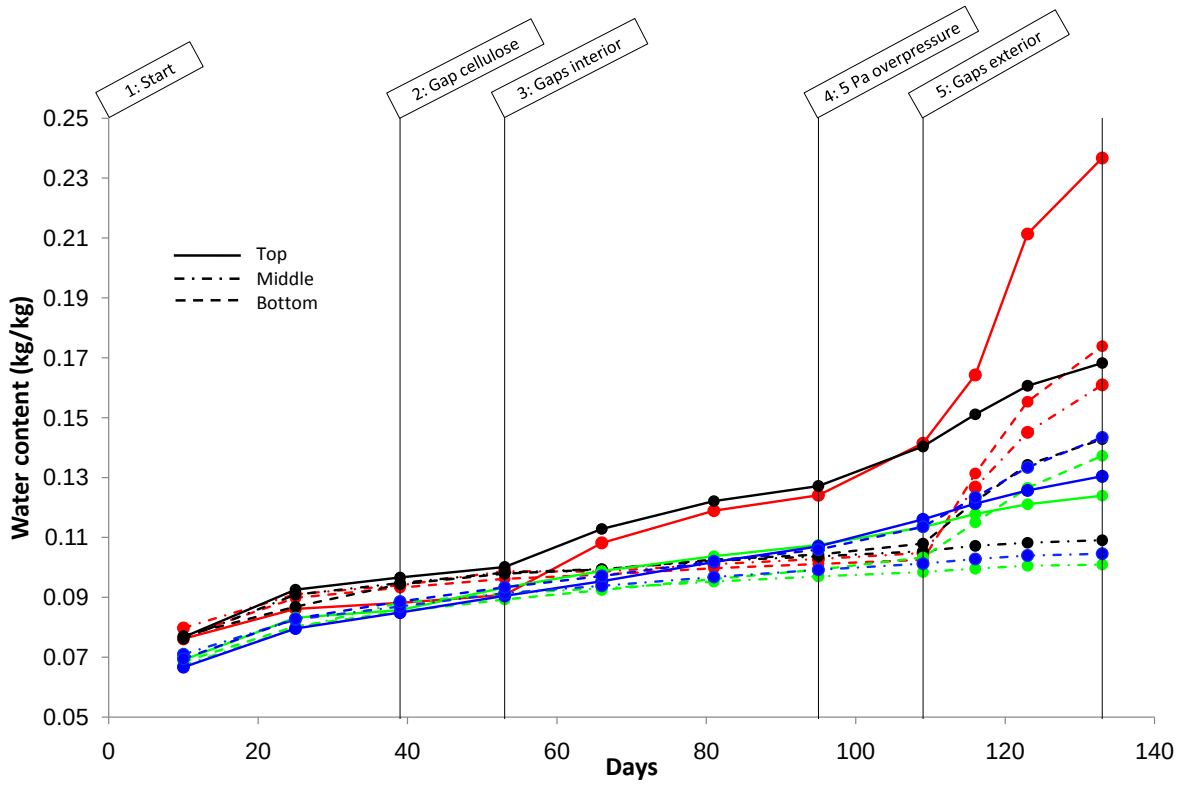

Figure 4.17: Moisture content evolution of weight specimens (IIa (red): MW30 with gap, IIb (black): MW30 without gap, IIc (green):CL60 with gap, IId (blue): CL60 without gap).

in the middle of the wall increased. Water droplets on the exterior sheathing were noticed during the weighing process at the beginning of step 5. After a week this was already evolved into run-off on the weight specimen. In order to inspect the run-off profile of the entire section, the wall was opened at the end of step 5. Figure 4.20 illustrates this run-off profile of condensate as a result of the forced convection conditions. Notwithstanding that higher moisture content levels were measured in Ic, such traces of run-off were not inspected. There, the high moisture contents resulted rather in mould growth on the exterior sheathing. This highlighted the importance of the air flow pattern and the time frame in which the interstitial condensation occurred on the exterior sheathing.
The other three wall sections of test series II were mainly locally affected at the bottom of the wall by the short air flow paths in step 5.

Influence of hygroscopic insulation material

The impact of the hygroscopic sheathing materials have been mentioned before in the discussion of Figure 4.12. A similar advantage was expected in using hygroscopic insulation materials. However, from the relative humidity sensors at the cold side of the insulation layer (for brevity not presented here) this impact seems to be limited. Furthermore, Figure 4.17 demonstrates that the effect of the hygroscopic insulation material was negligible when

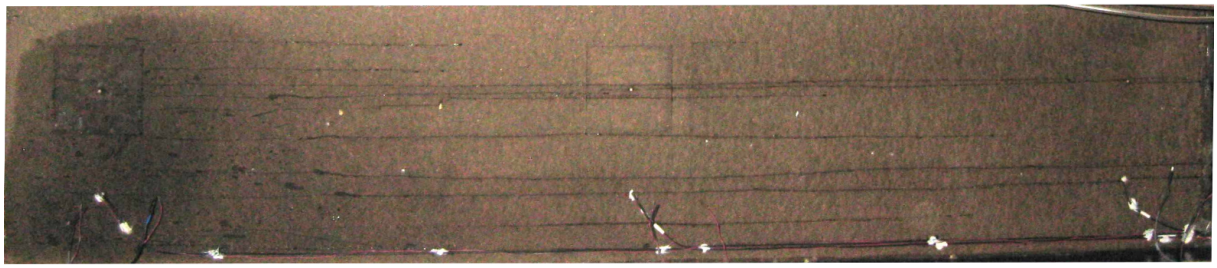

Figure 4.18: Interstitial condensation and corresponding run-off on the exterior air barrier of IIa (figure is rotated 90° counterclockwise).

it came to forced convection conditions. Here, the moisture content at the bottom row (short exfiltration path) showed the same trend for wall IIb (mineral wool) and wall IId (cellulose).

4.2 Onset of condensation on hygroscopic and/or capillary active materials

The full-scale laboratory investigation of the previous section demonstrated that most critical moisture limit state depends on the overall dominating airflow pattern within the component. Wall Ic, which had a rather air permeable exterior sheathing (BIFBII), showed a distributed forced convection profile over the height of the wall. This resulted in mould growth on the exterior air barrier before any traces of condensation were observed. For test wall IIa, however, in which concentrated air leakages were studied, the decisive moisture limit state was interstitial condensation. As a consequence of this observation, both moisture control limit states need to be considered in the hygrothermal analysis of lightweight walls.
Section 2.4.1 provided a brief outline of the current moisture limit states. This overview showed that a substantial amount of research was dedicated to mould prediction models. Regarding interstitial condensation and run-off conditions, however, only a limited number of studies exist. Moreover, when it comes to limit states of interstitial condensation, most often only non-hygroscopic and non-capillary materials are considered.

This section presents laboratory work on the behaviour of surface condensation on hygroscopic and capillary-active materials. The performance of two different materials has been studied: (a) impregnated wood fibreboard (BIFBI) and (b) fibre cement board (FCB). The first, also applied in the hotbox/coldbox investigation of section 4.1, is a highly hygroscopic but non-capillary active material. The latter, however, is both hygroscopic and capillary active. This material is commonly applied as underlay material in Belgian pitched roof systems and its capillary properties are often put forward by its manufactures as a solution to limit the amounts of interstitial condensation.
The aim of this investigation is to obtain more insight in the onset conditions for surface

condensation on these two underlay materials which are frequently applied in Belgium. Furthermore, the obtained data set will be applied in section 6.3.2 to verify the ability to predict the onset of surface condensation by numerical simulations.

4.2.1 Test setup and methodology

A small-scale test setup was designed to create instant condensation conditions. The configuration of the experiment, depicted in Figure 4.19, consists of a cooling element mounted at the back of an open box, constructed with polyurethane insulation panels with a thickness of 4 cm. The test samples are glued against the cooling element and additional silicone is provided around the edges of the specimens to avoid air leakages. A mineral wool insulation layer was placed at the warm side of the specimens to lower its surface temperature. Consequently, the condensation plane shifts to the visible side of the specimen. This 18 cm mineral wool layer was installed in a rectangular tube of rigid polyurethane boards which could easily be slid in the outer box, containing the specimen. In this way the specimens could regularly be checked to determine the onset of interstitial condensation, without affecting the position and density of the mineral wool layer. The test setup was placed in a climate chamber with controlled temperature and relative humidity.

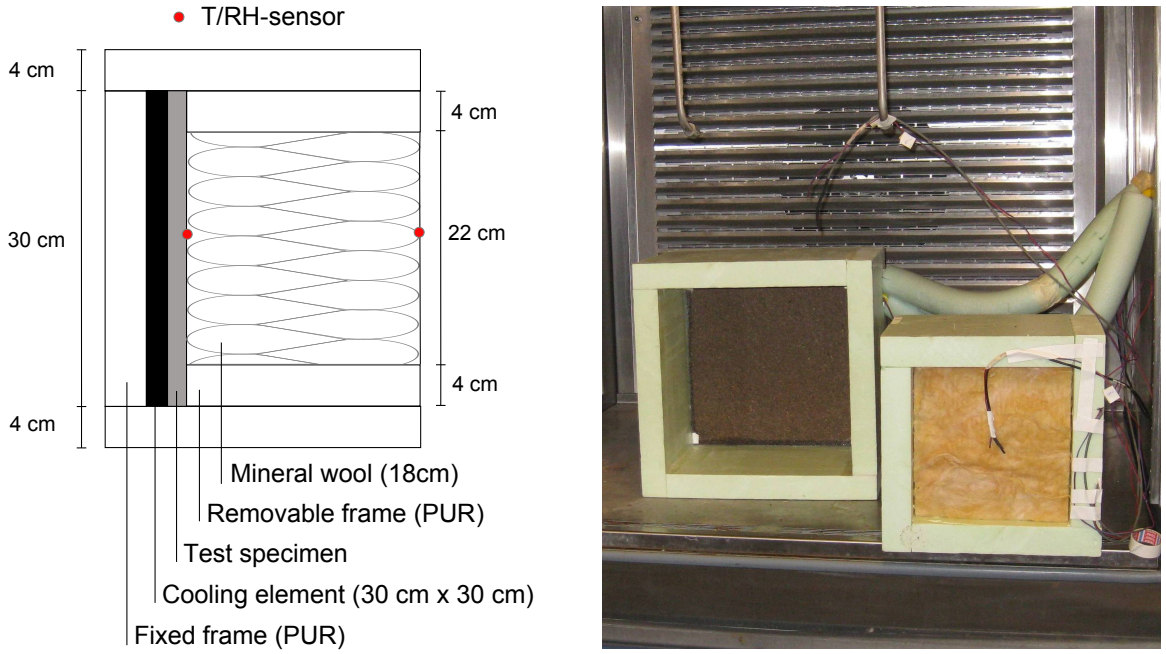

Figure 4.19: Test setup for the examination of the onset of interstitial condensation on hygroscopic and capillary materials.

Two relative humidity sensors and thermocouples[5] were installed in the set-up to monitor the conditions at the interface of the specimen and the mineral wool layer and in the climate chamber (depicted in red in Figure 4.19). The temperature in the climate chamber

[5]see Table 4.4 for specifications

was controlled at 20°C and the relative humidity at 70% or 80%. The cooling element, however, was set at a temperature of 6°C.
In total four runs were performed with this test setup: (a) two tests with BIFBI (18 mm) and (b) two tests with FCB (3 mm). The material properties of the first material are discussed in section 4.1.5. The properties of the latter, will be outlined in section 6.1. To reduce the length of the experiment, the initial moisture contents of the specimens were increased by conditioning them 3 weeks prior to the start of the experiment in a climate chamber with a relative humidity of 86 %.
The onset of interstitial condensation was verified by visual control during the experiment. The climate chamber was opened and the mineral wool layer removed to inspect the specimen. Opening the test setup temporary affects the boundary conditions and was therefore restricted to a minimum. The experiment was finished when the first signs of condensation were observed (Figure 4.20). The drawback of this manual method, however, is that the exact moment of condensation can never be detected. When condensation was detected the experiment was stopped and the specimens were sawn in 16 pieces for the determination of their moisture content.

4.2.2 Results

Figure 4.21 shows the measured relative humidity profiles for all four runs. In addition, this figure includes the measured moisture contents of the specimens at the end of the experiment and the averaged temperature of the condensation plane as well. The figure reveals that condensation first occurs on the FCB specimen. Notwithstanding its capillary-active properties, condensation droplets were already observed within the first two days for both tests with FCB. For the tests with BIFBI, however, the first signs of interstitial condensation were only noticed after 6 days. The observed condensation profiles on BIFBIa and CFBa

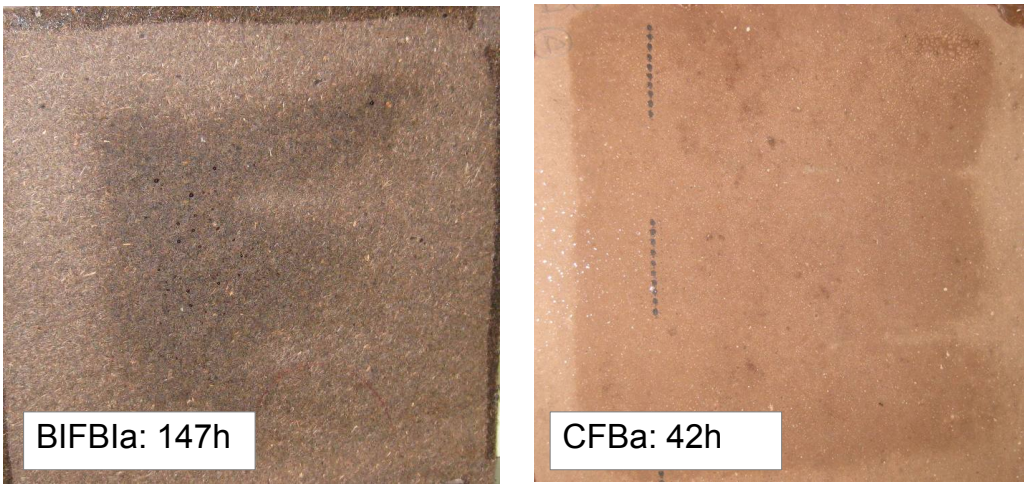

Figure 4.20: Observation of interstitial condensation on bituminous impregnated wood fibreboard (BIFBIa) and cement fibreboard (CFBa).

are depicted in Figure 4.20.

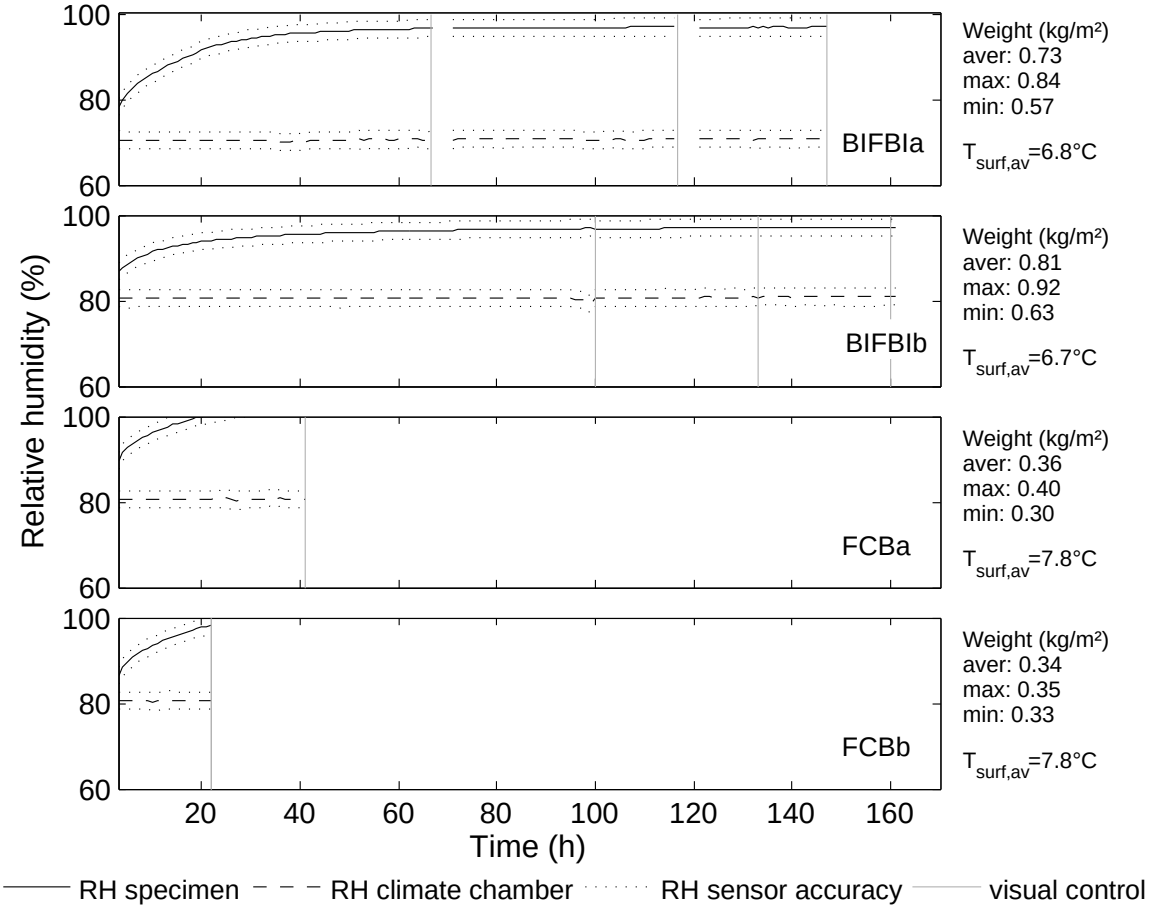

Figure 4.21: Measured relative humidity at the warm side of the specimens and in the climate chamber. Measurements were terminated when condensation was observed.

This experiment demonstrated that the capillary properties of fibre-cement boards, often put forward as a remedy to limit interstitial condensation, have only a limited potential to delay the onset of condensation conditions. In this context the bituminous wood fibreboards, which are non-capillary, outperformed the fibre cement boards. Consequently the moisture contents of the BIFB specimens were significantly higher than the FCB variant at the end of the experiment (Figure 4.21).

4.3 Conclusions

Full-scale experimental work on the hygrothermal behaviour of highly insulated walls with an exterior air barrier have been conducted under laboratory conditions. The results demonstrated an increased level of natural convection within wall elements with discontinuities in the interior vapour barrier. This led to higher moisture loads at the upper cold parts of the walls. The risk for moisture problems was highly dependent on the properties of the

applied materials. The measurements showed that a sufficiently airtight air barrier material is a prerequisite to avoid moisture problems. In this respect BIFB II (0.1 $m^3/(m^2\,h\,Pa)$) obviously failed, resulting in a forced exfiltration flow through the wall, and thus, very high moisture contents of the exterior sheathing. For BIFB I (0.005 $m^3/(m^2\,h\,Pa)$) and FOIL (<0.001 $m^3/(m^2\,h\,Pa)$) this effect was limited to a very minimum. Therefore, it can be concluded that such levels of air permeance are sufficiently low to prevent harmful amounts of forced exfiltration. In addition, the results illustrated the advantage of exterior air barrier materials with a thermal resistance. Also, hygroscopic exterior air barriers showed a better performance as these materials delayed interstitial condensation conditions. Yet the study could not identify the same positive effect for hygroscopic insulation materials. The measurements further revealed that the impact of natural convection on the moisture load can be reduced by applying denser insulation materials. Standard mineral wool in Belgium has a density of 20 kg/m^3. Yet installing mineral wool blankets with a density of 30 kg/m^3 could significantly reduce the moisture load. The study further showed that the installation of blankets is vulnerable for the introduction of small air channels along the insulation layer. Such imperfections along the insulation blankets, which can hardly be avoided in practice, highly increase the potential for natural convection, reducing the advantage of applying higher density insulation. In contrast to the use of insulation blankets, the level of natural convection, and thus, the increased moisture load, became negligible when applying standard blown-in cellulose insulation of 60 kg/m^3. The main origin for this effect can be ascribed to a combination of the higher densities and the close contact between the blown-in insulation and the adjacent layers in these walls assemblies. Even the test wall in which potential settling of the cellulose insulation was taken into account, was not affected. Finally, also the impact of bad workmanship in the exterior air barrier, which resulted in forced convection conditions, was evaluated. The results revealed that in this scenario the obtained air flow paths highly dominated the hygric response. As already numerically predicted by Ojanen & Kumaran (1996), the present measurements confirmed that long air flow paths are most critical. For the hygroscopic sheathing applied (BIFB I), this even led to interstitial condensation and run-off in the wall with improperly installed mineral wool.
The second part of this chapter presented additional small-scale measurements to extend the understanding of interstitial condensation on hygroscopic and/or capillary active exterior air barriers. Two different materials, commonly applied in Belgium, were investigated: (a) bituminous wood fibre board (BIFBI) and (b) fiber cement boards (FCB). In summary, the results indicated that the liquid moisture transport properties of commercially available FCB boards are insufficient to significantly postpone condensation conditions. Moreover, the study illustrated that the non-capillary active BIFB outperformed the FCB when it comes to extending onset conditions for surface condensation.

An additional aim of the full-scale experiments was to collect detailed data for the evaluation of the numerical HAM model in chapter 5. Therefore, several measures were taken in

order to minimise the number of potential uncertainties. Consequently, the measurements are simplifications of real walls which have wooden studs, top and bottom plates and are exposed to real climate conditions. For this reason, it is impossible to conclude to which level exterior air barriers will lead to moisture problems in real situations from these laboratory results only. But, after verification of the numerical model (chapter 5) with the obtained data, chapter 6 will perform a numerical parameter study to investigate this issue based on yearly simulations for real climate conditions.

Model requirements

The laboratory work of this chapter revealed the essential modelling features for a detailed numerical prediction of the hygrothermal performance of lightweight components with an exterior air barrier: (1) Ability to account for **forced and buoyancy-driven air convection** in combination with detailed heat and moisture transport, (2) Implementation of **installation deficiencies** such as small air cavities at material interfaces which largely affected the air flow pattern, (3) At least a **two-dimensional** simulation grid to cover various air flow patterns, (4) Implementation of **liquid moisture transport** for a detailed prediction of mass transport in capillary-active materials such as wood and fiber cement boards, and (5) The necessity of a **transient simulation approach**, exposed to realistic weather conditions.

5

Description and evaluation of numerical Heat, Air and Moisture model[1]

The observations in the previous chapter illustrated the need to consider both natural and forced air convection in combination with detailed heat and moisture transport in predicting the hygrothermal behaviour of lightweight walls with an exterior air barrier. This chapter presents the implementation of a quasi-steady state airflow model in an existing transient heat and moisture model. One particular aim is the prediction of significant effects such as overlaying buoyant and externally driven air flow on the hygrothermal behaviour of building envelope components with sound simulation performances. First, the implementation of the quasi-steady state airflow model will be presented. Second, the model will be evaluated with two benchmark cases from the literature and the experimental data of chapter 4 to show the applicability and limitations of the presented approach. This model will be applied in chapter 6 to assess the hygrothermal performance of lightweight walls with an exterior air barrier under real climatic conditions.

5.1 Introduction

Section 2.3 gave an impression of the large group of existing numerical tools for the hygrothermal simulation of building components. These so-called HAM-models differ from

[1] partially published in Langmans, Nicolai, Klein & Roels (2012)

each other by various assumptions in both the physical description and the numerical implementation. Though the major part of today's hygrothermal building component modelling focusses exclusively on combined heat and moisture transfer, several developed HAM-models have included air transport to some extent. Section 2.3 provided an outline of the different approaches applied to model air transport in combination with heat and moisture transport in building components. Yet it showed that none of the existing HAM-models fulfil the model requirements postulated in section 4.3.

This chapter describes a modelling and simulation approach that tries to bridge the accuracy requirements with acceptable solver performance. The major aim of the method is to present an accurate scheme with reasonable simulation times that can be used to simulate the transient behaviour of lightweight building components for several years.
Given the large number of existing HAM-models and the corresponding acquired knowledge (section 2.3), it was decided to extend a state-of-the-art building component model, rather than developing a new simulation tool. Therefore, air transport was implemented in an existing heat and moisture building component model. The applied model was Delphin 5, developed at the Technical University of Dresden (Grunewald 1997, Nicolai 2007*a*). Section 5.1.1 outlines the motivation for selecting this simulation model.
After the description of the modelling strategy, the main emphasis of this chapter is on the evaluation and applicability of the model. First, the coupling between the heat and air balance equations is evaluated with analytical and numerical results from the literature. Second, the results of the present model are compared with the full-scale laboratory investigations of chapter 4, studying the impact of air convection on the hygrothermal behaviour of timber frame walls.

5.1.1 Delphin framework

The Delphin simulation code is a numerical heat and moisture code, initially developed by Grunewald (1997). The most recent version of this commercial simulation package (Delphin 5) is documented by Nicolai (2007*a*). This version solves the detailed heat and moisture transport in porous building materials according to Hagentoft et al. (2004). In addition, a simplified forced air convection model in the porous domain is included. Yet natural convection, which is an essential transport mechanism within the research project at hand (section 2.3) is not included. Moreover, the calculation domain only contains porous materials, so, the model is not capable of including the effects of small air cavities at material interfaces. Nevertheless, as will be outlined below, Delphin 5 showed to be the most appropriate existing HAM-model to be extended to model the hygrothermal performance of timber frame building components in the present study.

Delphin, developed in C++, is provided with a convenient graphical user interface which enables to create and modify simulation projects within limited time. The source code, which is not public domain, was made available in the framework of this research collaboration, enabling to extend and adjust the code for the current research purposes.
Apart from the availability of its well-structured code, another decisive element in choosing this simulation code is its use of control volume methods (CVM) for spatial discretisation. It is well-known that the numerical methods, used to solve convection-dominated diffusion problems may result in unstable and oscillating solutions when a centered type discretisation is used for the advective terms (Van de Sande et al. 1999). This problem is shared by control volume methods as well as by (Galerkin) finite element methods (FEM). As a result several methods have been introduced in numerical literature to avoid this misbehaviour (Onate & Manzan 2000). For control volume methods these oscillations can be precluded by the straightforward use of upwind schemes for the advective terms. However, the methods to overcome these oscillations for finite element methods are more complex (Onate & Manzan 2000). In this respect the control volume method embedded in Delphin potentially facilitates the implementation of air transport.
Furthermore, the Delphin solver uses an implicit, variable-order, variable-step method (SUNDIALS:CVODE) for the integration in time. As liquid moisture transport, which is a highly non-linear phenomenon resulting in stiff problems (Van Daele 2012), is one of the studied transport mechanisms (section 4.3) in the present work, the use implicit integration methods is essential in obtaining reasonable simulation times (Janssen 2002).
A final reason for selecting the Delphin platform is that its combined heat and moisture transport was already extensively evaluated in the framework of the EU-initiated HAMSTAD-project.

5.2 Principal Model Equations

The first part of this section discusses the complete set of balance and transport equations in porous materials. However, as illustrated in chapter 4, when it comes to air transport in building components the simulation domain can no longer be treated as porous media only. Cracks and small air channels are inevitable in building components and can have a significant impact on its hygrothermal behaviour. To take these imperfections into account a hydraulic network methodology is introduced in the model. This means that the calculation domain is split up in two domains, consisting of porous media and well-defined interconnected air channels. The applied transport equations in and at the interface of these air channels with the porous domain, will be outlined in the second part of the section. Finally, the boundary conditions will be discussed in the third section.

5.2.1 Heat and mass transport in porous building materials

Balance equations in porous media

The physical equations describing the combined heat and moisture transport in multilayered porous building components, documented during the European project HAMSTAD (Hagentoft et al. 2004) are widely accepted and used in various publications (Li et al. 2009, Dos Santos & Mendes 2009, Janssen et al. 2007, Tariku et al. 2010). This set of partial differential equations is also solved in the simulation tool Delphin 5 (Grunewald 1997, Nicolai 2007*a*). For the discussion that follows the conservation equations for energy (Eqn 5.1a) and moisture (Eqn 5.1b) mass are briefly repeated from Nicolai (2007*a*) :

$$\frac{\partial u}{\partial t} = -\nabla\left[q_{cond} + h_v \left(j^v_{diff} + j^v_{conv}\right) + h_w j^w + h_d j^d \right] + \Sigma \dot{u} \tag{5.1a}$$

$$\frac{\partial \rho^{w+v}}{\partial t} = -\nabla\left[j^v_{diff} + j^v_{conv} + j^w \right] \tag{5.1b}$$

$$\varphi \frac{\partial \rho_a}{\partial t} = -\nabla\left(\rho_a v_a\right) \tag{5.1c}$$

Here, u is the energy density (J/m^3), ρ a mass density (kg/m^3), q an energy/enthalpy flux (W/m^2), j a mass flux (kg/m^2/s) and $\dot{u}$ an energy source density (W/m^3). The transport equations for q and j, will be discussed below. The superscripts w, v, a and d indicate liquid water, water vapour, humid air and the dry air components respectively. The subscripts describe the mode of transport through diffusion (*diff*) or convection (*conv*) and h_w, h_v and h_d are the specific enthalpies (J/kg) of the individual components considered. In contrast to liquid water and dry air mass (Eqn. 5.2a and 5.2b), the specific enthalpy of vapour consists of a sensible and latent part (Eqn. 5.2c):

$$h_w = c_w \left(T - T_{ref}\right) \tag{5.2a}$$

$$h_d = c_d \left(T - T_{ref}\right) \tag{5.2b}$$

$$h_v = c_v \left(T - T_{ref}\right) + H_e \tag{5.2c}$$

in which the corresponding levels of heat capacity are $c_v = 1840\,\mathrm{J/(kg\,K)}$, $c_w = 4180\,\mathrm{J/(kg\,K)}$ and $c_d = 1006\,\mathrm{J/(kg\,K)}$, $H_e = 2445\,\mathrm{kJ/kg}$ is the evaporation heat and T is the thermodynamic temperature (K).

The conservation of air mass in the porous medium is given in Eqn. 5.1c according to Nield & Bejan (2006). Here, φ corresponds to the open porosity, ρ_a to the air density and v_a is the average velocity (so-called seepage velocity). For the envisaged applications the transient term on the left hand side of Eqn. 5.1c can be questioned. Including the transient behaviour would allow to simulate the detailed dynamic evolution of the air transport, in direct interaction with moisture and temperature profiles. In this way specific effects such as the influence of air compression on the capillary moisture absorption rate can be cap-

tured (Descamps 1996). However, the main goals of the current air flow implementation is the prediction of the hygrothermal performance of building components over longer periods (up to several years). For such time scales, the mentioned effects become of minor importance. Furthermore, the transient behaviour of air transport in building components is several orders of magnitude faster than these of heat and moisture transport (Hens 2003, p. 103). As a result, the time derivative term in the left-hand side of Eqn. 5.1c can be safely omitted, and thus, air transport in building components can be modelled as a quasi-steady state phenomenon in combination with the transient heat and moisture transport. Hence Eqn. 5.1c simplifies to:

$$0 = \nabla(\rho_a v_a) = \nabla(j_a) \tag{5.3}$$

To increase the simulation performance some assumptions in the air properties can be introduced. The applied simplifications in the calculation of the air density, given in this paragraph, are based on Janssens (1998).
Humid air (a) is treated as a mixture of dry air (d) and water vapour (v) following the ideal gas equation:

$$\rho_i = \frac{p_i}{R_i\ T} \tag{5.4}$$

in which ρ_i represents the density of the component, p_i its partial pressure, R_i its gas constant and T the temperature. Thus, both components share the same volume and temperature of the mixture but have their individual partial pressure. The total pressure of the mixture follows from the sum of the individual components according to Daltons law (Eqn. 5.5):

$$p_a = p_d + p_v \cong p_{atm} \tag{5.5}$$

For building physical applications the fluctuations of the air pressure are negligible against the total air pressure. As a result, a first simplification is to assume that the sum of the partial pressures in Eqn. 5.5 equals the atmospheric air pressure ($p_{atm} = 101325\,\text{Pa}$). Following from the ideal gas law (Eqn. 5.4), the total humid air density can be expressed as the sum of the water vapour density and the dry air density (Eqn. 5.6). This expression is rewritten in Eqn. 5.7 as a function of the total air pressure and the vapour pressure. In hygrothermal processes in building components the second term in Eqn. 5.7 is typically two to three orders of magnitude lower than the first, so the this term can be safely neglected. In this way, the

air density is assumed to depend on the temperature only.

$$\rho_a = \frac{p_a - p_v}{R_d\ T} + \frac{p_v}{R_v\ T} \tag{5.6}$$

$$= \frac{p_a}{R_d\ T} - \frac{p_v}{T}\left(\frac{1}{R_d} - \frac{1}{R_v}\right) \cong \frac{p_{atm}}{R_d\ T} \tag{5.7}$$

Note that, omitting the second term in Eqn. 5.7 results in an increasing error for higher temperatures. However, for a combination of an exceptional high temperature of 50°C and relative humidity of 99 %, the air density is still only underestimated by less than 10 %.

Heat and mass transport equations in porous domain

The heat transport consists of heat conduction and enthalpy fluxes of the mass transport. The latter are already given in Eqn. 5.1a and are therefore not repeated here.The well-known transport equation for heat conduction, following Fourier's law, reads:

$$q_{cond} = -\lambda \nabla T \tag{5.8}$$

in which T the temperature (K) and λ the thermal conductivity (W/mK).
Moisture transport is induced by vapour and liquid water transport. Vapour transport consists of vapour diffusion (Eqn. 5.9a) and vapour convection (5.9b). Liquid water transport, also a convective process, is driven by capillary pressures (Eqn. 5.9c).

$$j^v_{diff} = -\frac{\delta_a}{\mu_{w+v}} \nabla p_v \tag{5.9a}$$

$$j^v_{conv} = \frac{\rho^v}{\rho^a} j^a = \rho^v v_a \tag{5.9b}$$

$$j^w = -K_w \nabla p_c \tag{5.9c}$$

in which δ_a (s) corresponds to the vapour permeability of a motionless air layer, μ_{w+v} (-) refers to the vapour resistance factor of the material and K_w (s) is the materials liquid water conductivity. A detailed description of the heat and moisture transport equations can be found in Nicolai (2007*a*).
The momentum equation in porous media is commonly expressed by the experimentally observed Darcy law (Nield & Bejan 2006):

$$v_a = -\frac{k_a}{\eta}\left(\nabla p_a + \rho_a g\right) \tag{5.10}$$

in which v_a is the seepage velocity, k_a corresponds to the air permeability (m^2), $g = 9.81$ m/s^2 is the gravity acceleration and $\eta = 1.8\ 10^{-5}$ Pa.s represents the dynamic viscosity. This phenomenological approach which neglects non-linear effects is justified for sufficiently low seepage velocities v_a. In this context, "sufficiently" small means that the Reynolds number

Re_k of the flow, based on the square root of the permeability is of order unity or smaller Nield & Bejan (2006):

$$Re_k = \frac{v_a\sqrt{k_a}}{\nu} < 1 \tag{5.11}$$

where ν represents the kinematic viscosity. In this regime the viscous force dominates over the inertial force, so, only the local geometry or pore structure influences the flow behaviour. For most air permeable building materials, such as mineral wool (see Table 4.7), the square root of the air permeability ($\sqrt{k_a}$) has the same order of magnitude of the kinematic viscosity ν. This means that external pressures up to more than 100 Pa are needed to exceed the criterion of Eqn. 5.11. Consequently it can be stated that for building physical applications Re_k is far below this criterion, justifying the use of Darcy flow in the porous domain.

5.2.2 Heat and mass transport in air channels

Cracks and small air channels between material interfaces are inevitable in building components and can have a great impact on their behaviour, as illustrated by the laboratory experiments in chapter 4. Therefore, the calculation domain was extended with air channels to model such imperfections around the porous materials. Air channels are introduced as a hydraulic network, assuming fully-developed laminar flow between parallel plates. These so-called Hagen-Poiseuille conditions are of course a simplification of reality. However, as air leakages in building components are unintended and can only be estimated roughly, it can be stated that this linearised approach is sufficient to evaluate the impact of air leakages on the hygrothermal behaviour of building components. This simplified method is used by various authors in the field of building physics such as Lecompte (1989), Kronvall (1980), Hagentoft (1991), Kohonen (1984), to describe combined heat and convection problems. The current implementation, presented in this section, is adopted from Janssens (1998) in which this methodology was extended with convective vapour transport in the numerical model 2DHAV.

Air transport in the air channels

Air transport in the channels is modelled as uni-directional flow between parallel plates. This means that the state variables inside the channels will be solved (see Figure 5.1) by mean of their averaged value across the channel width. The parabolic velocity profile corresponding to Hagen-Poiseuille's law are expressed as an averaged velocity in the air channel ($\overline{u}_a$) which is proportional to the pressure drop per unit length in the flow direction

(Bejan 2004):

$$\overline{u_a} = \frac{D^2}{12\eta}\left[-\frac{\partial p_a}{\partial x}\right] \tag{5.12}$$

The Hagen-Poiseuille law assumes laminar and fully-developed flow in the air channels. The first condition only applies for sufficiently low air velocities. Generally this corresponds to Reynolds numbers based on the hydraulic diameter (Re_{D_h}) lower than 2000. The second conditions requires the air leakage path to be sufficiently long to reach fully-developed conditions (Bejan 2004):

$$L > 0.05 \cdot Re_{D_h} \cdot D \tag{5.13}$$

Threshold velocity values for laminar flow conditions in, for example, an air channel of 5 mm are in the range of 3 to 4 m/s, which is typically one or two orders higher than the expected air velocities within these walls (see Figure 5.10). Entry lengths for such flow conditions are in the range of 50 cm, so, the channels are sufficiently long to reach fully-developed conditions for velocities of one or two orders of magnitude smaller. As a result, it can be stated that these two criteria generally hold for the wall configuration studied in this work.

In addition, it should be noted that no local losses are taking into account in this hydraulic network approach here. As stated by Janssens (1998), however, air leakages in building enclosures are unintended and the width of air gaps can only be estimated roughly. As a consequence, Janssens (1998) claimed that assuming laminar fully-developed conditions is a sufficient approximation to assess the effects of air leakages in building envelope systems.

Energy and moisture transport in air channels

The considered heat transport inside the air channels is subdivided in three components: (1) a longitudinal component in the air channel, (2) transverse component exchanging heat between the air channel and the porous medium and (3) a radiative term between the channels walls:

$$q_x = -\lambda_a \frac{\partial T_m}{\partial x} + \left(\frac{\rho_d}{\rho_a}.\overline{u_a}\right).h_d + \left(\frac{\rho_v}{\rho_a}.\overline{u_a}\right).h_v \tag{5.14a}$$

$$q_y = \alpha_{h,c}\left(T_{int} - T_m\right) + \rho_d.h_d.v_{int,d} + h_v.j_{v,y} \tag{5.14b}$$

$$q_{rad} = \frac{\sigma\left(T_{int,1}^4 - T_{int,2}^4\right)}{\frac{1}{e_1} + \frac{1}{e_2} - 1} \tag{5.14c}$$

which are illustrated in Figure 5.1. The longitudinal component q_x consists of a conductive and a convective term along the channel. In the latter, the specific enthalpies are calculated

from the mean temperature in the channel (so-called bulk temperature T_m). The transverse component, q_y, includes the convective heat exchange between the air mixture and the porous media and a convective term as result of the air mass transfer at the interface between the porous media and air channel. The convective heat exchange is expressed by means of a heat transfer exchange coefficient $\alpha_{h,c}$. This exchange coefficient depends on the Nusselt number and the width of the air channel:

$$\alpha_{h,c} = \frac{Nu.\lambda_a}{D/2} \tag{5.15}$$

Nusselt numbers for fully-developed laminar flow between infinite parallel plate are independent of the air velocity and can be found in various textbooks on fundamental heat transfer, such as Bejan (2004). Recalculated to match its expression in Eqn. 5.14b, Nu is 1.9 for a uniform surface temperature and 2.1 for uniform surface heat flux conditions. For the current purpose, Nu will vary between these two values and consequently Nu $\simeq$ 2 is assumed here.

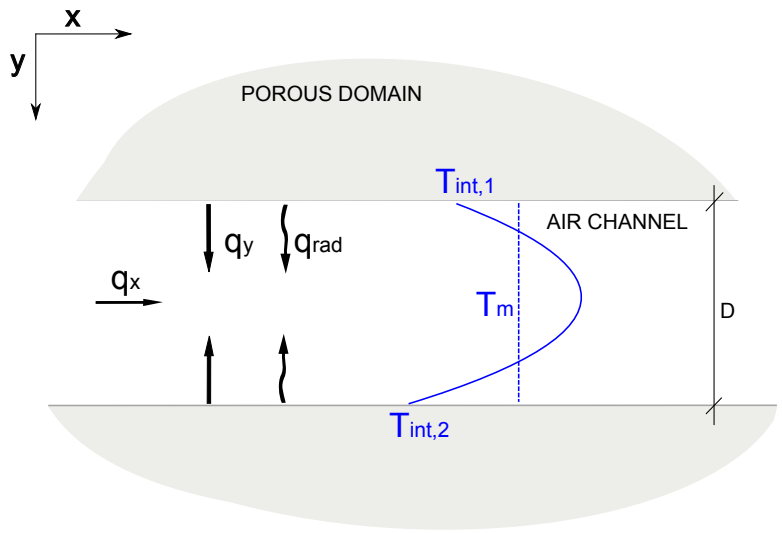

Figure 5.1: Heat transfer inside air channels and at interfaces with porous medium (Janssens (1998)).

The third component includes the radiative heat transfer between the opposite interfaces of the air channel and the porous medium. This process is expressed by the well-known Stefan-Boltzmann's law in which the radiation is linear to the difference of the fourth power of temperatures at the interfaces. Here, σ represents Stefan-Boltzmann constant ($5.7\,10^{-8}$ W/(m^2 K^4)) and e the surface emittance which is around 0.9 for most building materials.

Vapour transport in air channel and at the interfaces of the porous domain can be expressed in a similar way as the heat transport above:

$$g_{v,x} = -\delta_a \frac{\partial p_v}{\partial x} + \rho_{v,m} \overline{u}_a \tag{5.16a}$$

$$g_{v,y} = \beta_{v,c}(p_{v,int} - p_{v,m}) + \rho_{v,int} v_{int,a} \tag{5.16b}$$

Again the subscripts int and m refer to the properties at the interface and the averaged properties in the air channel respectively. The vapour transfer coefficient $\beta_{v,c}$ can be written as a function of the heat transfer coefficient α_c (Hens 2003), and thus, with the relation of Eqn. 5.15 as a function of the Nu:

$$\beta_{v,c} = \alpha_{h,c} \frac{\delta_a}{\lambda_a} = \frac{Nu.\delta_a}{D/2} \tag{5.17}$$

5.2.3 Boundary conditions

This section gives a brief overview of the boundary conditions implemented in the Delphin simulation platform. Heat transport at the exterior boundary (Eqn. 5.18) consists of an imposed heat flux in which convective heat transfer, long-wave radiation, solar radiation and the enthalpy fluxes corresponding to rain and convective air transport can be considered. Heat transfer at the interior boundary consists of a convective and long-wave radiation component imposed by a transfer coefficient (Eqn. 5.19). In addition, the enthalpy fluxes of convective air transport are taken into account as well:

$$q_e = \alpha_{h,ce}(T_e - T_{se}) + \alpha_{sw} q_{sw} + q_{lw} + h_w j_{rain} + h_d j^d_{conv} + h_v(j^v_{conv} + j^v_{diff}) \tag{5.18}$$

$$q_i = \alpha_{h,i}(T_i - T_{si}) + h_d j^d_{conv} + h_v(j^v_{conv} + j^v_{diff}) \tag{5.19}$$

in which $\alpha_{h,i}$ is the interior heat exchange coefficient (W/(m^{2}K)), including both convective and long-wave radiation. T_i and T_{si} are the interior air and interior surface temperature respectively (K), $\alpha_{h,ce}$ is the exterior convective heat exchange coefficient (W/(m^{2}K)), α_{sw} is the absorption coefficient for short wave radiation (-), q_{sw} the short-wave radiation heat flux normal to the component (W/m^2) and q_{lw} refers to the long wave radiation heat flux (W/m^2). In addition, the enthalpy flux corresponding to convective air transport, vapour diffusion and liquid uptake as a result of rain are included at the boundaries as well. More details on the boundary radiation heat fluxes can be found in section 6.2.1.

Surface air pressures are used as boundary conditions for air transport. The driving forces for air flows through building enclosures are mechanical ventilation, stack effect and wind pressure. Consequently, these three phenomena determine the interior (Eqn. 5.21)

and exterior (Eqn. 5.20) boundary conditions of building components.

$$p_e(z) = p_{e,ref} + \rho_e g\ (z_{ref} - z) + C_{p,e}\frac{\rho_e v^2}{2} \tag{5.20}$$

$$p_i(z) = p_{i,ref} + \rho_i g\ (z_{ref} - z) + \Delta p_{mech} + C_{p,i}\frac{\rho_i v^2}{2} \tag{5.21}$$

p corresponds to the total air pressure (Pa) in which for brevity index a is omitted here. Inner boundary conditions are indicated with index i and the exterior conditions are defined by index e. The first term corresponds to the reference pressure. The second term refers to the hydrostatic pressure in which g refers to the gravity acceleration. Pressure differences induced by mechanical ventilation are defined by Δp_{mech}. The last term in both the interior and the exterior pressure condition corresponds to wind pressure differences. Here, C_p is the surface wind pressure coefficient and v the local wind velocity (m/s).

Moisture exchange at the exterior boundary is defined by an imposed moisture flux in which convective vapour transfer and wind-driven rain are considered (Eqn. 5.22). Moisture flow at the interior boundary is imposed by a vapour transfer coefficient only (Eqn. 5.23):

$$j^{v+w}_{diff,e} = \beta_{v,e}(p_{v,i} - p_{v,si}) + j_{rain} \tag{5.22}$$

$$j^{v}_{diff,i} = \beta_{v,i}(p_{v,e} - p_{v,se}) \tag{5.23}$$

in which β_v corresponds to the vapour transfer coefficients, p_v and $p_{v,s}$ to the air and surface vapour pressures respectively and j_{rain} includes the moisture flow corresponding to wind-driven rain. The latter is limited to saturation conditions in the boundary layer and no run-off is included in the model. More details on the boundary conditions can be found in Nicolai (2007*b*).

5.3 Numerical implementation of the quasi-steady state air flow transport

5.3.1 Spatial discretisation

First, the system of partial differential equations (PDE) is transformed into a set of ordinary differential equations (ODE) through spatial discretisation. The Control Volume Method (CVM) is used and the computational domain is subdivided in a number of elements resulting in discrete balance equations for all elements. The flux terms are discretised by using central-difference approximations for the diffusion terms and upwind schemes for the convective terms. For example, suppose the left neighbour of element i is the element $i-1$ along the x-axis of a porous medium which is discretised in one direction, with Δx_i and Δx_{i-1} as the respective element widths. The discretised forms of the heat conduction and

enthalpy convection flux across interface $A_{L,i}$ between elements $i-1$ and i are given in Eqn. 5.24 and 5.25, respectively.

$$(q_{cond})_{L,i} = -\lambda_{L,i} \frac{T_i - T_{i-1}}{0.5\,(\Delta x_{i-1} + \Delta x_i)} \tag{5.24}$$

$$\left(h_d j^d\right)_{L,i} = \begin{cases} (h_d)_{i-1} j^d & j^d > 0 \\ (h_d)_i j^d & j^d \leq 0 \end{cases} \tag{5.25}$$

In which the thermal conductivity λ is averaged using harmonic distance-weighted averaging between the elements which is again indicated through the subscript L, i.
The analogy between the linear airflow equations in the porous domain (Darcy flow) and the fully-developed laminar airflow in the air channels (Hagen-Poiseuille flow) allows to solve both domains within the same system. From the solution point of view, no distinction is made between the air channels and the porous domain. The only differences between both domains lie in the applied transport equations and the restrictions in the spatial discretisation. The first refers to the different heat and mass transport equations in and at the interface between the air channels with the porous domain, which is outlined in section 5.2.1 and 5.2.2. The second difference is related to the spatial discretisation of the air channels. The control volumes in the air channels need to have the same width as the channel in which the state variables are treated as an averaged value across the width of the channel (see section 5.2.2). As the spatial discretisation is limited to control volumes, this implies a restriction of the spatial discretisation in the porous zones located in line with an air channel. Figure 5.2 shows an example of the spatial discretisation at the interface of an air channel to illustrate its interaction with the porous domain. This figure demonstrates

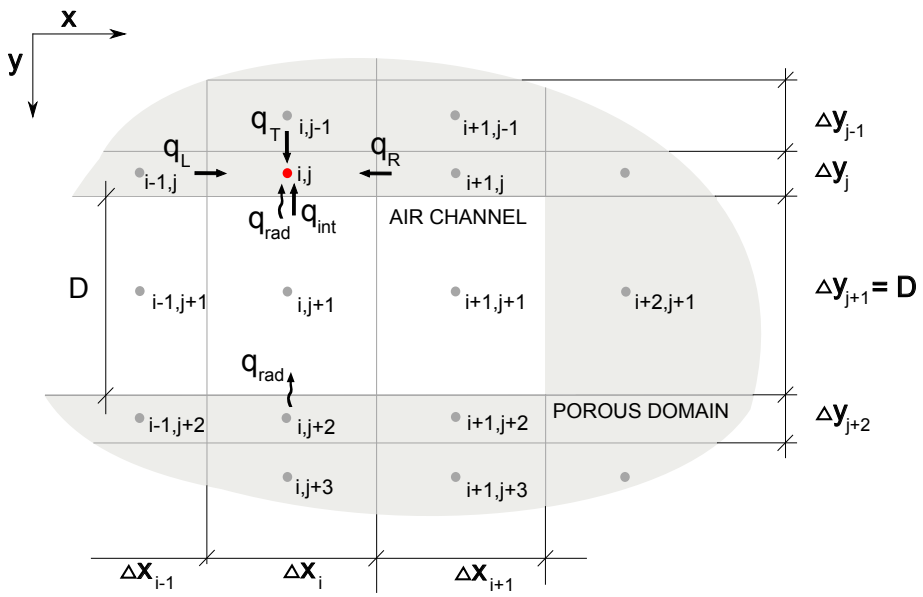

Figure 5.2: Spatial discretisation at the interface between porous domain and air channels.

that the spatial discretisation of element i+2,j+1 is restricted to the width of the channel (D) in the y-direction.
To clarify the integration of the hydraulic network approach of Janssens (1998) in Delphin, Figure 5.2 illustrates the heat balance for a control volume at the interface of the porous medium and an air channel. Vapour transport at these interfaces is similar and therefore not explicitly discussed here. The discretised heat balance equation for this element with index i,j is given below:

$$\frac{\partial u_{i,j}}{\partial t} = \left[\Delta y_j (q_L + q_R) + \Delta x_i (q_T + q_{int} + q_{rad})\right]_{i,j} \tag{5.26}$$

In which the heat fluxes in the porous domain (L=left, T=top and R=right) are:

$$q_{L,T,R} = (q_{cond} + h_d j^d)_{L,T,R} \tag{5.27}$$

Here the conduction heat flux is discretised by using central-difference approximations and the convective heat flux with upwind schemes as explained in Eqn. 5.25 and Eqn. 5.24.
A similar formulation holds at the boundary towards the air channels. Only the conductive term differs as it consists of the heat resistance of the boundary layer and the resistance of the porous material:

$$q_{int} = \left(\frac{1}{\alpha_{h,c}} + \frac{0.5\Delta y_j}{\lambda_{i,j}}\right)^{-1} (T_{i,j+1} - T_{i,j}) + (h_d j^d)_{int} \tag{5.28}$$

In addition this element (i,j) exchanges radiation heat with the element on the opposite side of the air channel (i,j+2). The implementation of the radiation heat in the channels is simplified in that (1) the surface temperature in the air channels is assumed to be equal to the temperature of the adjacent porous elements ($T_{i,j}$ and Ti,j+2), (2) only radiation between opposite elements is taken into account and (3) Stefan-Boltzmann law is linearised according to Hens (2003):

$$q_{rad} = \frac{\sigma(T_{i,j+2}^4 - T_{i,j}^4)}{e_1^{-1} + e_2^{-1} - 1} \simeq \frac{\sigma 4 T_{avg}^3 (T_{i,j+2} - T_{i,j})}{e_1^{-1} + e_2^{-1} - 1} \quad with \quad T_{avg} = \frac{T_{i,j+2} + T_{i,j}}{2} \tag{5.29}$$

As a consequence, radiation inside the air channel is included as source and sink terms into the general formulation of the matrix solution.

5.3.2 Integration in time

With all spatial gradients replaced with finite difference approximations of the transient heat and moisture balance equations, an ordinary differential equation system (ODE) is obtained. With the solution vector written as $y = \{u, \rho^{w+v}\}$, this system can be formally

written as Eqn. 5.30:

$$\dot{y} = f(y, t) \tag{5.30}$$

in which $\dot{y}$ represent the time derivatives of the solution vector. In the current version of Delphin this system of combined heat and moisture transport is solved using a Newton-Raphson iteration method implemented in the generic ODE-solver from the SUNDAILS solver package (Hindmarsh 2005). The implementation of this generic multi-step solver in the Delphin framework is extensively documented in Nicolai (2007*a*). However, since the air mass balance equation is simplified to a steady state formulation, its discretised form can not be included in the general form of Eqn. 5.30. Therefore, this set of linear equations is solved separately from the coupled transient heat and moisture transport. In this respect the quasi-steady state implementations means that during integration of the coupled energy and moisture balance equations, the air flow field is kept constant. At defined time intervals a new steady state solution of the air flow field is calculated and used during the continued integration of heat and moisture balances as depicted in Figure 5.3.

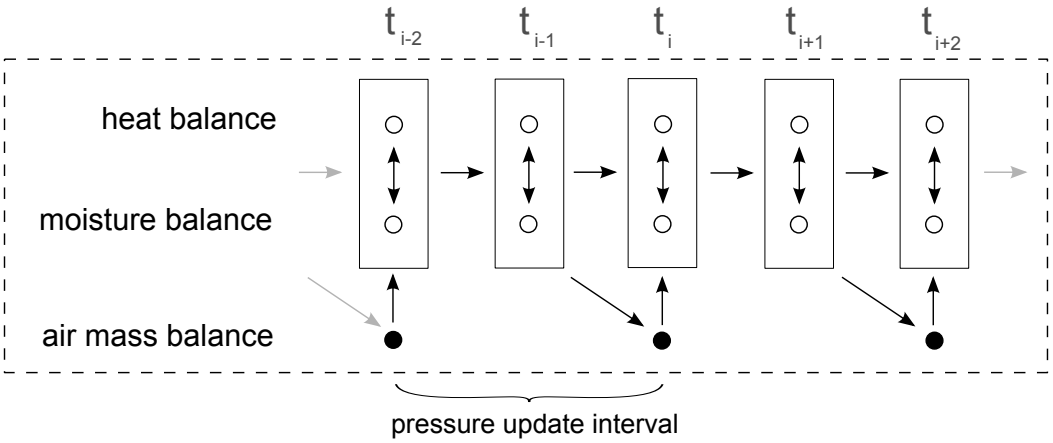

Figure 5.3: Integration schematics for computation of quasi-steady state air flow field and transient energy and moisture balances.

For forced convection scenarios, the air flow field is largely depending on the change of boundary pressures, which are commonly available as hourly weather data. The air flow field changes only very rapidly within the first few seconds after a new pressure condition is applied. For the remainder of the hour it will remain almost constant. As a result, a steady state air flow field can be calculated whenever boundary pressures change and be kept constant during the calculation of energy and moisture balance. This calculation method essentially decouples air balance from energy and moisture balances which improves simulation performance significantly. This assumption is relevant for forced convection scenarios because there is no direct coupling term between the air and heat balance equations (Eqn. 5.3 and Eqn. 5.1a). However, when applying this method to buoyancy dominated sim-

ulation problems, the pressure field becomes affected by the temperature distribution as the density in the second term of the right hand side of Eqn. 5.10 couples the energy and air mass balance equations. Given the decoupled solution method, it is advised to increase the frequency of air pressure calculations, so it will be updated after each time step of the integration of the heat and moisture balance equations. This will be addressed more in detail and illustrated with an example in section 5.4.2. In order to investigate the applicability of the proposed integration strategy, the second part of this chapter mainly focusses on the accuracy of simulating heat and moisture transport in combination with overlaying natural convection.

5.4 Evaluation of the model

The current section confronts the numerical simulation tool with analytical, numerical and laboratory results. The combined heat and moisture transport of the model (Delphin 5) is already extensively evaluated in the framework of the EU-initiated HAMSTAD (Heat, Air and Moisture Standards Development) project (Hagentoft 2002, Li et al. 2009, Tariku et al. 2010). As a consequence, the main focus of the present evaluation is on the impact of air convection on the heat and moisture transport. Particular interest lies on the effects of natural convection, as this implies a coupling between the heat and air balance equations through the density of air (second term in Eqn. 5.10). Therefore, the first two benchmark cases study free heat convection in porous media. The first example focusses on steady state conditions, while the second evaluates the prediction of transient conditions. In a final step the model is compared with the laboratory results of chapter 4, studying the effects of air convection on the hygrothermal behaviour of timber frame walls.

5.4.1 Steady state natural convection in porous media

The first test case investigates two-dimensional steady state natural convection through a vertically and horizontally positioned insulation layer. This topic is well-documented in the literature by theoretical and experimental results in the field of building physics, such as (Klarsfeld & Combarnous 1980, Powell et al. 1989, Silberstein et al. 1990). Consequently, the thermal performance of a porous insulation layer is a straightforward first step in evaluating the model. This configuration, investigated by Kohonen et al. (1985) and also applied and documented by Janssens (1998), consists of an anisotropic glass fibre layer of 2.2 m by 0.3 m. The imposed interior surface temperature is 20°C and the exterior surface temperature is -20°C, resulting in a temperature difference ΔT of 40°C across the wall. A hydrostatic pressure along both the exterior and interior boundary is assumed. The warm surface is supposed airtight, while the cold surface is either airtight or air permeable. Both short boundaries are adiabatic and impermeable. As a result of internal buoyancy, ad-

ditional heat losses occur as function of the air permeability of the insulation layer. The Nusselt number (Nu) quantifies this effect as the ratio of the heat loss through the structure to the total heat loss by conduction only (Eqn. 5.31). Figure 5.4 plots the computed Nusselt numbers as function of the dimensionless Darcy-modified Rayleigh number (Ra_D), which includes the anisotropicity of the material (Klarsfeld & Combarnous 1980):

$$Nu = \frac{Q_{tot}}{Q_{cond}} = \frac{Q_{tot}}{H\Delta T(\lambda_x/D)} \tag{5.31}$$

$$Ra_D = g\beta D\Delta T\Big(\frac{\rho c}{\nu}\Big)\frac{k_x}{\lambda_x}\frac{4a_k}{(\sqrt{a_\lambda}+\sqrt{a_k})^2} \tag{5.32}$$

in which Q_{tot} represents the total heat flux through the porous layer as a result of both conduction and natural convection, Q_{cond} is the heat flux including conduction only, H and D are the height and width of the layer. Furthermore β represents the thermal expansion coefficient of air ($3.7\,10^{-3}$ 1/K), ν the kinematic viscosity of air ($1.4\,10^{-5}$ m^2/s), k_x is the air permeability (m^2) in the x-direction and $a_k = 1.875$ and $a_\lambda = 1.021$ are the anisotropicity ratios of the air permeability and the heat conductivity respectively. Simulations are performed using an equidistant 20 by 20 grid.

The current model has been evaluated for both the vertical and horizontal porous layer. The simulations are conducted with the cold surface either permeable or impermeable. Figure 5.4a shows the results of the vertical layer and compares it with the analytical solution of Weber (1975) and the numerical results of Janssens (1998). The results show good agreement between the different models and the analytical solution.

Figure 5.4b summarises the results of the simulation of the horizontal layer heated from below. In contrast to the vertical insulation layer, the heat flux only starts to increase when a critical Ra_D is reached. For impermeable surfaces the critical Ra_D is $4\pi^2 \approx 39.5$, for a permeable cold surface and a isotropic media this threshold value is 27.1 (Bejan 2004). Buoyancy loops (known as Bénard-cells) develop above these critical Ra_D-numbers, resulting in an increased heat flux. Figure 5.4b shows that the critical Ra_D-numbers, predicted with the present model, are consistent with the theoretical values from the literature. In addition this figure shows that the simulations with both surfaces airtight are in good agreement with the analytical solution of Bories (1987) and the numerical results of Janssens (1998). The same applies for the results of the anisotropic and isotropic variants of the permeable cold boundary which are only compared with the results of Janssens (1998).

5.4.2 Transient free convection in a cavity filled with a porous medium

The previous benchmark showed the models capability of predicting free convection in a vertical and horizontal porous layer under steady state conditions. However, since the heat and air equations are basically decoupled in the presented model, main emphasis lies on

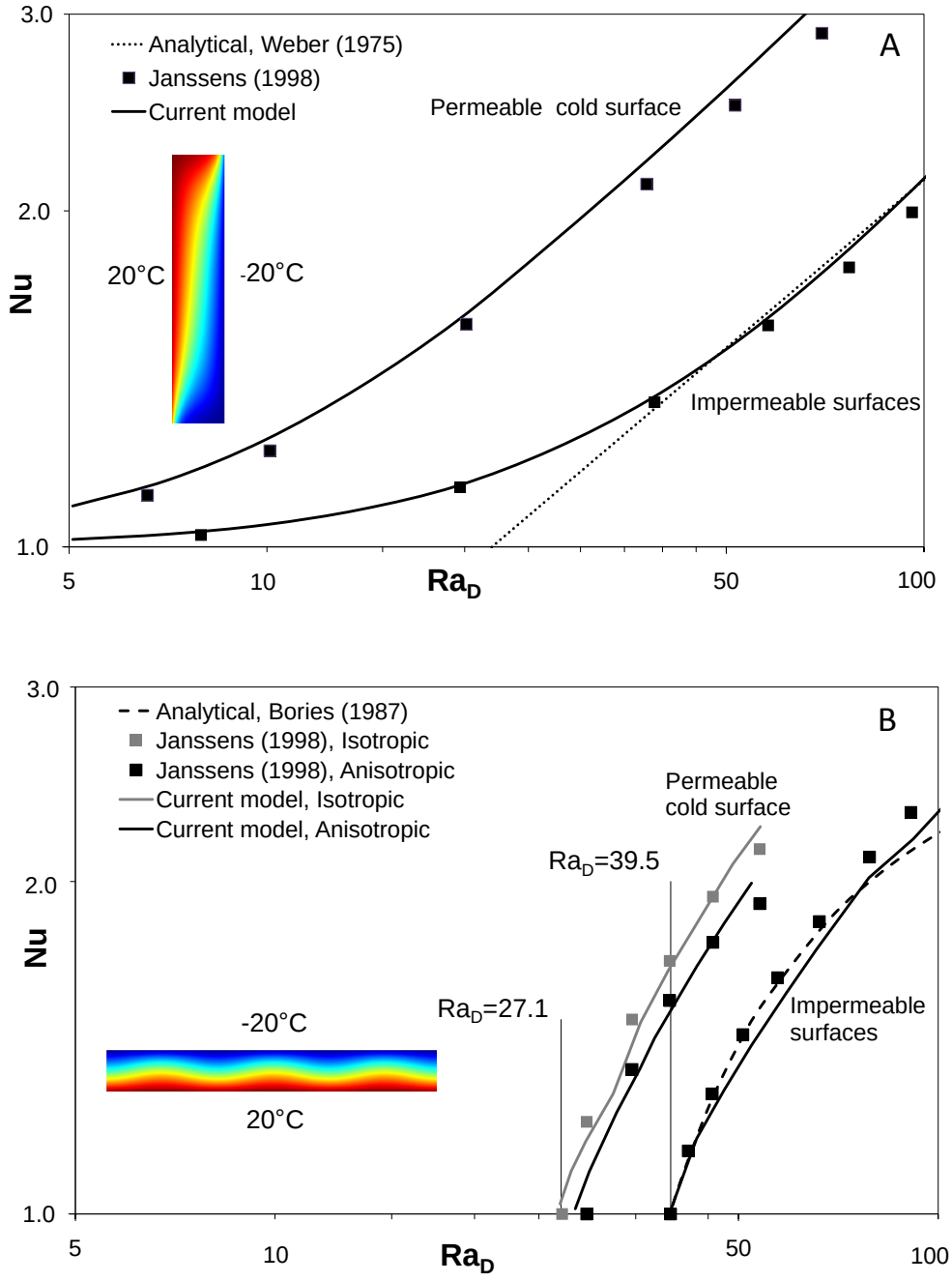

Figure 5.4: $Nu(Ra_D)$ relationship for (a) vertical insulation layer and (b) horizontal insulation layer.

the reliability of predicting transient conditions. As a logical next step, the current section investigates the model's ability to capture transient free convection. Detailed studies regarding transient natural convection are scarce, if not nonexistent in the field of building physics. As a consequence a more general reference study from the field of heat and mass transfer described by Saeid & Pop (2004) is selected first. This evaluation case corresponds to an abstract configuration instead of a typical building component. For the purpose of examining the transient behaviour of natural convection in a porous media, however, this is of

minor importance.
The second part of this section illustrates the impact of the frequency of the air flow field updates (see Figure 5.3). This will be investigated based on the vertical insulation layer of the previous caste study, but exposed to a fluctuating boundary temperature.

Description of the project Saeid & Pop (2004) studied transient free convection in a two-dimensional square cavity (side = L) filled with an isotropic porous medium (Figure 5.5). The initial uniform temperature of the cavity is $T_0 = (T_h + T_c)/2$. The left vertical wall is suddenly heated to a constant temperature T_h, while the right wall is cooled to a constant temperature T_c by equal amount relative to the initial temperature. Both horizontal walls are adiabatic. Saeid & Pop (2004) rewrote the governing equations in a non-dimensional form, which were then numerically solved with a control volume method based on convection-diffusion formulation of Patankar (1980).

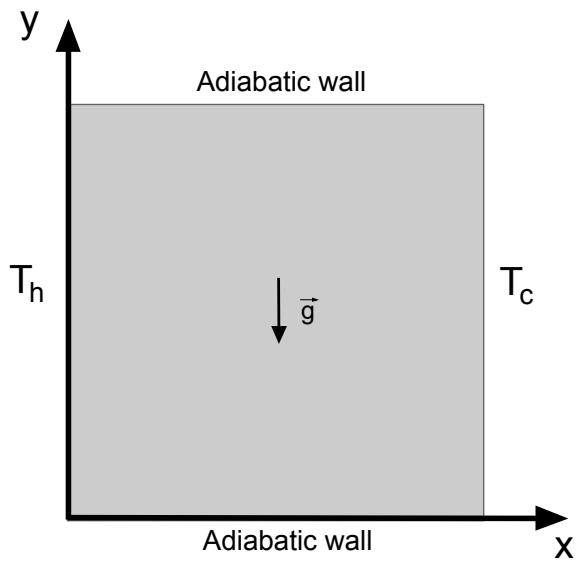

Figure 5.5: Configuration of the physical model and coordinate system (Saeid & Pop 2004).

The physical quantity of interest is the average Nusselt number ($\overline{Nu}$) along the warm wall as a function of the non-dimensional time τ (-), defined by:

$$\overline{Nu} = \int_0^1 (-\frac{\partial \theta}{\partial X})_{X=0}\, dY \qquad \text{with} \quad X = \frac{x}{L}, Y = \frac{y}{L} \tag{5.33}$$

$$\tau = \frac{\lambda t}{\rho c \xi L^2} \tag{5.34}$$

in which ξ, (-) corresponds to the ratio of the composite material heat capacity to the convective fluid heat capacity.

Simulation set-up and numerical results In order to simulated the discussed dimensionless case study, it is necessary to define its size and to assign material properties and

boundary conditions. The sides of the cavity are assumed to be 1m and standard mineral wool (λ=0.035 W/(m² K), ρ=20 kg/m³ and c = 840 J/(kg K)) is ascribed to the porous medium. In accordance with the validation project the porous medium is isotropic. The hot wall has a temperature of 10°C and the cold wall has a temperature of -10°C. The air permeability k is 6 10^{-8} m², so, the current configuration corresponds to a Rayleigh number of 100. Saeid & Pop (2004) gave the results for Rayleigh numbers ranging from 100 to 10 000. However, the maximum order of magnitude of Rayleigh numbers of building components is around 10. Consequently, the lowest Ra-number available in the benchmark of Saeid & Pop (2004) (Ra = 100) is chosen. This is still one order of magnitude higher, so, if the present model satisfies this benchmark, it can be safely used for lower Rayleigh numbers as well.

In accordance with Saeid & Pop (2004) a non-uniform grid of 41x41 elements is used such that the grid points are clustered near the walls. Furthermore, it is important to notice that the air flow calculation was updated after each time step of the integration of the heat balance equation. Figure 5.6 compares the simulation results of the present model with the results of Saeid & Pop (2004). The figure shows that the model is in very good agreement with the benchmark results, meaning that the decoupled integration strategy is capable of capturing transient free heat convection. Next section investigates the importance of the update intervals of the airflow field and illustrates the simulation performance of the present model for a more realistic configuration.

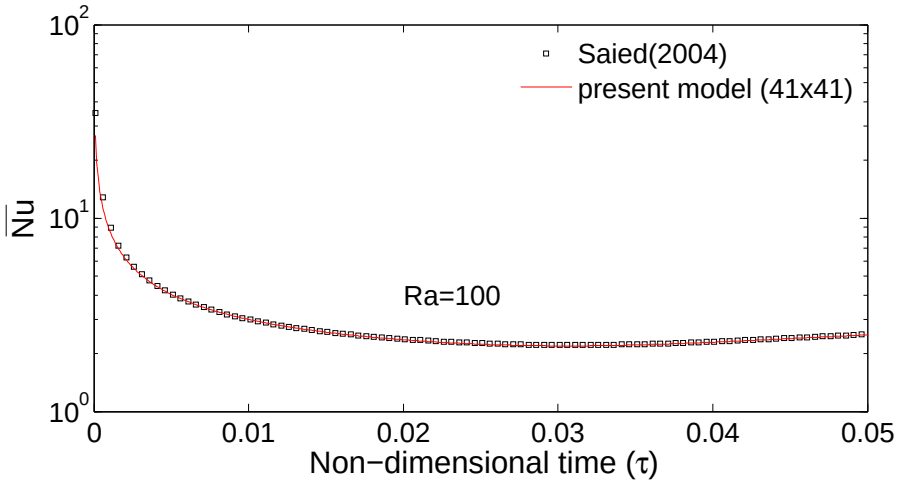

Figure 5.6: Evolution of the transient average Nusselt number ($\overline{Nu}$) as a function of the dimensionless time (τ) for Ra=100.

Pressure update intervals and simulation performance The current section investigates the impact of the pressure field update interval during the integration of the heat balance equation (see Figure 5.3). The configuration applied in this study corresponds to the vertical insulation layer of section 5.4.1. Instead of a constant exterior temperature, however, a cosine function with a period of one day, an amplitude of 10°C and a mean

value of -10°C is imposed. The interior temperature, on the other hand, is kept at 20°C and the initial temperature is also 20°C. The temperatures are imposed as surface values and both sides are assumed airtight. Furthermore, the same mineral wool of section 5.4.2 is used for the simulation. Only the air permeability of the insulation layer (k_x) was adjusted to $3.6\,10^{-8}$ m^2, so, that the Darcy-modified Rayleigh number (Ra_D) equals 50. This periodical situation was simulated for three days and the boundary conditions were imposed on hourly basis (which is most common in HAM-modelling). The simulation was performed using a variable distance grid with 27 by 27 nodes.
The simulations were repeated, varying the update interval of the air flow calculation. Figure 5.7 shows the total heat flux at the interior surface for three different update intervals. Furthermore, this figure also includes the simulation in which air transport was excluded. The average step size for the decoupled simulation was around 5 minutes. It was found that when the update interval lies between an update after each time step and a hourly update, the simulation results were identical. In addition, to illustrate the error when applying larger updates intervals, the figure also plots the simulation results corresponding to an 6-hourly update of the pressure field. Figure 5.7 shows that these simulation results only correspond to the correct solution shortly after an update of the air flow field.
Although the present example indicates that larger update intervals (up to one hour) can be used, it is suggested to update the airflow calculation after each time step of the heat and moisture integration. The additional calculation time for updating the pressure field is relatively small compared to the integration of heat and moisture balance equations. Only when the time steps of the heat and moisture calculation become very small (e.g. for water absorption as result of wind driven rain) larger update intervals of the pressure field become interesting to avoid superfluous calculations, and thus, increasing simulation times.

To compare the simulation performance of the decoupled strategy, the simulation was also repeated with a fully-coupled solution of the air and heat balance equations (Eqn. 5.3 and 5.1a). For this coupled simulation the DAE[2]-solver from the SUNDAILS generic solver package is applied. More detail about this solver and the implementation can be found in Langmans et al. 2011. This solver has similar performance properties as the ODE-solver which is used in the decoupled approach. The DAE-integrator allows, however, to solve the given set of differential-algebraic equations in a coupled way.
This additional simulation resulted in the same heat flow profile as depicted in Figure 5.7. Only small deviations (<3 %) near the upper values were found between the results, confirming again the accurate results of the decoupled calculation. In addition, this coupled simulation indicated that the decoupled strategy might lead to better simulation performances. When only the heat balance equation is solved, the DAE-solver was slightly faster, proving that the overall performance of both solvers is similar. When including air transport,

[2]Differential-Algebraic Equations

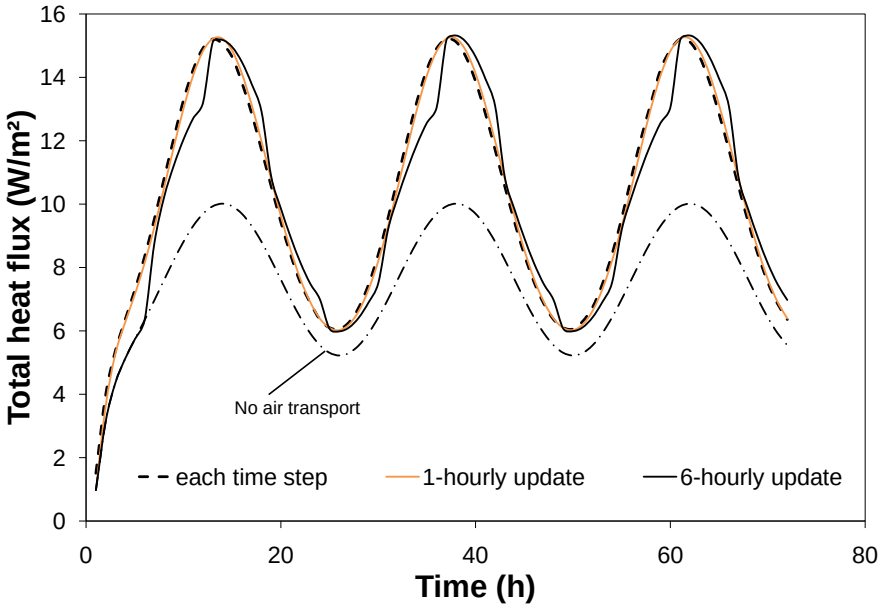

Figure 5.7: Total heat flux at the interior surface for different pressure update intervals.

however, the coupled simulation was around ten times slower than the decoupled strategy (even with a pressure update after each time step). This indicates the potential advantage of shorter simulation times for the decoupled approach. However, in order to draw general conclusions in this respect, the solver performances have to be studied more in depth which falls outside the scope of this work.

5.4.3 Impact of air convection on the hygrothermal behaviour of timber frame walls[3]

The first two benchmark projects in sections 5.4.1 and 5.4.2 confronted the present model with analytical and numerical results from the literature. The results show the model's ability to capture the coupled phenomena of free heat convection. Yet the main interest of developing the model lies on its prediction of combined heat, air and moisture transfer in building components. Therefore, this third section confronts the model with the well-controlled laboratory investigation of chapter 4, which studied the effect of air convection on the hygrothermal behaviour of timber frame walls. These tests have been conducted with high accuracy and with the objective to create two-dimensional conditions. In total eight walls were tested. For the evaluation of the model, however, only four test walls (test series I) will be compared with the simulations here. All the four walls were insulated with standard mineral wool of 20 kg/m^3 and three different exterior air barrier materials were applied: BIFB I, BIFB II and a foil. More details on the configurations of the test walls, the properties of the applied materials and sensors positions are documented in section 4.1.2.

[3]partially published in Langmans et al. (2013)

Boundary conditions and discretisation grid

The calculation domain was discretised in 1484 cells (28x53) using a variably distant grid as shown in Figure 5.8. The measured temperature, relative humidity and air pressure of the cold and warm boundary at the mid-height were applied as boundary conditions for the simulations. The boundary air pressures ascribed to the model were adjusted over the height with the hydrostatic air pressure based on the measured temperature at both sides and the neutral plane at the mid-height of the wall (Eqn. (5.20 and 5.21). The surface temperatures were measured on both sides (Fig. 4.5), so, they could be ascribed directly to the model as surface values. For the vapour pressures, on the other hand, this was only possible at the inside of the wall. At the outside of the wall tested, the vapour pressures were measured at 2.5 cm from the exterior air barrier. As a consequence, the exterior vapour pressure was ascribed to the configuration by a transfer coefficient. This vapour transfer coefficient was derived indirectly from the heat transfer coefficient (Eqn. 5.17), which was determined from velocity measurements, performed in a test run of the experiment. The intention of these measurements was to investigate the local air speeds at the walls surfaces as a function of the power to the ventilators in the cold box. The velocity was measured with a hot wire anemometer[4], from which the heat transfer coefficient was estimated from Hens (2003):

$$\alpha_{h,ce} = 5.6 + 3.9v \tag{5.35}$$

in which $\alpha_{h,ce}$ is the convective heat transfer coefficient and v corresponds to the measured velocity at 2.5 cm of the exterior air barrier. The measured velocities varied between 0.48 m/s and 0.65 m/s, which corresponds (based on Eqn. 5.35 and 5.17) to a vapour transfer coefficient ($\beta_{v,e}$) between $5.5\,10^{-8}$ s/m and $6.0\,10^{-8}$ s/m. Based on these results, a vapour transfer coefficient of $6\,10^{-8}$ s/m is used at the exterior of the walls. It should be noted however that the impact of the vapour transfer coefficient is limited as its resistance is an order of magnitude lower than the lowest vapour resistance values of the applied exterior air barriers (Fig. 4.8).
The air pressures were ascribed as surface values on both sides of the walls. Finally it should be mentioned that the boundary conditions were applied as hourly data to the transient simulations.

Comparison between measurements and simulations

Thermal The emphasis lies in a first step on the comparison of the temperature distributions within the test walls. Figure 5.9 provides the dimensionless temperature profiles of the four walls at the top and bottom row for measuring stage 1, 2 and 4 for both the simu-

[4]TSI, (Model 8475), ±3% of readings

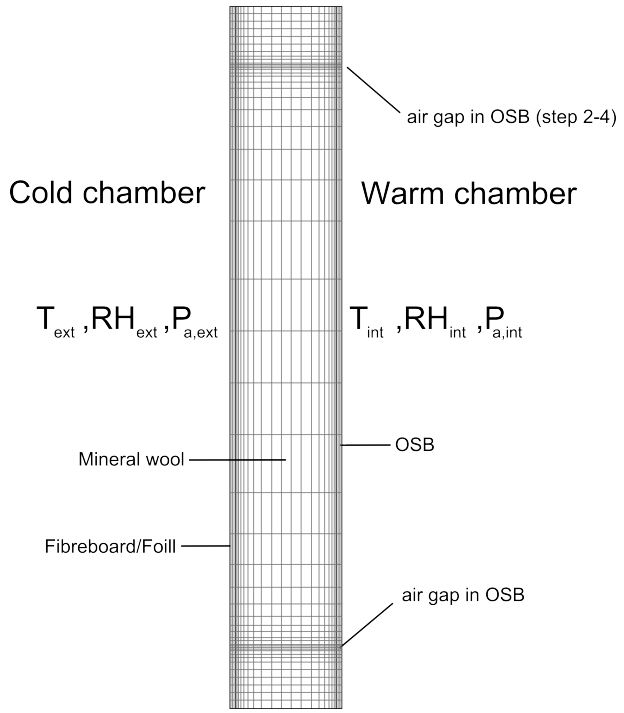

Figure 5.8: Variable discretisation grid (28x53) and applied boundary conditions.

lated and measured data. This corresponds to the situations with: (1) an intact interior OSB sheathing, (2) top and bottom gaps in the interior and (3) an overpressure of ±10 Pa in the warm chamber. The simulated temperature profiles are represented in Figure 5.9 as lines and the measured temperatures with markers. Full lines and markers correspond to the temperatures at the top position and dotted lines and hollow markers to the temperatures at the bottom position. The first measuring step is coloured in blue, the second in red and the fourth step in green.

During the first step, the measuring data shows that the temperature distribution bends upwards at the top and downwards at the bottom, which indicates the existence of natural convection within all four walls. This is confirmed by the simulations, which show an identical profile. However, where the simulated temperature profiles are the same for all four test walls during this step, small differences in the measured temperature profiles exists. During the second measuring step, the effect of natural convection on the temperature profile increases as a result of introducing gaps in the interior sheathing. Furthermore, both the simulations and measurements show that the temperature profile in wall Ic is shifted. This means that the exterior sheathing is even so air permeable that as a result of the 1.9 Pa pressure differential across this wall (introduced by the ventilators in the cold chamber, see Table 4.2) forced exfiltration already dominates the air flow pattern in this test wall. Finally, this effect becomes even more dominant in wall Ic when an overpressure of ±10 Pa is realised in the fourth step. Also for Ib the effect of forced exfiltration is (to a minor degree) observed. For the most airtight wall (Id) this remains negligible. In addition, the data of Ib is used to illustrate the order of magnitude of the air velocity levels within the insulation and

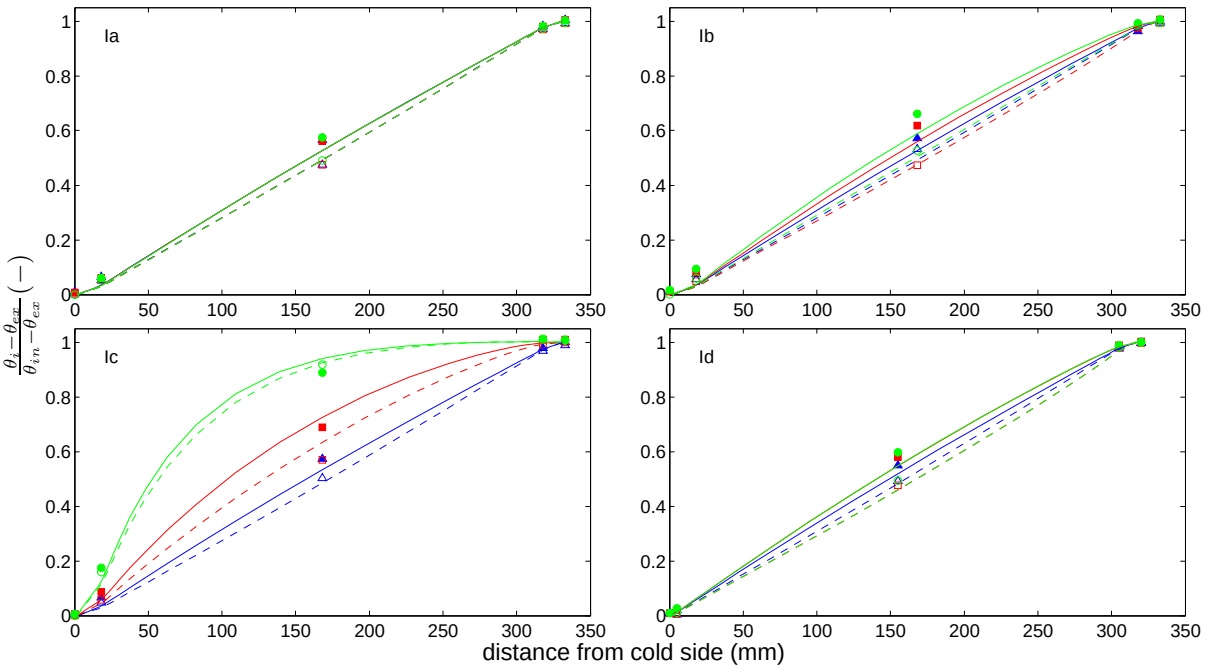

Figure 5.9: Simulated dimensionless temperature distribution versus measured temperatures at top row (filled markers) and bottom row (open markers) during measuring step 1 (blue triangle), step 2 (red square) and step 4 (green dot).

its impact on the temperature distribution in Figure 5.10. The plots compare the simulated temperature and air velocity field with and without the gaps in the interior sheathing (step 1 and step 2). The figure clearly demonstrates how the velocity field, and thus, the temperature distribution are changed by providing the interior gaps. Introducing gaps results in an overall increase of the air velocities in the insulation layer. The maximum velocity for

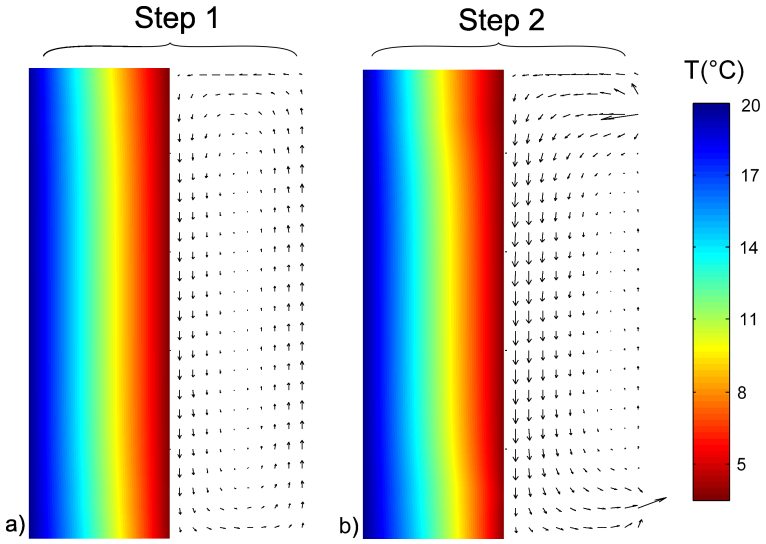

Figure 5.10: Simulated temperature and air velocity field in the insulation layer of Ib: (a) first measuring step, (b) second measuring step with gaps in interior sheathing (maximum velocity: (a) 0.12 mm/s and (b) 15 mm/s).

the closed situation is 0.12 mm/s and is located at the mid-height of the wall at the boundaries of the insulation. For the open situation the maximum velocity becomes 15 mm/s and is located near the gaps. The velocity at the mid-height of the wall at the cold boundary becomes 0.23 mm/s for the open situation.

Hygrothermal Figure 5.11 presents the dimensionless vapour pressure profiles across the test walls. Here, vapour pressures are derived from the measured temperatures and relative humidity levels according to Eqn. 4.5.

The measured data for all four walls shows a similar vapour pressure profile during the first step: a steep drop behind the vapour retarder (OSB) followed by a slight decrease towards the outer side. The simulated profiles follow this trend as well. Only for Ib the measured vapour pressure at the warm top row is somewhat deviating from the simulated profile. At this row, the vapour pressure is slightly higher than the simulated values. This can not be the result of air exfiltration since this should be noticed in the temperature distribution as well. A local decrease of the vapour resistance of the OSB might explain this (small) discrepancy. In the subsequent step, when the gaps in the interior sheathing are opened, the influence of natural convection on the moisture load becomes very pronounced. The measurements indicate that for all walls with interior gaps, the vapour pressure at the top row increases while the vapour pressure at the bottom row remains the same. Only for Ic also the vapour

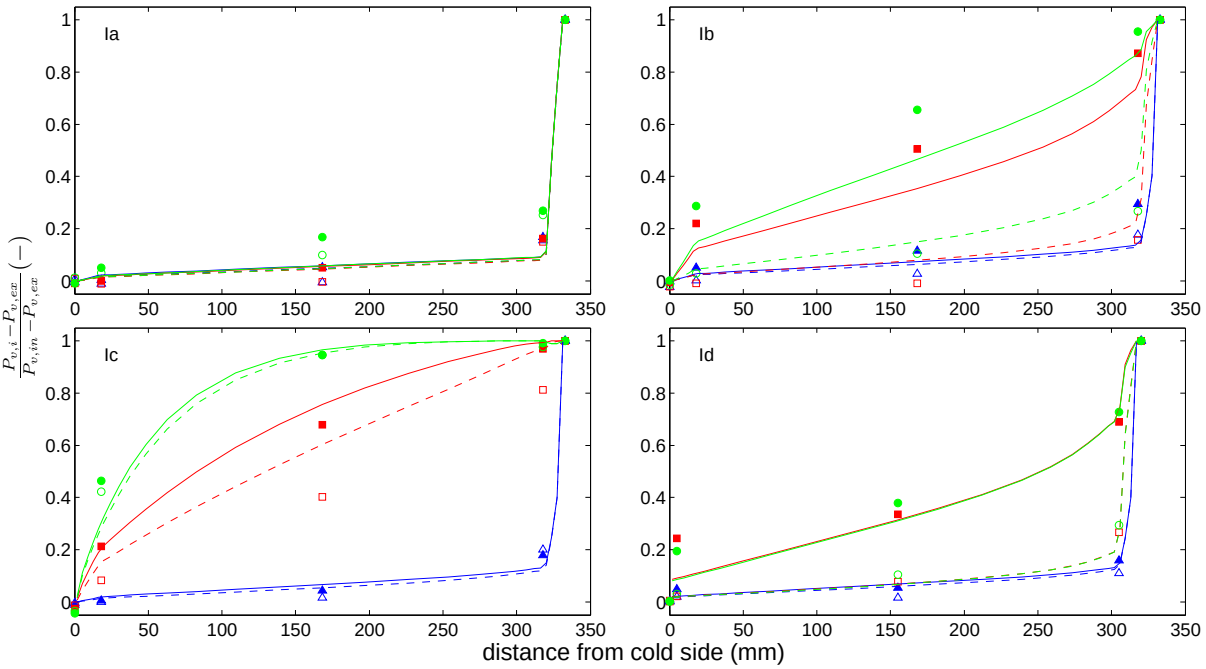

Figure 5.11: Simulated vapour pressure distribution at top and bottom position versus measured vapour pressure (via measured relative humidity and temperature) at top row (filled markers) and bottom row (open markers) during measuring step 1 (blue triangle), step 2 (red square) and step 4 (green dot).

pressure at the bottom row increases since forced exfiltration is than already dominant. The simulations follow the same trends. Yet the simulations underestimate the vapour pressure during this step in wall sections Ib and Id at the upper cold side.
In the next step, with an overpressure in the hotbox, the vapour pressure profiles support the observations regarding air convection on the temperature profiles: a slight increase in the vapour pressure of Ib is noticed as a result of forced exfiltration, while this effect is much stronger for the more air permeable wall section Ic. For the wall with the exterior foil this influence of forced convection is hardly noticed. Again the simulations show the same observations. The differences between the measured and simulated vapour pressure at the cold side of wall Id still remain, however. Moreover, the simulated vapour pressure at this position in section Ic starts to deviate from the measured values as well.
Figure 5.12 visualises the simulated relative humidity field before and after the gaps are created (step 1 and 2) for Ib. The plot corresponds to the situation at the end of both steps (day 34 and day 61 respectively). The figure shows how the relative humidity increases at the upper cold part of the insulation after creating top and bottom gaps. Combined with the fact that this region also becomes warmer (Figure 5.10), it can be concluded that this situation is more critical for mould growth.

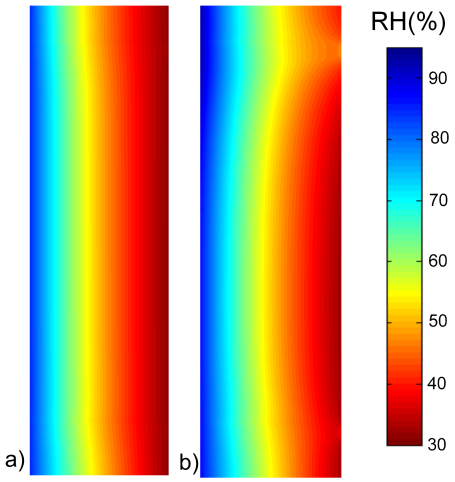

Figure 5.12: Simulated relative humidity in the insulation layer of Ib: (a) at the end of step 1, (b) at the end of step 2.

Figure 5.13 compares the simulated moisture content of the exterior fibreboard sheathing with the measured weight of the removable specimens in this layer. The measured weights are represented here as filled markers and the simulated values are shown as continuous lines. In addition, the effect of a 1 % uncertainty on the sorption isotherm is included in this figure (light-coloured surface) as will be explained later in this section. The top, mid and bottom height correspond to black, red and blue respectively. The measured moisture contents of wall Ia (Figure 5.13a) reach an almost constant value around 0.1 kg/kg at the

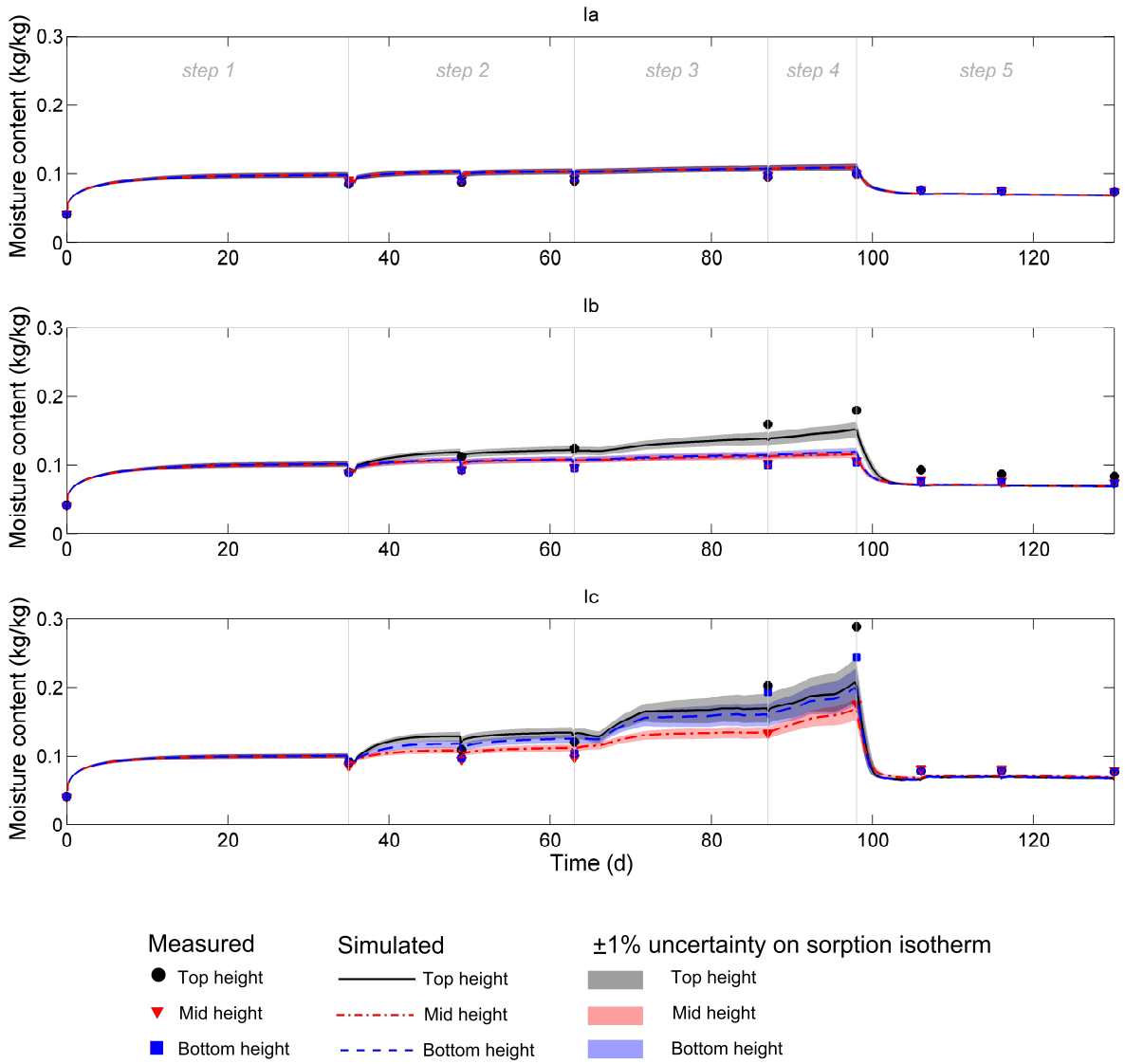

Figure 5.13: Measured versus simulated moisture content of the exterior air barrier.

three heights after a period of hygroscopic loading during the first step. This value drops down to 0.07 kg/kg when drying conditions are imposed in step 5. The same trend is predicted by the numerical simulations. The moisture contents are only slightly overestimated by the simulations during the first four steps. The moisture content evolution at the mid and bottom heights of Ib (Figure 5.13c) are exactly the same as these of the reference section (wall Ia). In contrast, from the moment gaps are introduced, the measured moisture content at the top position starts to increase up to 0.18 kg/kg at the end of step 4. The simulations follow the same trend. Yet the simulated moisture content at the top row is now slightly underestimated. In contrast to the first two test sections, the moisture content profiles of Ic (Figure 5.13c) are affected by convection at all three heights. As documented in Table 4.7 this exterior sheathing is twenty times more air permeable. Consequently, this test wall is more vulnerable to forced convection once gaps in the interior OSB sheathing

are created. Figure 5.13c shows that both the measured and simulated upper and bottom moisture contents simultaneously increase when a pressure differential of 5 Pa is applied in step 3. Next, when the pressure is doubled in step 4, the moisture evolution increases proportionally, reaching a maximum of 0.29 kg/kg at the end of this step. The moisture content at the mid-height also increases but to a smaller degree. This indicates that the main airflow paths through this wall are short and concentrated at the height of the gaps in the OSB. The figure shows a good agreement between the simulated and measured moisture content at the mid-height. However, as will be addressed in next section, the high moisture contents at the upper and bottom row are underestimated at the end of step 4 by 30 % and 20 % respectively. Finally, when drying conditions are applied in the final step the exterior sheathing dries out rapidly as a result of its high vapour permeability. A good agreement between the simulations and the measurements is found in this region, which indicates that the influence of hysteresis phenomena on the sorption isotherm are limited.

Impact of material uncertainties and air cavities between material interfaces

In the first step the simulated and measured temperature fields have been compared. Both the simulations and measurements show the same trends in the temperature profiles for the different measuring stages. Quantitatively, however, small discrepancies between the results were noticed. The temperature differences between the top and bottom position at the middle of the insulation were underestimated by the simulations for Ia and Ib. For example, during the fourth measuring step the difference between the simulated and measured temperature in the middle of the insulation layer at the top row is almost 10 %. The origin of these discrepancies are most probably related to inevitable (small) gaps between the mineral wool and the sheathing materials, which locally decrease the airflow resistance, and thus, increase the effect of natural convection. To illustrate this impact with a theoretical example, the simulation of wall Ib was repeated including a vertical air channel of 2 mm along the interface between the insulation and the exterior air barrier. Figure 5.14 compares the influence of introducing such a small air gap on the simulated temperature profile for wall Ib. The figure illustrates that natural convection in the insulation layer increases by the introduction of this gap, resulting in a higher temperature at the upper cold side on the insulation. As a result the difference between measured and simulated temperatures becomes lower than 3 % for all positions as depicted in Figure 5.14. In addition, the impact of an air gap on the simulated vapour pressure profile of Ib is given as well in Figure 5.15. This figure shows how the maximum deviation reduces from 24 % to 10 % by modelling an air channel along the insulation layer.

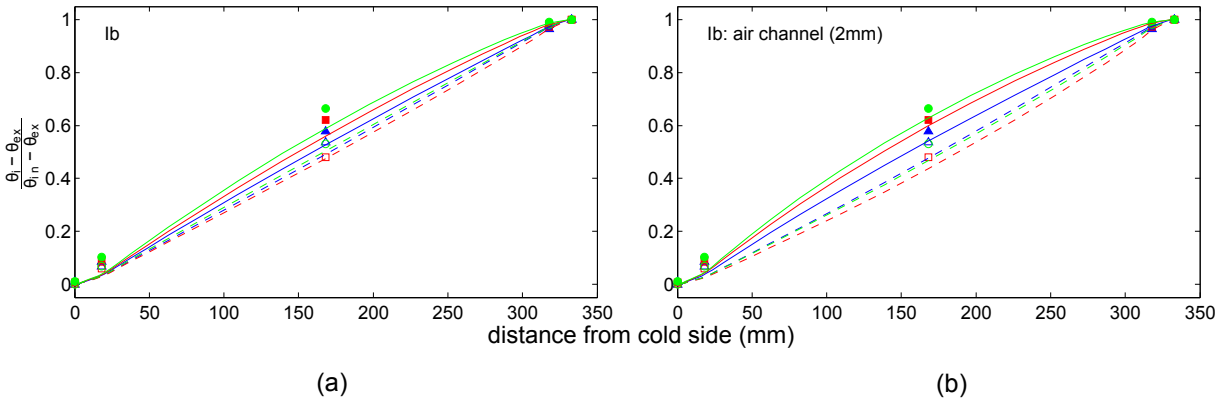

Figure 5.14: Comparison between simulated temperature profile in Ib (a) with and (b) without are gap of 2 mm along the interface of the insulation and the exterior air barrier.

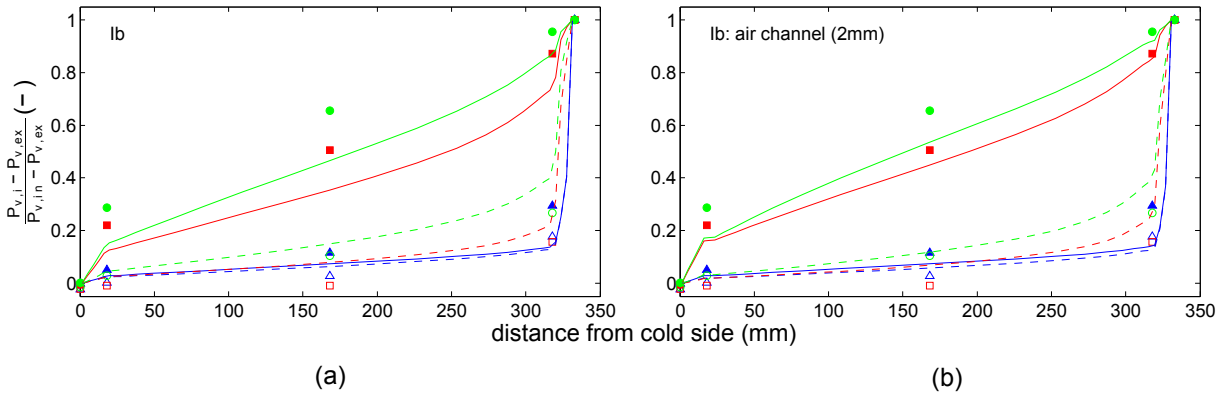

Figure 5.15: Comparison between simulated vapour pressure profile in Ib (a) with and (b) without are gap of 2 mm along the interface of the insulation and the exterior air barrier.

Apart from these unintended air cavities at material interfaces, the discrepancies between the simulations and the measured data can be induced by uncertainties of the material properties, such as the sorption isotherm and the vapour permeability. The sorption isotherms were determined based on the moisture equilibrium of specimens exposed to relative humidity conditions created by saturated salt solutions in closed desiccators. For this study seven different salts have been used with equilibrium relative humidity ranging from 12 % to 97 % (Figure 4.8a). It is difficult to estimate the possible error on these relative humidity levels. Yet to illustrate the impact on the simulations, an uncertainty of 1 % is assumed. Figure 5.16 illustrates the sensitivity of the sorption isotherm for the proposed uncertainty of 1 %. This figure clearly shows that in the higher relative humidity regime this uncertainly on the moisture content becomes very pronounced. The effects of this uncertainty on the simulation results are included as light-coloured surfaces in Figure 5.13. This figure shows that a small uncertainty in the sorption isotherm (±1 %) has a large impact on the moisture content prediction. In Figure 5.13c the uncertainty of the moisture content at the top row almost reaches 15 % at the end of step 4. In addition, Figure 5.17 illustrates the combined impact of an ±1 %-uncertainty on the sorption isotherm and an air

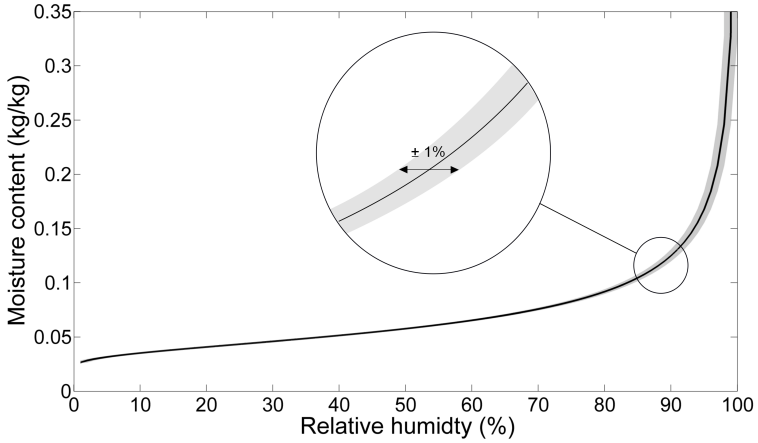

Figure 5.16: Impact of an 1% uncertainty on the sorption isotherm (for BIFB I).

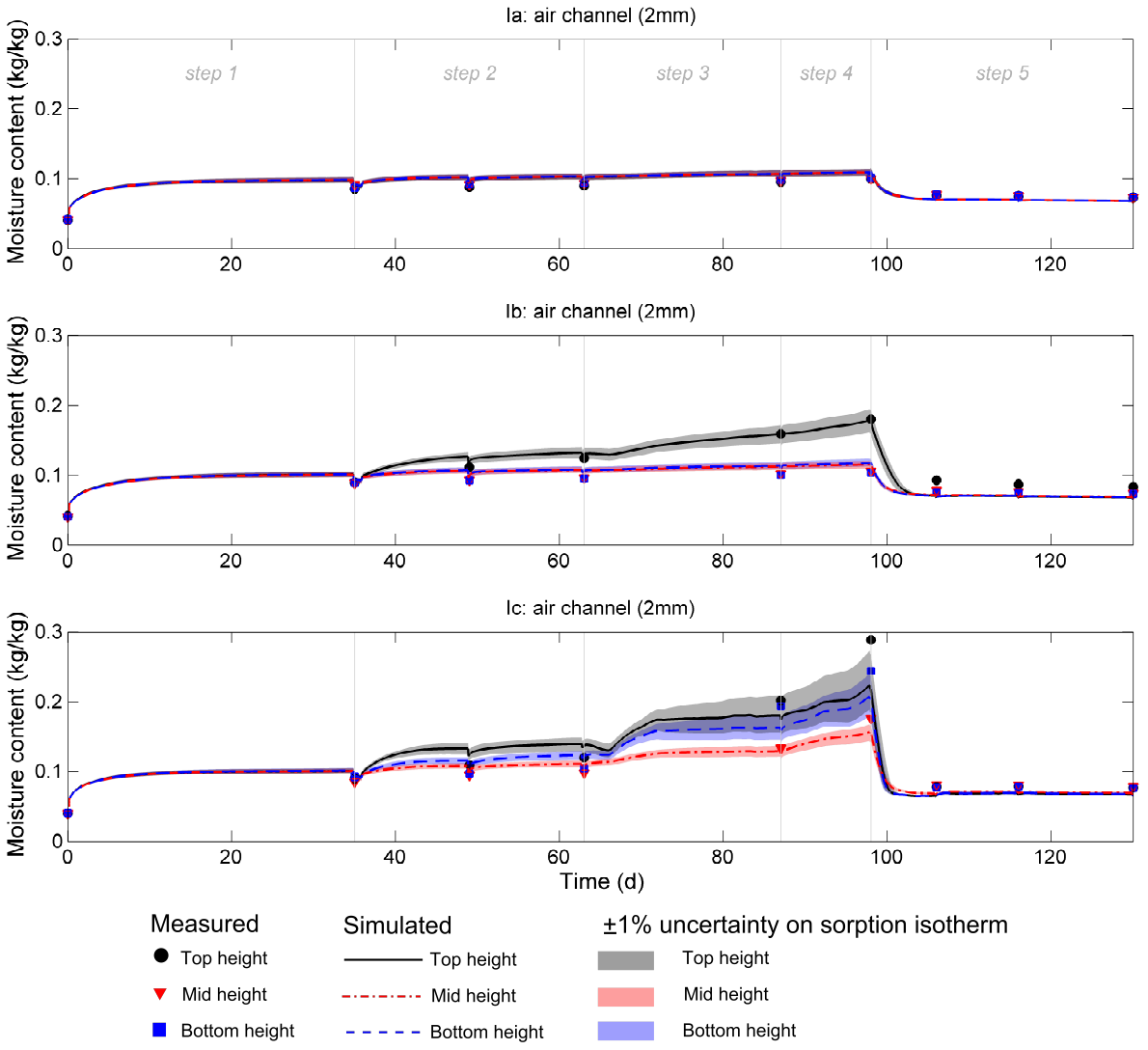

Figure 5.17: Impact of a 2 mm air cavity between the mineral wool and the exterior air barrier on the simulated moisture content of the exterior air barrier.

channel of 2 mm on the simulated moisture content profiles. Because it is very unlikely that there was a perfect air cavity of 2 mm on the cold side of the insulation in this test wall, it should be stressed again that these results should be interpreted as a theoretical example. Though, this figure demonstrates that simulating this air channel results in higher moisture contents at the upper weight specimen in Ib and Ic, and thus, corresponding better to the measurements. Consequently, this figure emphases the importance of taking deficiencies at material interfaces into account.

Finally, the impact of uncertainties in the vapour permeability are investigated. As mentioned in the discussion of Figure 5.11, the vapour pressure at the upper cold side was underestimated by the simulations. This was most significant for the wall with an exterior foil (Id). This can not be ascribed to an increased amount of natural convection induced by air channels, as for this wall close contact between the foil and the mineral wool could be physically checked. In addition, this is confirmed by the temperature profiles in Figure 5.9 which are in good agreement with the measured profiles. Hence, as both the mineral wool and the foil have no moisture buffer capacity, these discrepancies are most likely related to an overestimation of the vapour permeability of the foil. To verify this, the simulation of test wall Id was repeated assuming a constant s_d of 0.1 m for the foil, which corresponds to the lower accuracy limit defined in ISO:12572:2001. Figure 5.18 compares the resulting dimensionless vapour pressure profiles with the situation in which the foil is simulated according to Figure 4.8b. The figure reveals that limiting the s_d-value of the foil to a constant value of 0.1m results in higher vapour pressures at the upper cold side of the insulation, which is in better agreement with the measurements.

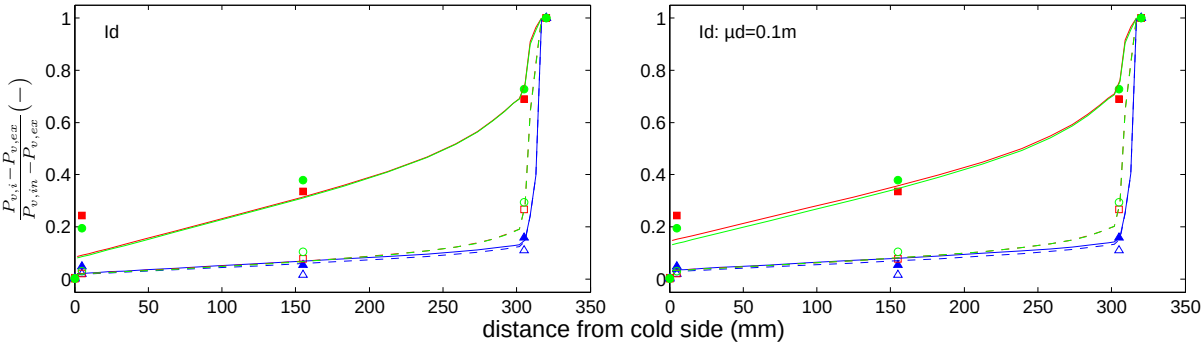

Figure 5.18: Comparison between simulated vapour pressure profile in Id with the vapour permeability of the foil according to (a) Figure 4.8b and (b) limited to 0.1 m.

This is investigated more in detail in Figure 5.19 by comparing the relative humidity at this position for both simulations with the measured data. Here, a steep rise of the measured relative humidity is noticed at the beginning of the second step, reaching almost immediately condensation conditions. Given the error of ±2 % on the relative humidity sensors

(see Table 4.4) this trend is most closely followed by the simulation in which the s_d-value of the foil is assumed constant (0.1 m). For the simulation in which the s_d of the foil is modelled according to Figure 4.8b, on the other hand, significant lower relative humidity levels are predicted without reaching condensation conditions. As a consequence, this example demonstrates the necessity to be careful with simulating very vapour open materials as this might result in too optimistic results.

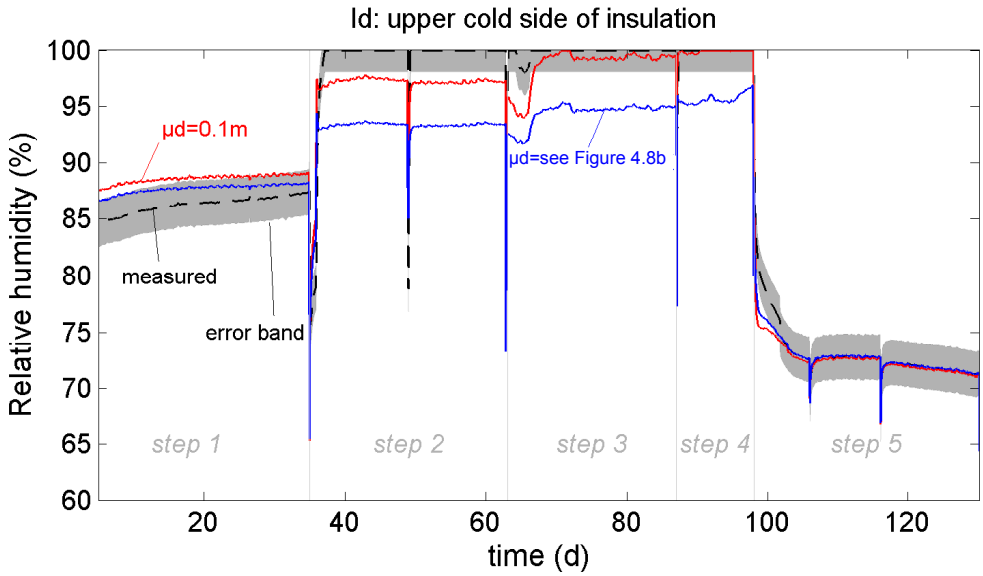

Figure 5.19: Comparison of the measured relative humidity at upper cold side of the insulation (dashed black line) and the simulation results, varying the s_d of the foil. (constant s_d of 0.1 m in red and s_d according to Figure 4.8b in blue).

5.5 Conclusion

This chapter presented the implementation of a quasi-steady state airflow model in the framework of the existing transient HAM-model, Delphin 5. The first section discussed the applied balance equations, transport mechanisms and the numerical strategy. The air transport is described as Darcy flow in porous media including a body force term to capture natural convection. To account for increased air transport through air channels and cracks, a hydraulic network methodology is used, that assumes fully-developed laminar flow in the interconnected channels. As a result of the different times scales between the combined heat and moisture transport and air transport, this chapter showed that it is justified to neglect the transient effects of air transport. Moreover, the air mass balance equation could be solved externally improving the simulation performance significantly.

The second part of the chapter confronts the presented model with analytical, numerical and laboratory results. Three two-dimensional benchmark cases are used: (1) steady state heat convection through a vertical and horizontal porous medium, (2) transient heat convection

through a porous media, (3) transient heat, air and moisture transport in lightweight building walls. The first evaluation project showed the models capability to predict the increased heat transport through lightweight building components induced by natural convection. Both the results of the vertical wall, as well as the unstable phenomenon of heat flow through a horizontal porous media heated from below, were in good agreement with the results from the literature. The second benchmark proofs that the decoupled calculation approach is justified for building physical applications. For Ra-numbers lower than 100, the transient free heat convection was correctly predicted. In the final step the model was evaluated with experimental hygrothermal laboratory results. As a consequence higher deviations were obtained for this confrontation. It was shown that these discrepancies could be explained by (1) small air channels around the insulation layer and (2) uncertainties in the hygric material properties. Consequently, this chapter emphasised the importance of taking these factors into account in assessing the hygrothermal behaviour of highly insulated wood frame walls with an exterior air barrier in the next chapter.

6

Numerical Investigation of Exterior Air Barrier Systems Performance Under Real Climate Conditions

Chapter 3 was particulary dedicated to the quantification of typical air leakages which may occur in high performance lightweight walls. Next, chapter 4 verified the hygrothermal performance of such systems in laboratory conditions. Thereafter, chapter 5 presented and evaluated a numerical modelling approach to simulate the heat, air and moisture transport in these components. Arrived here, the aim of this final chapter is to combine the achieved insights for a reliable prediction of the hygrothermal performance of lightweight walls with exterior air barriers under real climate conditions.

First, the general wall configuration, additional material properties and climate conditions will be addressed. Second, after selecting relevant moisture limit state criteria, the emphasis lies on the verification of modelling simplifications to improve simulation performance. Third, simulations will be performed on a reference case to identify the impact of the inner climate conditions and to select the most critical wall orientation. Finally, the main focus of this chapter lies on the last section which provides a parameter study to verify the reliability of different lightweight wall assemblies. Further, the study identifies the impact of bad workmanship and illustrates its behaviour in other European climates.

6.1 Wall configuration and material properties

The simulations throughout this chapter are restricted to wall elements only. Figure 6.1 shows the general configuration studied here. In addition to the simplified test walls of the laboratory study of chapter 4, its configuration is extended with wooden top and bottom plates, an exterior cladding and ventilated cavity, an inner service cavity and adjacent finishing layer as they commonly occur in practice today. The ventilated cavity has a width of 25 mm and contains top and bottom ventilation openings. The impact of these openings on the ventilation rate, and consequently the moisture performance of the wall will be investigated in section 6.4. The wooden top and bottom plates have a thickness of 40 mm and extend the full width of the insulation layer. A service cavity of 40 mm is applied at the inside of the wall element, which is covered with a gypsum board finishing layer. It is important to the note that both the interior vapour barrier and this gypsum board layer are not continuously airtight, so, they will not act as an air barrier. The air barrier, however, is positioned at the outer side of the insulation layer by sealing the joints in the wind barrier layer (see chapter 3). As a first approach, the deficiencies in the inner vapour barrier are adopted from the laboratory tests of chapter 4; 1 cm slot at 20 cm from the top and bottom of the wall. The influence of the width and position of these air leakages will be verified in section 6.6.2.

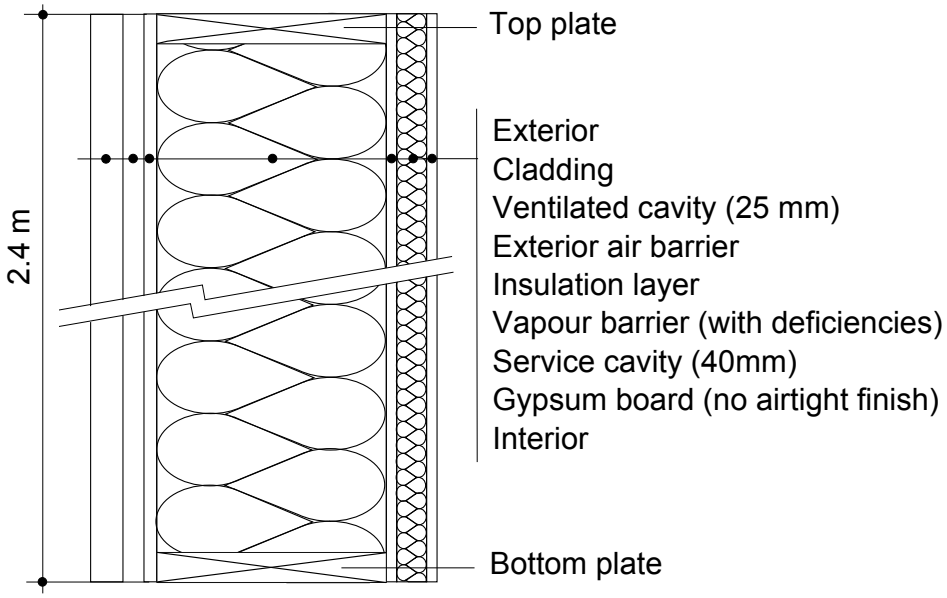

Figure 6.1: General wall configuration studied.

The numerical simulations of the present chapter will introduce several materials which were not documented in section 4.1.5, such as wood (cladding, top/bottom plates), fiber cement boards (exterior air barrier) and gypsum boards (finishing material). These additional materials will be outlined below.

Wood

The test walls in the laboratory investigation of chapter 4 were simplified by the omission of top and bottom plates. For the hygrothermal simulations in this chapter, however, these wooden plates will be included. The material properties of these components are based on measurements of Zillig (2009), who studied moisture transport in spruce (Picea abies), commonly used in European wood frame construction.
Moisture transport in wood is a complex phenomenon. Its material properties are highly anisotropic and have a multiscale character as results of its bi-layered structure. In order to model this behaviour, Zillig (2009) proposed a multiscale approach[1] in which the hygric properties are derived from the differences in density. Zillig (2009) addressed the large differences in the moisture uptake in longitudinal and radial/tangential direction. The moisture uptake in the longitudinal direction is significantly higher compared to the radial and tangential direction, for which the moisture transport properties are in the same range. The wooden plates are oriented according to their radial and tangential direction in the simulation grid (Figure 6.1). Since the moisture properties of these two directions are in the same range, the wooden plates can be safely modelled as a homogenous material layer. The adopted hygric properties from Zillig (2009) are summarised in Table 6.1 and the moisture retention curve is presented in Figure 6.2 (top figure). The liquid permeability, depicted at the bottom of Figure 6.2, was not directly determined by Zillig (2009) but estimated by assuming an exponential diffusivity according to Eqn. 6.1 which is adopted here:

$$K_l = D_{w,cap}\, exp(F\,\frac{w - w_{cap}}{w_{cap}})\left|\frac{\partial w}{\partial p_c}\right| \qquad \text{in which} \qquad D_{w,cap} = f(F)\left(\frac{A_{cap}}{w_{cap}}\right)^2 \tag{6.1}$$

The thermal properties of spruce, however, were retrieved from Kumaran (1996) and are also included in Table 6.1.

Fibre cement board

A second additional material in the simulations is fibre cement board, which will be applied as exterior air barrier. These panels (d = 3 mm) are commonly applied in Belgium as underlay material in roof constructions. The capillary-active properties of fibre cement boards are often put forward by their manufacturers as a potential to remove accumulated moisture, and thus, reducing interstitial condensation levels. However, its behaviour in condensation conditions is hardly documented in the literature (Janssens & Dobbels 2005, Steskens et al. 2012). To achieve more insight in the performance of these capillary-active underlay materials, fiber cement board is also included in the analysis here.
The moisture retention curve, depicted in Figure 6.2, was measured both in the hygroscopic[2]

[1] distinction between earlywood and latewood
[2] see section 4.1.5

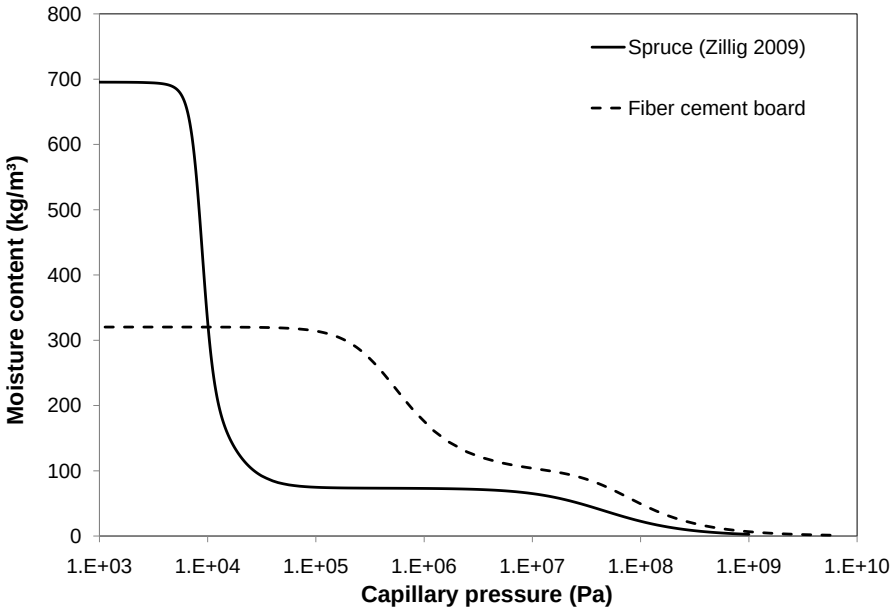

(a) Moisture retention curve

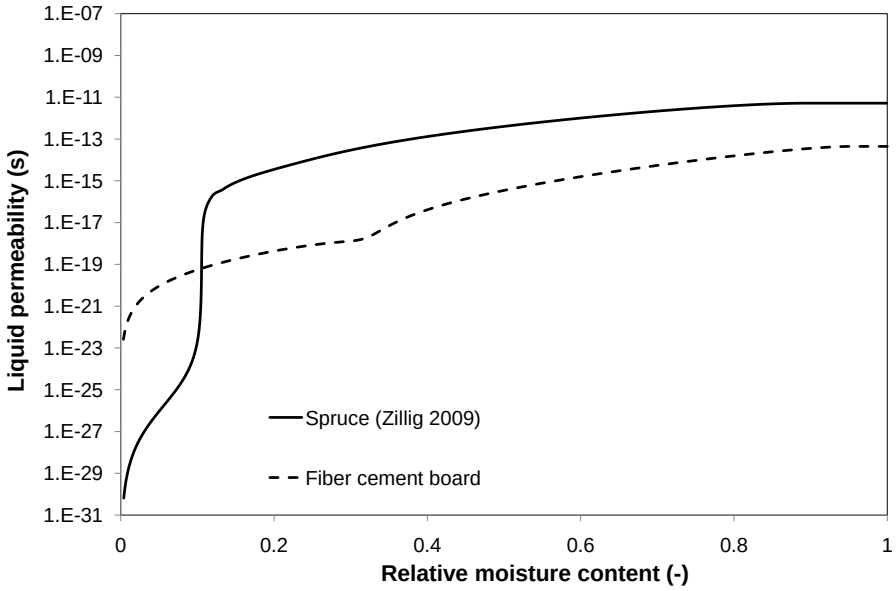

(b) Liquid permeability

Figure 6.2: Moisture retention curve and liquid permeability of spruce, ceramic brick and fibre cement board.

and over-hygroscopic range[3] according to the methods described by Roels (2004b). Similar to spruce, the liquid permeability, K_l, is estimated from the moisture retention curve according to Eqn. 6.1.

Gypsum board

Gypsum board will be applied as interior finishing material throughout the simulations in this chapter as mentioned in the previous section. The properties of gypsum board are

[3] mercury intrusion porosimetry measurement

	spruce[a]	**fibre cement board**	**gypsum board**[b]
d (m)	-	3	12
ρ (kg/m^3)	350	1400	690
c_p (J/(kg K)	1880	840	1090
λ (W/(m K))	0.1	0.18	0.2
A_{cap} (kg/(m^2 s$^{-0.5}$))	0.011-0.019	0.0029	/
w_{cap} (kg/m^3)	696	320	53
μ_{50} (-)	162	143	10
K_a (m^3/(m^2 h Pa))	-	<1.6 10^{-14}	<6.6 10^{-14}

[a]Zillig (2009)
[b]Roels et al. (2010)

Table 6.1: Overview of additional material properties (thermal properties were adapted from Kumaran (1996)).

documented by several authors (e.g. Kumaran 1996, Roels & Carmeliet 2005, Janssens 1998, Roels et al. 2010). Therefore, its hygric properties have not been determined in the laboratory, but are adopted from the literature (Roels et al. 2010). Only its air permeability was determined in the laboratory according to the method described in section 3.3.3. A summary of the applied material properties for gypsum board is included in Table 6.1.

6.2 Climate conditions

An important amount of uncertainties within hygrothermal simulations is related to the selection of representative weather data. In this context Geving (1997) defined a Moisture Design Reference Year (MDRY) as the climatic data of the year corresponding to the highest hygrothermal stress on a construction component within a period of 10 year. However, the selection of a MDRY is a challenging process as the outcome of such an analysis highly depends on the building component studied and the simulation models complexity. Janssens (1998), for example, found that the exterior temperature is the most decisive parameter in selecting a MDRY for lightweight components, while Geving (1997) put forward the exterior relative humidity. Origin of this difference lies in the fact that Janssens (1998) accounts for both diffusive and convective moisture transport while Geving (1997) only considered moisture transport by diffusion. Moreover, Vinha (2007) illustrated that the MDRY selection also depends on the applied moisture limit state criteria. Vinha (2007), who assessed the hygrothermal performance of a reference configuration for four different geographical locations in Finland and 30 consecutive years, showed that the MDRY for condensation conditions is not the most critical year for mould growth and vice versa.
In summary it can be stated that there is currently no consensus on reference climate data for hygrothermal building components simulations. Given its complexity, the selection of the most critical reference year to evaluate the performance of lightweight constructions

lies beyond the scope of the present work. As a remedy, commonly available Test Reference Year (TRY) data from building energy consumption simulations are used. Such climatological data sets are constructed from measured weather data to create an averaged representative climate file. Initially the TRY for Belgium (Uccle), retrieved from the building simulation software package TRNSYS 17[4] is used in this chapter. However, to verify its impact on the simulation results, section 6.5.3 provides a comparison between the ten-yearly minimum, maximum and average TRY's for Uccle retrieved from the software package METEONORM[5]. In addition, this comparison is extended with the TRY from Essen (Blümel 1986), closely located near Belgium. Following section will outline the applied assumptions in the determination of boundary conditions.

6.2.1 Radiation

The exterior radiative heat exchange on building envelopes is commonly divided in a short and long wave component (Eqn. 6.2):

$$q_{rad} = q_{lw} + q_{sw} \tag{6.2}$$

Short wave radiation The short wave radiative heat flux q_{sw} represents the solar energy absorbed by the building envelope. The total short wave radiation on a horizontal surface I_{sw}, consisting of a direct and diffuse component, is collected from Meteonorm[5]. For the transformation from this horizontal component (I_{sw}) to the tilted component normal to the wall surface $I_{sw,T}$ the model of Perez et al. (1988), embedded in the Meteonorm software package, is applied. The corresponding short wave radiation heat flux is obtained from:

$$q_{sw} = \alpha_{sw} I_{sw,T} \tag{6.3}$$

where α_{sw} represents the absorption coefficient for short wave radiation and $I_{sw,T}$ (W/m^2) the total short wave radiation on a tilted surface.

Long wave radiation The long wave radiation on a building envelope follows from its interaction with the surrounding and the sky. The resulting heat flux is derived from Stefan-Boltzmann law, considering the building component infinitesimal small and surrounded by a black body hemispherical region composed of the sky and surroundings (Hens (2007)):

[4] BE_UCCLE_64470
[5] www.meteonorm.com

$$q_{lw} = f_{sky}\sigma(T_{sky}^4 - T_s^4) + f_{gr}\sigma_{sb}(T_{gr}^4 - T_s^4) \tag{6.4a}$$

$$f_{sky} = cos^2(\frac{\beta}{2})\epsilon_{lw,s} \tag{6.4b}$$

$$f_{gr} = sin^2(\frac{\beta}{2})\epsilon_{lw,s} \tag{6.4c}$$

here, σ corresponds to Stefan-Boltzmann constant ($5.67\,10^{-8}$ W/(m^2 K^4)), f represent the radiation factor for the ground (gr) and the sky (sky), β is the inclination angle (from the horizontal), T to the temperature and ϵ the emissivity. Furthermore, the subscripts lw refers to long wave radiation and s to the surface of the corresponding building component. Most commonly the temperature of the surrounding (T_{gr}) is assumed equal to the air temperature (T_a). For the calculation of the effective sky temperature (T_{sky}) several estimation methods exist in the literature. In this work we apply the approach proposed by Martin & Berdahl (1984):

$$T_{sky} = T_a(\varepsilon_0 + 0.8(1 - \varepsilon_0)\,C_{cover})^{0.25} \tag{6.5}$$

in which T_a corresponds to the ambient air temperature and C_{cover} to the cloud cover fraction. The emittance of the clear sky, ε_0, which is a function of the vapour content of the ambient air is derived according to Martin & Berdahl (1984) as well. To illustrate the order of magnitude of the short and long wave radiation, Figure 6.3 compares the absolute value of the radiation on a North and South oriented wall under Belgian climate conditions for the wall configuration of Figure 6.1 without exterior cladding. In this example, the long wave emissivity ($\epsilon_{lw,s}$) and the short wave absorption coefficients (α_{sw}) of the building envelope equal 0.9 and 0.6 respectively. The interior of the wall, with a U-value of 0.13 W/(m^2 K), was

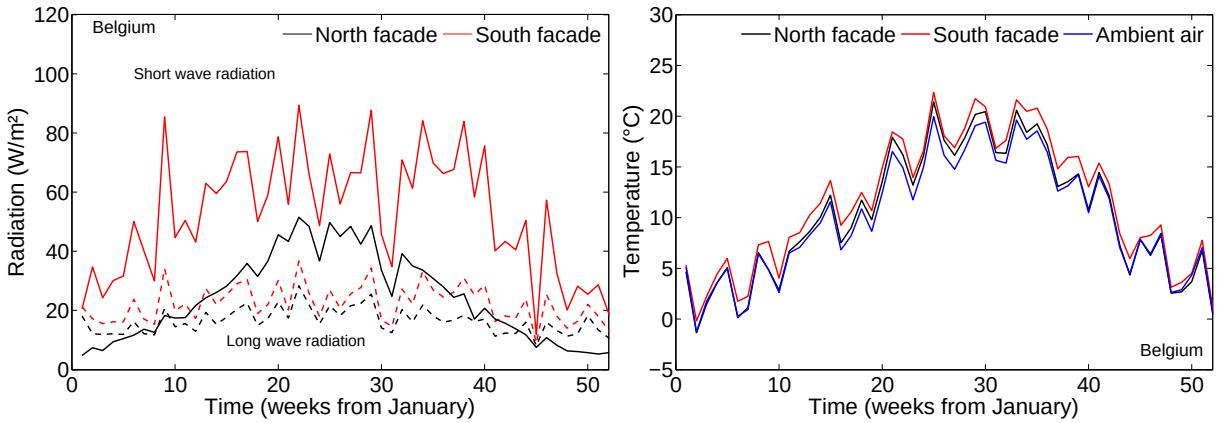

Figure 6.3: (a) Absolute short and long wave radiation on a North and South oriented wall and (b) corresponding surface temperature compared with the ambient temperature for a Belgian climate (weekly averaged values).

exposed to a constant temperature of 20°C. The figure shows that the short wave radiation, which is an incoming heat flux, is most of the year dominating the outgoing long wave radiation. Only for the winter months on the North facing wall the outgoing long wave radiation exceeds the incoming short wave radiation heat flux. This means that the lowest surface temperatures occur on North facing walls, as depicted in Figure 6.3b.

6.2.2 Air pressure difference

Air pressure differences across a building envelope are induced by interaction of wind, stack effects and mechanical ventilation:

$$p_{tot} = p_{wind} + p_{stack} + p_{mech} \tag{6.6}$$

In which positive values correspond to an overpressure in the building. In contrast to outdoor temperature and relative humidity, the pressure differential is, apart from the outdoor climate, influenced by many other parameters. This section briefly summarises the origins of air pressure differentials and shows how they will be applied in the remainder of this work.

Stack pressure Temperature differences between the inner and outer climate cause pressure differentials across the building envelope. The resulting pressure distribution, induced by this so-called stack effect, highly depends on the position and magnitude of the air leakages in the building envelope. The calculation of the stack pressure is most often determined by the concept of a neutral plane (Hens (2007)), corresponding to the level for which the interior stack air pressure equals the exterior stack air pressure. The position of the neutral plane can be determined by solving an air mass balance across the building envelope taking the position of the leakages into account. The stack pressure through the building envelope, $p_{stack}(h)$, can be expressed as a function of $H_{np,h}$, which is the height to the neutral plane.

$$p_{stack}(h) = (\rho_e - \rho_i).g.H_{np}(h) \tag{6.7}$$

In winter conditions, when the interior air temperature is higher, this will result in positive pressures[6] above the neutral plane and negative pressures below this height. As positive pressure differentials can potentially induce exfiltration conditions across the building envelope, the most critical positions are above the neutral plane. Consequently, as a conservative assumption a highly airtight dwelling for which the largest deficiencies are located near the foundation is considered. Such a leakage distribution results to the largest possible positive pressure differences across the building envelope (see Figure 6.4). The target group of dwellings of this work corresponds to a single family house with one or two floors.

[6] positive pressure correspond to a building overpressure

The maximum pressures differentials caused by stack for such buildings in a Belgian climate are presented in Figure 6.4. This graph represents the stack pressure at the ground, the first and the second floor. The figure shows - for this rather extreme conditions - that air density differences across the building envelope can cause pressures differentials up to 10 Pa for typical single family houses.

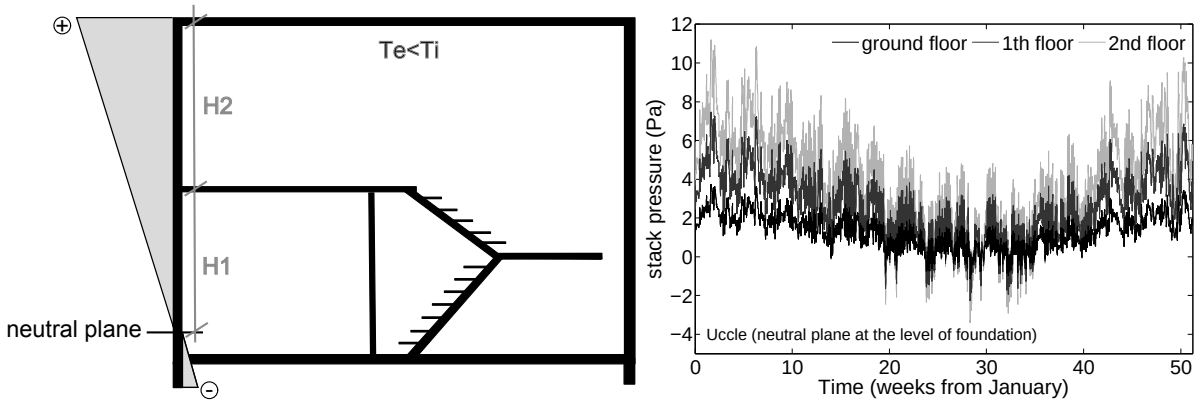

Figure 6.4: (a) Stack pressure along building height, (b) hourly stack pressure at mid-height for ground level, first level and second level (Uccle).

Wind pressures The surface wind pressures on a building envelope depend on the direction and magnitude of the wind. In addition, the terrain category and the shape of the building influence the pressure distribution as well. The detailed prediction of the surface wind pressures is a complex process, and thus, requires case specific input parameters. However, in the literature several simplified models to estimate the surface wind pressure can be found. The present work applies a calculation method based on averaged surface pressures for low rise buildings, presented in ASHRAE (2009). Here, the time averaged surface wind pressure p_w is assumed proportional to the wind velocity pressure p_v, derived from Bernoulli's equation ASHRAE (2009):

$$p_{wind} = C_p p_v = C_p \frac{\rho_a U_H^2}{2} \tag{6.8}$$

in which U_H corresponds to the air velocity at the upwind wall height H (m/s) and C_p to the surface averaged wind pressure coefficient. The C_p-coefficients in this work are determined according to Swami & Chandra (1987).
The wind speed in Eqn. 6.8, U_H can be derived from Eqn. 6.9 as a function of the building terrain class:

$$U_H = U_{met} k_{met} \left(\frac{H}{\delta}\right)^a = U_{met} \left(\frac{\delta_{met}}{H_{met}}\right)^{a_{met}} \left(\frac{H}{\delta}\right)^a \tag{6.9}$$

in which δ and a represents the atmospheric boundary layer thickness and the exponent for the local building terrain respectively. Typical values for δ and a are listed in ASHRAE

(2009) for various building terrains. The parameter taking the building terrain and height of the meteorological station into account are converted in a multiplication factor k_{met} in Eqn. 6.9. For most stations this factor equals 1.59 (ASHRAE (2009)), corresponding to an anemometer that records at a height of 10 m in an open area.

Figure 6.5b shows the weekly-averaged surface wind pressures for the four main wind directions in a Belgian climate, according to the calculation method described above. Overall it can be concluded from this figure that the averaged wind pressures on low rise buildings varies between -4 and 4 Pa. Again, the positive pressure differentials correspond to buildings overpressure. Consequently, the North and East oriented walls are most critical when it comes the exfiltration conditions. This was expected, as the main wind direction in Belgium equals the South-West (Figure 6.5a).
In addition, it should be stressed that Figure 6.5b presents weekly-averaged values, but that the hourly wind pressure differences are highly variable and can temporarily reach values exceeding the weekly averaged values by more than an order of magnitude.

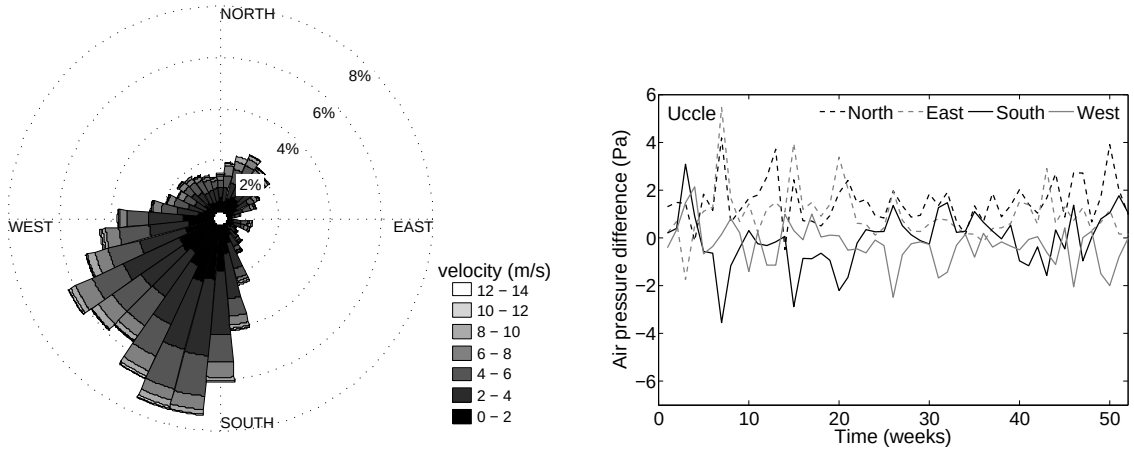

Figure 6.5: (a) Wind velocity distribution and (b) corresponding weekly averaged surface wind pressures on North, East, South and West oriented facades.

The drawback of using surface-averaged wind pressure coefficients is that no wind-induced cavity ventilation can be included because this method assumes a constant pressure across the height of the wall. As a remedy, for the simulations with a ventilated cladding layer, the differences between local C_p-coefficients at the level of the inlet and outlet are applied on top of the surface-averaged coefficients. The applied local wind pressure coefficients in this work were adopted from Nore (2009), who determined the local C_p-coefficient at the inlet and outlet of the cavity of a single storey building by CFD-simulations. As a conservative assumption the C_p-coefficients in the middle of Nore's test building were adopted here. Nore (2009) provided these coefficients for four wind directions, so, interpolation is applied for the intermediate wind directions in this study.

Mechanical ventilation Finally, also ventilation systems can cause pressure differentials across the building envelope. Kalamees et al. (2010) stated, based on field measurements combined with computer simulations, that very airtight dwellings are susceptible for higher air pressure differences induced by mechanical ventilation systems. Kalamees et al. (2010) reported values up to 30 Pa as a result of unbalanced ventilation systems. However, as most of today's high performance buildings are provided with balanced ventilation, this study only ascribes an overpressure of 5 Pa to the mechanical ventilation.
In summary Figure 6.6 illustrates the total air pressure difference across a North facing wall combined with its different components.

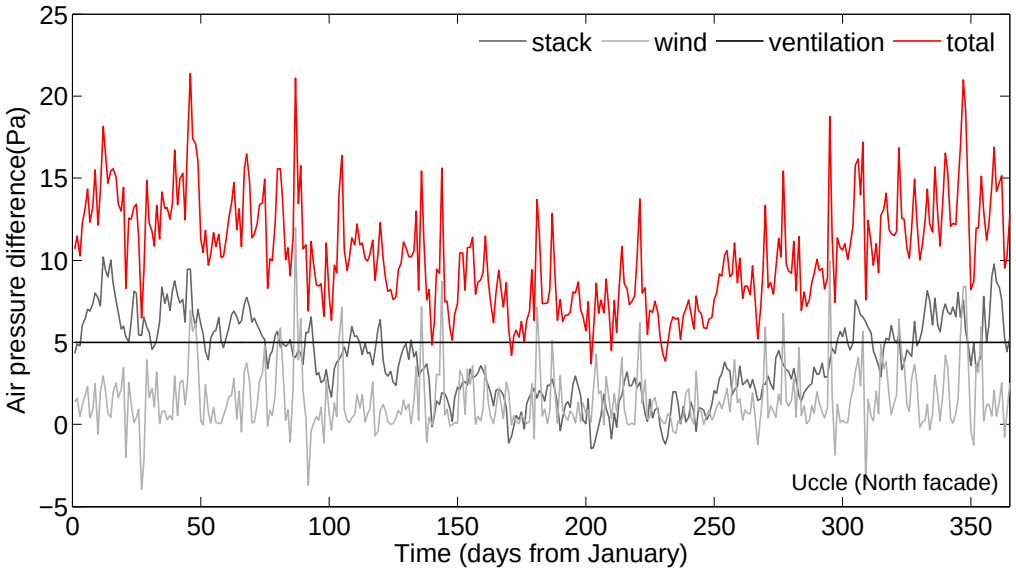

Figure 6.6: Overview of air pressure differences (daily averaged).

6.2.3 Interior relative humidity

The interior relative humidity depends mainly on the weather conditions, ventilation rate, vapour production and hygroscopic properties of the corresponding rooms. Several simplified algorithms have been proposed in the scope of standard condensation assessment methods to approximate the interior humidity levels.
The most simplified approaches correspond to yearly functions, independent of the outer climate, such as proposed in WTA 6-2 01/E in Germany. According to this method, the interior relative humidity and temperature are sinusoidal functions with a period of one year and the maximum value in summer. To differentiate between different vapour production levels, three moisture load classes (low, medium, high) are introduced in this model.
A second method, ISO 13788:2001, is most often used for hygrothermal simulations in Europe. This approach, summarised in Figure 6.7, expresses the vapour pressure difference between the interior and exterior air as a function of the monthly mean exterior air temper-

ature. Depending on the vapour production level, this method differentiates between five climate classes. As this method is implemented in a European standard, it aims to cover a whole range of climates and building practices. Therefore, it is of interest to verify the accuracy of this approach by comparing it with measured *in situ* data. A German study by Künzel (1997) measured during one year the humidity levels and outdoor conditions in 10 different spaces. The result of this limited study showed that all monitored rooms correspond to climate class II or lower. In addition, a more detailed survey in Finland by Kalamees (2006), compared the measured conditions for 101 lightweight family houses with the proposed methodology of ISO 13788:2001. The results of Kalamees (2006) revealed that, for cold periods, 90% of the measured data lies within climate class II, corresponding to very low vapour production levels. Yet the data set of Kalamees (2006) included normal family houses which are expected to correspond to class III or IV. Hence, in summary the measured data of Künzel (1997) and Kalamees (2006) both showed that the calculation method in ISO 13788:2001 is rather conservative.

A similar method is the Belgian classification of Indoor Climate Classes (TV215). This methodology is based on a statistical analysis on data from long periods of monitoring, carried out between 1974-1992 in about fifty social houses in Belgium (Hens 1992). Figure 6.7 demonstrates the calculation procedure in which the interior humidity levels are based on the weekly outer air temperatures. Here, the limit of the climate classes corresponds to the 5, 50 and 95 % percentile of the measured data. Similar to the European method (ISO 13788:2001), the vapour supply decreases with higher exterior temperatures in the Belgian classification method. This trend can be explained by typical occupant behaviour in buildings with natural ventilation; less ventilation and higher vapour production in colder periods. Furthermore, it can be noted that, compared to ISO 13788:2001, the Belgian classification method predicts lower vapour supply levels in residential buildings. It can be questioned, however, to which extent this approach - based on measured data of older dwellings - is still valid for the current building stock and more specifically for high performance buildings with mechanical ventilation systems.

More accurate predictions of the indoor humidity, however, can be obtained from building simulation models. Most simplified versions of such models assume a single zone in direct interaction with the outer air. This approach, which basically solves a vapour mass balance, is only justified if the input parameters, such as the ventilation rate and moisture production, can be estimated with sufficient accuracy.
Vereecken et al. (2011) presents a single zone model, taking hygric buffering capacity of the room into account:

$$\left(\frac{V}{R_v T_i} + \frac{100 HIR^* V}{p_{v,sat}(T_i)}\right)\frac{\partial p_{vi}}{\partial t} = (p_{ve} - p_{vi})\frac{nV}{3600 R_v T_i} + G_{vp} \tag{6.10}$$

in which V (m^3) corresponds to the volume of the room and HIR^* (kg/(m^3 %RV)) to its hygric

inertia, n (1/h) is the ventilation rate and G_{vp} (kg/s) is the vapour production in the room. The advantage of this single zone model is that these parameters can be adjusted depending on the purpose of the simulation. Yet occupant behaviour, such as lower moisture production and higher ventilation rates in summer, which are captured in the statistical approach of Hens (1992) are difficult to include in Eqn. 6.10 as such data is not available in the literature.

The models based on a classification system tend to overestimate the interior vapour pressure (Künzel 1997, Kalamees 2006). In order to quantify this observation for a Belgian climate, this section compares the above-mentioned models.
The parameters for the single zone model are chosen conservative: a small volume of 50 m^3 with a high moisture load of two active persons (120 gram/h)[7] between 8h-22h. The nominal ventilation rate in living spaces is 3.6 $m^3/(m^2\,h)$ according to the Belgian standard (Limb (2001)), corresponding to a ventilation rate of 1.5 1/h for this room. A recent Belgium study by Stranger et al. (2012), however, revealed that the operation ventilation rates in low-energy dwellings are far lower than the prescribed nominal rates. Therefore, to verify the effect of lower ventilation rates in operation, also the indoor humidity level with a ventilation rate of 0.5 1/h was simulated. Nevertheless this value is three times lower than the nominal ventilation rate for the current case, it still corresponds to the upper limit of the measuring results of Stranger et al. (2012). Finally, a value of 1.5 gram/(m^3%RV) was chosen for the hygric inertia based on the measured values by Janssen & Roels (2009). Furthermore, it should be noted that the interior vapour pressure is assumed equal to the exterior vapour pressure when the exterior temperature exceeds 20°C.
The results for both ventilation rates (0.5-1.5 1/h), calculated on a hourly basis, are compared with the European and Belgian classification system in Figure 6.7. Here, the calculated weekly averaged vapour pressure differences (interior - exterior) based on the different models are presented. In addition, measured inner climate conditions of a recent dwelling with a balanced ventilation systems (KUL 2011) are included in this figure (in red). This figure indicates that, for the ventilation rate in operation (0.5 1/h) in the single zone model (referred to as HIR*), the inner vapour pressures still correspond to the lower part of CC III in the Belgian system and upper bound of the CC II in the European system in the winter period. Moreover, for the situation in which the minimum ventilation requirements of 3.6 $m^3/(m^2\,h)$ (1.5 1/h) are applied, the indoor humidity corresponds to the lowest climate class in both the Belgian and European system. Consequently, this comparison confirms the findings of Künzel (1997) and Kalamees (2006), stating that the European classification system is overestimating the indoor humidity levels of residential buildings. Figure 6.7 further demonstrates that the measured indoor climate follows most closely the trend of the inner vapour pressures according to Eqn. 6.10 with a ventilation rate of 1.5 1/h and the lower climate class of European and Belgian classification system.

[7] according to Hens (2010)

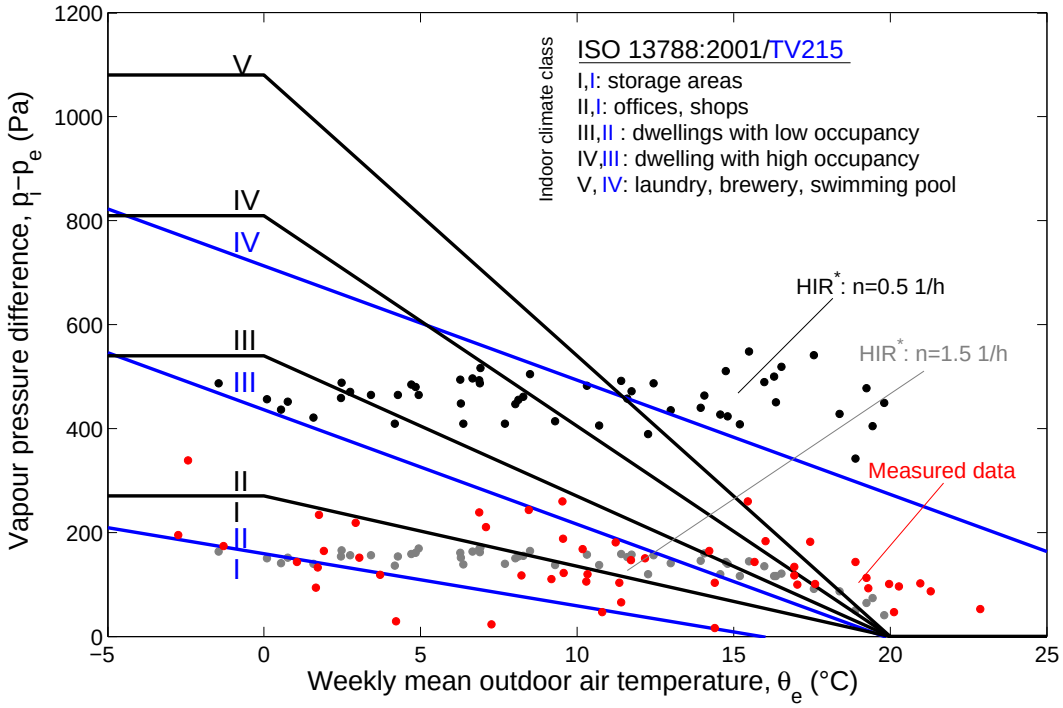

Figure 6.7: Comparison of three prediction methods for indoor humidity levels: ISO 13788:2001 (in black), TV215 (in blue) and Vereecken et al. (2011) (dotted) and recently measured interior climate in a dwelling with a balanced ventilation system (KUL 2011) (in red).

Finally, this figures shows that the vapour pressures are higher in the single zone model than the other models in summer conditions. This is attributed by the omission of seasonal human behaviour in this model, as mentioned earlier in the section. Nevertheless, the single zone model follows most closely the trend of the measured data in the range of interest (winter conditions). The building envelopes studied in this work are most often applied in buildings provided with mechanical ventilation systems. Consequently, the ventilation rates can be estimated accurately which is one of the prerequisites to obtain realistic results from Eqn. 6.10.

Based on the findings presented in this section, it is decided that the single zone model of Vereecken et al. (2011) is most suitable for the prediction of the interior humidity levels in the scope of this work. In the remainder of this chapter two variants will be applied as inner conditions; ventilation rate of 0.5 and 1.5 1/h. The impact on the simulation results will be explicitly compared in section 6.5.2.

6.3 Selection of moisture limit state criterion

The laboratory investigations of chapter 4 demonstrated that, depending on the configuration and material properties, the decisive moisture limit state criterion can either be mould

growth or interstitial condensation. As a consequence both criteria will be considered in the numerical analysis of the present chapter.
Section 2.4.1 already discussed various existing moisture performance limit states for the evaluation of timber frame building envelopes. The aim of the present section is to select appropriate methods for the verification of the hygrothermal risk of the simulation results of this work. In addition, the proposed methods will be verified with the laboratory results of chapter 4. First, a mould prediction model will be selected. Second, a method to predict interstitial condensation levels will be outlined.

6.3.1 Mould growth

Section 2.4.1 presented a brief overview of existing mould prediction models for the assessment of building components. It appeared that currently two models, the biohygrothermal model of Sedlbauer (2001) and the VTT-model of Hukka & Viitanen (1999), are capable of taking transient effects of mould growth into account. As mentioned in section 2.4.1, the main drawback of the bio-hygrothermal model is its high uncertainty in defining the 'material' properties of mould. Given this high uncertainty in combination with the lack of physical background on this approach, the VTT-model is selected for the evaluation of the mould growth in this work. This model, purely based on linear regression relations of laboratory measurements, is most recognised amongst the existing mould growth prediction methods in the international literature (e.g. Vinha 2007, Black 2006). An additional advantage of this model is its direct applicability as postprocessing tool, deriving the mould growth index from the temperature and relative humidity outputs. Vereecken & Roels (2012) showed, however, that induced by the various assumptions in mould prediction models, large differences can be obtained. As a consequence it should be stressed that such tools are preferably used to compare the mould growth risk of different components rather than making absolute predictions (Vinha 2007).
The following paragraphs first provides a brief description of the VTT-model and confronts thereafter this model with the laboratory observations of section 4.1.6 (Figure 4.14).

Brief description of VTT-model[8] The original VTT-model (Hukka & Viitanen 1999) is restricted to wood only (pine and spruce). Later this model was updated by including prediction methods to simulate mould growth on other building materials, such as concrete, wood based materials, insulation materials (Ojanen et al. 2010). As the general methodology remained the same, emphasis of this section is on the original VTT-model for wood only. The extension towards other materials is briefly touched at the end of this description.

The VTT-model applies a mould grow index (M), defined in Table 6.2, to express the presence of surface mould growth. The model starts with the definition of the critical relative

[8] Based on Ojanen et al. (2010)

humidity (RH_{crit}) for different temperatures (Eqn. 6.11). This critical value is the lowest humidity where mould growth is possible when the material (wood) is exposed to it for a long enough period:

$$RH_{crit} = \begin{cases} -0.00267\theta^3 + 0.160\theta^2 - 3.13\theta + 100, & \text{when } \theta \leq 20°C \\ RH_{min}, & \text{when } \theta > 20°C \end{cases} \tag{6.11}$$

For wood and wood-based products, RH_{min} is 80 %.
In the original model for wood, the mould growth is calculated from Eqn. 6.12:

$$\frac{dM}{dt} = \frac{k_1 k_2}{7 t_{M=1}} \tag{6.12}$$

in which k_1 represents the intensity of growth (Eqn. 6.13) and $t_{M=1}$ the time needed to start the growth (M = 1) (Eqn. 6.14). Factor k_2 represents the moderation of growth intensity when the mould index level (M) approaches the maximum peak value in the range of 4 < M < 6 (Eqn. 6.13).

M (-)	Description of the growth rate
0	No growth
1	Small amounts of mould on surface (microscope), initial stages of local growth
2	Several local mould growth colonies on surface, <10% coverage (microscope)
3	Visual findings of mould on surface, <10% coverage (visual), or <50% coverage of mould (microscope)
4	Visual findings of mould on surface, 10%-50 % coverage (visual), or <50% coverage of mould (microscope)
5	Plenty of growth on surface, >50% coverage (visual)
6	Heavy and tight growth, coverage about 100%

Table 6.2: Definition of Mould index (M) according to Hukka & Viitanen (1999).

$$k_1 = \begin{cases} 1, & \text{when } M < 1 \\ \dfrac{2}{t_{M=3}/t_{M=1} - 1}, & \text{when } M > 1 \end{cases}, \qquad k_2 = max[1 - exp(2.3(M - M_{max})] \tag{6.13}$$

$$t_{M=1} = exp(-0.68ln(\theta) - 13.9ln(RH) + 0.14W - 0.33SQ + 66.02) \tag{6.14}$$

$$t_{M=3} = exp(-0.74ln(\theta) - 12.72ln(RH) + 0.06W + 61.50) \tag{6.15}$$

where $t_{M=3}$ is the time needed to reach level M = 3 (Eqn. 6.15), W is the timber species (0 = pine and 1 = spruce), and SQ is the surface quality (SQ = 0 for sawn surface, SQ = 1 for kiln-dried quality). For other materials than wood, the value SQ = 0 is used, which omits this factor. The maximum growth conditions are restriced by the prevailing temperature and

relative humidity conditions by:

$$M_{max} = max\left(A + B\frac{RH_{crit} - RH}{RH_{crit} - 100} - C\left(\frac{RH_{crit} - RH}{RH_{crit} - 100}\right)^2\right) \tag{6.16}$$

in which the model parameter are A = 1, B = 7 and C = 2 for wood.
For unfavourable conditions (θ>20°C or $RH<RH_{crit}$) a delay of mould growth is defined by Eqn. 6.17, where $t - t_1$ is the time exposed to unfavourable conditions.

$$\frac{dM}{dt} = \begin{cases} -0.00133, & \text{when } t - t_1 \leq 6\text{h} \\ 0, & \text{when } 6\text{h} < t - t_1 \leq 24\text{h} \\ -0.000667, & \text{when } < t - t_1 \geq 24\text{h} \end{cases} \tag{6.17}$$

So far the description was restricted to the original VTT-model for wood. This model was extended for other building materials by Ojanen et al. (2010), as mentioned at the beginning of the section. This model distinguishes between four material classes related to their sensitivity for mould growth: (1) very sensitive, (2) sensitive, (3) medium resistant and (4) resistant for mould growth. The main difference of this updated version is the definition of the model parameters k_1, A, B and C and a reduction factor C_{eff} for mould growth delay under unfavourable conditions. The first four parameters directly depend on the materials sensitivity for mould growth. The latter on the material mould decline behaviour. More details on the updated VTT-model can be found in Ojanen et al. (2010).

Confrontation of VTT-model with laboratory results Key question remains the applicability of the presented mould prediction model. In order to verify its accuracy and examine the impact of the discussed model parameters, the present section confronts this model with the limited amount of mould observations in the hotbox/coldbox investigation in section 4.1.6. There, the least airtight wall of the first test series (Ic) showed traces of mould on the warm side of the weight specimen. No mould could be visually observed for this wall (M ≤ 2) at the start of measuring step 3. Mould was however clearly developed at the time of the following visual control at the end of this step (Figure 4.14). According to the classification system of Table 6.2, the top specimen corresponded to M = 4, the middle specimen to M ≤ 2 and the bottom sample to M = 3.
The VTT-model is applied to derive the mould index from the measured relative humidity levels and temperatures at these positions. Figure 6.8 shows the resulting mould index for the three positions: (1) top (black), (2) middle (red) and (3) bottom (blue). In addition, the impact of the measuring uncertainty on the RH-sensor (±2%) is presented as dotted lines. The material of interest in this test wall is bituminous impregnated wood fibre board (BIFBII). As this material is not included in the material classification system of the updated VTT-model, the calculations are performed for both the 'very sensitive' and 'sensitive' ma-

terial classes. The mould index in the left hand side figure is calculated with the original VTT-model and assuming pine (W = 0, SQ = 0). These model parameters correspond to the 'very sensitive' material class of the updated model. The right hand side figure, however, is modelled according to the 'sensitive' material class of the updated model. This material class, which is less susceptible for mould growth than pine, includes materials such as glued wooden boards and spruce boards.

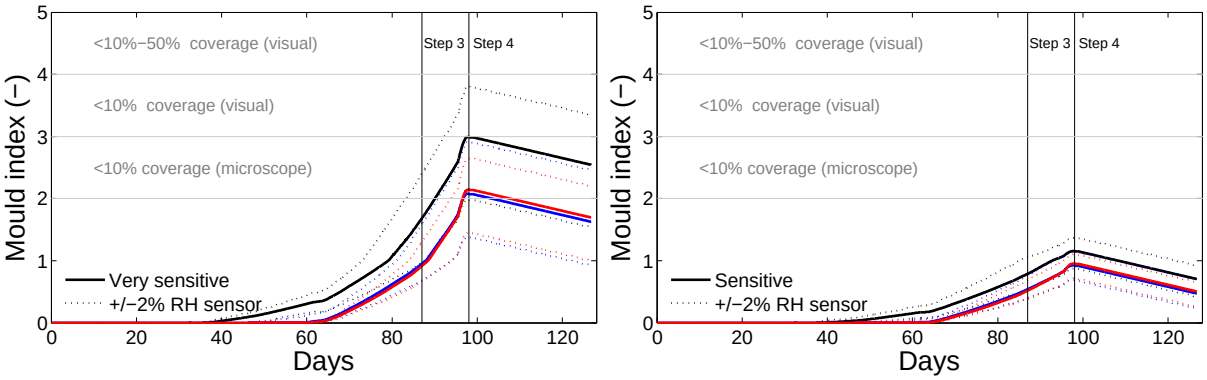

Figure 6.8: Mould index calculated from the measured relative humidity and temperature at top (black), middle (red) and bottom (blue) height for test wall Ic (section 4.1.6). Left: very sensitive material class and Right: sensitive material class.

Figure 6.8 indicates that no visual mould is obtained when processing the measured data with the 'sensitive' material class parameters (right figure). Better agreement with the experiment is found when mould growth is modelled according to the 'very sensitive' material class (=original VTT-model). Here, the mould index at the top level reaches M = 3, while the middle and bottom position has a maximum of M = 2. Still, this is an underestimation of the experimental observation. But, the trend that the first visible mould growth occurred at the end of measuring step 3 is in accordance with the experimental results. Additionally, this figure indicates the large uncertainty on the calculated mould index as a result of the uncertainty on the RH-sensor.
In summery it can be stated that the experimental observations lie within the uncertainty interval of the modelled mould index according to the 'very sensitive' material class. As a consequence, these model parameters are adopted for the prediction of mould growth on BIFB in the simulations here.

6.3.2 Interstitial condensation

Restricting interstitial condensation within the building components is an indirect method to prevent biological growth. This limit state corresponds to the starting point of drainage of the condensate to prevent its accumulation on lower positioned biological materials, such as wooden beams and plates. The model description of chapter 5 showed that condensation rates are not directly calculated within the Delphin framework. As a remedy, potential

condensation planes are introduced by providing a material layer, modified to capture condensation. The moisture retention curve of this material layer remains zero over the full range of capillary pressures. Only for very low capillary pressures[9] its moisture retention curve shoots to high values.

In order to verify the applicability of the proposed method, the small-scale experiments of section 4.2, imposing condensation conditions on BIFB and FCB specimens, are simulated here. Figure 6.9 compares the measured and simulated relative humidity levels for test series FCBa and BIFBb, both exposed to 20°C and 80 %. As discussed in section 4.2, condensation conditions first occurred on the FCB specimen. This is shown by the black curve in Figure 6.9, which represents the measured relative humidity at the condensation plane. Saturation was already measured after the first day for this material. The measured relative humidity increased much slower for the test with BIFB and reaches after one week condensation conditions. The same trend is predicted by the numerical simulations. The simulated relative humidity, depicted in red, shows a faster increase for the FCB specimen in comparison with the BIFB. The first specimen reached a relative humidity of 100 % after 40 hours. The latter, however, only after 120 hours. When saturation conditions are reached, the simulated condensate start to accumulate (in blue) at the surface of the specimen.

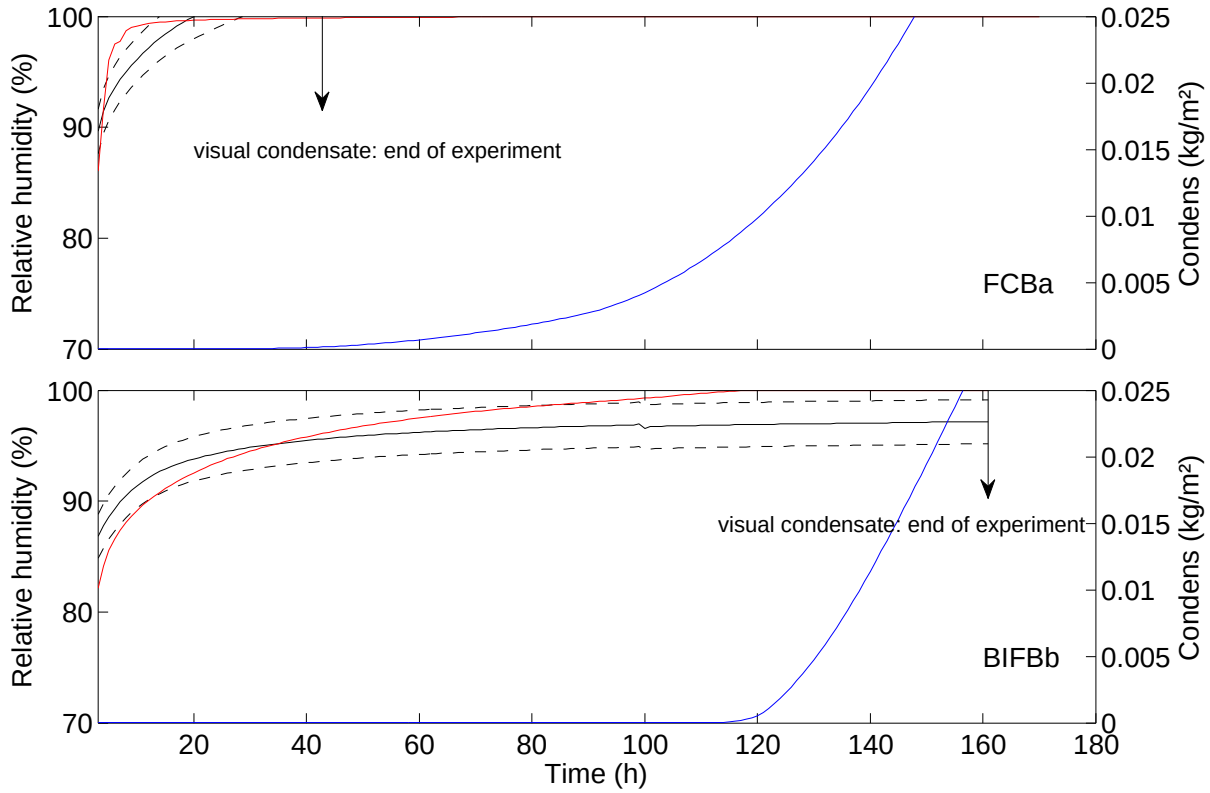

Figure 6.9: Simulation of condensation experiment of section 4.2 (simulated relative humidity (red), measured relative humidity (black) and simulated condensation (blue)).

In summary, it can be stated that it is difficult to draw general conclusions on the ap-

[9] <10 Pa, which corresponds to a relative humidity levels > 99.9999 %

plicability of the discussed simulation method to incorparte interstitial condensation. The brief evaluation with a limited amount of small-scale experiments showed, however, that the general trends are in good agreements with the measured data.

6.3.3 Proposed moisture limit states

The previous two sections verified the simulation of mould growth and interstitial condensation with the numerical model of chapter 5. Though the simulation results follow the same trends as the laboratory tests under steady-state conditions, it should be recognised that higher deviations from reality are expected under transient conditions. As a result, the definition of moisture limit states for the assessment of the numerical results in the remainder of this chapter should be read as a transition zone rather than a strict threshold value.

Mould spores are most obvious airborne components of fungal contamination, influencing occupant's health due to the settling and spreading of pathogens (e.g. Piecková & Jesenská 1996, Reboux et al. 2010). It remains, however, difficult to verify to which degree mould spores, located within the building envelope, influence the indoor air quality. Keeping in mind that this limit value will be treated more as a transition zone, a maximum mould growth level of 3 is applied in this work. This limit corresponds to a visual mould growth covering less than 10 % of the surface which seems to be reasonable for building materials located at the outside of the building envelope. This value is also mentioned in a Canadian study by Rao et al. (2009), who studied the transport of mold spores from slightly mouldy wooden studs to the indoor environment on full-scale test walls. Wooden studs with slightly visible surface mould (10 % of surface area, which equals a mould index of 3) were used for some of the wall assemblies, while clear studs were used for the remainder. The results from this experiment did not support a statistically significant increase of spore movement into the indoor space due to the use of slightly mouldy studs.

When it comes to interstitial condensation, on the other hand, the moisture limit state should avoid run-off, and thus, moisture accumulation on lower regions within the building envelope. The onset of run-off caused by condensation is a complex phenomena depending for example on the materials surface roughness. As the detailed determination of these conditions, such as in Van den Brande et al. (2012), falls beyond scope of the present work, a conservative simplified criteria is applied. The applied threshold value for condensation is adopted from Janssens (1998) who proposed a maximum value of 0.1 kg/m^2. This limit is based on laboratory work on spunbonded foils. Such materials have a low surface roughness in comparison to the fibreboards applied in this work (BIFB), so, the proposed limit state corresponds to a conservative assumption.

6.4 Precision/simplification of simulation grid

This paragraph verifies the impact of several modelling simplifications to reduce simulation times for a reference wall configuration (Figure 6.10). This reference assembly corresponds to wall Ib, tested in laboratory condition (see chapter 4). This exterior wall is insulated with 30 cm mineral wool (MW20) with a density of 20 kg/m^3 and has a BIFBI exterior air barrier. OSB is applied on the inner side as interior vapour barrier in which a 1 cm slot at 20 cm from the top and bottom is modelled in accordance with the experiment (see Figure 4.4). In addition, this wall is extended with top and bottom wooden plates and the interior side is provided with an insulated service cavity, finished with gypsum board. Note that significant air leakages (30 m^3/(m h Pa)) are modelled at the top and bottom of the gypsum board to avoid a continuous inner air barrier. Furthermore, the wall is extended with a wooden cladding system. The material properties of the cladding system are based on Nore (2009); the wood cladding layer is modelled according to Zillig (2009) and its exterior paint layer has an s_d-value of 0.1 m.
The wall was oriented to the North and exposed to Belgian climate conditions on hourly basis for these exploring simulations. The impact of the boundary conditions on the results will be examined in the following section. This section studies the impact of three grid simplifications: (1) removing top and bottom plate, (2) excluding cavity ventilation and (3) including the service cavity as transfer coefficients. Additionally, the impact of the pressure update interval is studied as well. Main emphasis is on the justification and the corresponding simulation performance of the proposed modelling simplifications.

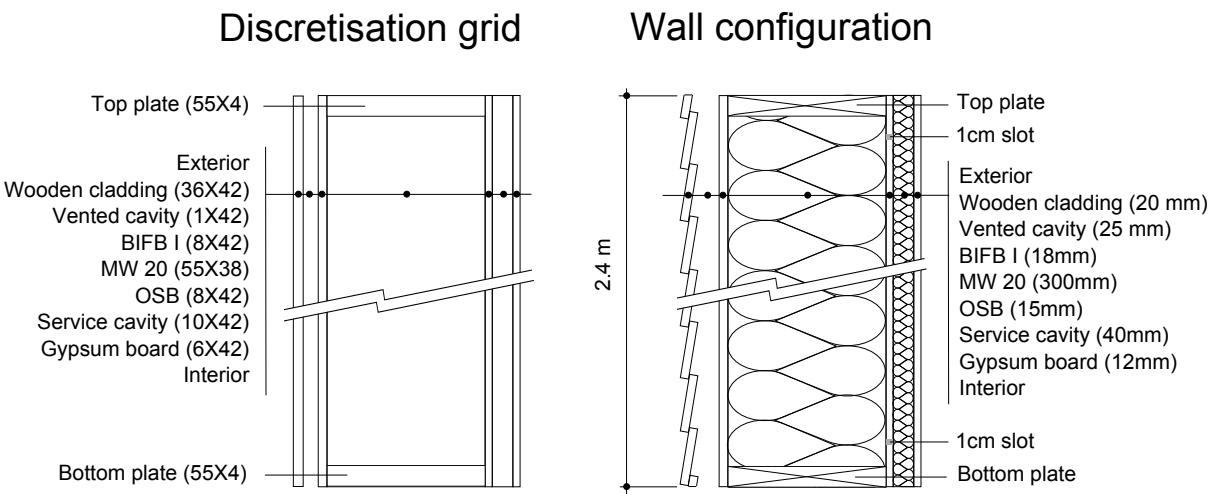

Figure 6.10: Wall configuration (right) and corresponding simulation grid (left) in which the number of elements are mentioned between brackets.

6.4.1 Simulation grid

Before modelling simplifications can be introduced, a reliable reference simulation grid needs to be defined first. Therefore, this section starts with a grid sensitivity analysis. Best simulation performance was obtained with an equidistant grid. Consequently, an equidistant 124 by 42 grid, depicted in Figure 6.10, was selected. To verify the accuracy of this proposed grid, a sensitivity analysis was performed with a refinement factor of 1.5. Figure 6.11 investigates the impact of this grid refinement for (a) the moisture content at the top of the exterior air barrier and (b) the ventilation rate behind the cladding. The results show that the obtained differences between these two grids are less than ±5 % for both the moisture content levels and the ventilation rates. This is an acceptable error level, so, the proposed grid of Figure 6.10 can be safely applied for the further simulations in this chapter.

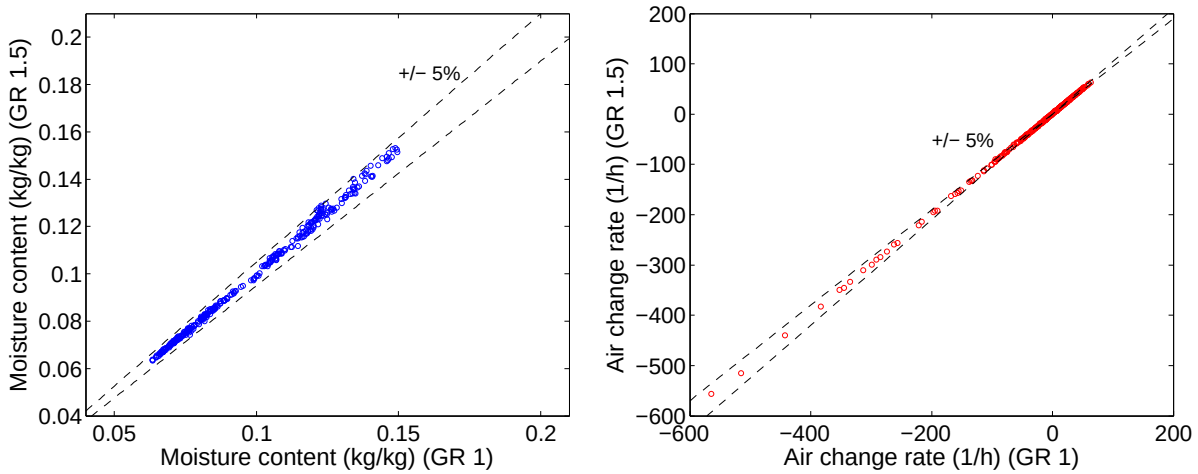

Figure 6.11: Impact of a 1.5 times grid refinement on (a) the top moisture content of the exterior air barrier and (b) the ventilation rate behind the cavity (daily averaged).

Impact cavity ventilation

Including cavity ventilation in the hygrothermal simulations may significantly increase simulation times. Therefore, this section investigates the necessity of taking this air cavity into account. As mentioned above the configuration studied here corresponds to a North facing wall (Figure 6.10) with a cladding system of wooden sidings (20 mm) with a ventilated cavity of 25 mm.

The airflow in the ventilated cavity is calculated according to Hagen-Poiseuille's law (Eqn. 5.12), assuming fully-developed laminar flow between parallel plates. So far, no local losses have been included in the hydraulic network approach in this work. This simplification holds for sufficient narrow channels, such as small deficiencies around the insulation layer (Janssens 1998). However, for the ventilated cavity behind the cladding, which has a width of 25 mm, this assumption is no longer realistic. To take the local losses of the inlet and outlet of cavity

into account, Eqn. 5.12 can be rewritten in its Darcy-Weisbach formulation:

$$\Delta p = \left(\frac{f L}{D_H} + \Sigma C\right)\left(\frac{\rho \overline{u_a}^2}{2}\right) \tag{6.18}$$

in which Δp refers to the pressure drop across the cavity, L its length, ΣC the local losses and f the Darcy-Weisbach friction factor, which equals $96/Re$ for fully-developed laminar flow. Hydraulic resistance data sets (e.g. ASHRAE 2009) provide standard values for simplified inlet and outlet geometries. However, inlet and outlet losses for specific cavity ventilation geometries are only scarcely documented in the literature. Nore et al. (2010) report values between 0.59-0.65 for the ratio of the local losses to the total losses for a one story height cavity[10] (25 mm) with free top and bottom openings. Given the uncertainty on the local losses at the level of the inlet and outlet, these resistances were included as a parameter to verify their impact. Simulations were performed with a ratio of the local losses to the total losses of 0.7, 0.8, 0.9 and 0.99.

Figure 6.12b presents the simulated daily-averaged ventilation rates in the cavity. This figure, in which positive values corresponds to upward airflow, indicates that the daily-averaged airflow pattern is rising in summer conditions. This flow is mainly driven by short wave radiation, increasing the temperature of the cladding. Yet the highest ventilation rates are wind-driven, and thus, result to short peaks corresponding to a downward airflow field. In winter conditions, when short wave radiation on this North facing wall is limited, the cavity air flow is mainly driven by wind pressure differences only, resulting in downward airflow peaks. Figure 6.12b further shows the importance of the local resistances on the overall cavity ventilation. For the most open situation the ventilation rate can reaches averaged values up to 600 ACH. For the situation with the highest inlet and outlet resistances (0.99), on the other hand, the ventilation rate equals almost zero throughout the year.

The corresponding moisture contents at the top and bottom of the exterior air barrier are presented in Figure 6.12a. This graph shows that the moisture content levels are only slightly influenced by the inlet and outlet resistances. Only for very high inlet and outlet resistances (0.99) higher moisture content levels and longer drying periods are noticed. This observation indicates that for the current wall configuration, a cladding with normal openings is capable to evacuate the incoming vapour flux.

In addition, a simulation for which the ventilated cavity and the cladding layer were excluded from the model was performed. For this situation the exterior climate is directly imposed to the exterior air barrier. Figure 6.13 compares the obtained moisture content levels with the configuration including a cavity with a ratio of the local losses to the total losses of 0.8 (Figure 6.12). As the exterior air barrier is now directly exposed to the exterior

[10] wooden sidings

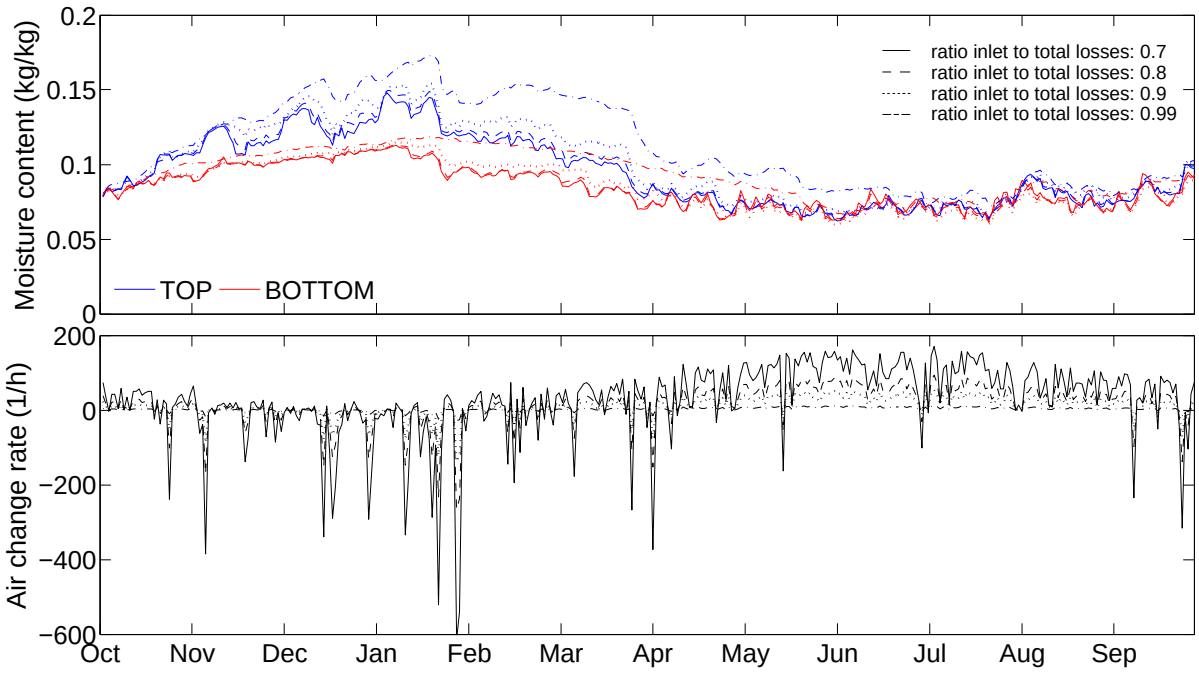

Figure 6.12: (a) Top and bottom moisture content of exterior air barrier for a configuration with a cladding system with ventilation openings, (b) Air change rate in the ventilated cavity (bottom) (daily averaged values).

climate, higher fluctuations in its moisture content are noticed. Furthermore, it can seen that the results of the simulation without cladding system are most of the winter period higher than for the situation with a ventilated cavity. The main reason for these differences are the colder surface temperatures of the exterior air barrier in case the cladding is excluded from the model. The surface temperature of the exterior air barrier is lower for the simulation without cladding system because long wave radiation is then directly exposed to this surface. When a cladding system is included in the model, this cooling effect of long wave radiation becomes less dominant as the cladding is also warmed up in winter conditions by the air flow in this cavity. For the current configuration, the surface temperature of the exterior air barrier is on the average 0.6°C warmer when the cladding is included in the model for the winter months January and December.

Besides underestimating the temperatures of the exterior air barrier in winter conditions, the simulation without cladding might result in too optimistic exterior vapour pressure boundary conditions. When the ventilation rate is too low to evacuate the incoming vapour flux, the vapour pressure in the cavity increases. This is not taken into account for the simulation without cladding system, which basically ascribes the vapour pressure of the exterior climate to the wall. To illustrate this statement, Figure 6.14 compares the top and bottom temperatures and vapour pressures in the cavity with the exterior climate conditions for the simulation in which the ratio of the local losses of to the total losses equal 0.8 for the month January. This figure demonstrates that the temperature at top of the cavity is only slightly

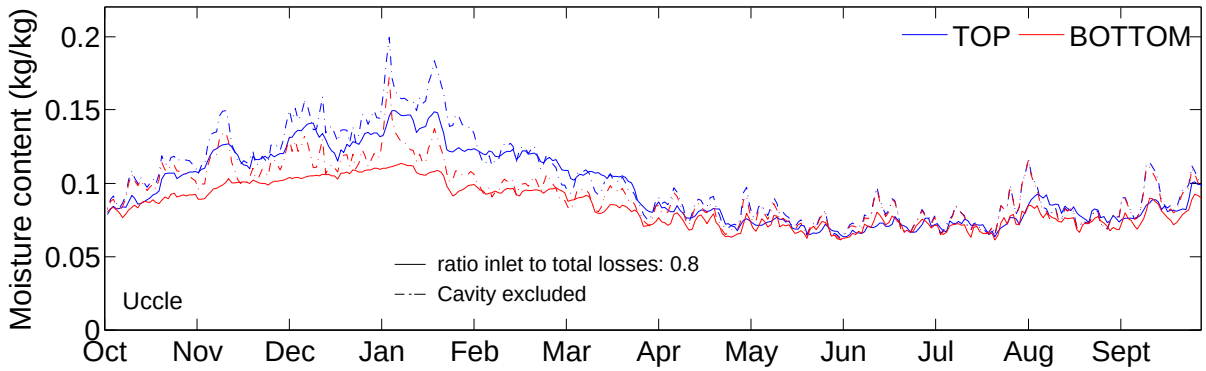

Figure 6.13: Comparison of moisture content of exterior air barrier for a configuration with a cladding system (0.8) and configuration without cladding and ventilated cavity (daily-averaged values).

higher than the bottom temperature. In addition, both the temperature at the bottom and the top of the cavity are more or less the same as the exterior temperature. However, Figure 6.14 shows that the vapour pressure in the cavity mostly exceeds the exterior vapour pressure. Moreover, this figure illustrates that the vapour pressure at the top of the cavity is higher than the bottom value. This effect, which can not be taking into account without including the cladding in the simulation grid, becomes even more important for situations with higher vapour fluxes towards the cavity such as for less airtight exterior barriers.
Based on the findings in this paragraph, it is decided to retain the cavity ventilation in the simulation grid. Though the simulation time could be reduced with 50% by excluding the cavity ventilation from the model, this section emphased the importance of taking cavity ventilation into account in the simulations. It was illustrated that the importance of the inlet and outlet resistance had limited impact when the ratio of the local losses to the total losses was lower than 0.9. Therefore, a value of 0.8 for this ratio is assumed in the further simulations.

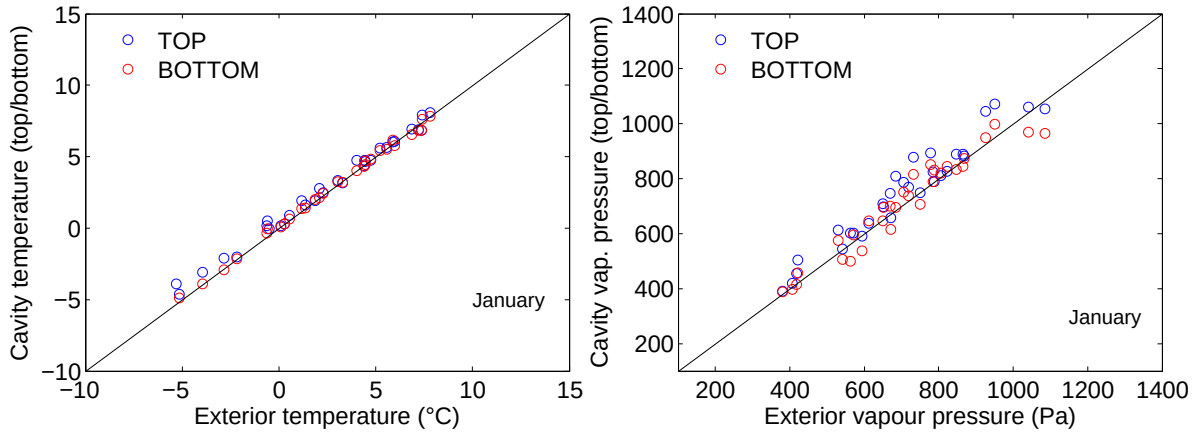

Figure 6.14: Comparison of exterior temperature and vapour pressure with the conditions at the top and bottom of the cavity (daily-averaged).

6.4.2 Interior finishing materials

As the highest moisture levels are concentrated at the exterior of the building component, it can be questioned whether the inner service cavity and adjacent finishing layers should be modelled in detail (Figure 6.10). To answer this question Figure 6.15a compares the moisture content of the exterior air barrier for the simulation including these layers and the simulation wherein these layers are incorporated in the heat and vapour transfer coefficients. Note that the air resistance of the service cavity and the inner finishing board are neglected in the latter approach. Figure 6.15a illustrates that the impact of this simplification is less than 5 %. As a result, the inner service cavity and gypsum board can be safely modelled as transfer coefficients, corresponding to a 30 % reduction of the simulation time.

6.4.3 Top and bottom plate

A third potential simplification in the simulation grid is the omission of the top and bottom plates. Commonly, these top and bottom plates are included in hygrothermal modelling of lightweight walls (e.g. Geving 1997, Økland 1998). For the current configuration, however, it was noticed that including the top plate did not significantly change the hygrothermal risk of the component. In contrast, it was observed that the moisture content level at the top of the exterior air barrier increased by excluding the wooden plates from the simulation grid.

This can be explained by a combination of the higher thermal conductivity and hygroscopic buffer capacity of the wood in comparison with the mineral wool. The first results in higher temperatures at top of the exterior air barrier, and thus, lower relative humidity levels when the plates are present. The latter reduces the moisture load on the exterior barrier as the incoming vapour flux can be partly stored in the wood. Figure 6.15(b) compares the moisture content at the top of the exterior air barrier for the simulation with and without top and bottom plates (in blue). In addition, also the moisture content of the exterior barrier just below the top plate is included in this comparison (in green). The figure illustrates that the highest moisture content is shifted downward by including the top plate in the calculation grid. Additional simulations in which the wooden plates were modelled with the same thermal conductivity as the mineral wool layer revealed that the hygroscopic buffer capacity of the wooden plates has the highest impact on the reduced moisture load on the exterior air barrier. Furthermore, the impact on the mould growth index was verified as well. For both the simulation with and without plates the maximum mould growth index equals 3.4 (-) and is located at 16-18 cm from the top of the wall. This is significantly higher than the most critical mould growth level obtained in the wooden plates, which was only 0.65 (-).
In summary, it can be concluded that excluding top and bottom plate from the simulation grid results in a slightly more critical situation. As a consequence it is a safe assumption to remove both plates from the simulation grid. By excluding the wooden plate from the grid the simulation time could be reduced by 25 %.

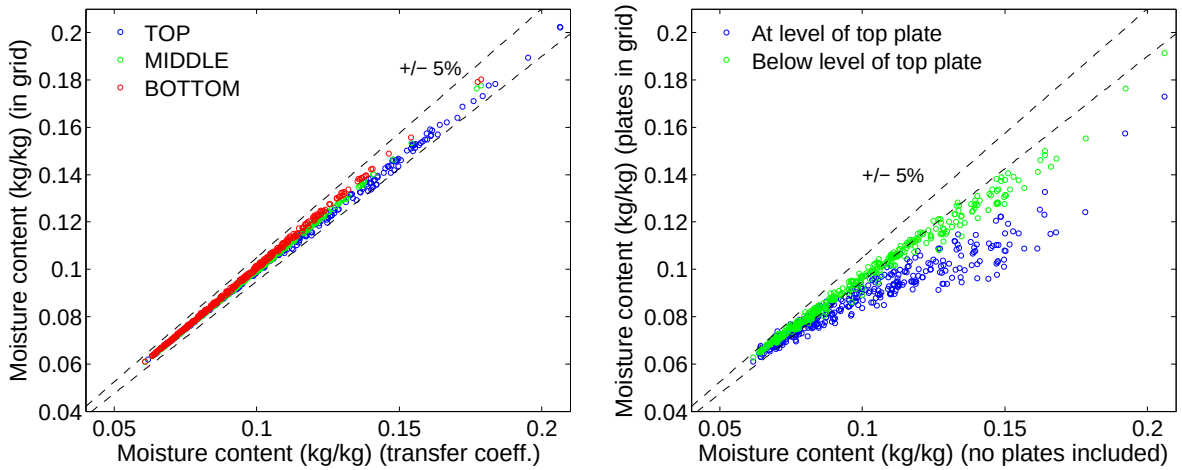

Figure 6.15: (a) Impact of introducing inner finishing layers as transfer coefficient and (b) simulation with and without wooden plates (daily-averaged values).

6.4.4 Update interval of air pressure field

A staggered scheme is applied for the integration of the heat and moisture balance and the air mass balance equations in time (Figure 5.3). The present section verifies the impact of the air pressure update interval. Figure 6.16 compares the moisture content at the top of the exterior air barrier and the ventilated cavity's air change rate for the simulation in which the pressure field is updated after each time step (blue), each 10 minutes (red) and each 30 minutes (green). This figures illustrates that the impact on the results is negligible when the update interval is 10 minutes or less. For an update interval of 30 minutes, deviations of more than 5 % on the ventilation rate are noticed. However, its influence on the moisture content largely remains below 5 %. Similar conclusions were drawn in model evaluation section 5.4.2.

The impact on the simulation time, on the other hand, was limited to less than 7 %. It appeared even that the longer update intervals resulted in longer simulation times. As a consequence, in the remainder of this chapter the air pressure field is update after each time step in the integration of the heat and moisture transport.

6.4.5 Summary

In summary this section demonstrated the necessity to include cavity ventilation in the simulation grid. Furthermore, it has been shown that top and bottom wooden plates can be safely excluded from the calculation model. Also ascribing the inner service cavity and interior finishing material as a transfer coefficient to the wall did not influence the hygrothermal risk. As a result of these simplifications, the simulation time could be reduced to approximately 4 hours[11] for the configuration studied.

[11] on a 3.07 GHz / 48 GB computer

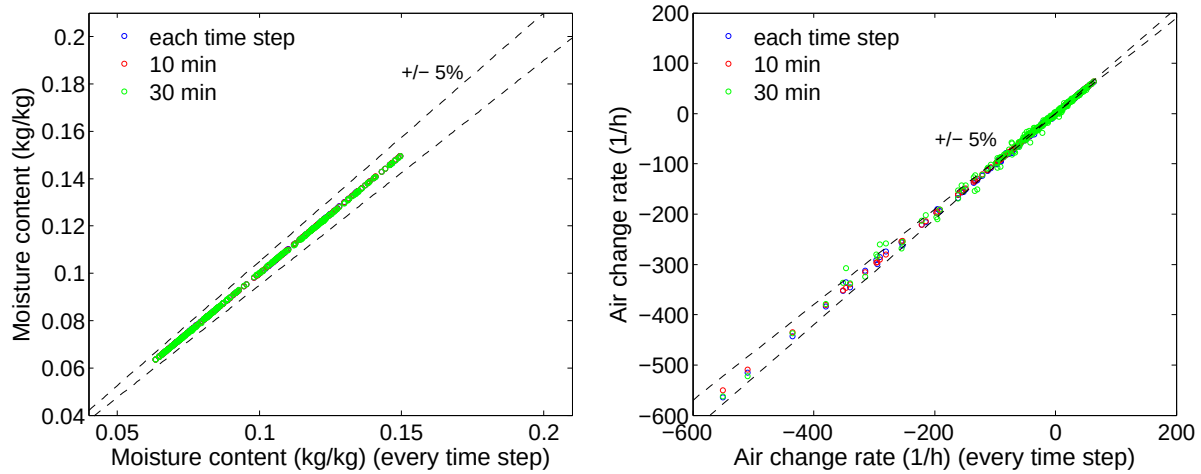

Figure 6.16: Impact of the air pressure update interval on the exterior air barriers moisture content and ventilation rate of the cavity ventilation (daily-averaged values).

6.5 Reference simulation

The hygrothermal performance of building components highly depends on both the exposed interior and exterior boundary conditions. Section 6.2 illustrated the important impact of the walls orientation on the exterior surface conditions, and e.g. the large influence of the buildings ventilation rate on the interior humidity levels.
Consequently, before investigating the performance of various wall configurations in the next section, it is important to identify the impact of the suggested climate conditions on the simulation results. The aim of the current section is to define the most critical wall orientation and verify the impact of the inner relative humidity levels. Moreover, the effect of different climate files for the same location (Belgium) will be compared. These reference simulations, performed on the configuration depicted in Figure 6.10[12], will form a basis for the parameter investigation in section 6.6.

6.5.1 Orientation

From Sections 6.2.1 and 6.2.2 it followed that a North facing wall corresponds to the lowest surface temperatures and that North and North-East faced walls have the highest potential for air exfiltration conditions in a Belgian climate. On the other hand, South-West has the most significant rain load in Belgium. Yet wind-driven rain is not taken into account in the reference simulations as painted wooden cladding is applied, as mentioned in section 5.4.2. Based on this, it can be expected that the North and North-East walls will result in the highest risk for interstitial condensation in winter conditions. Deriving the most favourable orientation for mould growths conditions, however, is more complex because this depends on the interaction of both temperature and relative humidity levels within the structure (sec-

[12]grid simplifications according to section 6.4

tion 2.4.1).

Figure 6.17 compares the simulation results for the eight main wind directions. It was found that no condensation occurred for any of the orientations. Therefore, the comparison in the left hand side figure is based on the maximum moisture content of the exterior air barrier, also representative for the corresponding moisture load. The moisture content on the North facing wall is applied as a reference in this figure; the moisture contents of the eight main wind directions are plotted against the moisture levels on the North wall. The figure shows that the North facing wall results in the highest moisture content levels in winter conditions, closely followed by the North-East oriented wall. The right hand side figure evaluates the maximum mould growth index on the interface between the mineral wool and the exterior air barrier layer. This figure displays that the highest risk for mould growth can be expected on North-West to North-East oriented walls. The maximum value on these orientations is 3.2 (-), which is significantly higher than the other orientations. Based on these findings, North is selected as the most critical orientation. As a result, the simulations in the remainder of the chapter will be North oriented.

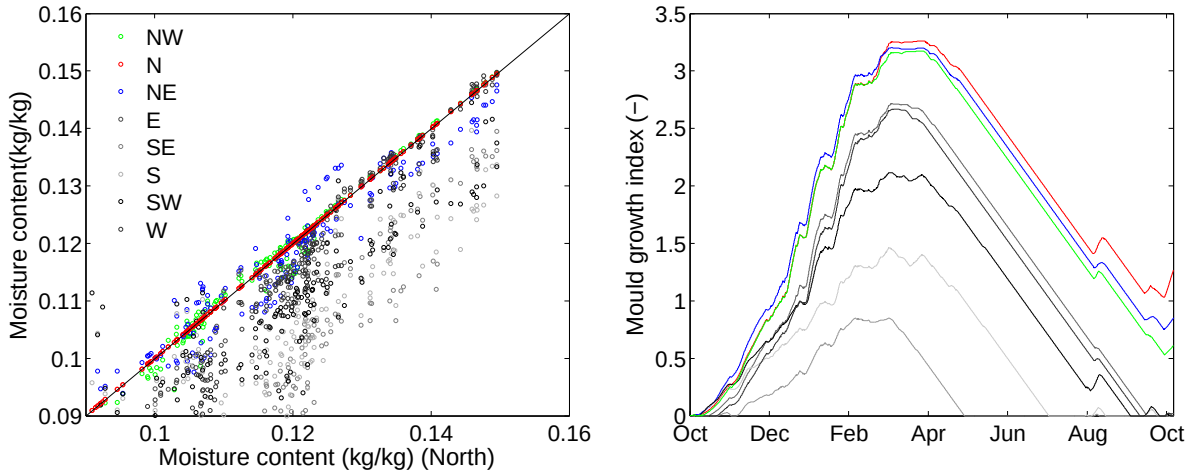

Figure 6.17: Impact of orientation on the moisture content of exterior air barrier (left) and the maximum mould growth index (right).

6.5.2 Inner climate - ventilation rate

The ventilation rate in operation was chosen three times lower than the nominal ventilation rate in the previous simulations (0.5 1/h, see section 6.2.3). In order to verify the impact of this assumption, this section simulates the reference configuration for a ventilation rate of 1.5 1/h and 0.5 1/h. The first corresponds to the minimum hygienic ventilation rate for the assumed room configuration and occupancy (section 6.2.3). The latter, however, is three times lower, considering lower ventilation rates of systems in operation (as explained in section 6.2.3). In addition, simulations are performed for which the deficiencies in the interior OSB are removed (see Figure 6.10), so that the vapour barrier (OSB) acts as an interior air

barrier as well.

Figure 6.18 illustrates the large impact of the ventilation rate on both the moisture content of the exterior air barrier and the maximum mould growth index. Most significant difference is noticed for the mould growth index; by increasing the ventilation rate from 0.5 1/h to the nominal ventilation rate of 1.5 1/h the mould growth index on the inner surface of the exterior air barrier decreases from 3.2 to less than 0.5, a level for which no spores are activated anymore. This figure further demonstrates that for a continuous interior OSB layer (intact), the mould growth index undershoots critical levels for both ventilation rates. In summary, this figure reveals the importance of considering lower ventilation rates for systems in operation (0.5 1/h). As outlined in the discussion of Figure 6.7 this assumption is more realistic than applying the standard European or Belgian classification system, which results in an overestimation of normal humidity levels in winter conditions (see Figure 6.7). As a consequence the ventilation rate of 0.5 1/h, representing a ventilation system in operation, will be applied throughout the remainder of this work, unless explicitly mentioned.

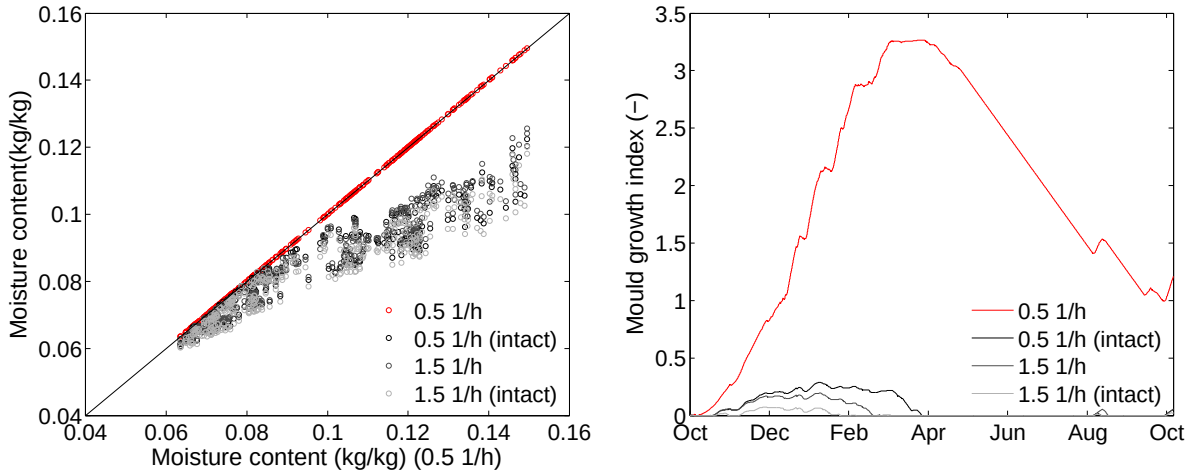

Figure 6.18: Impact of ventilation rate on (a) the moisture content at the top of the exterior air barrier and (b) maximum mould growth index on the exterior barrier for a North facing wall.

6.5.3 Exterior climate

Section 6.2 stressed that the climate files applied in hygrothermal building component simulations remain an important uncertainty. Therefore, this section reflects on the influence of various climate files for the same location. The previous simulations applied the TRY for Uccle, provided within the simulation package TRNSYS[13] (referred to as TRNSYS in the remainder). Here, three other variants for the weather data of Uccle are compared with these results. The alternative climate files are retrieved from the simulation package Meteonorm 6.1 in which the TRY are based on measured data from the period 1996-2005 for

[13]BE_UCCLE_64470 (TRY for the period 1961-1990)

the temperatures and 1981-2000 for the radiation data. The comparison is performed for three different climate files which were selected on the ten-yearly (a) minimum, (b) average and (c) maximum temperature and radiation within this period. In addition, this comparison is extended with the climate file of Essen (Blümel 1986). This climate file is used by various authors for hygrothermal simulation of building components (Abuku 2009, Janssen 2002) in Belgian conditions. This weather file, standard available in HAM simulation packages, such as Delphin, WUFI and HAMFEM is therefore included in this comparison as well.
Figure 6.19 compares the weekly-averaged moisture content at the top of the exterior air barrier and the maximum mould growth index on the sheathing for these different climate files. The left hand side figure demonstrates that the maximum moisture content levels are in the same range. Higher deviations are noticed for the predicted mould growth index, depicted in the right hand side figure. For example, this figure reveals that the maximum mould growth index is less than 2 for the simulation with a TRY based on the minimum temperatures (MIN), while this index reaches 3.2 for the results corresponding to the climate file for Uccle, provided in TRNSYS. Moreover, while the hygroscopic exterior air barrier is dried out after summer for all climates, the mould growth index of the latter still maintains around 1 after one year. Consequently, the mould growth index of the second winter exceeds its level of the previous year. It was found that after four years convergence was reached, resulting in a maximum mould growth index of 4 for this climate file (TRNSYS).
In summary this paragraph showed that the highest influence of the weather file can be

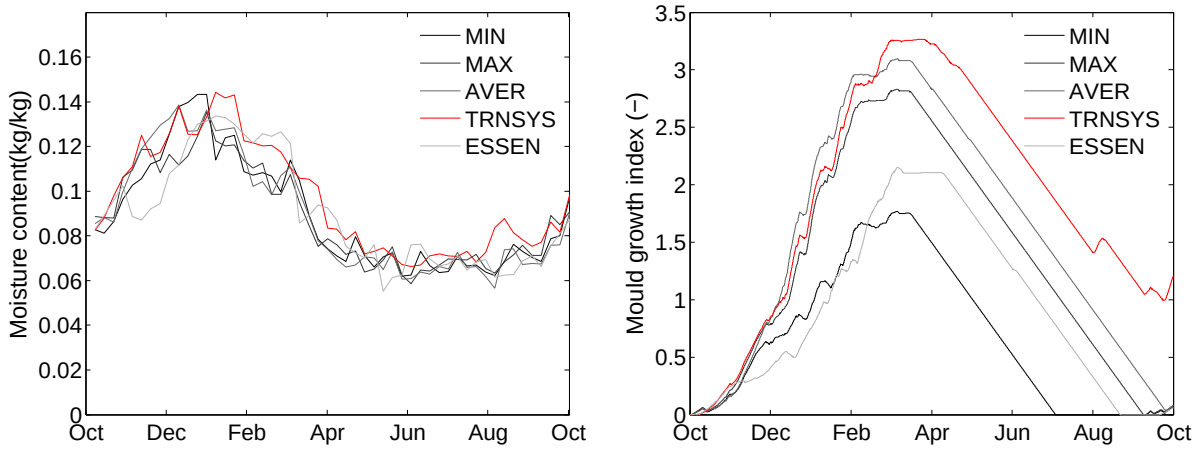

Figure 6.19: Impact applied climate file on the (a) moisture content at the top of the exterior air barrier and (b) maximum mould growth index on the exterior barrier for a North facing wall.

expected on the predicted mould growth index. Most critical results for a Belgian climate were obtained with the TRY provided in TRNSYS. Consequently this weather file is applied in the parameter investigation of section 6.6.

6.5.4 Summary

This section performed simulations on the reference wall configuration of Figure 6.10, studying variations in the applied interior and exterior climate. It was shown that the most critical moisture loads on this highly insulated lightweight wall with an exterior air barrier can be expected for North-East to North-West orientations in Belgium. Furthermore, this section addressed the large influence of the assumed indoor ventilation rate. No mould problems were found for the situation in which the minimum hygienic ventilation (Limb (2001)) was applied (1.5 1/h). Yet assuming a lower ventilation rate (system in operation) (0.5 1/h) resulted in a mould index of 4.3 (-) at the upper position of the exterior air barrier after the fifth winter. Finally, this section illustrated a significant impact of the applied climate files on the simulation results. The simulations were repeated for four different available TRY's for Uccle (Belgium) and one TRY from Essen, closely located to Belgium. Deviations up to two mould index classes were observed as a result of these different climate files.
Based on the findings in this section the worst case climate conditions were selected for the simulations in the remainder of this work. In summary, the simulations in this section will be performed on North faced walls, the interior climate will be based on a ventilation rate of 0.5 1/h and the exterior climate will correspond to the TRY retrieved from the building simulation software TRNSYS.

6.6 Parameter variation

This section provides a parameter analysis on the reference simulation discussed in the previous section. First, the hygrothermal performance of two different commonly applied insulation materials is studied: (a) mineral wool and (b) loose-fill cellulose insulation. Thereafter, the influence of the position and magnitude of air leakages in the interior vapour barrier are examined. This section should bring insight in how precisely the inner vapour barrier needs to be installed when applying exterior air barriers. Additionally, different types of inner sheathing materials are included in this analysis as well. Next, focus lies on the effect of forced convection conditions induced by unintended air leakages in the exterior air barrier layer. The aim of this section is to verify whether exterior air barrier systems are more critical for the effects of unforeseen leakages compared to the interior air barriers. In addition, the performance of several other potential exterior air barrier materials, such as OSB, fibre cement board, foils and gypsum board, are investigated. Finally, several variants of the reference case are simulated under other European climate conditions, from Lisbon to Helsinki.
The assessment of the simulation results in this section is based on the moisture limit states proposed in section 6.3.3. Here, a maximum accumulated condensation amount of 0.1 kg/m^2 was suggested to prevent run-off conditions. In addition, a maximum mould index

(M) of 3 was put forward. Figure 6.18 illustrated that the exterior air barrier was dried out after summer for the reference cases. The corresponding mould index, however, was not necessarily decreased to zero. Consequently, the mould growth index of the second winter may exceed its level of the previous year. Therefore, the mould index applied in this section is calculated for 5 years by assuming a yearly repetition of climate conditions.

6.6.1 Insulation material

First, the impact of the insulation material is investigated. The steady-state laboratory measurements of chapter 4 demonstrated a significant impact of the type of insulation material on the observed levels of natural convection, and thus, the moisture conditions of the exterior air barrier (Table 4.8). Question remained, however, to which degree the insulation layer influences the hygrothermal performance under transient climate conditions.
Two commonly applied groups of insulation materials are selected for the numerical investigation here: (1) mineral wool and (2) cellulose insulation. Most often mineral wool insulation with a density of 20 kg/m^3 (MW20) is used in Belgium. Densities of 30 kg/m^3 (MW30), which have a slightly better thermal resistance performance, have only a limited market as they are more expensive. Nevertheless, both densities (MW20 and MW30) are included in the investigation here. For blown-in loose-fill cellulose insulation, however, densities of around 60 kg/m^3, commonly applied in practice, are adopted here. In addition, cellulose insulation with lower densities (40 kg/m^3 and 50 kg/m^3) are examined as well. The air permeability levels for these lower densities are based on measurements of Yarbrough & Wudhapitak (1992).
Table 6.3 presents the maximum mould index and accumulated condensate on the exterior air barrier for the reference configuration (Figure 6.10) with the discussed insulation materials. The predicted maximum mould index never exceeds the proposed limit of 3 and no condensation occurred for this type of insulation for the wall elements insulated with cellulose. For the mineral wool insulation, however, mould growth problems are predicted for the standard density of 20 kg/m^3. A mould index of 4.3 was found for this density, corresponding to a visual mould covering percentage between 10-50 %. Mineral wool with increased density (30 kg/m^3), in contrast, meets the proposed moisture limit state. Finally, this table shows that no condensation occurred for both the mineral wool and cellulose insulated walls.

	Cellulose			**Mineral wool**	
ρ (kg/m^3)	40	50	60	20	30
M (-) / AC_{max} (kg/m^2)	2.3/-	1.8/-	1.6/-	4.3/-	2.3/-

Table 6.3: Maximum mould index (-) and accumulated condensate for different insulation materials and densities.

In summary, Table 6.3 demonstrated that no moisture problems are expected for loose-

fill cellulose insulated wall elements. Even for densities significantly lower than 60 kg/m^3 - rarely applied in practice - no problems occurred. In addition, however, the simulations predicted critical mould levels for standard mineral wool insulation (MW20). From this table it can be concluded that applying high density mineral wool (30 kg/m^3) is an effective measure in decreasing the moisture load. It should be stressed however that the results of Table 6.3 correspond to an 'ideal' installation of the insulation layer, in that, perfect contact between the insulation and the adjacent layers is assumed. On the contrary, verification of the laboratory measurements of chapter 4 by numerical simulations (section 5.4.3) proved the importance of small discontinuities along the interface of mineral wool insulation layers. Such small air cavities are responsible for increased levels of natural convection and consequently higher moisture loads. As a result the presence of small air cavities around mineral wool insulation should be considered.

Therefore, the simulations with mineral wool insulated elements were repeated, introducing imperfections along the interface for the insulation and the adjacent layers. Herein, six configurations are considered, varying the position of these air cavities: an air channel along the (a) cold sides of the insulation, (b) warm side of the insulation layer, (c) at the top of the insulation, (d) both cold and warm sides, (e) both the cold and warm side and at the top of the insulation, and (f) at all four sides of the insulation. For these configurations the impact of channels of 1 mm, 3 mm and 5 mm have been studied. All combinations are simulated for both mineral wool with a density of 20 kg/m^3 and 30 kg/m^3 for which the corresponding simulation results are summarised in Table 6.4.

	Mineral wool											
												
	20	30	20	30	20	30	20	30	20	30	20	30
1	4.5/-	2.8/-	4.4/-	2.5/-	4.5/-	2.9/-	4.6/-	3.7/-	4.8/-	4.1/-	4.8/-	4.1/-
3	5.5/-	4.6/-	4.6/-	3.2/-	4.7/-	3.6/-	5.8/-	5.1/-	6/1.1	6/0.6	5.9/1.4	6/1.2
5	5.9/-	4.9/-	4.8/-	4/-	4.7/-	3.7/-	6/0.1	5.6/-	6/>5	6/4.5	6/>5	6/>5

Table 6.4: Impact of air cavities (1 mm, 3 mm and 5 mm) around insulation layer on the maximum Mould index (-) and maximum accumulated condensation (kg/m^2) for mineral wool with a density of 20 kg/m^3 and 30 kg/m^3.

This table confirms that the risk for moisture problems is highly influenced by the presence of small air channels along the mineral wool layer. Even a small air channel of 1 mm at both sides of the insulation increases the mould index from 2.3 to 3.7 for MW30. As a consequence, the above-mentioned conclusion that higher mineral wool densities decrease the risk for moisture problems only holds for perfect contact conditions. From the moment imperfections around the mineral wool insulation layer (which definitely occurs in practice) are considered, the density of the mineral wool becomes of minor importance.

In addition, Table 6.4 shows that most critical moisture limit state again corresponds to

mould growth. Only for air channels of 3 mm and 5 mm on at least two side of the insulation condensation occurred. To illustrate the obtained condensation profiles, Figure 6.20 depicts the hourly condensation along the height of the exterior air barrier for MW20 with air channels of 5 mm at both sides. This graph demonstrates that condensation clearly occurs during winter periods and is concentrated at the upper height of this layer.

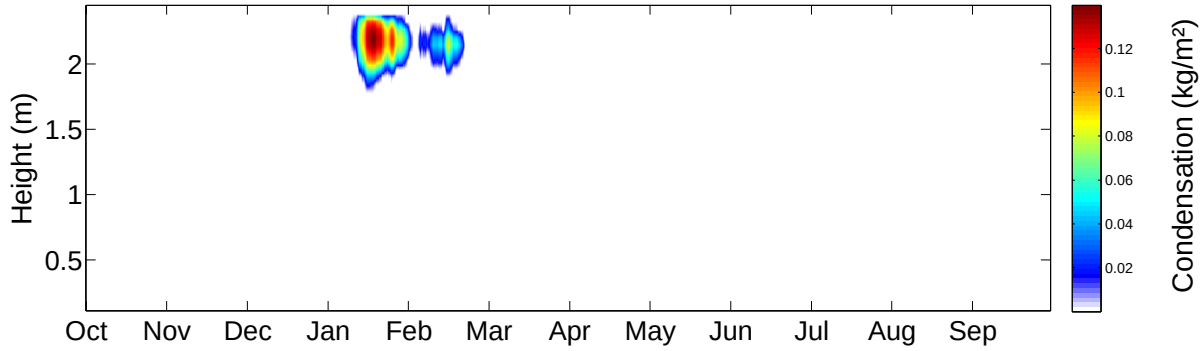

Figure 6.20: Hourly condensation along the exterior air barrier for mineral wool of 20 kg/m^3 and air channels of 5 mm on both vertical sides of the insulation layer.

Besides its impact on the moisture load, it is interesting to verify the influence of these air channels on the thermal performance of the walls. Figure 6.21 presents the yearly heat losses through the six configurations studied above for MW20. Again the width of the channels is varied between 1 mm, 3 mm and 5 mm. This figure indicates that the impact on the thermal performance is negligible for air channels of 1 mm. Also for air channels of 3 mm the increase of the overall heat losses is restricted to less than 10 %. Only for the configuration with air channels on both vertical sides and at the top of the insulation or for a continuous air channel surrounding the complete mineral wool layer, higher losses are obtained for a channel of 3 mm. Highest deviations are found for a channel width of 5 mm. Leaving such air spaces on both sides of the insulation results in a 22 % decrease of the thermal resistance. Moreover, combined with an air channel at the top or both at the top and bottom this difference rises up to 44 % and 106 %, respectively.
These results are higher than the values mentioned in the literature by Brown et al. (1993), Janssen (1997), Uvsløkk et al. (2010), discussed in section 2.2.1. Main difference with these studies, however, are the air leakages in the interior vapour barrier. In the study at hand slots of 1 cm at the top and bottom are introduced in this layer (Figure 6.10), where the other studies assume perfectly airtight sheathings on both sides of the insulation layer. The introduction of deficiencies in one of the adjacent sheathing layers increases the level of natural convection, and thus, the total heat losses. This was observed both experimentally (Figure 4.10) and numerically (Figure 5.4) in this work. Therefore, additional simulations have performed with a continuous interior and exterior layer, to verify the importance of this effect. The results are presented in Figure 6.21 as red markers, which indeed confirm

the importance of the air leakages in the inner layer. The higher heat losses induced by air leakages in the inner layer become more pronounced for the situations with wider air channels.

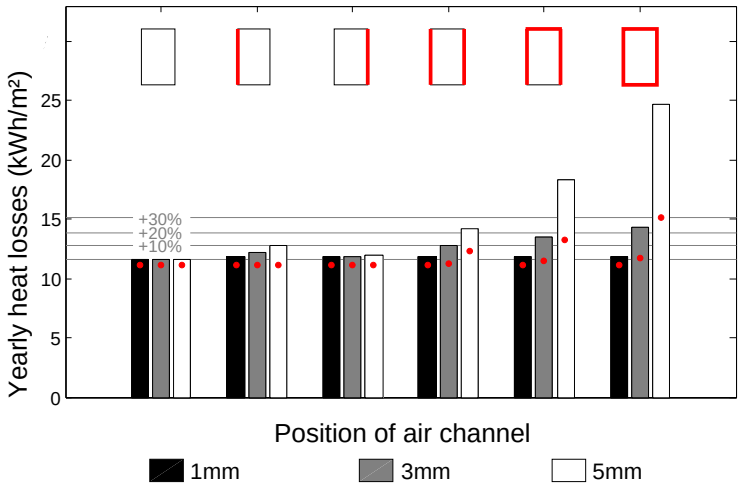

Figure 6.21: Yearly heat losses for various air channel widths and positions for mineral wool insulated walls (MW20) for the reference configuration (Figure 6.10). Red dots correspond to the simulation results for the configuration without air leakages in the inner OSB sheathing.

6.6.2 Interior vapour retarder

So far the air leakages in the interior vapour retarder (OSB) corresponded to slots of 1cm at 20 cm from the top and bottom of the wall (Figure 6.10), adopted from the hotbox/coldbox investigation of chapter 4. The aim of this chapter is to verify the impact of the position and width of these gaps and examine the importance of the vapour retarder material. First, the impact of the position and width of the gaps is studied for the configuration with an OSB vapour retarder and BIFBI applied as exterior air barrier. The positions of air leakages are depicted as red dots at the bottom of Figure 6.22. The width of these deficiencies was varied between 5 mm, 10 mm and 20 mm. Second, simulations were performed for two different interior sheathing materials: (a) a vapour open gypsum board layer ($s_{d,50} = 0.15$ m) and (b) a vapour tight PE-foil ($s_{d,50} = 100$ m). Three variants for the insulation layer are considered for this investigation: (a) mineral wool of 20 kg/m^3 (MW20), (b) mineral wool of 30 kg/m^3 (MW30) and (c) loose-fill cellulose insulation 60 kg/m^3 (CL60). The previous section demonstrated the necessity of taking air channels along the mineral wool insulation layer into account. Based on the experience of the laboratory experiments in chapter 4, air channels of 3 mm on both sides of the insulation layer are considered for mineral wool.

Figure 6.22 presents the maximum mould index for the configurations in which OSB is applied as inner vapour barrier. This graphs shows that for none of the cellulose insulated

wall elements critical mould growth levels are reached. On the contrary, when gaps are

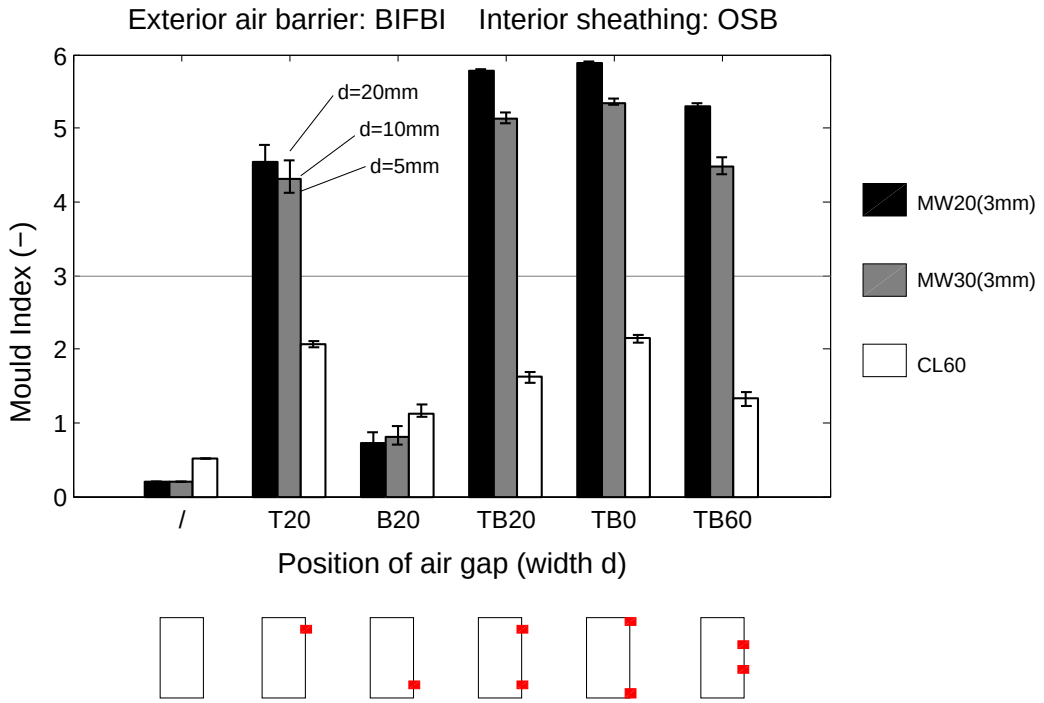

Figure 6.22: Impact of position and width of deficiencies in the interior vapour barrier (exterior air barrier: BIFBI and interior sheathing: OSB). Error bars correspond to the different widths of the gaps in the inner sheathing: 5 mm, 10 mm or 20 mm.

present, all except one mineral wool insulated wall result in a mould index exceeding the proposed threshold of 3. Only for the situation in which a single leakage is located at the bottom of the wall lower mould growths are found. This is caused by the fact that the concentrated vapour diffusion is counterattacked by convective vapour transport at the bottom of the wall as illustrated by numerical simulations in Figure 5.10 in the previous chapter. The predicted mould growth for all other configurations insulated with mineral wool lies in the same high range (4.3-5.9) and are only slightly influenced by the insulation density and the width of the air leakage in the interior layer (presented as error bars in Figure 6.22).

Next, simulations were conducted to verify the importance of the inner vapour barrier. Therefore, the vapour retarding OSB layer ($s_{d,50} = 4\,\text{m}$)[14] was replaced by a vapour open gypsum board ($s_{d,50} = 0.15\,\text{m}$) and vapour tight PE-foil ($s_{d,50} = 100\,\text{m}$), considering two extreme scenarios. As expected, the left hand side graph in Figure 6.23 indicates mould problems for all 6 mineral wool insulated wall configurations. Even for the walls with no air leakages in the interior lining, very high mould indexes are found, pointing out the importance of vapour diffusion through the gypsum board. In contrast, this figure reveals, however, that for the cellulose insulated elements no mould problems are obtained. Main potential explanation for these limited mould growth levels follows from the lower air perme-

[14] see Figure 4.8 for $s_d(\phi)$

ability and higher vapour resistance factor of the cellulose insulation compared to mineral wool[15]. The first limits the amount of moisture redistribution by natural convection within the structure. The latter decreases the vapour pressure across the cellulose, resulting in less critical conditions at the interface between the exterior air barrier and the insulation. This statement was verified by a simulation in which the vapour diffusion resistance factor of the cellulose was adjusted to the value of mineral wool. In decreasing the vapour diffusion resistance factor of cellulose from 2 to 1, the predicted mould index for the configuration for which gaps are present increased from 1.15 to 4.50, justifying the above conclusion.
The right hand graph in Figure 6.23, corresponding to the configuration with a PE-foil vapour barrier, shows the same profile as the wall with an OSB vapour retarder (see Figure 6.22). As a consequence, this graph illustrates the insignificance of the very high vapour resistance of the PE-foil. The effect of discontinuities in this layer, resulting in convective vapour transport driven by buoyancy are far more dominant than the vapour resistance of the interior lining. However, it should be noted that a minimum vapour diffusion resistance on the inner side is still required, as illustrated on the left hand side figure. From these simulations it follows that the vapour resistance of OSB is sufficiently high to avoid problematic levels of vapour diffusion ingress.

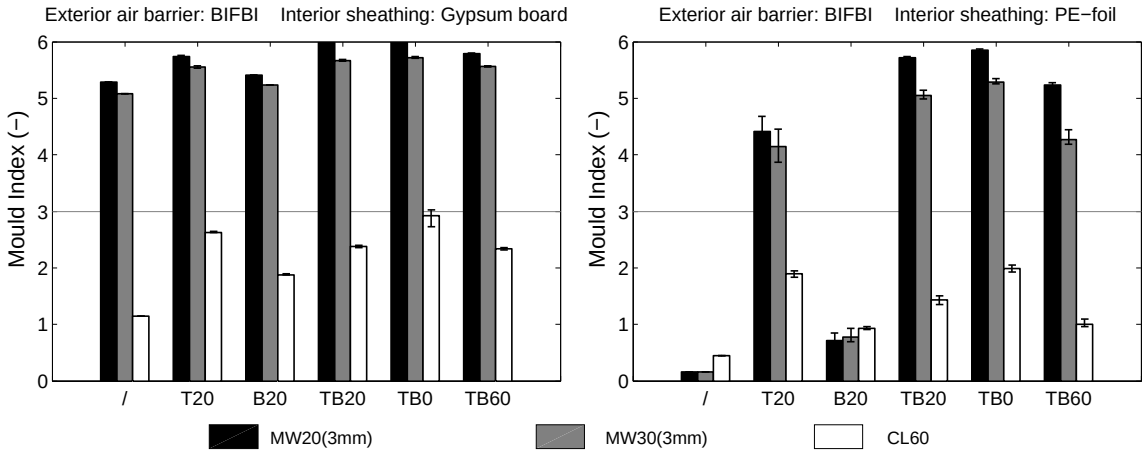

Figure 6.23: Impact of position and width of deficiencies in the interior vapour barrier. Left: exterior air barrier: BIFBI and interior sheathing: gypsum board. Right: BIFBI and interior sheathing: PE-foil. Error bars correspond to the different widths of the gaps in the inner sheathing: 5 mm, 10 mm or 20 mm.

6.6.3 Bad workmanship in exterior air barrier

Up to now, the presence of forced convection was limited for the discussed simulations as a result of the continuous exterior air barrier. However, as demonstrated by the *in situ* pressurisation tests of chapter 4, unforeseen air leakages through this layer can not be excluded

[15] $\mu_{MW} = 1$ (-) and $\mu_{CL} = 2$ (-)

since its execution remains vulnerable to human errors (herein referred to as 'bad workmanship'). Several numerical (e.g. Ojanen & Kumaran 1996, Janssens 1998, Kalamees & Kurnitski 2009) and experimental (e.g. Derome 2005, Kalamees & Kurnitski 2009) investigations have shown that forced air convection highly increases the moisture loads within lightweight walls. As a remedy, the building envelope design should by guarded to limit the effects of unforeseen air convection. Most common redundant strategies mentioned in the literature are increased thermal resistance and vapour permeability levels of the exterior sheathing (e.g. Janssens 1998, Kalamees & Kurnitski 2009). However, in the light of providing additional moisture safety against unintended forced convection, exterior air barriers may be more susceptible compared to traditional inner air barriers. For example, one air leakage in a perfectly sealed exterior air barrier system will cause an air flow path concentrating towards the cold, and thus, most critical side of the building envelope. In contrast, this path is mirrored for an interior air barrier, so, that this amount of air flow is distributed over the exterior surface.
The aim of the present section is to verify the above hypothesis that exterior air barrier systems may be more critical than traditional interior air barriers, considering effects of forced convection induced by unintended air leakage paths.

In a first step the impact of a potential deficiency in the exterior air barrier is verified. Reference case (Figure 6.10) is compared with the situation for which an air leakage is present in the middle of the exterior air barrier (see configurations at the top of Figure 6.24). This simulated deficiency in the air barrier corresponds to a gap of 4 mm, based on the measurement results on unsealed tongue and groove joints between OSB panels (Table 3.9 and Figure 3.14). In the interior vapour barrier, on the other hand, again slots of 1cm are introduced at 20 cm from top and bottom in accordance with the reference situation (Figure 4.7). The air flow resistances of these leakages are linearised by applying a flow exponent of 1. This is due to the model limitations, assuming a linear relation between pressure drops and air flows (fully-developed laminar flow in channels).
In case the wall is insulated with mineral wool (MW30), considering air channels of 3 mm on both sides, this deficiency increases the air permeance of the wall from $1.4\,10^{-6}$ kg/(m^2 s Pa) to $1.5\,10^{-5}$ kg/(m^2 s Pa). The air permeance of the cellulose insulated wall (CL60), however, increases only to $6.9\,10^{-6}$ kg/(m^2 s Pa) as a result of the lower air permeance of this insulation material. Figure 6.24(left) illustrates the effect of this central air leakage on the maximum mould index on the exterior air barrier. For the configuration without gap in the exterior barrier the maximum mould index is 1.6 for CL60 and 4.3 for MW30, both located the upper part of the wall (dashed lines). When introducing a deficiency in the middle of the exterior air barrier, the maximum mould index for the mineral wool insulated wall shoots to 6 and increases up to 3.8 for the cellulose insulated wall. In addition, it is noticed that the maximum values are now located at the opposite side of the gaps in the interior layer.

The right graph in Figure 6.24 gives further the maximum accumulated condensation on

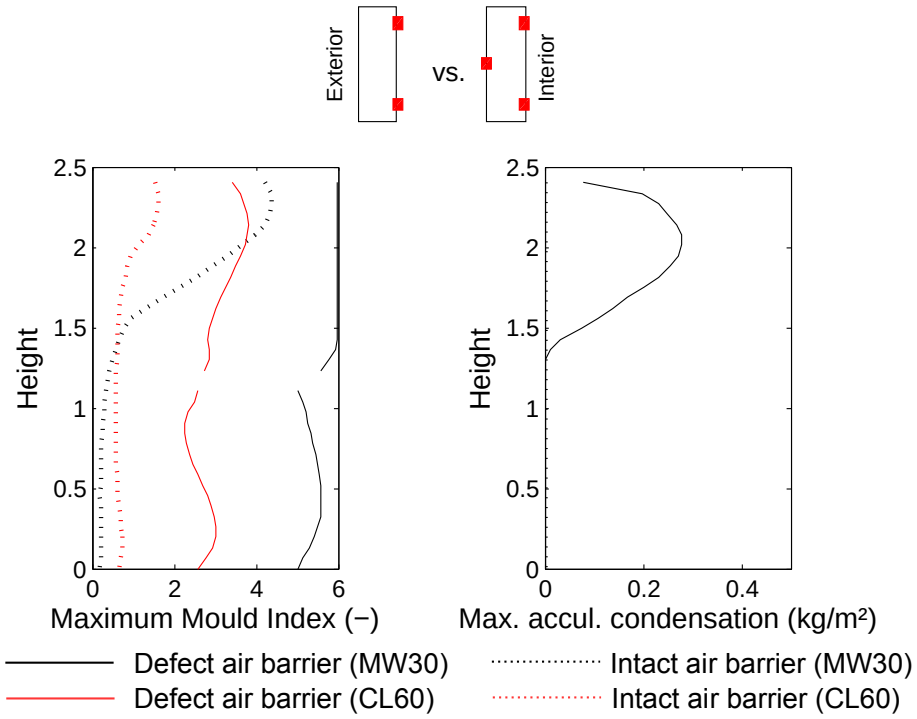

Figure 6.24: Impact of a defect in the exterior air barrier on the maximum mould index (left) and the maximum accumulated condensation (right). (defect = joint of 4 mm in air barrier).

the exterior sheathing. This figure illustrates that by introducing the air leakage in the exterior barrier, condensation occurs at the upper part of the mineral wool insulated wool. For the cellulose insulated wall, on the other hand, no condensation was observed for both configurations. In summary Figure 6.24 illustrates the well-understood phenomena that forced exfiltration significantly increase the risk for hygrothermal problems in lightweight construction elements. The main goal of the current section, however, is to verify whether exterior air barriers are more critical than interior air barrier when it comes to unintended air leakages.

For this investigation three configurations, varying the width and positions of air leakages, are considered. Again, the simulations are performed for walls insulated with mineral wool (MW30) with air channels of 3 mm on both sides and loose-fill cellulose insulation (CL60). For the configuration with an exterior air barrier, gaps of 1 cm are considered in the inner vapour retarder in accordance with the reference case. In the exterior air barrier, however, gaps of 0 mm, 2 mm and 4 mm are left, based on the measurement results of unsealed tongue and groove joints between OSB panels (Table 3.9 and Figure 3.14). The three configurations studied are depicted at the top of Figure 6.26: (a) inner gaps at 20 cm from top and bottom and an outer gap in the middle of the wall, (b) identical as system (a) but with the introduction of an additional inner gap in the middle of the wall, and (c) inner gaps at 20 cm from the top and bottom of the wall and an outer gap at 20 cm from the bottom of

the wall. The same distribution of air leakages is considered in the walls with an interior air barrier as depicted in Figure 6.26. As a consequence, the resulting overall air permeability levels of the corresponding configurations are equal, so, they can be compared directly. Figure 6.25 examines the simulated maximum mould index for both walls with an exterior and interior air barrier. This graph suggests that the exterior air barrier system is more susceptible for the effects of forced convection, in that for most configurations higher levels of mould growth are found for the same amount of forced convection. A detailed analysis of

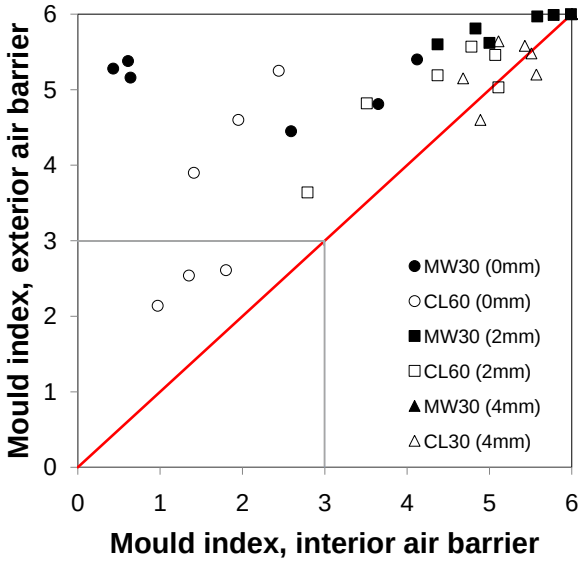

Figure 6.25: Comparison of simulated mould index for interior and exterior air barrier systems, considering unintended air leakages.

the simulation results reveals that the amount of natural convection is in the same order of magnitude as forced convection for the small deficiencies in the air barrier (0 mm - 2 mm). As a consequence, the configuration with an exterior air barrier cumulates the hygric effects of natural convection with forced convection which explains the higher moisture load. For larger air leakages (4 mm), however, also situations occur for which the predicted mould growth is higher for the interior air barriers. To study this more in depth, Figure 6.26 shows the predicted maximum mould growth levels (top) and amounts of condensation (bottom) along the height of the exterior air barrier for the configuration with air leakages of 4 mm in the air barrier. In this figure the profiles for cellulose insulated elements are depicted in red and for the mineral wool insulated walls in black. The results of the exterior air barrier correspond to the full lines and the interior air barrier to the dashed lines. The maximum mould index profiles (top) demonstrate that the highest mould levels are positioned at the opposite side of the air leakages in the inner sheathing. The profiles for the cellulose insulation (in red) show that the maximum predicted mould growth levels are similar or even slightly lower for the exterior air barrier systems under these forced convective air flow scenarios. For the walls with mineral wool (in black), however, this can not be stated as the maximum mould index is 6 for both positions of the air barrier.

The above findings that unintended leakages in exterior air barriers are not necessarily more susceptible for mould problems compared to inner air barriers are confirmed by the maximum condensation profiles, depicted at the bottom of Figure 6.26. For the first leakage distribution (a) the highest accumulated condensate corresponds to the exterior air barrier system. For the other two configurations (b,c), however, highest condensation rates are found for the interior air barrier systems. Additionally, it should be noted that for none of the cellulose insulated walls condensation occurred. In summary, these observations do not completely confirm the above hypothesis that exterior air barrier systems are more critical to effects of unintended air leakages in the air barrier layer. Certainly for dominating forced convection conditions exterior air barriers are not always more vulnerable than interior barriers. However, when the amount of forced convection is in the range of natural convection, exterior air layer result in more critical conditions than traditional interior systems. The results showed that the maximum mould growth and condensation profiles highly depend on the distribution of the air leakages. It followed that the distribution of the leakages in the inner and outer sheathing is more important than the position of the air barrier itself when forced convection dominates the air transport. Finally, it should be stressed that - independently of its position - deficiencies in air barrier need to be avoided as this results in severe moisture problems induced by air forced convection.

6.6.4 Exterior air barrier material

Next, the impact of the exterior air barrier material is investigated. So far, all simulations were performed with bituminous impregnated wood fibreboards with a coating (BIFBI), because this material provided best results in the full-scale laboratory experiments of chapter 4. This section examines the performance of other potential air barrier materials: (a) bituminous impregnated fibreboard without additional coating (BIFBII), (b) fibre cement board (FCB), (c) spunbonded foil (FOIL), (d) gypsum board (GB), (e) OSB, (f) BIFBII + FOIL, (g) GB + FOIL and (h) OSB + FOIL. These materials and their combinations are commonly applied as wind barrier in Belgium, except gypsum board which is rarely applied at the exterior of the building envelope. Yet his material is included in the analysis, as it is frequently used as wind barrier in Norway (see section 3.1). It should be noted that gypsum board applied for exterior applications is water resistant in contrast to its generally known variant used as interior finishing layer. The material properties of these materials are documented in section 6.1 and 4.1.5. In addition to the very vapour permeable spunbonded foil, discussed in section 6.1 (FOIL[16]), two variants with higher vapour resistances are included in the analysis here: FOIL01 and FOIL02, corresponding to a constant s_d-value of 0.1 m and 0.2 m, respectively.

These potential air barrier materials are investigated for the reference configuration (see

[16] $s_{d,92}$ = 0.05 m

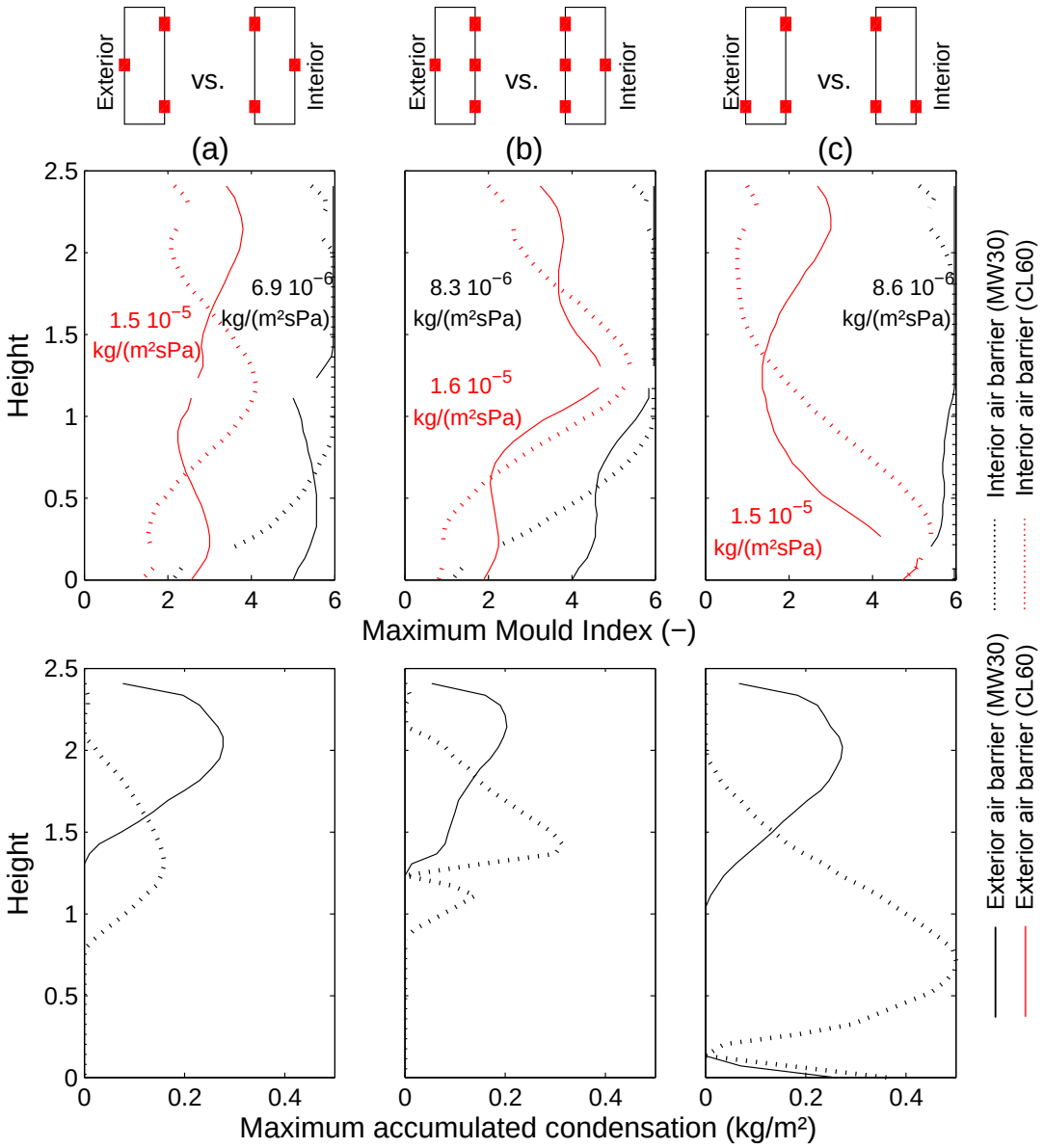

Figure 6.26: Influence of unintended air leakages in systems with an interior air barrier and systems with an exterior air barrier: maximum mould index along the interface between the exterior air barrier and the insulation layer (top) and maximum accumulated condensation at the exterior air barrier (bottom).(joints of 4 mm in air barrier).

section 6.5), insulated with mineral wool (MW30)[17] and loose-fill cellulose insulation (CL60).

Section 6.3.1 demonstrated that BIFB should be classified as a 'very sensitive' material according to the updated VTT-model (Ojanen et al. 2010). However, the other potential air barriers mentioned above (FCB, GB, OSB) are less susceptible to mould growth. The first two, FCB and GB, contain added components to prevent mould growth. In addition, glued

[17] considering air channels of 3 mm on both sides of the insulation layer

wooden boards such as OSB are also less vulnerable to mould compared to e.g. plywood (Black 2006). As a consequence, these three materials are treated as 'sensitive' materials in the mould prediction analysis here. Finally, it should be noted that the risk for mould growth on the foil material is not verified. Most of the commonly applied foils do not contain organic materials, so, they are very resistant for mould growth. Consequently, the maximum allowed accumulated condensate is the most decisive moisture limit state for these materials.

Table 6.5 gives the overview of the simulated maximum mould growth index and the accumulated condensation. This table confirms the above observation that the mineral wool insulated walls result in higher moisture loads compared to loose-fill cellulose insulation. For all except one of these walls, critical mould levels are predicted. Only for gypsum board the simulated mould index is lower than the threshold of 3. However, when this gypsum board is combined with a spunbonded foil on the exterior side (as commonly applied in Norwegian building practice, see section 3.1) the risk for mould growth increases. Moreover, the combination of gypsum board covered with a foil results in an accumulated condensation amount of 0.53 kg/m^2, exceeding the proposed limit state.
Condensation is predicted for all configurations applying foils as exterior air barrier. The amounts for the foil with the highest vapour diffusion permeability (FOIL) are limited, passing the moisture limit state of 0.1 kg/m^2. However, the foils with increased vapour diffusion resistance exceed this threshold value, resulting in run-off conditions.

	MW30		**CL60**		
	M_{max}	AC_{max}	M_{max}	AC_{max}	$MC_{cel,max}$
BIFBI	5.1	/	1.6	/	0.16
BIFBII	6	0.17	5.6	/	0.42
FCB	4.9	/	1.7	/	0.36
GB	1.2	/	0.4	/	0.16
OSB	4.4	/	1.4	/	0.20
GB+FOIL	3.8	0.53	0.6	/	0.17
BIFBII+FOIL	4.2	/	0.6	/	0.14
OSB + FOIL	4.5	/	1.4	/	0.18
FOIL	x	0.04	x	/	0.17
FOIL01	x	0.19	x	/	0.19
FOIL02	x	0.73	x	/	0.32

Table 6.5: Maximum mould index (-), Accumulated Condensation (kg/m^2) and Moisture Content of the cellulose insulation (kg/kg) for configurations with different exterior air barrier materials.

For the wall elements insulated with loose-fill cellulose insulation, on the other hand, only moisture problems are predicted for the BIFBII air barrier materials (M=5.6). As already observed in the full-scale laboratory investigation in chapter 4 this materials is relatively

air permeable, resulting in a substantial amount of forced convection, and thus, moisture loads. However, still no condensation was predicted for this configuration by the simulations. Therefore, also the maximum moisture content of the cellulose are included in the Table 6.5. The results show that the highest moisture content of the cellulose corresponds to simulation with BIFBII (0.42 kg/kg). Yet this value only slightly exceeds the highest measured moisture content in the determination of the hygroscopic curve ±0.35 kg/kg (Figure 4.8 (top)). Thus, the laboratory results of section 4.1.5 confirm that such levels of moisture can effectively be temporarily stored within this cellulose insulation layer, without deformations or caking (Derome 2005).

6.6.5 Different European Climates

Finally, the hygrothermal response of wall elements with an exterior air barrier is studied for various European climate conditions. The selected locations cover a wide range of different climates from South to North Europe. Main focus, however, is on the latter and particularly on Scandinavian regions. Recent building practice in Norway tend to focus more and more and the airtightness of the exterior layer, as stated in section 3.1. Therefore, special attention was given to this country by including Stavanger, Oslo, Bergen and Trondheim in the analysis. Figure 6.27 shows an overview of all locations studied. The corresponding climate files have been retrieved from the software package Meteonorm (see section 6.2). The simulations are performed on the reference case of section 6.5 for which either MW30 with two vertical channels of 3 mm on both sides or CL60 is applied. For the exterior air barrier material, on the other hand, two variants are included: (a) BIFBI and (b) FOIL (see section 4.1.5 for material properties).

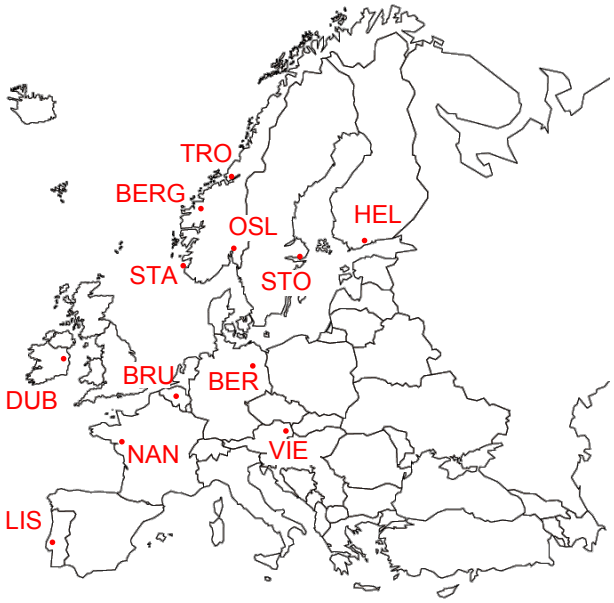

Figure 6.27: European locations for which simulations are performed.

Two parameters are applied in the analysis of the obtained simulation results for these climates. First, the averaged outdoor winter temperatures[18] (θ_{winter}), providing a direct indication of the level of buoyancy driven air flow within the insulation layer, and thus, the increased moisture loads. Second, the Π_y-factor is applied to express the severeness of the exterior climate. This factor (kg/m^3), proposed by Hagentoft & Harderup (1993) for the selection of reference years, calculates the yearly averaged difference between the vapour concentration in the outdoor air and the maximum moisture concentration on the building envelope surface on hourly data:

$$\Pi_y = \overline{v_{out,sat}(\theta_s) - v_{out}|_{year}} \tag{6.19}$$

in which $v_{out,sat}(\theta_s)$ represents the saturation vapour concentration at the buildings surface for a North oriented wall and v_{out} corresponds to the moisture concentration of the outdoor air. As this value is calculated on a yearly basis, it represents the drying potential of the climate. This expression is typically applied for purposes in which wind driven rain is not dominating. For configurations in which wind driven rain is important, such as brick veneer cladding systems, this Π_y-factor becomes less relevant as it does not incorporates rain loads. The configurations studied in this work, however, assume painted wooden cladding systems, so, wind driven rain is not considered in the simulations. As a consequence, the Π_y-factor is a relevant indicator of the severeness of the climate for the current purpose.

Both the averaged outdoor winter temperatures (θ_{winter}) and the Π_y-factor of the climates investigated are depicted in Figure 6.28 (top). This graph illustrates how the Southern European climate, Lisbon, combines a high averaged winter temperature with a high Π_y-factor. Furthermore, this figure clearly shows higher Π_y-factors for Eastern European climates (Berlin, Vienna) compared to the Western European locations (Brussels, Nantes, Dublin). In contrast the Western European climates tested correspond to milder winter temperatures. Most critical locations expected are Helsinki, Stockholm and Trondheim, in that they combine low winter temperatures with low Π_y-factors. Furthermore, this graph illustrates great differences between the four Norwegian climates included.
In addition, it should be noted that no freezing effects are included in the model (see chapter 5). Frozen condensate against the exterior air barrier increases the vapour resistance of the exterior layer which may in turn increase the level of condensation. These effects are not considered in the model. Consequently, the current simulation results may be rather optimistic for the coldest climates.

The simulations are presented as a function of the two climate parameters discussed above. Figure 6.28 (middle) provides the wall elements insulated with MW30. Here, the maximum mould growth index on the walls using BIFBI exterior air barriers is indicated in black and the maximum accumulated condensation amounts for the elements with a FOIL

[18] average of December, January and February

are given in red. These two graphs contain the same information, however, the left hand side is given as a function of θ_{winter} and the right hand side is presented as a function of Π_y. Out of the 12 climates tested only the Eastern European (Berlin, Vienna), the Southern European (Lisbon) and two of the Northern European locations (Oslo, Bergen) result in mould growth levels lower than 3. From this figure it follows that Π_y is the most dominating climate parameter in the prediction of mould growth. For these limited number of climates it appears that no problematic mould growth is observed for Π_y-factors higher than 2 kg/m^3. When it comes to condensation amounts on the non-hygroscopic foil, however, it appears that the temperature is the dominating climate parameter. Here only the coldest climates results in excessive condensation levels (Stockholm, Helsinki, Oslo and Trondheim).
In contrast to the mineral wool insulated walls, no moisture problems were found for the wall elements simulated with loose-fill cellulose insulation. Because no condensation was found for these configurations, the highest moisture contents of the cellulose insulation are given here (in red). Highest moisture content of the cellulose insulation are found for Stockholm and Helsinki. These values are, however, still lower than 0.3 kg/kg for which no problems were found in the laboratory (see section 4.1.5).

In summary, this section explored the hygrothermal response of highly insulated wall elements with an exterior air barrier in various European climates. In total 12 climates were verified, covering a range from North to South Europe. From this limited amount of data it follows that Northern and Western Europe are most vulnerable to moisture problems when such wall systems are insulated with mineral wool. When these walls are insulated with loose-fill cellulose insulation, however, no moisture problems were obtained for the European climates tested.

6.6.6 Summary

This section presented a parameter analysis on the reference wall configuration discussed in section 6.5. The simulation results identified a large impact of the applied insulation material on the hygrothermal performance of this component. No moisture problems were found for the walls insulated with loose-fill cellulose insulation. For mineral wool insulated walls, however, excessive mould growth levels are obtained on the upper parts the exterior air barrier (BIFB). Furthermore, the simulations emphasised the impact of small air channels (1-5 mm) along the mineral wool insulation and the adjacent layers. Such limited deficiencies highly increased the risk for mould growth and harmful condensation amounts against the exterior air barrier. In addition, these vertical air channels may increase the total heat losses. The simulations showed for example that air channels of 3 mm on both sides of the mineral wool layer corresponded to a 10 % increase of the yearly heat losses.
Furthermore, the present section examined the impact of the position and width of air leak-

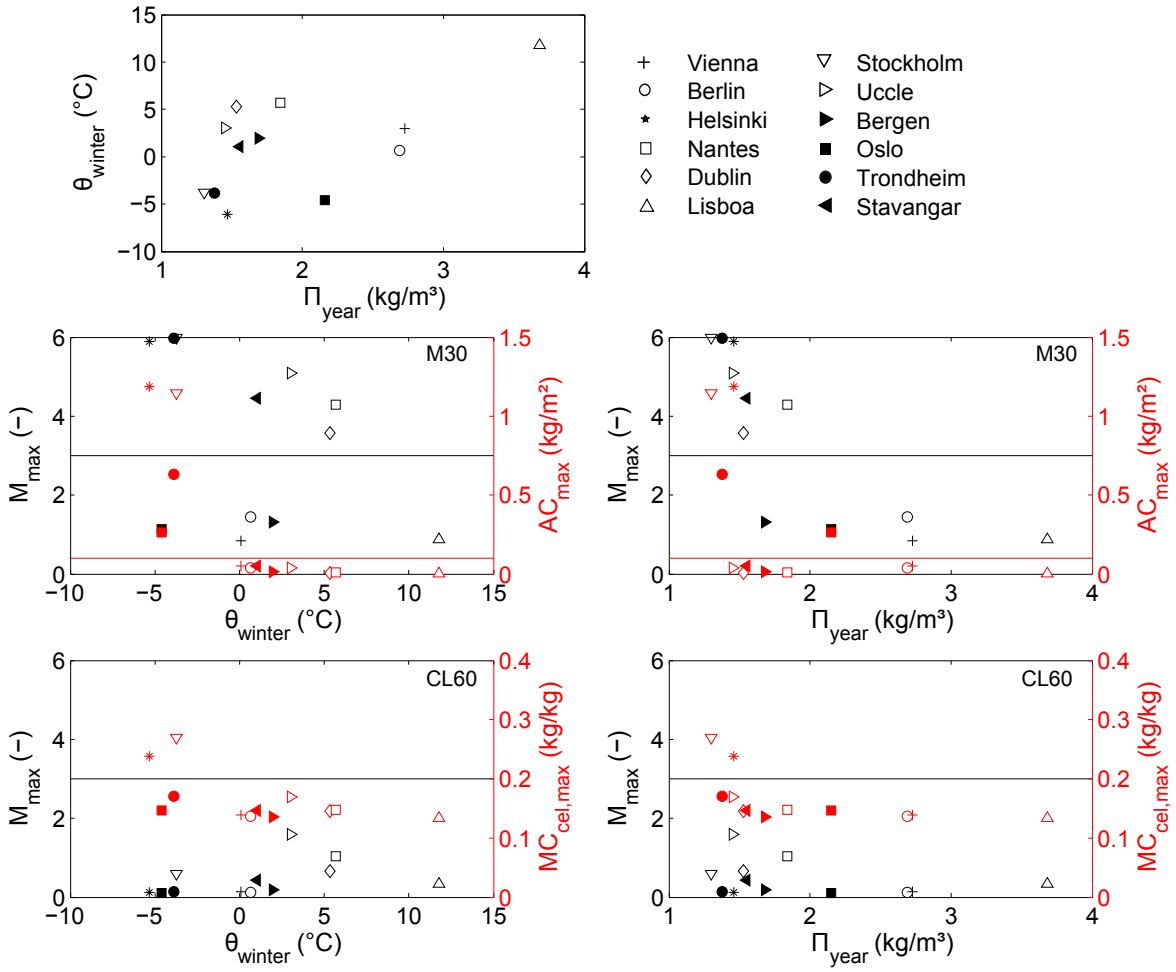

Figure 6.28: Top: overview of climate conditions, Middle: maximum mould index on BIFBI and accumulated condensation on FOIL as a function of θ_{winter} (left) and Π_y (right) for MW30 insulated elements, Bottom: maximum mould index on BIFBI and maximum moisture content of cellulose insulation as a function of θ_{winter} (left) and Π_y (right) for CL60 insulated elements.

ages in the interior vapour barrier. The results revealed that the most critical situation corresponds to gaps at the top and bottom of this layer. However, the overall impact of the position is limited. Only for the configuration with a single gap at the bottom of the vapour barrier lower moisture loads were found. In addition, the simulations showed that the width of these gaps only slightly influenced the predicted mould growth. Consequently it can be stated that the higher moisture loads within walls with an exterior air barriers are mainly related to natural convection rather than concentrated diffusion through the discontinuities in the interior vapour barrier.

One of feared drawbacks of exterior air barriers in cold and moderate climates is its increased sensitivity towards forced convection conditions induced by unintended air leakage in this layer. The simulations, however, do not completely confirm this hypothesis. It was observed that exterior air barriers are definitely more critical than interior air barriers when

the effects of forced convection are in the same range as natural convection. When forced convection dominates the air flow pattern, however, the position of the air barrier becomes less important.
Additionally, the performance of various potential exterior air barrier materials, such as OSB, FCB, BIFBII and spunbonded foils, were analysed. Similar to the reference simulation with an BIFBI air barrier, moisture problems are limited to the mineral wool insulated wall elements. For the walls with loose-fill insulation only excessive mould growth levels were found for the BIFBII air barrier (as results of its limited air flow resistance).
Finally, wall configurations with either a bituminous impregnated fibreboard (BIFBI) or spunbonded foil (FOIL) were simulated in 12 different European climates. From the limited amount of locations tested, it follows that Northern and Western Europe regions are most vulnerable to moisture problems. No moisture problems were found for the more continental climates such as Berlin and Vienna for the examined configurations. Notwithstanding the lower winter temperatures of these climates, which increase the moisture loads induced by natural convection, these regions seems to be sufficiently dry to reduce the risk for moisture problems in walls with an exterior air barrier.

6.7 Conclusions

The present chapter performed numerical simulations to asses the hygrothermal response of timber frame elements with an exterior air barrier under realistic climate conditions. These yearly simulations have been conducted with the numerical model, outlined in chapter 5, and were restricted to highly insulated wall elements only.
The first section provided a detailed discussion on the applied climate conditions. The following section introduced the applied moisture limit state criteria: (1) mould growth, and (2) interstitial condensation. The VTT-model of Hukka & Viitanen (1999) is selected for the prediction of mould growth. The quantification of interstitial condensation, on the other hand, was introduced in the model by means of additional calculation nodes at potential condensation surfaces. Both, the prediction of mould growth and interstitial condensation have been verified with the laboratory results of chapter 4. The results indicated that the presented methods were able to predict the overall trends of the mould and condensation observations. Yet it was observed that a significant uncertainty remained in the prediction of mould growth and interstitial condensation amounts. Therefore, this section stated that the applied moisture limit states - a mould index of 3 and an accumulated condensation level of 0.1 kg/m^2 - should be seen as a transition zone, rather than a strict threshold.
The following two sections discussed exploratory simulations. The first series of simulations verified potential modelling simplifications to reduce calculation times. It has been shown that excluding the top and bottom wooden plates and ascribing the inner service cavity and adjacent finishing material as transfer coefficient did not affect the simulation results. In

contrast, however, these calculations revealed the necessity of simulating the exterior cavity ventilation. The second series of exploratory simulations examined the impact of the indoor and outdoor climate conditions. The main interest was in the applied weather data and the indoor humidity. This section showed large differences on the predicted mould growth levels for the 5 different climatic files tested. The climate file corresponding to the highest moisture problems (TRNSYS) was selected for the further simulations. In addition, the simulations demonstrated the significant impact of the indoor ventilation rate on the simulation results. No mould problems were predicted for the reference situation in which the nominal hygienic ventilation rate was applied. Yet reducing the ventilation rate to account for systems in operation (Stranger et al. (2012)), resulted in mould problems at the upper position of the exterior air barrier. Notwithstanding that applying a reduced ventilation rate is a conservative assumption, the results showed that standard assessment methods (TV215 and ISO 13788:2001) use even higher indoor humidity levels. Nevertheless, it should be stressed again that relative severe boundary conditions have been applied in this chapter.

The final section conducted a parameter investigation to (1) verify the reliability of several lightweight wall assemblies, (2) identify the impact of bad workmanship and (3) illustrate its behaviour in other European climates. The simulation results identified a large impact of the applied insulation material on the performance of these components. In summary, the cellulose insulated walls outperformed the mineral wool insulated elements. The main reasons for this lie in the lower air and vapour permeance and higher hygroscopic buffering capacity of the cellulose insulation. In addition, highly insulated walls with mineral wool are more vulnerable to air layers at material interfaces. Such deficiencies greatly amplify the level of natural convection, and thus, the risk for moisture problems. Besides different insulation materials, various exterior air barriers have been studied as well. Most of the exterior barriers resulted, in combination with mineral wool, in excessive mould growth and/or interstitial condensation. Only for the most vapour open spunbonded foil and gypsum board no problems were found. Yet in combination with cellulose insulation, the majority of the exterior air barrier materials performed well. The simulations further revealed that the overall impact of the position of discontinuities in the interior sheathing is limited. It even appeared that the width of these gaps only slightly influenced the predicted moisture load. Consequently, it can be stated that the increased hygrothermal risk of timber frame walls with an exterior air barriers is mainly related to natural convection rather than concentrated diffusion through the discontinuities in the interior vapour barrier. Furthermore, it was observed that exterior air barriers are more critical than interior air barriers when forced convection is in the same range as natural convection. Yet when forced convection dominates the air flow pattern, the position of the air barrier becomes less important. Finally, the performance of highly insulated walls was verified in various European climates. From the limited amount of locations tested, it followed that Northern and Western Europe regions were most vulnera-

ble to mould problems. No mould problems were found for the (dryer) continental climates, such as Berlin and Vienna. For interstitial condensation on spunbonded foils, however, the decisive climate parameter appeared to be the winter temperatures. Excessive amounts of interstitial condensation were found for the coldest climates, such as Helsinki, Oslo, Trondheim and Stockholm.

7

Conclusions and perspectives

The airtightness of timber frame construction is commonly achieved with an interior air barrier in Europe. Yet the realisation of high airtightness levels, required for low energy buildings, is often labour-intensive. The main origin of this problem lies in the high number of joints in the interior lining. Consequently, the timber frame building industry is in search of cost-effective alternatives, such as realising the airtightness on the exterior of the building fabric. The first experiences with improved wind barriers in Norway have indicated that this may greatly facilitate achieving high airtightness levels. The main question, however, remains the hygrothermal risks involved in realising the most airtight layer on the exterior of the building envelope.

The present research project has examined the hygrothermal response of lightweight construction with an exterior air barrier in cold and moderate climates. Both experimental and numerical work have been conducted to assess the performance of these elements. This chapter summarises the obtained results and the main conclusions. Throughout this dissertation, however, some assumptions have been introduced. Hence, the conclusions drawn in the first section of this chapter are followed by a description of these assumptions and limitations, which allows to provide some future directions for building physics research related to the hygrothermal assessment of lightweight components.

7.1 Main results and general conclusions

First, field and laboratory measurements have explored the practical feasibility of exterior air barriers in timber frame construction. The potential of exterior air barriers has been verified with two case studies, in which this technique was applied. Both studies demonstrated that with good workmanship and appropriate materials, airtightness levels lower than 1 ACH at 50 Pa can be reached without problems. The joints between the adjacent walls and between the roof and walls were the most critical. Through sealing only these connections, an airtightness level, that followed the requirement of the Passivhaus-standard (< 0.6 ACH at 50 Pa) could be achieved. Furthermore, the first case study revealed that the labour costs for the current case could be reduced with 60 % by realising the airtightness at the exterior of the building envelope. Yet these on site investigations likewise identified practical drawbacks of exterior air barriers, which should be tackled in the future.
Additional laboratory measurements on specimens of the exterior air barrier quantified the different leakages, encountered in the field tests. A direct comparison of the *in situ* and laboratory measurements, however, led to the conclusion that laboratory tests are only suitable to predict the lower limit of the whole-building airtightness. The laboratory tests further recognised the impact of rain on the applied exterior air barrier. The influence on not completely closed joints and the influence on the board material during and short after a rain shower were most significant.

Second, the present study has conducted laboratory work on the hygrothermal behaviour of highly insulated walls with an exterior air barrier. These full-scale experiments recognised the occurrence of natural convection within mineral wool insulated wall elements. These air movements led to higher moisture loads at the upper cold parts of the walls. This risk for moisture problems appeared to be highly dependent on the properties of the applied exterior air barrier materials. The measurements showed that a sufficient airtightness (>0.005 $m^3/(m^2\,h\,Pa)$) is a prerequisite to avoid moisture problems induced by forced convection. The results likewise illustrated the advantage of exterior air barrier materials with a thermal resistance and moisture buffer capacity. In this respect the fibreboard air barriers outperformed the spunbonded foils.
The hotbox/coldbox investigation further revealed that the impact of natural convection on the moisture load can be reduced through the application of denser mineral wool insulation (30 kg/m^3). But, it was found that mineral wool blankets were vulnerable to small installation deficiencies. In the installation of these blankets it is very difficult to guarantee close contact between the insulation and adjacent sheathings. These small vertical air channels increase the level of natural convection, which counteract the air resistance of higher insulation densities. In contrast to mineral wool blankets, blown-in cellulose insulation appeared to be not susceptible for such channels. In combination with its lower air permeance, it reduced the

amount of natural convection, and thus, the additional moisture load to negligible levels. Finally, the introduction of deficiencies in the exterior air barrier identified the large impact of forced exfiltration conditions. The long air flow paths were most critical. Even for the hygroscopic barrier tested, this led to interstitial condensation and run-off within the mineral wool insulated wall.

Third, a numerical modelling approach has been presented to assess the hygrothermal response of highly insulated timber frame walls under atmospheric conditions. A quasi-steady state airflow model has been implemented in the framework of the existing transient two-dimensional HAM-model, Delphin 5. The air transport was simplified to Darcy flow in porous media, including a body force term to capture natural convection. In addition, to account for increased air transport through air channels and cracks, a hydraulic network methodology was used, assuming fully-developed laminar flow in the interconnect channels. An extensive comparison of the model with analytical, numerical and experimental benchmarks illustrated that the applied modelling strategy was justified. Moreover, the simulation model resulted in reasonable simulation times. The most significant deviations between the modelling results and the generated experimental data were related to uncertainties in the geometry (air channels) and the hygric material properties in the high humidity range, rather than to simplifications in the air transport equations.

Fourth, this study performed numerical simulations to asses the hygrothermal response of timber frame elements with an exterior air barrier under realistic climate conditions. These annual simulations affirmed the experimental observation that the applied insulation material had a large impact on the hygric response of these components. In summary, the blown-in cellulose insulated walls outperformed the elements insulated with glass wool blankets. The main reasons lie in the lower air and vapour permeance and the higher hygroscopic buffering capacity of the cellulose insulation. The laboratory investigation showed that highly insulated walls with mineral wool blankets are more susceptible for air channels at material interfaces, which may significantly increase the amount of natural convection. In this respect, the numerical simulations confirmed that the occurrence of air channels along the mineral wool layer greatly increased the risk for moisture problems. Though it is not explicitly studied in this work, the simulations indicate the potential of applying blown-in mineral glass wool insulation to prevent natural convection. In addition to various insulation materials, several exterior air barriers (bituminous impregnated wood fibreboards, OSB, fibre cement boards, gypsum board and different foil materials) have been studied as well. Most of the board materials resulted, in combination with mineral wool, in excessive mould growth. The foils, on the other hand, led to interstitial condensation at the upper cold side of the mineral wool. Yet in combination with cellulose insulation, the majority of the exterior air barrier materials performed well. Only the most air permeable wood fibreboard

($0.1 m^3/(m^2\,h\,Pa)$) still resulted in excessive mould growth for this insulation material. The simulations further revealed that the overall impact of interior sheathing material and the position of its discontinuities was limited. Also the width of these gaps only slightly influenced the predicted moisture load. Furthermore, it was observed that exterior air barriers are more critical than interior air barriers when forced convection is in the same range as natural convection. When forced convection dominated the air flow pattern, however, the position of the air barrier became less important. Finally, the performance of highly insulated walls with either an exterior bituminous impregnated fibreboard or a spunbonded foil was examined for various European climates. From the limited amount of locations tested (12), it followed that Northern and Western Europe regions were most sensitive for mould problems. A sound performance, however, was found for the (dryer) continental climates studied. When it came to interstitial condensation on spunbonded foils, however, the decisive climate parameter appeared to be the winter temperatures. For these foils, excessive amounts of interstitial condensation were found for the coldest climates.

7.2 Limitations and future perspectives

Throughout this work several assumptions have been introduced, that limit the above-mentioned conclusions. The present section will place the general conclusions in perspective by listing the main limitations. This offers, in addition, the opportunity to outline relevant future research topics.

- This thesis recognised the potential of reducing labour costs by realising the air barrier on the exterior of the building envelope. It showed, however, that exterior air barriers have important drawbacks as well. One of the major disadvantages is the increased weather load and the corresponding uncertainties in the durability of applying exterior tapes, which this study did not address. Important challenges lie in the product development of durable exterior air barrier systems.

- A quasi-steady state air flow model was solved staggered from the coupled transient heat and moisture transport. Preliminary results indicated that this decoupled modelling strategy may significantly reduce the simulation times in comparison with fully-coupled approaches. However, in order to draw general conclusions in this respect, the solver performances have to be studied more in depth.

- The study revealed the importance of considering ventilation cavities in the hygrothermal simulation of lightweight walls. Although in Belgium often brick cladding systems are applied, the present work was restricted to walls with a wooden cladding only. Further research should therefore verify the performance of lightweight walls with brick cladding systems and likewise consider the impact of wind driven rain.

- The study observed the large impact of uncertainties in the hygric material properties (in the high humidity range). From this follows that the key success factor to improve the overall reliability of today's HAM-modelling lies in a more accurate determination of material properties.

- The research project at hand identified the influence of the applied climatic data on the final simulation results. Yet most climatic data, applied in current HAM-modelling, are designed for building energy simulations. More expertise on reference climatic data is thus required for the prediction of heat, air and moisture transport in building component.

- The present study applied the state-of-the-art VTT-model (Hukka & Viitanen 1999) for the assessment of mould growth. This model is, however, solely based on (mainly stationary) laboratory measurements. Vereecken & Roels (2012) showed that important uncertainties are introduced when this model is applied in transient conditions. Hence, the evaluation of this model under atmospheric excitation is vital.

- The simulations in the present work applied relative severe climate conditions. For example, the indoor ventilation rate was limited and the parameters involved in the calculation of the air pressure difference were chosen conservatively. As a consequence of these assumptions, the performed simulations should be read as worst-case scenarios. A stochastic simulation approach may allow the formulation of more general conclusions.

7.3 Recommendations for practice

Despite the limitations mentioned above, the present study enables the formulation of several clear recommendations for a reliable application of exterior air barriers in timber frame construction.

Moving the interior air barrier to the outer layer of the building implies different attention points in detailing the building envelope. Building practitioners should pay particular attention to (1) the design of the connection of the exterior walls to the foundation and (2) the joints at the level of the eaves. The design of the first detail should consider the difficulty of using tapes on the foundation because this region is typically sandy during the construction stage. The latter should avoid that the roof construction interrupts the continuity of the exterior air barrier. The application of a separate roof overhang after sealing the air barrier may address this problem. Furthermore, the execution of a pressurisation test in dry weather conditions is highly recommended in order to avoid an underestimation of the global building airtightness.

In addition, the experimental and numerical findings of the present study contribute various

advisory implications as to the hygrothermal design of highly insulated timber frame walls in cold and moderate climates. Building designers should limit the risk for natural convection in the porous insulation layer when opting for an exterior air barrier system. In this context, the use of blown-in insulation materials with sufficient density levels (>40 kg/m^3) is recommended. This improves the contact between the insulation layer and the adjacent building layers. On the contrary, the use of insulation blankets is discouraged for this application because this insulation method is vulnerable for small air channels, which greatly increase the risk moisture problems related to natural convection. Furthermore, the applied air barrier should be sufficiently airtight. Based on the hygrothermal laboratory measurements, a material airtightness of 0.005 m^3/(m^2 h Pa) is recommended to avoid moisture problems due to forced convection. In addition to the application of exterior air barrier materials with a sufficient vapour permeability (s_d < 0.1 m) and a minimal thermal resistance, the study encourages selecting materials which have hygroscopic buffering properties. Yet this feature may also be provided by the insulation material through the use of cellulose insulation for instance. Finally, the numerical simulations revealed that the size and position of small deficiencies (0.5 - 2 cm) in the interior vapour barrier only have a limited impact on the hygrothermal performance of the system. Therefore, the present research would like to suggest a visual control of the interior vapour barrier, during which leakages of more than 1 cm should be closed.

References

Abuku, M. (2009), Moisture stress of wind-driven rain on building enclosures, PhD thesis, Departement of Civil Engineering, KU Leuven, Belgium.

Acke, A., Caillou, S., De Cuyer, K., Delmotte, C., Dobbels, F., Gerin, O., Lassoie, L., Loncour, E., Mahieu, E., Martin, Y., Mees, C., Michaux, B. & Schietecat, J. (2012), 'Special issue of WTCB contact: airtightness', pp. 10–23.

Aho, H., Vinha, J. & Korpi, M. (2008), Implementation of airtight constructions and joints in residential buildings, *in* '8th Nordic Building Physics Symposium', Copenhagen, Denmark.

Alturkistani, A., Fazio, P., Rao, J. & Mao, Q. (2008), 'A new test method to determine the relative drying capacity of building envelope panels of various configurations', *Building and Environment* **43**(12), 2203–2215.

ASHRAE (2009), F24 SI: Airflow Around Buildings, *in* 'ASHRAE Handbook Fundamentals', Atlanta, USA.

Aurlien, T. (2008), Airtightness revival in Norway, Presentation, *in* 'ASIEPI: Intelligent Energy Europe'.
URL: *www.asiepi.eu*

Aurlien, T. & Rosenthal, B. (2008), International comparison of envelope airtightness requirements & success stories that could inspire the EC and other MS, *in* 'EPBD buildings platform', EPBD buildings platform, ASIEPI.
URL: *www.asiepi.eu*

Axén, B. & Pettersson, B. (1977), *Investigations of thermal insulation and airtightness of buildings using thermography*, Swedisch Council for Building Research, Stockholm.

Bankvall, C. (1972), Natural convective heat transfer in insulated structures, PhD thesis, Division of building technology, Lund institute of technology, Sweden, Lund, Sweden.

Bejan, A. (2004), *Convection heat transfer*, Vol. Third, John Wiley & Sons, New Jersey, USA.

Bjerkevoll, G. O. (1994), Hot box measurements on structures with thick insulation layer, Master thesis, Department of Civil and Transport Engineering, Norwegian University of Science and Technology, Norway.

Black, C. D. (2006), Mould Resistance of Full Scale Wood Frame by, Master thesis, Universtity of Waterloo, USA.

Blümel, K. (1986), Entwicklung von Testreferenzjahren (TRY) für Klimaregionen der Bundesrepublik Deutschland, Technical report, BMFT-Bericht FB-T 86-051.

Bories, S. (1987), Natural convection in porous media, *in* J. B. Corapcioglu & M.Y., eds, 'Advances in transport phenomena in porous media', Martinus Nijhoff, pp. 77–141.

Borsch-laaks, R. (2011), 'Advanced building physics (in German)', *Holzbau* **5**, 18–23.

Brown, W. C., Bomberg, M. T., Ullett, J. M. & Rasmussen, J. (1993), 'Measured thermal resistance of frame walls with defects in the installation of mineral fibre insulation', *Journal of Building Physics* **16**(4), 318–339.

Burch, D. M. & Tenwolde, A. (1993), 'A computer analysis of moisture accumulation in the walls of manufactured housing', *ASHRAE Transactions* **99**(2), 977–990.

Caillou, S. & Van Orshoven, D. (2010), Report on the building airtightness measurement method in European countries, *in* 'ASIEPI: Intelligent Energy Europe', ASIEPI.
URL: *www.asiepi.eu*

Carlsson, B., Arne, E. & Engvall, P.-A. (1980), *Airtightness and thermal insulation : building design solutions*, Swedisch Council for Building Research, Stockholm, Sweden.

Carrié, F. R. & Rosenthal, B. (2008), 'An overview of national trends in envelope and ductwork airtightness', *Ventilation Information Paper, AIVC* **29**(August), 1–6.

Clarke, J., Johnstone, C., Mclean, R., Anderson, J., Rowan, N. & Smith, J. (1998), 'A

technicque for prediction of the conditions leading to mould growth in buildings', *Building and Environment* **34:4**.

Cornelis, R. & Appelmans, J. (2011), Practical investigations on the feasibility of exterior air barriers (in Dutch), Master thesis, University college, KAHO Sint-Lieven, Ghent, Belgium, Gent.

Cunningham, M. (1990), 'Modelling of moisture transfer in structures - A description of a finite-difference nodal model', *Journal of building and environment* **25**(1), 55–61.

Defraeye, T., Blocken, B. & Carmeliet, J. (2012), 'Analysis of convective heat and mass transfer coefficients for convective drying of a porous flat plate by conjugate modelling', *International Journal of Heat and Mass Transfer* **55**(1), 112–124.

Derome, D. (2005), 'Moisture accumulation in cellulose insulation caused by air leakage in flat wood frame roofs', *Journal of Thermal Envelope and Building Science* **28**(3), 269–287.

Derome, D. & Carmeliet, J. (2010), The nature, significance and control of solar-driven water vapor diffusion in wall systems - synthesis of research project RP-1235, Technical report, Concordia University, Canada.

Derome, D., Desmarais, G. & Thivierge, C. (2007), Large-scale experimental investigation of wood-frame walls exposed to simulated rain penetration in a cold climate, *in* 'Thermal Performance of the Exterior Envelopes of Whole Buildings', Clearwater, USA.

Descamps, F. (1996), Continuum and discrete modelling of isothermal water and air flow in porous media, PhD thesis, Departement of Civil Engineering, KU Leuven, Belgium.

Desmarais, G., Derome, D. & Fazio, P. (2000), 'Mapping of air leakage in exterior wall assemblies', *Journal of Building Physics* **24**(2), 132–154.

Desta, T. Z., Langmans, J. & Roels, S. (2011), 'Experimental data set for validation of heat, air and moisture transport models of building envelopes', *Building and Environment* **46**(5), 1038–1046.

Di Lenardo, B. (2009), A Method for Evaluating Air Barrier Systems and Materials, Technical report, NRC-CNRC, Canada.

Di Lenardo, B., Brown, W. C., Dalgliesh, A., Kumaran, K. & Poirier, G. (1995), Technical guide for air barrier systems for exterior walls of low-rise buildings, Technical report, guide for air barrier systems for exterior walls of low-rise buildings. Candian Construction Materials Centre, NRC, Ottawa, Ontario.

DIN4108 (1981), 'Thermal insulation in high rise buildings (in German)'.

Dos Santos, G. H. & Mendes, N. (2009), 'Combined heat, air and moisture (HAM) transfer model for porous building materials', *Journal of Building Physics* **32**(3), 203–220.

Dyrbøl, S., Svendsen, S. & Elmroth, A. (2002), 'Experimental Investigation of the Effect of Natural Convection on Heat Transfer in Mineral Wool', *Journal of Building Physics* **26**(2), 153–164.

Eek, M. (2009), Airtightness of the Basement Wall : Wood Frame Wall Junction, Master thesis, Norwegian University of Science and Technology, Trondheim, Norway.

Elmroch, A. (1980), 'Build Tight - Ventilate Right', *Air Information Review* **1**(4), 6–7.

Erhorn, H. & Erhorn-Kluttig, H. (2011), Terms and definitions for high performance buildings, *in* 'Concerted action: energy performance of buildings'.
URL: *www.epbd-ca.org*

Eykens, J. (2011), Compact flat roofs with variable vapour retarder: hygric optimisation of the roof assembly based on dynamic computer simulations (in Dutch), Master thesis, Catholic University College Sint Lieven, Ghent, Belgium.

Feist, W., Schnieders, J., Dorer, V. & Haas, A. (2005), 'Re-inventing air heating: Convenient and comfortable within the frame of the Passive House concept', *Energy and Buildings* **37**(11), 1186–1203.

Ge, H. & Fazio, P. (2004), 'Experimental evaluation of thermal response and condensation performance of metal curtain walls subjected to air leakage', *Journal of Architectural Engineering* (June), 61–68.

Geving, S. (1997), Moisture design of building constructions: hygrothermal analysis using simulation models, PhD thesis, NTNU Trondheim.

Geving, S. & Holme, J. (2010), 'The drying potential and risk for mold growth in compact

wood frame roofs with built-in moisture', *Journal of Building Physics* **33**(3), 249–269.

Geving, S. & Uvsløkk, S. (2000), Moisture conditions in timber frame roof and wall structures, Technical report, Norwegian University of Science and Technology, Trondheim, Norway.

Glaser, H. (1958), 'Temperatur und Dampfdruckverlauf in einer homogen Wand bei Feuchteausscheiding', *Kältetechnik* **174**.

Gnoth, S. (2007), The thermal and hydric behavior of components with open and closed cavities (in German), PhD thesis, Technical Universtity of Dresden.

Grunewald, J. (1997), Diffusive and convective mass and energy transport in capillary porous building materials (in German), PhD thesis, University of Technology Dresden, Germany.

Gudum, C. (2003), Moisture Transport and Convection in Building Envelopes, PhD thesis, Department of Civil Engineering, Technical University of Denmark.

Gusdorf, J. (1992), 1D airflow through a wall structure - WALLFEM, Technical report, IEA/Annex 24 T1-CA-92/03.

Guyot, G., Carrié, R. & Schild, P. (2010), Stimulation of good building and ductwork airtightness through EPBD, *in* 'ASIEPI: Intelligent Energy Europe', number March, ASIEPI.
URL: *www.asiepi.eu*

Hagentoft, C. E. (1991), Forced and natural convection coupled with heat conduction in walls with air gaps, *in* 'Proceedings of the seventh international conference of Numerical methods in thermal problems', Standford, USA.

Hagentoft, C.-E. (2002), HAMSTAD: WP2: Benchmark package, Technical report, University of Technology, Chalmers, Gothenburg, Sweden.

Hagentoft, C.-E. & Blomberg, T. (2000), 1D-HAM: Coupled Heat, Air and Moisture Transport in Multi-layered Wall Structures, Manual with brief theory and an example, Technical report, Chalmers University of Technology, Gothenburg, Sweden.

Hagentoft, C.-E. & Harderup, E. (1993), Reference years for moisture calculations, Technical report, T2-S-94/01, IEA Annex 24, HAMTIE.

Hagentoft, C. E., Kalagasidis, A. S., Adl-Zarrabi, B., Roels, S., Carmeliet, J., Hens, H., Grunewald, J., Funk, M., Becker, R., Shamir, D., Adan, O., Brocken, H., Kumaran, K. & Djebbar, R. (2004), 'Assessment method of numerical prediction models for combined heat, air and moisture transfer in building components: benchmarks for one-dimensional cases', *Journal of Thermal Envelope and Building Science* **27**(4), 327–352.

Hens, H. (1987), Interstitial condensation in timber framed walls: influence of diffusion, stack effect and pressure differences, *in* 'CIB -W40 Meeting', Boras, Sweden.

Hens, H. (1990), The hygrothermal behaviour of sloped roofs, *in* 'International CIB W67 Symposium on 'Energy, moisture and climate in Buildings", Rotterdam, The Netherlands.

Hens, H. (1992), Package of Climatological Data measured in Belgian Buildings, *in* 'Energy Conservation in Buildings and Community Systems Program, Annex 24 Heat, Air and Moisture Transfer in Insulated Envelope Parts (HAMTIE)', Internal Report T2B92/01, International Energy Agency.

Hens, H. (1999), 'Fungal defacement in buildings: A performance related approach', *International Journal of Heating, Ventilation, Air-Conditioning and Refrigerating Research* **5**(3), 256–280.

Hens, H. (2003), *Heat and moisture transport (in Dutch)*, 6 edn, Acco, Leuven, Belgium.

Hens, H. (2006), 'The vapor diffusion resistance and air permeance of masonry and roofing systems', *Building and Environment* **41**(6), 745–755.

Hens, H. (2007), *Building Physics - Heat Air and Moisture, Fundamentals and Engineering Methods with Examples and Exercises*, Ernst and Sohn.

Hens, H. (2010), *Applied Building Physics: Boundary Conditions, Building Performance and Material Properties*, Ernst & Sohn Verlag Gmbh (a John Wiley Company), Berlin, London, New York.

Hens, H. & Janssens, A. (1996), Enquiry on HAMCAT codes, Technical report, Catholic Universtity of Leuven, Annex 24, Task 1: Modelling.

Hindmarsh, A. (2005), SUNDIALS:Suite of Nonlinear and Differnential/Algebraic Equations Solvers., Technical report, Lawrence Livermore National Laboratory, USA.

Holøs, S. B. & Relander, T.-O. (2010), Airtightness Measurements of Wood Frame Low Energy Row Houses, *in* '2nd Building Enclosure Science and Technology conference', Portland, pp. 1–11.

Homb, A., Skogstad, H. B. & Thue, J. V. (1993), Laboratory tests of moisture conditions in different wood frame walls, *in* 'Proc. 3rd Symp. Building Physics in the Nordic Countries', Thermal Insulation Lab., Lyngby, Denmark, pp. 633–641.

Hukka, a. & Viitanen, H. a. (1999), 'A mathematical model of mould growth on wooden material', *Wood Science and Technology* **33**(6), 475–485.

ISO10456 (2007), 'Hygrothermal properties - Tabulated design values and procedures for determining declared and design thermal values'.

ISO12572 (2001), 'Hygrothermal performance of building materials and products - Determination of water vapour transmission properties'.

ISO13788 (2001), 'Hygrothermal performance of building components and building elements - Internal surface temperature to avoid critical surface humidity and interstitial condensation - Calculation methods'.

ISO13829 (1996), 'Thermal performance of buildings-Determination of air permeability of buildings-Fan pressurization method'.

ISO8302 (1991), 'Thermal insulation - Determination of steady-state thermal resistance and related properties - Guarded hot plate apparatus'.

Jacobsen, E., Pedersen, O. & Vejlgaard, K. (2008), Analyzing different sealing techniques in low energy projects, Master thesis, Oslo University College, Oslo, Norway.

Janssen, H. (1997), Thermal performance of highly insulated wood frame walls, Master thesis, Norwegian University of Science and Technology, Norway.

Janssen, H. (2002), The influence of soil moisture transfer on building heat loss via the ground, PhD thesis, Departement of Civil Engineering, KU Leuven, Belgium.

Janssen, H., Blocken, B. & Carmeliet, J. (2007), 'Conservative modelling of the moisture and heat transfer in building components under atmospheric excitation', *International Journal of Heat and Mass Transfer* **50**(5-6), 1128–1140.

Janssen, H. & Roels, S. (2009), 'Qualitative and quantitative assessement of interior moisture buffering by enclosures', *Energy and Buildings* **41**(4), 382–394.

Janssens, A. (1998), Reliable control of interstitial condensation in lightweight roof systems: calculation and assessement methods, PhD thesis, Departement of Civil Engineering, KU Leuven, Belgium.

Janssens, A. & Dobbels, F. (2005), 'Development and application of airtightness requirements for pitched roof construction (in Dutch)', *Bouwfysica* **16**.

Janssens, A. & Hens, H. (2003), 'Interstitial condensation due to air Leakage: a sensitivity analysis', *Journal of Thermal Envelope and Building Science* **27**(1), 15–29.

Janssens, A. & Hens, H. (2007), 'Effects of wind on the transmission heat loss in duo-pitched insulated roofs: A field study', *Energy and Buildings* **39**(9), 1047–1054.

Johannessen, E. (1995), Hot box measurements on Structures with thick insulation layer. Examenation woork (In Norwegain), PhD thesis, NTNU.

Jokisalo, J., Kurnitski, J., Korpi, M., Kalamees, T. & Vinha, J. (2009), 'Building leakage, infiltration, and energy performance analyses for Finnish detached houses', *Building and Environment* **44**(2), 377–387.

Kalamees, T. (2006), 'Indoor humidity loads and moisture production in lightweight timber-frame detached Houses', *Journal of Building Physics* **29**(3), 219–246.

Kalamees, T. (2007), 'Air tightness and air leakages of new lightweight single-family detached houses in Estonia', *Building and Environment* **42**(6), 2369–2377.

Kalamees, T. & Kurnitski, J. (2009), 'Moisture convection performance of external walls and roofs', *Journal of Building Physics* **33**(3), 1–23.

Kalamees, T., Kurnitski, J., Jokisalo, J., Eskola, L., Jokiranta, K. & Vinha, J. (2010), 'Measured and simulated air pressure conditions in Finnish residential buildings', *Building Services Engineering Research and Technology* **31**(2), 177–190.

Kalamees, T. & Vinha, J. (2003), 'Hygrothermal calculations and laboratory tests on timber-framed wall structures', *Building and Environment* **38**(5), 689–697.

Karagiozis, A. (1999), Moisture Engineering, *in* 'Performance of Exterior Envelopes of Whole Buildings VII International Conference', Clearwater, USA.

Karagiozis, A. & Künzel, H. (2009), 'The Effect of Air Cavity Convection on the Wetting and Drying Behavior of Wood-Frame Walls Using a Multi-Physics Approach', *Journal of ASTM International* **6**(10), 101455.

Karagiozis, A. N. (2001), Advanced Hygrothermal Modeling MOISTURE-EXPERT, *in* '35th International Particleboard/Composite Materials Symposium'.

Kim, A., Shaw, C., Saum, D., Shaw, J. & Colliver, D. (1986), 'Seasonal variation in airtightness of two detached houses', *ASTM special technical publication* **904**, 17–32.

Klarsfeld, S. & Combarnous, M. (1980), 'Analyse des transferts thermiques convectifs dans les isolants poreux perméables', *Revue generale de thermique* **228**, 977–983.

Kohonen, R. (1984), 'Transient analysis of the thermal and moisture physical behaviour of building constructions', *Building and Environment* **19**(1), 1–11.

Kohonen, R., Kokko, E., T., O. & M., V. (1985), Thermal effects of air flows in building structures, Technical report, Technical Reserach Centre Finland, VTT Espoo. Research reports 367.

Kronvall, J. (1978), 'Testing of houses for air leakage using a pressure method', *ASHRAE transactions* **NO 2473**.

Kronvall, J. (1980), Air flows in building components, PhD thesis, Lund institute of technology, Sweden.

KUL (2011), Indoor climate in Passive house: case study, Technical report, Departement of Civil Engineering, KU Leuven, Belgium.

Kumaran, K. (1996), Material properties - Annex 24, Technical report.

Künzel, H. M. (1995), Simultaneous Heat and Moisture Transport in Building Components: One- and two-dimensional calculation using simple parameters, Technical report, Fraunhofer IRB Verlag Stuttgart, Germany.

Künzel, H. M. (1997), Indoor air humidity conditions in living spaces (in German), Technical report, 314, Fraunhofer Institute for Building Physics, Germany.

Künzel, H. M., Karagiozis, A. N. & Kehrer, M. (2008), Assessing the benefits of cavity ventilation by hygrothermal simulation, *in* R. S. & V. G., eds, 'Building physics symposium in honour of Prof.Hugo L.S.C Hens', Leuven, Belgium.

Kurnitski, J. & Kalamees, T. (2000), Moisture convection around a crack by pressurization, *in* 'Proceedings of Estonian Academic Science Engineering', Vol. 6, pp. 48–60.

Labat, M., Woloszyn, M., Garnier, G., Rusaouen, G. & Roux, J. J. (2012), 'Impact of direct solar irradiance on heat transfer behind an open-jointed ventilated cladding: Experimental and numerical investigations', *Solar Energy* **86**(9), 2549–2560.

Langmans, J., Klein, R., De Paepe, M. & Roels, S. (2010), 'Potential of wind barriers to assure airtightness of wood-frame low energy constructions', *Energy and Buildings* **42**(12), 2376–2385.

Langmans, J., Klein, R. & Roels, S. (2010), Air Permeability Requirements for Air Barrier Materials in Passive Houses, *in* 'International Symposium on Building and Ductwork Airtightness', Energie + Umwelt Zentrum, Copenhagen, Denmark.

Langmans, J., Klein, R. & Roels, S. (2012), 'Hygrothermal risks of using exterior air barrier systems for highly insulated light weight walls: a laboratory investigation', *Building and Environment* **56**(10), 192–202.

Langmans, J., Klein, R. & Roels, S. (2013), 'Numerical and experimental investigation of the hygrothermal response of timber frame walls with an exterior air barrier', *Journal of Building Physics* **36**(4).

Langmans, J., Nicolai, A., Klein, R., J., G. & Roels, S. (2011), Numerical Simulation of Building Components - Towards an Efficient Implementation of Air Convection in HAM-models, *in* '9th Nordic Symposium on Building Physics', Tampere University of Technology, Tampere,Finland, pp. 399–405.

Langmans, J., Nicolai, A., Klein, R. & Roels, S. (2012), 'A quasi-steady state implementation of air convection in a transient heat and moisture building component model', *Building and Environment* **58**(12), 208–218.

Lawton, B. & Limited, P. (1992), *Airtightness and air quality of preserved wood-foundations*,

Canada Mortgage and Housing Corporation, Ottawa, Canada.

Lecompte, J. (1989), The influence of natural convection on the thermal quality of insulated cavity walls constructions (in Dutch), PhD thesis, Departement of Civil Engineering, KU Leuven, Belgium.

Li, Q., Rao, J. & Fazio, P. (2009), 'Development of HAM tool for building envelope analysis', *Building and Environment* **44**(5), 1065–1073.

Liddament, M. (1996), *A guide to energy efficient ventilation*, Oscar Faber Partnership, U.K.

Limb, M. J. (2001), A Review of International Ventilation, Airtightness, Thermal Insulation and Indoor Air Quality Criteria, Technical report.

Lorentzen, G. & Brendeng, E. (1959), On the influence of free convection in insulated vertical walls, *in* '10th International congress of refrigeriation', p. 294.

Lstiburek, J., Pressnail, K. & Timusk, J. (2002), 'Air pressure and building envelopes', *Journal of Building Physics* **26**(1), 53–91.

Mao, Q., Fazio, P. & Rao, J. (2009), 'In-cavity evaporation allowance-A drying capacity indicator for wood-frame wall system', *Building and Environment* **44**(12), 2418–2429.

Maref, W., Armstrong, M., Rousseau, M. & Lei, W. (2010), A field monitoring investigation of the effect of adding different exterior thermal insulation materials on the hygrothermal response of wood-frame walls in a cold climate, *in* 'BEST conference', Portland, pp. 1–15.

Maref, W., Lacasse, M. & Booth, D. (2002), Bechmarking of IRC's advanced hygrothermal model - hygIRC using mid and large scale experiments, Technical Report December, IRC-RR-126,NRC.

Martin, M. & Berdahl, P. (1984), 'Characteristics of Infrared Sky Radiation in the United States', *Solar Energy* **33**(3/4).

Mason, G. (1974), 'Rising damp', *Building Science* **9**(3), 227–231.

Mattsson (2004), Air leakage in Dwellings: Literature Survey, Modelling and Measurements, Master thesis, Chalmers Technical University, Götenborg, Sweden.

Merill, J. & Tenwolde, A. (1989), 'Overview of Moisture-Related Damage in One Group of Wisconsin Manufactured Homes', *ASHRAE Transactions* **95**(1).

Mukai, K., Hokoi, S., Kominami, K., Abuku, M., Suzuki, H. & Iba, C. (2008), 'Thermal and moisture characteristics in insulated wall of conventional wooden house', *Journal of Environmental Engineering* **73**(623).

Myhre, L. & Aurlien, T. (2005), Measured airtightness in low-energy houses, *in* '7th Nordic Building Physics Symposium', Reykjavik, Iceland.

Nicolai, A. (2007*a*), Modelling and numerical simulation of salt transport and phase transitions in unsaturated porous building materials, PhD thesis, Syracuse University, USA.

Nicolai, A. (2007*b*), 'www.bauklimatik-dresden.de/delphin5'.

Nield, D. & Bejan, A. (2006), *Convection in porous media*, 3rd edn, Springer-Verslag New York.

Nore, K. (2009), Hygrothermal performance of ventilated wooden cladding, PhD thesis, Norwegian University of science and technology, Norway.

Nore, K., Blocken, B. & Thue, J. V. (2010), 'On CFD simulation of wind-induced airflow in narrow ventilated facade cavities: Coupled and decoupled simulations and modelling limitations', *Building and Environment* **45**(8), 1834–1846.

Ojanen, T. & Kohonen, R. (1989), Hygrothermal influence of air convection in wall structures, *in* 'Thermal performance of the exterior envelope of buildings IV.', ASHRAE, Atlanta, USA.

Ojanen, T. & Kohonen, R. (1995), Hygrothermal performance analysis of wind barrier structures, *in* 'ASHRAE Transactions', Chicago, USA.

Ojanen, T., Kohonen, R. & Kumaran, M. K. (1994), Modeling heat, air, and moisture transport through building materials and components, *in* H. R. Trechsel, ed., 'Moisture control in buildings', ASTM International, chapter 2.

Ojanen, T. & Kumaran, K. (1996), 'Effect of exfiltration on the hygrothermal behaviour of a residential wall assembly', *Journal of Building Physics* **19**(3), 215–227.

Ojanen, T., Viitanen, H., Peuhkuri, R., Vinha, J. & Salminen, K. (2010), Mold Growth Modeling of Building Structures Using Sensitivity Classes of Materials, *in* ASHRAE, ed., 'Build-

ing XI conference', Clearwater, USA.

Økland, Ø. (1998), Convection in highly-insulated building structures, PhD thesis, Norwegian University of Science and Technology, Trondheim, Norway.

Onate, E. & Manzan (2000), Stabilization techniques for finite element analysis of convection-diffusion problems, *in* 'CIMNE', number February.

Patankar, S. V. (1980), *Numerical Heat Transfer and Fluid Flow*, Series in computational methods in mechanics and thermal sciences, Hemisphere, Washington, USA.

Penne, A. & Vandeweerd, R. (2012), Air permeability of window connection in timber frame construction (in Dutch), Master thesis, University college, KaHo Sint-Lieven, Ghent, Belgium.

Perez, R., Stewart, R., Seals, R. & Guertin, T. (1988), The development and verification of the Perez diffuse radiant model, Technical report, Sandia Report SAND88-7030.

Peuhkuri, R., Viitanen, H. & Ojanen, T. (2008), Modelling of mould growth in building envelopes, Technical report, IEA ECBCS Annex 41 Closing Seminar, Copenhagen, Denmark.

Piecková, E. & Jesenská, Z. (1996), 'Microscopic fungi in dwellings and their health implications', *Ann Agric Environ Med* **6**(1).

Powell, F., Krarti, M. & Tuluca, A. (1989), 'Air movement influence on the effective thermal resistance of porous insulations: a literature survey', *Journal of Building Physics* **12**(3), 239–251.

Proclima (2009), Long-term tests - durability with Tescon/Budax tapes on wood fiberboards, Technical Report 1, Cologne, Germany.

Rao, J., Fazio, P., Bartlett, K. & Yang, D.-Q. (2009), 'Experimental evaluation of potential transport of mold spores from moldy studs in full-size wall assemblies', *Building and Environment* **44**(8), 1568–1577.

Reboux, G., Bellanger, A., Roussel, S., Grenouilllet, F. & Millon, L. (2010), 'Moulds in dwellings: health risks and involved species (in french)', *Rev. Mal Respir.* **27**(2), 118–121.

Reiss, J. & Erhorn, H. (2003), Technical feasibility of a large scale implementation of the energy concept of Passivhaus (in German), Technical report, Fraunhofer Institute for Building Physics, WB 117/2003.

Relander, T.-O. (2011), Airtightness of wood-frame houses, PhD thesis, Norwegian University of Science and Technology, Trondheim, Norway.

Relander, T.-O., Bauwens, G., Roels, S., Thue, J. V. & Uvsløkk, S. (2011), 'The influence of structural floors on the airtightness of wood-frame houses', *Energy and Buildings* **43**, 639–652.

Relander, T.-O., Heiskel, B. & Tyssedal, J. S. (2011), 'The influence of the joint between the basement wall and the wood-frame wall on the airtightness of wood-frame houses', *Energy and Buildings* **43**(6), 1304–1314.

Riesner, K. (2003), Natural convection in exterior walls (in German), Phd thesis, Univeristy of Rockstock, Germany.

Riesner, K. (2009), Prevention strategies for condensation and mould growth in exterior wall systems caused by natural convection in the insulation (in German), Technical report, Fraunhofer IRB.

Riesner, K., Hagentoft, C.-E. & Mainka, G.-W. (2004), Condensation risk within loose fill insulation due to natural convection in vertical cavities, *in* 'Performance of Exterior Envelopes of Whole Buildings IX International Conference', Clearwater, USA.

Rode Pedersen, C. (1990), Combined heat and moisture transfer in building constructions, PhD thesis, Technical University of Denmark, Lyngby.

Roels, S. & Carmeliet, J. (2005), Water vapour permeability and sorption isotherm of coated gypsum board, *in* 'Nordic Building Physics Symposium', Reykjavik, Iceland.

Roels, S., Carmeliet, J., Hens, H., Adan, O., Brocken, H., Cerny, R., Pavlik, Z., Ellis, A. T., Hall, C., Kumaran, K., Pel, L. & Plagge, R. (2004), 'A comparison of different techniques to quantify moisture content profiles in porous building materials', *Journal of Thermal Envelope and Building Science* **27**(4), 261–276.

Roels, S. & Langmans, J. (2009), Airtightness problems in low-energy dwelling, Technical

report, 2009/08, Section Building Physics, Leuven, Belgium.

Roels, S., Talukdar, P., James, C. & Simonson, C. J. (2010), 'Reliability of material data measurements for hygroscopic buffering', *International Journal of Heat and Mass Transfer* **53**(23-24), 5355–5363.

Rousseau, M. Z. (1983), Control of surface and concealed condensation, *in* 'Humidity, Condensation and Ventilation in Houses', Canada.

Rousseau, M. Z. (2003), Control Strategies for Managing Condensation in Walls, *in* 'BSI 2003', IRC Building science insight 2003 seminar series, Canada, pp. 1–11.

Saeid, N. H. & Pop, I. (2004), 'Transient free convection in a square cavity filled with a porous medium', *International Journal of Heat and Mass Transfer* **47**(8-9), 1917–1924.

Said, N. (2007), 'Measurement methods of moisture in building envelopes - a literature review', *Journal of Architectural Heritage* **1**(3), 293–310.

Salonvaara, M. H., Ojanen, T. T., Kokko, E. & Karagiozis, A. (1998), Drying Capabilities of Wood Frame Walls with Wood Siding, *in* 'Thermal envelope VII'.

Salonvaara, M., Karagiozis, A., Pazera, M. & Miller, W. (2007), Air Cavities Behind Claddings - What Have We Learned?, *in* 'Thermal Performance of the Exterior Envelope of Buildings X Conference', Clearwater, USA.

Salonvaara, M. & Nieminen, J. (2002), Hygrothermal Performance of Low-Sloped Roofs with Groove Ventilation, *in* '6th Symposium on Building Physics in the Nordic Countries', Trondheim, Norway.

Sedlbauer, D. K. (2001), Prediction of mould growth on and in building components (in German), PhD thesis, University of Stuttgart, Germany.

Sherman, M. & Chan, R. (2004), Building Airtightness : Research and Practice 1, Technical report, Lawrence Berkeley national laboratory report no. LBNL-53356, Berkeley, USA.

Sherman, M. H. & Palmiter, L. (1994), Uncertainties in Fan Pressurization Measurements, *in* 'Air Flow Performance of Building Envelopes, components and systems', Special Technical Publication of ASTM, USA.

Siitonen, V. (1982), *Measurments of local air tightness in buidings*, Technical Research Centre of Finland, Espoo.

Silberstein, A., Langlais, C. & Arquis, E. (1990), 'Natural convection in light fibrous insulating materials with permeable interfaces: onset criteria and its effect on the thermal performances of the product', *Journal of Building Physics* **14**(1), 22–42.

Steeman, H.-J., T'Joen, C., Van Belleghem, M., Janssens, A. & De Paepe, M. (2009), 'Evaluation of the different definitions of the convective mass transfer coefficient for water evaporation into air', *International Journal of Heat and Mass Transfer* **52**(15-16), 3757–3766.

Steskens, P., Dobbels, F., Loncour, X. & Flamant, G. (2012), The influence of air permeability and type of underlay on the hygrothermal performance of an inclined roof, *in* '5th International Building Physics Conference', Kyoto, Japan.

Stranger, M., Verbeke, S., Verbeke, L., Geyskens, F., Swinnen, R., Goelen, E., Taubel, M., Hyvarien, A., Laverge, J., Janssens, A., Wuyts, D. & Ingelaere, B. (2012), Exploratory research on the quality of the indoor environment in energy efficient buildings: the influence of outdoor environment and ventilation, *in* 'Clean Air, Low Energy', LNE.

Straube, J. (2001), Pressure Moderation and Rain Penetration Control, *in* 'Pressure Equalized Rainscreens: Design and Performance'.

Straube, J. & Burnett, E. (2005), *Building science for building enclosures*, Building Science Press.
URL: *www.buildingscience.com*

Straube, J. & Finch, G. (2009), Report 0906: Ventilated wall claddings: review, field performance, and hygrothermal modeling, Technical report, Waterloo.
URL: *www.buildingscience.com*

Swami, M. & Chandra, S. (1987), Procedures for calculating natural ventilation airflow rates in buildings, Technical report, FSEC-CR-163-86, Florida Solar Energy Center, Cape Canaveral, Florida, USA.

Syversen, E. & Ulimoen, I. (2009), Designing airtight wood-frame houses, Master thesis, Norwegian University of Science and Technology,Trondheim, Norway.

Tariku, F., Kumaran, K. & Fazio, P. (2010), 'Transient model for coupled heat, air and moisture transfer through multilayered porous media', *International Journal of Heat and Mass Transfer* **53**(15-16), 3035–3044.

Teasdale-St-Hilaire, A. & Derome, D. (2007), 'Comparison of experimental and numerical results of wood-frame wall assemblies wetted by simulated wind-driven rain infiltration', *Energy and Buildings* **39**(11), 1131–1139.

Tenwolde, A. (1985), 'Steady-state one-dimensional water vapor movement by diffusion and convection in a multilayered wall', *ASHRAE Transactions* **91**(1).

Tenwolde, A. & Carll, C. (1992), Effect of cavity ventilation on moisture in walls and roofs, *in* 'Thermal Performance of the Exterior Envelope of Buildings VI Conference', Clearwater, USA.

Tenwolde, A., Carll, C. & Malinauskas, V. (1993), Airflows and Moisture Conditions in Walls of Manufactured Homes, *in* M. P & A. Persily, eds, 'Airflow performance of building envelopes, components, and systems', Philadelphia, pp. 137–155.

Tenwolde, A., Carll, C. & Malinauskas, V. (1995), Airflows and Moisture Conditions in Walls of Manufactured Homes, *in* 'ASTM STP 1255', Philadelphia, pp. 137–155.

Tenwolde, A. & Rose, W. B. (1994), 'Moisture Control Strategies for the Building Envelope', *Wood design focus* **5**(4), 7–10.

Tenwolde, A. & Rose, W. B. (1996), 'Moisture control strategies for the building envelope', *Journal of Building Physics* **19**(3), 206–214.

Thue, J. V., Skogstad, H. B. & Homb, A. (1996), 'Wood frame walls in cold climate - vapour barrier requirements', *Journal of Building Physics* **20**(1), 63–75.

Timusk, J., Seskus, A. & Ary, N. (1991), 'The control of wind cooling of wood frame building enclosures', *Journal of buildings Physics* **15**(1).

Trechsel, H. R. (2001), *Moisture Analysis and Condensation Control in Building Envelopes: (MNL 40)*, ASTM International.

TV215 (2000), Flat roof constructions: configuration, materials, implementation, maintenance (in Dutch), Technical report, Belgium Building Research Insitute, Brussels, Belgium.

Uvsløkk, S. (1996), 'The Importance of Wind Barriers for Insulated Timber Frame Constructions', *Journal of Building Physics* **20**(1), 40–62.

Uvsløkk, S., Skogstad, H. B. & Grynning, S. (2010), How to prevent natural convection causing extra heat loss and moisture problems in thick insulation layers, *in* '3rd Nordic Passive House Conference 2010 -Towards 2020 Sustainable Cities and Buildings'.

Van Daele, M. (2012), *Numerical method for differential equations*, Ghent Univeristy, Belgium.

Van de Sande, H., De Gersem, H. & Hameyer, K. (1999), Finte element stabilization techniques for convection-diffusion problems, *in* '7th International journal of theoretical electrotechnics', number 2, pp. 56–79.

Van den Brande, T., Blocken, B. & Roels, S. (2012), Influence of facade materials on runoff due to wind-driven rain, *in* 'Proceedings of the 5th International Building Physics Conference (IBPC)', Kyoto, Japan.

Van den Brande, T. & Wouter, W. (2011), Hygrothermal analysis of timber frame wall elements: experimental investigation (in Dutch), Master thesis, Departement of Civil Engineering, KU Leuven, Belgium.

Van Schijndel, J. (2007), Integrated Heat Air and Moisture Modeling and Simulation, PhD thesis, Eindhoven University of Technology, The Netherlands.

Vereecken, E. & Roels, S. (2012), 'Review of mould prediction models and their influence on mould risk evaluation', *Building and Environment* **51**, 296–310.

Vereecken, E., Roels, S. & Janssen, H. (2011), 'In situ determination of the moisture buffer potential of room enclosures', *Journal of Building Physics* **34**(3), 223–246.

Viittanen, H. & Salonvaara, M. (2001), Failure criteria, *in* Trechsel, ed., 'Moisture analysis and condensation control in building envelopes MNL40', ASTM USA, pp. 66–80.

Vinha, J. (2007), Hygrothermal performance of timber-framed external walls in Finnish climatic conditions: A method of determing a sufficient water vapour resistance of the internal lining of a wall assembly, PhD thesis, Tampere University, Finland.

Vinha, J. & Kakela, P. (2000), Water vapour transsmission in wall structures due to diffusion and convection, *in* 'Proceedings of Healthy Buildings, Finland', Vol. 3.

Wang, J. & Hagentoft, C.-E. (2001), 'A numeical method for calculating combined heat, air and moisture transport in building envelope components', *Nordic journal of building physics* **2**.

Weber, J. E. (1975), 'The boundary-layer regime for convection in a vertical porous layer', *International Journal of Heat and Mass Transfer* **18**(4), 569–573.

Wouters, P., Heijmans, N. & Carrié, F. R. (2008), Implementation of Energy Performance Regulations: Opportunities and Challenges related to Building Airtightness, *in* 'EPBD buildings platform', p. 10.
URL: *www.asiepi.eu*

Wouters, P., Loncour, X., Vandaele, L., Janssens, A., De Paepe, M., Roels, S., Honoré, R. & Carrié, R. (2012), Towards a framework for the implementation for minimal building airtightness requirements, Technical report, VEA/EPB/2011/WL/1.

Yarbrough, D. & Wudhapitak, S. (1992), Air permeability of loose-fill residential insulations, *in* '8th international conference on thermal insulation', Millbrae, California, pp. 8–14.

Zillig, W. (2009), Moisture transport in wood using a multiscale approach, PhD thesis, Departement of Civil Engineering, KU Leuven, Belgium.

Zirkelbach, D., Künzel, H. M. & Schafaczek, B. (2009), Vapour convection becomes predictable - Transient model taking moisture convection into account in the simulation of light weight building components (in German), *in* '4th International Symposium on Building and Ductwork Airtightness & 30th AIVC Conference', Berlin, pp. 1–8.

Curriculum vitae

Jelle Langmans

Personal information

Nationality:	Belgium
Date of birth:	February 07, 1986 Herentals, Belgium
Contact:	Fritz de Beulestraat 31 9000 Gent, Belgium +32 (0)495 63 92 68 langmans.jelle@gmail.com
Marital status:	Married to Aurélie van de Peer

Education

2009	Predoctoral program, Arenberg doctoral school KU Leuven, Belgium
2008	Master degree in industrial engineering (construction) De Nayer Instituut, Sint-Katelijne-Waver, Belgium (great distinction) M.Sc Thesis: *Optimisation of the energy use of office buildings with verification towards the EPBD-regulation (in Dutch)*
2004	Vrij Technisch Instituut, Zandhoven, Belgium

Present and previous positions

2009-2012	Ph.D. student at the Section of Building Physics Department of Civil Engineering, KU Leuven, Belgium
2008	Researcher at the Sustainable Building Research Group Department of Industrial Engineering, Ghent, Belgium

Grants and funding

2009-2012 Personal Ph.D. grant (grant number 81153) of the Institute for the Promotion of Innovation through Science and Technology in Flanders (IWT-Vlaanderen).

Distinctions and Awards

2009 Best Paper Award (30nd AIVC & 4th BUILDAIR conference, Berlin)

2008 Willy Asselman-award (M.Sc. Thesis)

2008 STRABAG prize (M.Sc. Thesis)

Research activities

2011- Reviewer for "Energy and Buildings"

2009-2012 Preparation of a Ph.D. entitled "Feasibility of exterior air barriers in timber frame construction".

Scientific publications

International journal publications

- Langmans, J.,Klein R., and Roels S., (2013), 'Numerical and experimental investigation of the hygrothermal response of timber frame walls with an exterior air barrier' *Journal of Building Physics* **36** (4).
- Langmans, J., Nicolai A., Klein R., and Roels S., (2012), 'A quasi-steady state implementation of air convection in a transient heat and moisture building component model' *Building and Environment* **58** (12): 208-218.
- Langmans, J., Klein R., and Roels S., (2012) 'Hygrothermal risks of using exterior air barrier systems for highly insulated lightweight walls: a laboratory investigation', *Building and Environment* **56** (10): 192-202
- Desta, T. Z., Langmans J., and Roels S., (2011), 'Experimental data set for validation of heat, air and moisture transport models of building envelopes.' *Building and Environment* **46** (5): 1038-1046
- Langmans, J., Klein R., De Paepe M. and Roels S., (2010). 'Potential of wind barriers to assure airtightness of wood-frame low energy constructions'. *Energy and Buildings* **42** (12): 2376 - 2385

Publications in proceedings of international conferences

- Langmans, J., Klein R. and Roels S., (2013),'Quantitative study on the hygric response of timber frame walls with exterior air barriers'. In Proceedings of the 17th Passive House Conference, Frankfurt, Germany. pp 167-172
- Langmans, J., Klein R. and Roels S., (2012),'Numerical and experimental investigation of the hygrothermal response of timber frame walls with an exterior air barrier', In Proceedings of the 5th International Building Physical Conference, Kyoto, Japan. pp 369-375
- Langmans, J., Klein R. and Roels S., (2011), 'Laboratory investigation of timber frame walls with an exterior air barrier in a temperate climate', In Proceedings of the 32nd AIVC - 1th TightVent Conference, Brussels, Belgium, pp 266-270
- Langmans, J., Nicolai A. Grunewald J., Klein R. and Roels S., (2011), 'Numerical Simulation of Building Components - Towards an Efficient Implementation of Air Convection in HAM-models', In Proceedings of the 9th Nordic Symposium on Building Physics, Tampere, Finland. pp 399-405
- Langmans, J., Klein R. and Roels S., (2011), 'Hygrothermal response of highly insulated timber frame walls with an exterior air barrier system: laboratory investigation', In Proceedings of the 9th Nordic Symposium on Building Physics, Tampere, Finland. pp 525-531
- Langmans, J., Klein R. and Roels S., (2010), 'Air Permeability Requirements for Air Barrier Materials in Passive Houses', In Proceedings of the 5th International Symposium on Building and Ductwork Airtightness. Copenhagen, Denmark. (CD-ROM)
- Langmans, J., Klein R., De Paepe M., Eykens P. and Roels S., (2009), 'Feasibility of Using Wind Barriers as Air Barriers in Wood Frame Construction', In Proceedings of the 11th Thermal Performance of the Exterior Envelopes of Whole Buildings. Clearwater Beach, USA. (CD-ROM)
- Langmans, J., Klein R., De Paepe M., Eykens P. and Roels S., (2009), 'Potential of using windbreakers as air barrier in lightweight constructions'. In Proceedings of the 4th International Symposium

on Building and Ductwork Air tightness (BUILDAIR) / 30th AIVC conference. Berlin, Germany. (CD-ROM)

Leuven, 22. April 2013